

University of St Andrews



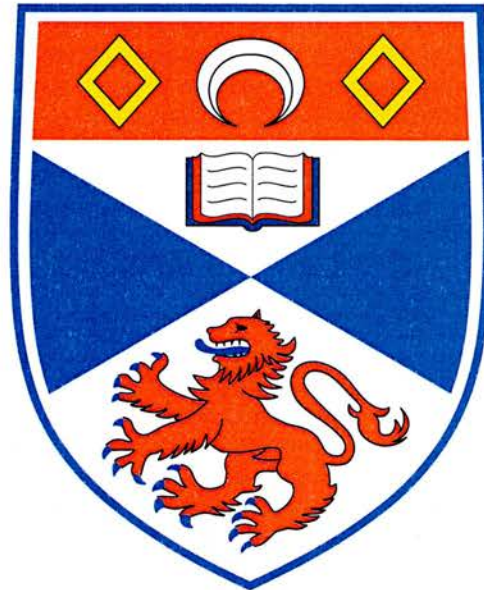
Full metadata for this thesis is available in
St Andrews Research Repository
at:

<http://research-repository.st-andrews.ac.uk/>

This thesis is protected by original copyright

Magnetohydrodynamic Oscillations in the Solar Corona

Gavin Robertson Donnelly



Thesis submitted for the degree of Doctor of Philosophy
of the University of St Andrews

8 March 2006



Abstract

The aim of this thesis is to explore the oscillatory properties of coronal structures through theoretical modelling. We consider structures such as a magnetic flux tube or coronal loop arcade. These structures are found to support a wide range of magnetohydrodynamic modes of oscillation. Observations have recently shown directly the occurrence of many of these modes of oscillation. As with any wave mode, the oscillations present in the corona carry information about the medium in which the wave propagates. Combining the knowledge and understanding obtained through research into theoretical wave models and the detailed observational data currently available, it is possible to extract the information the observed wave carries about the medium it resides in. This method, known as coronal seismology, allows in some cases the determination of plasma parameters which are not otherwise determined by direct observation.

The first structure we consider in Chapter 2 is a uniform flux tube embedded in a homogeneous environment, following Edwin and Roberts (1983). The tube can be defined by variations in plasma pressure, temperature, density and magnetic field strength, but remains in total pressure balance. The magnetic flux tube is modelled using cylindrical coordinates and the linearised equations of magnetohydrodynamics are employed. Transcendental dispersion relations and the associated eigenfunctions are derived, and these are examined in detail in two cases: the $\beta = 0$ and $\beta \neq 0$ plasmas. The $\beta = 0$ plasma permits a study of the fast modes only while the $\beta \neq 0$ plasma gives rise to both fast and slow modes.

In Chapter 3 a study of the trapped oscillatory modes of a line-tied longitudinally structured magnetic flux tube embedded in a longitudinally structured environment is carried out. In previous theoretical studies of this type, a longitudinally homogeneous environment is assumed; here we consider the role of chromospheric layers in the tube and in its environment. This is a first step towards understanding the role of footpoint structuring on the modes of oscillation. As a result of structuring, the cutoff frequency for trapped modes is modified: the fundamental kink mode becomes leaky for certain parameters, so the loop is unable to sustain any trapped fast modes.

For Chapter 4 we move away from the study of an isolated flux tube and look at a coronal arcade. We model the arcade as a 2D cartesian structure with magnetic field lines fixed in the dense photospheric surface. The $\beta = 0$ approximation is used so the slow mode is eliminated from the system. The influence of longitudinal structuring is examined and comparisons made with the uniform arcade. It is found that the introduction of longitudinal structuring results in modifications to oscillatory frequency and in particular to the ratio of the periods of the fundamental mode and its first harmonic. This is a quantity recently identified to be of use in coronal seismology. The additional structuring of the equilibrium also causes modifications to the behaviour of the

eigenfunctions and allows for mode interactions at avoided crossings.

Chapter 5 returns to the study of an isolated line-tied loop similar to that of Chapter 3. However, the aim of this chapter (as in Chapter 4) is to examine the influence of longitudinal structuring. It is again found that the main effect of the external structuring is to alter the cutoff frequency of trapped modes while the internal structuring results in modifications to the oscillatory frequency. In comparisons with a uniform loop it is found that the best agreement between a structured and a uniform model is obtained when the integrated density profiles of the stratified loop and the uniform loop are matched inside and outside the loop.

Declaration

I, Gavin R. Donnelly, hereby certify that this thesis, which is approximately 40,000 words in length, has been written by me, that it is the record of work carried out by me and that it has not been submitted in any previous application for a higher degree.

08/03/2006

Date: **Signature of Candidate:**

I was admitted as a research student in September 2002 and as a candidate for the degree of Doctor of Philosophy in September 2003; the higher study for which this is a record was carried out in the University of St Andrews between 2002 and 2006.

Date: 08/03/2006 **Signature of Candidate:**

In submitting this thesis to the University of St Andrews I understand that I am giving permission for it to be made available for use in accordance with the regulations of the University Library for the time being in force, subject to any copyright vested in the work not being affected thereby. I also understand that the title and abstract will be published, and that a copy of the work may be made and supplied to any bona fide library or research worker.

Date: 08/03/2006 **Signature of Candidate:** .

I hereby certify that the candidate has fulfilled the conditions of the Resolution and Regulations appropriate for the degree of Doctor of Philosophy in the University of St Andrews and that the candidate is qualified to submit this thesis in application for that degree.

08/03/2006

Date: **Signature of Supervisor:** ...

Acknowledgements

The assistance and guidance from my supervisor Prof Bernard Roberts has been very much appreciated. Also special thanks to Dr Antonio Díaz who has provided so many good ideas and always had time to discuss my work. They both have been excellent friends and colleagues and I have very much enjoyed working with them.

Thanks also to my Mum, Dad and brother Iain who must feel they too have studied solar physics for the past three years. The support and encouragement they provided on a daily basis has kept me going through my ups and downs.

Duncan McGregor and James McLaughlin, who I have shared an office with for the past three years also deserve my thanks. They created a great atmosphere in the office and I couldn't have asked for nicer people to spend my days with.

Contents

1	Introduction	1
1.1	The Sun	1
1.1.1	Interior	1
1.1.2	Atmosphere	2
1.2	Oscillations	4
1.2.1	TRACE	5
1.2.2	SUMER	7
1.2.3	SECIS	8
1.3	MHD equations	9
1.3.1	Ideal MHD equations	10
1.3.2	Equilibrium state	11
1.3.3	Wave speeds	12
1.3.4	Linearised MHD equations	13
1.3.5	MHD equation simplification	14
1.3.6	Plasma β	16
1.3.7	Equations in the zero β limit	17
1.3.8	MHD boundary conditions	17
1.4	Method used for structured loop	19
1.4.1	Sturm-Liouville theorem	19
1.4.2	Separation of variables	20
1.4.3	Radial structuring	21
1.4.4	Runge-Kutta method	23
1.4.5	Dispersion relation	23
1.5	MHD waves in a homogeneous medium	26
1.5.1	Alfvén mode	27
1.5.2	Fast and slow modes	28

1.6	Thesis outline	29
2	The Edwin and Roberts Model	31
2.1	Edwin and Roberts (1983)	32
2.2	Derivation of governing equations	33
2.3	Uniform flux tube embedded in a uniform medium	35
2.4	Dispersion relation	38
2.5	Eigenfunctions	39
2.5.1	Displacement of the tube centre	41
2.5.2	Shear motions	42
2.5.3	Relations between pressures	42
2.5.4	Forces	43
2.6	Cold plasma	44
2.6.1	Dispersion diagram $\beta = 0$	45
2.6.2	Eigenfunctions $\beta = 0$	48
2.6.3	Long wavelength limit	48
2.6.4	Short wavelength kink modes	51
2.6.5	Short wavelength sausage modes	57
2.6.6	Characterizing the sausage and kink modes	59
2.7	$\beta \neq 0$	59
2.7.1	Fast mode eigenfunctions	60
2.7.2	Slow modes	67
2.7.3	Sausage mode	71
2.8	Conclusions	75
2.8.1	What is the difference between a slow sausage or kink mode?	75
2.8.2	What is the difference between fast and slow modes for sausage or kink modes?	75
3	Line Tying and Longitudinal Structuring	76
3.1	Introduction	76
3.2	Equilibrium and basic equations	77
3.3	Analytical method	80
3.4	Uniform loop	82
3.4.1	Dependence on loop radius a	85
3.4.2	Dependence on chromospheric depth	87

3.4.3	Unrealistic chromospheric densities	94
3.5	Non-uniform loop	96
3.5.1	Case 1	97
3.5.2	Case 2	103
3.6	Conclusions	109
4	Arcade	110
4.1	Introduction	110
4.2	Equilibrium and basic equations	112
4.3	Analytical method	113
4.4	Results	114
4.4.1	Homogeneous medium	114
4.4.2	Case: 1 an exponential profile	116
4.4.3	Numerical results	124
4.4.4	Analytical work	126
4.4.5	Case 2 an exponential profile with uniform region	128
4.4.6	Changing W	136
4.5	Comparison with observations	138
4.6	Conclusions	138
5	Exponential Loop Profile	141
5.1	Introduction	141
5.2	Case 1: the exponentially stratified corona	142
5.2.1	Uniform loop and environment	144
5.2.2	Stratified loop	146
5.2.3	Changing $\rho_i(L)/\rho_i(0)$	153
5.2.4	Stratified environment	154
5.2.5	Changing $\rho_e(L)/\rho_e(0)$	157
5.2.6	Stratification in both loop and environment	158
5.3	Varying the magnitude of stratification	159
5.4	Case 2: the exponentially stratified chromosphere	162
5.4.1	Stratified loop	162
5.4.2	Changing a	162
5.4.3	Changing W	163
5.4.4	Stratified environment	165

5.4.5	Changing a	165
5.4.6	Changing W	166
5.5	Stratification in both loop and environment	167
5.5.1	Changing a	167
5.5.2	Changing W	168
5.6	Conclusions	169
6	Conclusions	170
6.1	Future work	176
6.1.1	Longitudinal flows	176
6.1.2	Azimuthal symmetry	176
6.1.3	Radial profiles	176
A	Derivation of equation (3.30)	178
B	Expansions for the solutions of equations (4.28) and (4.29)	180
C	The arcade dispersion relation	182
D	Derivation of solution (4.24)	185
E	Derivation of dispersion relation (4.44)	187
	Bibliography	190

Chapter 1

Introduction

1.1 The Sun

The Sun is our closest star by a great distance (4.2 light years) and provides an ideal opportunity to study a typical middle aged G2 V spectral class yellow dwarf. Its colossal size (radius $R_{\odot} \approx 696000\text{km}$) is composed of 92% hydrogen, 7.8% helium and trace elements oxygen, carbon, nitrogen, neon and iron to name a few. These elements are in what is often thought of as the fourth state of matter, a plasma, which is an ionised gas. Therefore the ions and electrons move freely but the plasma remains closely charge neutral. The energy to maintain such extreme temperatures to ionise this material is provided by the central fusion reaction operating at this stage in the Sun's life cycle, combining hydrogen to produce helium. See Priest (1982), Goedbloed (1983) and Lang (2001) for extensive reviews.

1.1.1 Interior

The solar interior can be roughly broken up into three concentric spheres each categorised by the method of energy transport. Firstly, the central *core* is a fusion reactor stretching to $0.25R_{\odot}$; it has a typical temperature of the order 10^7K and mainly emits at the gamma ray wavelength. Above the core is the *radiative zone* where energy is slowly propagated outward by radiative diffusion to approximately $0.7R_{\odot}$, where convective processes take over in the outer most region of the solar interior known as the convective zone. See Fig. 1.1.

The solar interior is optically thick so photons emitted in the core take on average 10^7 years to reach the surface. The processes of absorption and emission (which occurs many times) results in the reduction in frequency of the γ rays produced in the core to the visible spectrum. As a result

of the optically thick nature of the solar interior direct observations are impossible and therefore we rely on indirect methods, such as helioseismology (e.g. Kosovichev, 2003). Helioseismology studies the internal acoustic modes of the Sun, providing us with valuable information such as the differential rotation depending on latitude and also depth, with the core rotating as a solid body. This is displayed in Fig. 1.2 showing the rapidly rotating equator (shown in red) in contrast to the slow motions of the poles (coloured blue).

At the bottom of the convective zone lies a region known as the *tachocline* where it is believed the magnetic dynamo resides (Spiegel and Weiss, 1980, Ossendrijver, 2003). This is the mechanism by which the Sun's large-scale (and possibly the small-scale) magnetic field is maintained and manipulated (Ossendrijver, 2003). Much of solar activity, especially in the atmosphere, is dominated by magnetic field which follows an approximate eleven year cycle marking highs and lows in activity (Priest, 1982). Also every twenty-two years the polarisation of the Sun's magnetic field is reversed.

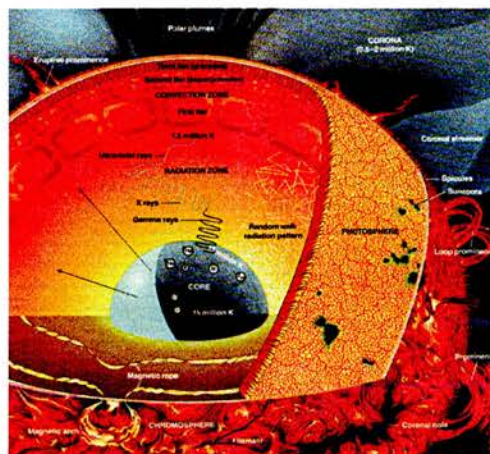


Figure 1.1: Schematic showing the different layers of the solar interior and atmosphere, together with some solar phenomena.

1.1.2 Atmosphere

The solar atmosphere can be conveniently separated into three regions: the *photosphere*, *chromosphere* and *corona*. The photosphere is the thin layer (500 km) representing the visible surface of the Sun. This level is relatively cool (5800 K) and dense (10^{14} m^{-3}). Internal structure and activity manifest themselves on the photospheric surface in the form of granules, of roughly 1000 km in diameter with a life-time of 10 minutes, marking convective flows emerging from below. Also supergranules, of diameter 30000 km mark the tops of large scale convective cells. Also magnetic structures are seen in the photosphere, where intense flux tubes penetrate the solar surface in the

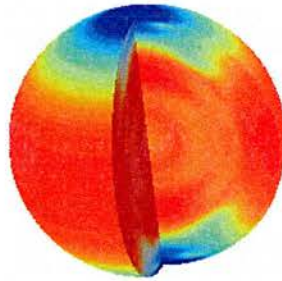


Figure 1.2: Spherical plot of the differential rotation of the Sun as a function of latitude and depth. Rotation rate is depicted by a red to blue scale representing rapid to slow rotation respectively.

form of sunspots with often several occurring in close proximity to form an active region.

Counter-intuitively, the temperature profile in the atmosphere (see Fig. 1.3) passes a local minimum at the top of the photosphere and thereafter begins a steady increase in the chromospheric layer, followed by a rapid increase over the transition region. The corona is the outer most section of the Sun's atmosphere and will be described more fully below. From the corona flows the solar wind, a streaming of coronal material into interplanetary space. We can see the interaction of the solar wind and Earth's atmosphere in the form of auroras and geomagnetic storms, occurring especially during periods of heightened solar activity.

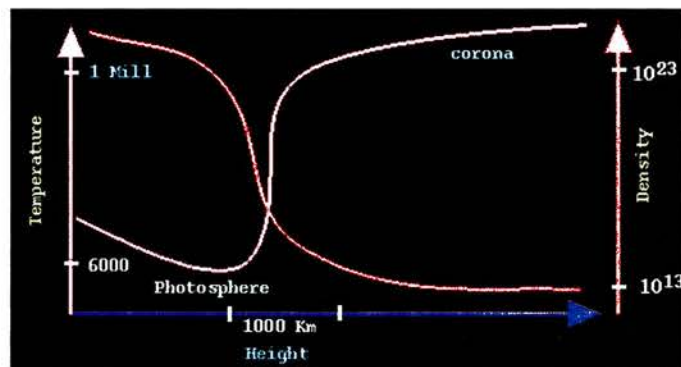


Figure 1.3: Temperature profile as a function of the radial coordinate from the centre to the outer layers of the atmosphere of the Sun.

The outer most layer of the solar atmosphere is known as the corona. As a result of its low level of emission compared with the dazzling photosphere, it cannot generally be seen in white light. However, the solar corona is visible to the naked eye during an eclipse or the same effect can be archived using a coronagraph (Gallagher et al., 1997, Schultz et al., 2000). Early observers,

looking at the corona in white light, were baffled as to its composition, thinking they may have found new elements (Phillips, 1992). This was only resolved when it was discovered that the corona is at a temperature of order 10^6 K and so the main constituent elements, hydrogen and helium, are both fully ionised (as are the trace elements such as oxygen and nitrogen). However, some of the heavier ions like iron and calcium are able to retain a few electrons at such high temperatures. It is the emission lines from these heavier elements which were being observed and causing the confusion in the nineteenth century.

The corona is the layer of the Sun furthest away from the energy source in the core, so it seems counter-intuitive that it would be hotter than the lower levels of the atmosphere. In fact, there is a very rapid change in temperature between the chromosphere and corona over the transition region; this is illustrated in Fig.1.3. The details of how the corona is heated to such high temperatures is unknown and has become a long standing key problem of solar physics (Priest et al., 2000). The magnetic field is generally regarded as central to this problem, playing a role in mechanisms such as the dissipation of magnetohydrodynamic waves (Heyvaerts and Priest, 1983, Steinolfson and Davila, 1993, Ofman et al., 1994a,b, De Moortel et al., 2000a,b, Ruderman and Roberts, 2002, Goossens et al., 2002) and current dissipation (Parker, 1987, Priest and Forbes, 2000).

Aside from the heating aspect, there are many other interesting effects produced by the magnetic field. Regions of open magnetic field, where field lines are connected to interplanetary space, are called coronal holes and are predominantly a polar feature. From coronal holes, the solar wind - a streaming of charged particles along the magnetic field lines - flows. There are also regions where the magnetic field forms closed field lines, with both end points of the field line anchored in the photosphere. Closed regions are made of many coronal loops of differing dimensions, densities and temperatures. There are also many other structures in the corona: prominences, streamers, plumes, and so on (Priest, 1982). In this work we are concerned with the ability of coronal loops to support magnetohydrodynamic (MHD) oscillations and the properties of these oscillations.

1.2 Oscillations

Recent advances in solar observational technology have allowed increased spatial and temporal resolution both in space telescopes such as TRACE (Transition Region and Coronal Explorer) and SoHO (Solar and Heliospheric Observatory) and the ground-based telescope SECIS (Solar Eclipse Corona Imaging System). This has resulted in the first direct detection of many MHD waves in the solar atmosphere. The first temporally resolved longitudinal waves were detected by the Ultraviolet Coronagraph Spectrometer (UVCS) on board SoHO (Ofman et al., 1997). Other examples of such detections are: standing slow waves in a coronal loop, detected by the SUMER spectrometer on SoHO (Wang et al., 2002a,b,c, 2003) and identified as the slow MHD wave (Of-

man and Wang, 2002); transverse oscillations of coronal loops observed by TRACE (Aschwanden et al., 1999, Nakariakov et al., 1999); propagating slow modes in cool coronal loops observed in EUV (Nakariakov et al., 2000, Robbrecht et al., 2001, De Moortel et al., 2000c, 2002a,b,c,d). For a comprehensive review of these observations, see Aschwanden (2003, 2004), Nakariakov and Verwichte (2005). With the ability to detect these waves, we now have the opportunity to compare observational results with the long standing theoretical models, and in doing so we will extend our knowledge of the medium through which the waves are propagating, giving a coronal seismology (Roberts et al., 1984, Nakariakov et al., 1999, Nakariakov and Ofman, 2001, De Moortel, 2006).

Despite the corona being the outer layer of the Sun's atmosphere, it is the hottest region. This unexplained phenomena is known as the coronal heating problem and has been studied for decades but remains to be fully understood (Narain and Ulmschneider, 1990). One of the contributing factors to the extreme temperature of the corona is thought to be wave damping and so models are investigated to obtain estimates for the magnitude of the energy waves provide and by which processes waves are dissipated.

1.2.1 TRACE



Figure 1.4: An image of coronal loops obtained by TRACE.

The TRACE (Transition Region and Coronal Explorer) instrument (Handy et al., 1999) is a space-based telescope launched on the 2nd April 1998 in order to make detailed observations of the solar transition region and the corona in several passbands two of which are: EUV (Extreme Ultra-Violet) and UV (Ultra-Violet), at 171 \AA and 195 \AA . TRACE has a high spatial and temporal resolution with the ability to resolve structures at 1 arc sec and a cadence in the range 20-60 s,

providing observers with the capacity to resolve loop structures in such detail as shown in Fig. 1.4. These high spatial and temporal resolutions have allowed, for the first time, the detection of transverse oscillations of a coronal loop (Aschwanden et al., 1999). The first detection of oscillations was made in data from 14th July 1998. The oscillations were detected in a set of loops with lengths in the range $L=130\,000 \pm 30\,000$ km and temperatures of 1.0-1.5 MK, and were deemed to be flare excited standing waves of the fast kink mode with transverse displacement of 4100 ± 1300 km and period of 280 ± 30 s (Aschwanden et al., 1999). These modes are strongly damped during the 20 minute period of their detection when they were most prominent (Nakariakov et al., 1999).

Outwardly propagating intensity fluctuations have been found to be a common occurrence in large, quiescent coronal loops (De Moortel et al., 2002a,b,c,d) and have been identified as slow mode magnetoacoustic waves (Nakariakov et al., 2000, De Moortel et al., 2002b). These modes having two distinct period categories: 172 ± 32 s for those loops above sunspots, and 321 ± 74 s in the case of loops not above sunspots. Both waves are rapidly damped as they are not seen to propagate into higher regions of the loops, being detected over approximately 10 Mm range close to the loop footpoints (De Moortel et al., 2002c, McEwan and de Moortel, 2006). The oscillations are not associated with flare-like events and are thought to be driven by footpoint movements (De Moortel et al., 2002b).

Analysis of loop oscillations on 14th July 1998 (Nakariakov et al., 1999) revealed transverse oscillations of long ($130 \pm 6 \times 10^6$ m), thin (diameter $2 \pm 0.36 \times 10^6$ m) loops; the oscillations were flare excited. Identified as the global kink mode of the loop (Nakariakov et al., 1999), the displacement amplitude of this oscillation was in the range 2030 ± 580 km, with a peak velocity of the loop of 47 ± 14 km s⁻¹. These global kink oscillations were seen to have periods 258-320 s and dissipation occurred on timescale of 2 to 3 periods, the decay time determined to lie in the range 14.5 ± 2.7 min. Footpoint leakage is ruled out as the main dissipative mechanism for transverse oscillations (Nakariakov et al., 1999), as it occurs over timescales two orders of magnitude larger than the observed decay time, but resonant absorption, viscous and resistive dissipation seems a more feasible mechanisms (Nakariakov et al., 1999). However, viscous and resistive damping requires strongly enhanced shear viscosity coefficients of the same order of magnitude as the bulk viscosity coefficients if it is to match the observed times; such anomalous damping cannot be ruled out, but other mechanisms (e.g. phase mixing and resonant absorption) are actively being investigated.

From this observational data it was inferred that the Alfvén speed $v_A \approx 770 \pm 40$ km s⁻¹ and the kink speed (see Section 1.3) was deduced as $c_k \approx 1040 \pm 50$ km s⁻¹, based on the magnetic field being uniform and the loop defined by a density enhancement of one order of magnitude above its environment. The coronal shear viscosity dissipation coefficient was suggested to be eight to nine orders of magnitude larger than previously estimated (Nakariakov et al., 1999). TRACE data taken

on 4th July 1999 was also found to contain loop oscillations (Schrijver and Brown, 2000). The detection was made at 8:21 UT, after a solar flare, and after a gap in the data of roughly 1 decay time (Nakariakov et al., 1999) detection resumed. Three loops, oscillating with approximately a 5 min period, were found. The two most prominent loops had maximum displacements of 3000 km and 6700 km, but it is thought these are values arose following oscillation decay and so would have been larger at the onset of the oscillation. The two prominent loops exhibit oscillations that are roughly in phase and the third loop was in antiphase (Schrijver and Brown, 2000).

1.2.2 SUMER

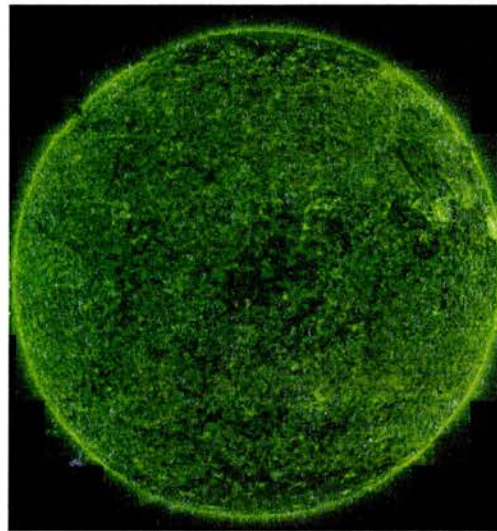


Figure 1.5: The Sun seen in the emission line of Neon VIII at 770.4 Å (corona, temperature 600 000 K). The picture was put together from eight horizontal raster scans in alternating directions and of different length, starting in the solar SE. Each raster scan includes 664 to 1074 exposures, lasting 7.5 seconds each. The picture is shown in bins of 3x3 pixels, one pixel being approximately 1 arcsec². Some image corrections were performed and most data faults were eliminated by replacing them with the average of their neighbours (approximately 4 per 1000 raster steps). The brightest pixels in this picture correspond to an intensity of approximately 260 counts/line/arcsec² whereas the intensity is generally below 40. The average intensity on the disk is around 6.

The Solar Ultraviolet Measurement of Emitted Radiation (SUMER) is one of several instruments on board the Solar and Heliospheric Observatory (SoHO) (Wilhelm et al., 1995). It is a spectrometer capable of high cadence observations. The SoHO spacecraft has provided valuable observational data since its launch on 2nd December 1998. Within the data from SUMER many examples of oscillations in coronal structures such as coronal loops have been detected. It has been found that damped Doppler shift oscillations detected by SUMER in hot coronal loops generally have periods of 7-31 min and damping times of 6-37 min (Wang et al., 2003). Analysis from three dates, 9th March 2001, 6th November 1999 and 29th September 2000, were examined to find

oscillatory behaviour in hot ($\sim 10^7$ K) coronal loops (Wang et al., 2002a).

On 9th March 2001 flux enhancements in hot loops were observed with no detection below 2×10^6 K and no associated flare. A loop was determined to be of length 140 Mm with sound speed 295 km s^{-1} and temperature 6×10^6 K (Wang et al., 2002a). The period of the oscillation was in the range 14-18 min; this suggests a slow mode standing wave, which has a calculated theoretical period of 15.8 min under the given loop conditions. The incompressible Alfvén and almost incompressible kink modes were excluded because their theoretically predicted periods were in the range 3-4 min; however, the lack of brightness fluctuation points to an incompressible or weakly compressible mode. It has been concluded that slow standing modes occur (Wang et al., 2002a, 2003, Wang, 2004). The 6th November 1999 event gave an oscillation of period 11.7 min and was flare excited.

On 29th September 2000, four oscillatory events were observed in hot coronal loops. All four events began with a strong red shift. The oscillations following the second flare had period 25-31 min, which is close to that of an expected slow standing wave; a decay time of 8.8-28.9 min (Wang et al., 2002a) was obtained. It was suggested that these events did not cause substantial changes to the loop system (Wang et al., 2002a).

On 15th April 2002, two oscillation events were detected following a flare (Wang et al., 2003). It was established that these were compressive standing slow modes. The first was of period 16 min, with a decay time of 11.4 min. The second event, observed in both Doppler and intensity oscillations, lasted for about five periods. The Doppler velocities were in the range $18.0 \pm 1.5 \text{ km s}^{-1}$, with period 17.6 ± 0.1 min and decay time 36.8 ± 2.6 min; the intensity oscillations had period 17.1 ± 0.1 min and decay time 21.0 ± 1.6 min. A quarter period phase shift between the Doppler and intensity oscillations was observed which theoretically points to a standing mode (Wang et al., 2003). The difference in decay times is suspected to be as a result of a plasma density one or two orders of magnitude greater than previously thought. Numerical simulations by Ofman and Wang et al. (2002a) of oscillations in hot coronal loops have been found to agree well with the observational data; Ofman and Wang (2002) conclude that the dominant damping mechanism is thermal conduction.

1.2.3 SECIS

The Solar Eclipse Coronal Imaging System (SECIS) is a ground-based observational system for use during a solar eclipse or a coronagraph which archives the same effect by artificially blocking the rays from the solar disk (Phillips et al., 2000). Its purpose is to search for high frequency modulations in the solar corona. To achieve this a high cadence is required as well as high spatial resolution; SECIS has the capability of taking 70 images per second. The spatial resolution is

dependent on which of the two passbands the observations are being made; in the Fe XIV (or green line) passband length scales can be resolved to 4.07 arcsec and in white light 4.04 arcsec. Images can be recorded simultaneously and are of the same region in both passbands and have the capacity to store about four mins of observations. The first version of the SECIS instrument was used during the eclipse on 26th February 1998: further versions of the SECIS instrument have since been developed and tested against Yohkoh and TRACE data (Phillips et al., 2000, Williams et al., 2001, 2002, Katsiyannis et al., 2003).

During the eclipse on the 11th of August 1999, SECIS made observations for a duration of 2 min 23.5 s from the Bulgarian Air Force Base in Shabla, Bulgaria. 6364 images were taken at a frame rate of 44 Hz. Analysis of the first 1800 frames (40 sec) revealed oscillations of period 6 sec (Williams et al., 2001). This wave was later determined to be an impulsively generated fast magnetoacoustic wave which propagated along a coronal loop (Williams et al., 2002). The observed propagation speed, of 2100 km s^{-1} , has been interpreted by Williams et al. (2002) to be the group velocity of a fast magnetoacoustic mode. Williams et al. (2002) also suggest that the group velocity and the phase velocity are comparable; based on this assumption the wavelength of this mode would be $1.2 \times 10^4 \text{ km}$. The loop had 2.5 times higher density than its surroundings but approximately the same temperature of $2.5 \times 10^6 \text{ K}$, which underwent little variation along the loop. Through coronal seismology, the local magnetic field strength was estimated to be 25 G (Williams et al., 2002).

1.3 MHD equations

The material present in much of the Sun is under such extreme pressure and temperature conditions that it is almost fully ionised (only some of the heavier elements retain some electrons), meaning that ions and electrons move freely but it is assumed it remains in quasi-neutrality. Material in such a state is said to be a plasma. The abundance of free charges present in a plasma results in them having a significant influence over the behaviour of the system and must be accounted for in the governing equations, by combining Maxwell's equations for electromagnetism and the Navier-Stokes equations of fluid dynamics.

In order to model the solar plasma we use the MHD equations, combining the equations of electromagnetism and fluid dynamics through Ohm's law. The MHD equations are a set of coupled nonlinear second order partial differential equations for a single fluid. A fluid model removes all kinetic effects by considering the plasma as a continuous medium and so restricts the length scales which can be considered to be greater than the typical kinetic length scales, such as the Larmor radius. The MHD equations have already had many simplifications. For example, there are no quantum effects or relativistic corrections; this restricts the speeds the model can describe to be

much less than the speed of light. Also the displacement current is neglected in Ampere's law, which eliminates the electromagnetic waves. Further simplifications would result in the loss of fundamental plasma properties which we wish to study, although it is generally useful to remove all but the central effect you are interested in to obtain a more simplistic model. In more complex models it is possible to represent a plasma as a two fluid model, treating the ions and electrons separately, or as a kinetic model (the MHD equations can be derived directly from the kinetic equations by means of averaging over velocity space).

Although the MHD equations provide us with a simplified description of the behaviour of a plasma analytical solutions to this set of equations are few and far between and therefore further simplification is necessary if an analytical approach is to be taken. The first of these simplifications is to consider the ideal MHD equations, which neglect all dissipative terms. Also simplifications can be made based on the aspect of plasma behaviour to be modelled; for example, to carry out a wave analysis of a particular equilibrium it is useful to allow small perturbations about this equilibrium and then take advantage of the linearised MHD equations (Lighthill, 1978, Cowling, 1976).

1.3.1 Ideal MHD equations

The following set of equations are the ideal MHD equations in which all dissipative terms have been removed. The equations are for the following variables: \mathbf{v} is the plasma velocity, \mathbf{j} the current density, \mathbf{B} the magnetic induction (normally called the magnetic field), \mathbf{E} the electric field, P the plasma pressure, T the plasma temperature, ρ the plasma density, R the gas constant and t time.

The equation of motion is given by

$$\rho \frac{D\mathbf{v}}{Dt} = \rho \left(\frac{\partial \mathbf{v}}{\partial t} + \mathbf{v} \cdot \nabla \mathbf{v} \right) = -\nabla P + \mathbf{j} \times \mathbf{B}, \quad (1.1)$$

which essentially states that the net force is equal to mass times acceleration. We will not include gravity in any of our models. The ideal induction equation, describing how the magnetic field is advected with plasma motions, is

$$\frac{\partial \mathbf{B}}{\partial t} = \nabla \times (\mathbf{v} \times \mathbf{B}), \quad (1.2)$$

with the implication that plasma moves freely along field lines but drags the magnetic field during transverse motions (Alfvén, 1943). The induction equation is complemented with the solenoidal condition (indicating there exists no magnetic monopoles),

$$\nabla \cdot \mathbf{B} = 0. \quad (1.3)$$

The equation of mass continuity, stating that mass cannot be created nor destroyed, is

$$\frac{\partial \rho}{\partial t} + \nabla \cdot (\rho \mathbf{v}) = 0. \quad (1.4)$$

The adiabatic energy equation, which implies that there is no gain or lose of energy from the system, is

$$\frac{\partial P}{\partial t} + \mathbf{v} \cdot \nabla P = \frac{\gamma P}{\rho} \left(\frac{\partial \rho}{\partial t} + \mathbf{v} \cdot \nabla \rho \right). \quad (1.5)$$

In the equation of motion (1.1) it can be seen that there are two forces acting on the plasma: those from the plasma pressure, $-\nabla P$, and the magnetic force $\mathbf{j} \times \mathbf{B}$. The magnetic force can be expressed in the form

$$\mathbf{j} \times \mathbf{B} = (\mathbf{B} \cdot \nabla) \frac{\mathbf{B}}{\mu} - \nabla \left(\frac{B^2}{2\mu} \right) \quad (1.6)$$

where $\frac{B^2}{2\mu}$ represents the magnetic pressure, denoted by P_m , and $(\mathbf{B} \cdot \nabla) \frac{\mathbf{B}}{\mu}$ is the magnetic tension force, denoted by \mathbf{M}_T . Therefore we can define the total pressure as the sum of the plasma and magnetic pressures; $P_T = P + P_m$. We can then express the equation of motion in the form

$$\rho \frac{D\mathbf{v}}{Dt} = -\nabla P_T + (\mathbf{B} \cdot \nabla) \frac{\mathbf{B}}{\mu} = -\nabla P_T + \mathbf{M}_T. \quad (1.7)$$

1.3.2 Equilibrium state

An equilibrium is a state in which the plasma is under force balance. In ideal MHD this means the plasma pressure force must match magnetic forces. So, for example, taking a uniform magnetic tube of radius a , aligned with the z axis, of constant density ρ_i , pressure P_i , temperature T_i and magnetic field strength B_i , with the equivalent values in the exterior denoted by a subscript 'e', then, from the equation of motion (1.7) it is required that

$$P_i + \frac{B_i^2}{2\mu} = P_e + \frac{B_e^2}{2\mu}; \quad (1.8)$$

the loop is in pressure balance with its environment. Throughout the following chapters static equilibria are considered. However, special cases can be found where the equilibrium is not static. For example, it is possible to allow for field aligned flows in the loop interior or exterior; for an in-depth discussions of this case and the nature of its oscillation, see Nakariakov and Roberts (1995b); Somasundaram et al. (1999); Terra-Homem et al. (2003).

1.3.3 Wave speeds

Within the basic equilibrium there are several local speeds which can be defined; they characterize the propagation speeds of many of the basic modes oscillation. We also give typical values in our main area of interest, the solar corona. Firstly the local sound speed is denoted by c_0 and defined by

$$c_0 = \left(\frac{\gamma P_0}{\rho_0} \right)^{\frac{1}{2}} \quad (1.9)$$

where P_0 and ρ_0 are the equilibrium pressure and density and γ is the ratio of specific heats. The sound speed has a typical coronal value of $c_0 = 150 - 200 \text{ km s}^{-1}$ and is the characteristic speed of acoustic waves in a homogeneous medium.

The local Alfvén speed v_A is defined by

$$v_A = \left(\frac{B_0^2}{\mu \rho_0} \right)^{\frac{1}{2}} \quad (1.10)$$

where B_0 is the strength of the equilibrium magnetic field and μ is the magnetic permeability of free space; v_A is generally thought to be in the range of $1000 - 2500 \text{ km s}^{-1}$ in the corona. The Alfvén speed is the speed with which an Alfvén wave propagates along the magnetic field lines in a homogeneous magnetised plasma.

The tube (or cusp) speed c_T is defined from c_0 and v_A by

$$c_T = \frac{c_0 v_A}{(c_0^2 + v_A^2)^{\frac{1}{2}}}; \quad (1.11)$$

it should be noted that the tube speed is less than both the sound speed c_0 and the Alfvén speed v_A . In the corona, the tube speed can take values in the range $c_T = 140 - 200 \text{ km s}^{-1}$.

The fast speed c_F is defined by

$$c_F = (c_0^2 + v_A^2)^{\frac{1}{2}} \quad (1.12)$$

and so is the square root of the sum of the squares of the sound and Alfvén speeds. This is associated with the propagation of a fast magnetoacoustic mode across to the applied magnetic field in a homogeneous unbounded medium, and takes a value in the range $c_F = 1000 - 2000 \text{ km s}^{-1}$ based on the typical values of the sound and Alfvén speeds in the corona.

The kink speed c_k (Ionson, 1978) arises through

$$c_k = \left(\frac{\rho_0 v_A^2 + \rho_e v_{Ae}^2}{\rho_0 + \rho_e} \right)^{\frac{1}{2}}; \quad (1.13)$$

this is important in the propagation of kink modes in a magnetic flux tube (Edwin and Roberts, 1983) or in surface waves on a magnetic interface (Roberts, 1981). Subscripts are used to denote different regions: the plasma density in the environment region is ρ_e and the Alfvén speed in that region is v_{Ae} . The speed c_k is independent of the sound speed.

Assuming a density enhancement of $\rho_0 = 10\rho_e$, a uniform magnetic field ($B_0 = B_e$) and a tube Alfvén speed of $v_A = 1000 \text{ km s}^{-1}$ in an environment with Alfvén speed $v_{Ae} = 3000 \text{ km s}^{-1}$, a typical coronal value of the kink speed is $c_k = 1350 \text{ km s}^{-1}$.

The speeds defined here can be separated into two categories, the fast speeds characterizing the fast wave modes and the slow speeds associated with the slow modes. Which speeds fall into each category depends on the nature of the medium, except for the fast speed c_F (which is always associated with the fast mode). Under coronal conditions the Alfvén and kink speeds are the fast speeds and the sound and tube speeds are the slow speeds. However, in some photospheric regions the sound speeds may exceed the Alfvén speed and so the association with fast and slow modes is there reversed.

1.3.4 Linearised MHD equations

In many wave analyses (Goedbloed, 1983, Roberts, 1985) it is useful to consider small amplitude oscillations about an equilibrium. Here we consider a general spatially structured static equilibrium state which satisfies the nonlinear MHD equations (1.1) to (1.3). Equilibrium quantities are denoted by a subscript '0', $\mathbf{B}_0(\mathbf{r})$, $\rho_0(\mathbf{r})$ and $P_0(\mathbf{r})$ denote the magnetic field, density and plasma pressure respectively. The equilibrium is then perturbed by small quantities, with perturbations denoted by a subscript '1' :

$$\mathbf{B}(\mathbf{r}, t) = \mathbf{B}_0(\mathbf{r}) + \mathbf{B}_1(\mathbf{r}, t), \quad (1.14)$$

$$\mathbf{v}(\mathbf{r}, t) = \mathbf{0} + \mathbf{v}_1(\mathbf{r}, t), \quad (1.15)$$

$$\rho(\mathbf{r}, t) = \rho_0(\mathbf{r}) + \rho_1(\mathbf{r}, t), \quad (1.16)$$

and

$$P(\mathbf{r}, t) = P_0(\mathbf{r}) + P_1(\mathbf{r}, t). \quad (1.17)$$

We now linearise the MHD equations about the equilibrium, neglecting squares or products (and higher order terms) of small quantities:

$$\rho_0 \frac{\partial \mathbf{v}_1}{\partial t} = -\nabla P_1 + \frac{1}{\mu} (\nabla \times \mathbf{B}_1) \times \mathbf{B}_0 + \frac{1}{\mu} (\nabla \times \mathbf{B}_0) \times \mathbf{B}_1, \quad (1.18)$$

$$\frac{\partial \mathbf{B}_1}{\partial t} = \nabla \times (\mathbf{v}_1 \times \mathbf{B}_0), \quad (1.19)$$

$$\frac{\partial \rho_1}{\partial t} + (\mathbf{v}_1 \cdot \nabla) \rho_0 + (\nabla \cdot \mathbf{v}_1) \rho_0 = 0, \quad (1.20)$$

$$\frac{\partial P_1}{\partial t} + (\mathbf{v}_1 \cdot \nabla) P_0 = c_0^2 \left(\frac{\partial \rho_1}{\partial t} + (\mathbf{v}_1 \cdot \nabla) \rho_0 \right) \quad (1.21)$$

and

$$\nabla \cdot \mathbf{B}_1 = 0. \quad (1.22)$$

The linearised magnetic tension force is

$$(\mathbf{B}_0 \cdot \nabla) \frac{\mathbf{B}_1}{\mu} + (\mathbf{B}_1 \cdot \nabla) \frac{\mathbf{B}_0}{\mu} \quad (1.23)$$

and the linearised total pressure is

$$P_T = P_1 + \frac{\mathbf{B}_0 \cdot \mathbf{B}_1}{\mu}. \quad (1.24)$$

Thus we can write the linearised equation of motion as

$$\rho_0 \frac{\partial \mathbf{v}_1}{\partial t} = -\nabla P_T + (\mathbf{B}_0 \cdot \nabla) \frac{\mathbf{B}_1}{\mu} + (\mathbf{B}_1 \cdot \nabla) \frac{\mathbf{B}_0}{\mu}. \quad (1.25)$$

1.3.5 MHD equation simplification

The following sections outline the methods used when we consider longitudinal structuring of a loop. This is the same method as employed by Díaz (2004). A homogeneous equilibrium pressure and magnetic field are considered. We take the equilibrium magnetic field to be aligned with the z -axis. We now manipulate the linearised MHD equations (under these conditions) into a form that is easier to work with. The linearised equation of motion (1.25) takes the form

$$\rho_0 \frac{\partial \mathbf{v}_1}{\partial t} = -\nabla P_T + \frac{B_0}{\mu} \frac{\partial \mathbf{B}_1}{\partial z}. \quad (1.26)$$

The induction equation (1.19) can be written in the form

$$\frac{\partial \mathbf{B}_1}{\partial t} = \mathbf{v}_1(\nabla \cdot \mathbf{B}_0) + (\mathbf{B}_0 \cdot \nabla)\mathbf{v}_1 - \mathbf{B}_0(\nabla \cdot \mathbf{v}_1) + (\mathbf{v}_1 \cdot \nabla)\mathbf{B}_0. \quad (1.27)$$

The assumption of a uniform equilibrium magnetic field parallel to the z direction reduces this equation to

$$\frac{\partial \mathbf{B}_1}{\partial t} = B_0 \frac{\partial \mathbf{v}_1}{\partial z} - \mathbf{B}_0(\nabla \cdot \mathbf{v}_1). \quad (1.28)$$

As the equation mass continuity (1.20) is not dependent on derivatives of magnetic equilibrium or magnetic or pressure quantities, it is unchanged. However, the energy equation reduces to

$$\frac{\partial P_1}{\partial t} = c_0^2 \left(\frac{\partial \rho_1}{\partial t} + (\mathbf{v}_1 \cdot \nabla)\rho_0 \right). \quad (1.29)$$

We may eliminate the perturbed magnetic field \mathbf{B}_1 and density ρ_1 in favour of the perturbed total pressure and velocity. First we eliminate the perturbed magnetic field between the equation of motion (1.26) and the induction equation (1.27) (which requires z and t derivatives to be taken), resulting in the equation

$$\rho_0 \frac{\partial^2 \mathbf{v}_1}{\partial t^2} = -\nabla \frac{\partial P_T}{\partial t} + \frac{B_0^2}{\mu} \frac{\partial^2 \mathbf{v}_1}{\partial z^2} - \mathbf{e}_z \frac{B_0^2}{\mu} \frac{\partial}{\partial z} \nabla \cdot \mathbf{v}_1. \quad (1.30)$$

Now, taking the perpendicular components, denoted by a subscript ' \perp ', and using a cylindrical coordinate system (which will be needed later as we will consider cylindrical structures), with the applied magnetic field aligned with the z -axis, we express $\mathbf{v}_1 = \mathbf{v}_\perp + v_z \hat{\mathbf{z}}$. We obtain the first of the equations we will work with later:

$$\rho_0 \left[\frac{\partial^2}{\partial z^2} - v_A^2 \frac{\partial^2}{\partial z^2} \right] \mathbf{v}_\perp = -\nabla_\perp \frac{\partial P_T}{\partial t}. \quad (1.31)$$

Next, eliminating the perturbed density between the energy and mass continuity equations we find

$$\frac{\partial P_1}{\partial t} = -c_0^2 \rho_0 \nabla \cdot \mathbf{v}_1. \quad (1.32)$$

Adding this to the z component of the induction equation multiplied by B_0/μ , we obtain the second of the equations we desire:

$$\frac{\partial P_T}{\partial t} = -\rho_0 c_F^2 \nabla \cdot \mathbf{v} + \rho_0 v_A^2 \frac{\partial v_z}{\partial z}. \quad (1.33)$$

Finally, by eliminating the perpendicular components of the velocity between the z derivative of

equation (1.33) multiplied by v_A^2 and the z component of equation (1.30) multiplied by c_F^2 , we obtain

$$\rho_0 \left[\frac{\partial^2}{\partial t^2} - c_T^2 \frac{\partial^2}{\partial z^2} \right] v_z = - \frac{c_0^2}{c_F^2} \frac{\partial^2 P_T}{\partial z \partial t}. \quad (1.34)$$

Equations (1.31), (1.33) and (1.34) are valid for any density and speed profiles structured in both longitudinal and transverse directions, provided the product of the density and square of the speed profiles are constants with the implication that the equilibrium plasma pressure and the equilibrium magnetic field strength are constants. Equations (1.31), (1.33) and (1.34) have also been derived in Roberts (1991).

1.3.6 Plasma β

In all of the models we consider there are two forces acting upon the plasma, the plasma pressure gradient and magnetic forces. In many regions of the solar interior and atmosphere the plasma behaviour is dominated by one of these two forces. The plasma beta is a parameter which can be defined by making a comparison between the magnitudes of these effects:

$$\beta = \frac{\text{gas pressure}}{\text{magnetic pressure}} = \frac{P}{B^2/2\mu} \quad (1.35)$$

where the magnetic pressure comes from the Lorentz force $\mathbf{j} \times \mathbf{B}$. We can also write the plasma β as

$$\beta = \frac{2c_0^2}{\gamma v_A^2} \quad (1.36)$$

where $\gamma (= \frac{5}{3})$ is the adiabatic constant and c_0 and v_A are the local sound and Alfvén speeds. Using the typical coronal values of c_0 and v_A given in the previous section, we attain a typical coronal range for the plasma β of

$$\beta \approx 4.8 \times 10^{-2} - 4.3 \times 10^{-3}. \quad (1.37)$$

In regions of large plasma beta, plasma pressures effects dominate over those produced by the magnetic field; this is the case in the solar interior. If we move to the other extreme, where the beta is small, then this would represent a magnetically dominated environment such as the corona. In this case we can make an important simplification by assuming $\beta = 0$ and therefore entirely neglecting pressure effects; this is known as the cold plasma approximation (Priest, 1982).

Making the simplification $\beta = 0$ results in the model becoming considerably easier to deal with,

since the acoustic aspects of the oscillation have been eliminated (Díaz et al., 2004). Thus the slow mode is removed but the Alfvén and fast modes remain, and depending upon the geometry in the equilibrium these modes may decouple so no resonances between the two modes occurs.

1.3.7 Equations in the zero β limit

In the previous section the linear MHD equations have been reduced to the form

$$\rho_0 \left[\frac{\partial^2}{\partial t^2} - v_A^2 \frac{\partial^2}{\partial z^2} \right] \mathbf{v}_\perp = -\nabla_\perp \frac{\partial P_T}{\partial t} \quad (1.38)$$

$$\frac{\partial P_T}{\partial t} = -\rho_0 c_F^2 \nabla \cdot \mathbf{v} + \rho_0 v_A^2 \frac{\partial v_z}{\partial z} \quad (1.39)$$

and

$$\rho_0 \left[\frac{\partial^2}{\partial t^2} - c_T^2 \frac{\partial^2}{\partial z^2} \right] v_z = -\frac{c_0^2}{c_F^2} \frac{\partial^2 P_T}{\partial z \partial t}. \quad (1.40)$$

We now express this system of equations in the zero β limit. With $\beta = 0$, $c_0 = c_T = 0$ and $c_F = v_A$ and equation (1.40) is satisfied by $v_z = 0$, so there are no flows along the equilibrium magnetic field; this is also found from a previous equation before time derivatives are taken.

Eliminating the perpendicular velocity component \mathbf{v}_\perp from equation (1.38) dotted by ∇_\perp , and using equation (1.39) and integrating in time, we find the total pressure perturbation is governed by the three-dimensional wave equation

$$\left[\frac{\partial^2}{\partial t^2} - v_A^2 \nabla^2 \right] P_T = 0, \quad (1.41)$$

with equation (1.38) determining the behaviour of the perpendicular velocity components once the total pressure perturbation is known.

1.3.8 MHD boundary conditions

In any model boundary conditions are very important in order to capture the correct physics of the system the model represents. Commonly in MHD there are two types of boundary conditions: conditions which determine the behaviour across an interface separating plasmas of different properties, and conditions which prevent divergence of a solution at a singular point or prevent energy entering the system from the exterior. The second type of boundary condition is more specific to each model, and so is discussed when the need arise.

At a contact interface the equilibrium quantities experience a jump in moving between media of

different properties; we are interested in how the perturbed quantities behave across these boundaries. To establish the jump conditions (Goedbloed, 1983, Díaz, 2004) we write the nonlinear MHD equations in conservative form, from which it becomes apparent that there are two types of boundary condition, depending on whether the magnetic field is parallel or inclined to the interface.

First we consider an interface which is parallel to the magnetic field. Let $\hat{\mathbf{n}}$ be a unit vector that is normal to the interface, then $\hat{\mathbf{n}} \cdot \mathbf{B} = 0$. Then the boundary conditions are

$$\hat{\mathbf{n}} \cdot [\mathbf{v}] = \hat{\mathbf{n}} \cdot [\mathbf{B}] = 0, \quad [P + B^2/(2\mu)] = 0 \quad (1.42)$$

where $[\mathbf{a}] = \mathbf{a}_2 - \mathbf{a}_1$, and the subscripts 1 and 2 represent the quantity on either side of the interface. These conditions imply that the normal component of the velocity, magnetic field and also total pressure must be continuous at the interface. This type of boundary is fairly common in MHD as the magnetic field allows for inhomogeneities across it but, for example, as it restricts thermal conduction perpendicular to field lines.

The second possibility is that the magnetic field has a component perpendicular to the interface, so $\hat{\mathbf{n}} \cdot \mathbf{B} \neq 0$. In this case it is required that

$$[\mathbf{v}] = [\mathbf{B}] = 0, \quad [P] = 0 \quad (1.43)$$

so all components of velocity and magnetic field as well as pressure must be continuous at the interface. This set of conditions is more restrictive than (1.42).

Equations (1.42) and (1.43) are the boundary conditions for nonlinear ideal MHD but as we here deal with linearised systems these conditions must also be linearised. We will now consider equilibrium and perturbed quantities denoted by subscript '0' and '1', taking care to account for the moving boundary. We find the linearised form of (1.42) to be

$$\hat{\mathbf{n}}_0 \cdot [\mathbf{v}_1] = \hat{\mathbf{n}}_0 \cdot [\mathbf{B}_1] = 0, \quad [P_1 + \mathbf{B}_1 \cdot \mathbf{B}_0/(2\mu)] = [P_T] = 0, \quad (1.44)$$

while (1.43) gives simply

$$[\mathbf{v}_1] = [\mathbf{B}_1] = 0, \quad [P_1] = 0. \quad (1.45)$$

For a full discussion of boundary conditions (1.44), see Goedbloed (1983) and Díaz (2004); Díaz (2004) also deals with both (1.44) and (1.45). Note that often the natural assumption that either the total pressure perturbation or a velocity perturbation perpendicular to the interface is continuous will often allow the boundary conditions to be deduced from the governing equation for one of these quantities. This is the approach taken in Roberts (1981), in discussing boundary conditions

for linear MHD surface waves on an interface.

Finally, in many circumstances we will consider a coronal structure which has footpoints anchored in the chromospheric or photospheric surface. In these cases we can employ a boundary condition known as a line-tying condition (Hood, 1986), which forces the perpendicular velocity components to be zero at the footpoints of the structure,

$$\mathbf{v}_{\perp}(\text{loop footpoints}) = 0. \quad (1.46)$$

This reflects the fact that a weak perturbation of the fine coronal plasma has little influence on the denser photospheric plasma. Note that this condition allows flow of plasma through the photospheric surface into the loop and vice versa.

1.4 Method used for structured loop

In later chapters we will discuss a line-tied loop with longitudinal structuring. To deal with this structure we can develop a general form for the dispersion relation which considers any vertical structuring or stratification. To discuss this we need to introduce some mathematical methods.

1.4.1 Sturm-Liouville theorem

We will use the Sturm-Liouville theorem (Arfken, 1985) later in order to derive the dispersion relation in the zero β limit of a line-tied loop, allowing for a general longitudinal structuring. This theorem allows any piecewise continuous function on a closed interval to be expanded in terms of a generalized Fourier series; the terms of this series are solutions of a differential equation which takes a specific form. A differential operator of the form

$$L = p_0(x) \frac{d^2}{dx^2} + p_1(x) \frac{d}{dx} + p_2(x) \quad (1.47)$$

where $p_0(x), p_1(x), p_2(x)$ are real valued functions defined in the region $a \leq x \leq b$, say, is known as self-adjoint (in the region $a \leq x \leq b$) if the first $2 - i$ derivatives of $p_i(x)$ are continuous, $p_0(x)$ does not vanish in the region $a \leq x \leq b$, and

$$p_0'(x) = p_1(x). \quad (1.48)$$

Thus a self-adjoint operator L , acting on u , can be written equivalently as

$$L(u(x)) = \frac{d}{dx} \left[p(x) \frac{du(x)}{dx} \right] + q(x)u(x) \quad (1.49)$$

where $p_0(x)$ is replaced by $p(x)$ and $p_2(x)$ is replaced by $q(x)$.

Given an eigenvalue equation

$$L(u(x)) + \lambda w(x)u(x) = 0 \quad (1.50)$$

where L is self-adjoint, $w(x)$ a weight function and there are set boundary conditions at $x = a$ and $x = b$, then a solution $u_\lambda(x)$ is known as an eigenfunction corresponding to the eigenvalue λ . The eigenvalues form an infinite monotonic set and can be put in one to one correspondence with the natural numbers. Often the boundary conditions will be $u(x = a) = 0$ and $u(x = b) = 0$; this is the case when line-tying is considered.

The eigenfunctions form an orthogonal set with respect to the weight function $w(x)$ on the interval $[a, b]$, so that

$$\int_a^b u_i(x)u_j(x)w(x)dx = 0 \quad (1.51)$$

for $i \neq j$, and they can be normalised so

$$\int_a^b [u_i(x)]^2 w(x)dx = 1. \quad (1.52)$$

Hence the set of eigenfunctions form a complete set on the interval $[a, b]$ and any piecewise continuous function $F(x)$ can be expressed as a generalised Fourier series

$$F(x) = \sum_{n=0}^{\infty} C_n u_n(x) \quad (1.53)$$

where the coefficients C_n are calculated by inverting the series: assuming the eigenfunctions are normalised,

$$C_n = \int_a^b F(x)u_n(x)w(x)dx. \quad (1.54)$$

1.4.2 Separation of variables

In the situation where we consider a domain which is finite in some directions and our governing equation (the wave equation in this case) is of a suitable form, separation of variables is an ideal method of finding solutions (Kreyszig, 1993). In an infinite domain integral transforms are often a more suitable option. Also, since we seek solution of an oscillatory nature in a cylindrical geometry, Fourier analysis of the time component is appropriate. Therefore we assume a solution

of the form

$$P_T(r, \theta, z, t) = u(r) \Phi(\theta) h(z) \exp(i\omega t). \quad (1.55)$$

Substitution of equation (1.55) for P_T into equation (1.41) for a $\beta = 0$ plasma leads to the following set of ordinary differential equations:

$$\frac{d^2 u}{dr^2} + \frac{1}{r} \frac{du}{dr} - \left(\lambda^2 + \frac{m^2}{r^2} \right) u = 0, \quad (1.56)$$

which is the Bessel or modified Bessel equation for the radial dependence, $u(r)$;

$$\frac{d^2 \Phi}{d\theta^2} + m^2 \Phi = 0, \quad (1.57)$$

giving the simple harmonic oscillator equation for the azimuthal coordinate $\Phi(\theta)$; and

$$\frac{d^2 h}{dz^2} + \left(\frac{\omega^2}{v_A^2(z)} + \lambda^2 \right) h = 0 \quad (1.58)$$

for the longitudinal dependence $h(z)$. Here λ and m are separation constants. Notice that equations (1.56) and (1.57) for the radial and longitudinal components are coupled through the separation constant λ . Notice also that the equation for the z dependence is dependent on the longitudinal structuring of the loop, since the Alfvén speed is present in this equation and the differential operator in (1.58) is of self-adjoint form since $h(z = \pm L) = 0$ follows from $P_T(z = \pm L) = 0$, as a result of loop line-tying. Therefore, as a consequence of the Sturm-Liouville theorem equation (1.58) has solutions forming a complete set on $z \in [-L, L]$.

1.4.3 Radial structuring

We now assume the loop is defined by a step function in Alfvén speed and density so

$$v_A(r, z) = \begin{cases} v_{Ai}(z), & r < a \\ v_{Ae}(z), & r > a. \end{cases} \quad (1.59)$$

Thus we have internal regions denoted by subscript ‘ i ’ and external regions denoted by subscript ‘ e ’ where equations (1.56) to (1.58) must be solved, allowing us to construct P_T in each region. Boundary conditions (1.44) are then applied at the interface $r = a$.

Consider equation (1.56) for the radial dependence remembering that we consider trapped modes so $P_T(r \rightarrow \infty) \rightarrow 0$ and $v_\perp(r \rightarrow \infty) \rightarrow 0$; so $u(r \rightarrow \infty) \rightarrow 0$ and $u(r)$ must not be divergent at

any point. Therefore inside the loop ($r < a$) we have a solution of the form

$$u_n^i(r) = B_n \begin{cases} J_m(\{\lambda_n^i\}^* r), & [\lambda_n^i]^2 < 0 \\ I_m(\{\lambda_n^i\} r), & [\lambda_n^i]^2 > 0 \end{cases} \quad (1.60)$$

where $[\{\lambda_n^i\}^*]^2 = -[\lambda_n^i]^2$. The Bessel solutions Y_m and K_m have been omitted as they are divergent within the domain. We have labelled solutions with the subscript 'n' representing the solution corresponding to the n^{th} solution of equation (1.58) after the boundary conditions have been applied. In the exterior $r > a$

$$u_n^e(r) = C_n K_m(\lambda_n^e r); \quad (1.61)$$

$[\lambda_n^e]^2 > 0$ is required for trapped modes and the $I_m(\lambda_n^e r)$ solutions are rejected as they diverge with growing r , for $[\lambda_n^e]^2 > 0$.

Equation (1.57) has solution

$$\Phi(\theta) = \Phi(0) \exp(im\theta), \quad (1.62)$$

which is the same dependence as has been assumed for many other models (such as Edwin and Roberts (1983)). Since the internal and external solutions for P_T must be matched at $r = a$ the θ dependence must be the same in both regions. Also note the special case $m = 0$ when equation (1.57) takes the form $\frac{d^2\Phi}{d\theta^2} = 0$, which has general solution $\Phi(\theta) = \Phi(0) + A\theta$. As we require a solution which is periodic over 2π , $A = 0$ and then $\Phi(\theta)$ is the same as solution (1.62) for $m = 0$.

Finally we come to equation (1.58). We will not here specify the Alfvén profile in the z direction. Instead, we make the important observation that using the Sturm-Liouville Theorem, we can expand the external solution in terms of the internal solution in a generalized Fourier series:

$$h_n^e(z) = \sum_{m=1}^{\infty} H_{nm} h_m^i(z) \quad (1.63)$$

where the coefficients H_{nm} are given by

$$H_{nm} = \int_{-L}^L h_m^i(z) h_n^e(z) dz. \quad (1.64)$$

This will come into play when we derive the dispersion relation for an arbitrary longitudinal structuring.

1.4.4 Runge-Kutta method

In certain cases equation (1.58) cannot be solved analytically, in which case the numerical scheme we apply is a Runge-Kutta method (Kreyszig, 1993). This method propagates a solution to a differential equation of the form

$$\frac{dy}{dx} = f(x, y) \quad (1.65)$$

over an interval by combining derivative information from several trial intervals to match a Taylor series expansion up to some high order. The use of mid-points cancels out the lower-order error terms, so the method is $\mathcal{O}(h^{n+1})$ accurate if a n^{th} order scheme is used. Below we give an illustrative example of the 4th order method:

$$\begin{aligned} k_1 &= hf'(x_n, y_n), & k_2 &= hf'\left(x_n + \frac{h}{2}, y_n + \frac{k_1}{2}\right), \\ k_3 &= hf'\left(x_n + \frac{h}{2}, y_n + \frac{k_2}{2}\right), & k_4 &= hf'(x_n + h, y_n + k_3), \\ y_{n+1} &= y_n + \frac{k_1}{6} + \frac{k_2}{3} + \frac{k_3}{3} + \frac{k_4}{6} + \mathcal{O}(h^5). \end{aligned}$$

This method is reasonably simple to apply and is robust. In Chapters 4 and 5 we employ higher order methods, using either a 6th or 8th order methods when necessary. The use of two different order methods enables an estimation of the error in the solution to be obtained by comparing the difference in the solutions produced by these different order Runge-Kutta schemes.

1.4.5 Dispersion relation

In this section we follow Díaz (2004) who has shown how to use separable solutions to obtain a general dispersion relation with arbitrary longitudinal structuring. We take the solutions for P_T and v_r and apply boundary conditions (1.44) at the loop radius in order to derive the dispersion relation for the general longitudinal structuring in both the loop exterior and interior. Firstly, we write down the general solution for $P_T(r, \theta, z)$ as

$$P_T(r, \theta, z) = \Phi_m(\theta) \sum_{n=1}^{\infty} u_n(r) h_n(z). \quad (1.66)$$

This solution is expressed as a sum over all solutions in order to satisfy the boundary conditions at $r = a$ for all values of $z \in [-L, L]$. The loop ends are at $z = \pm L$. Now we must assume that v_r has the same z dependence as P_T and therefore satisfies

$$\left[\frac{\omega^2}{v_A^2} + \frac{\partial^2}{\partial z^2} \right] v_r = -\lambda_n^2 v_r. \quad (1.67)$$

Then, from the r component of equation (1.38), we obtain

$$\left[\frac{\omega^2}{v_A^2} + \frac{\partial^2}{\partial z^2} \right] v_r = \frac{i\omega\Phi_m(\theta)}{\rho_0 v_A^2} \sum_{n=1}^{\infty} \frac{du_n}{dr} h_n. \quad (1.68)$$

Therefore, using equation (1.67), v_r has the form

$$v_r(r, \theta, z) = -i\omega\Phi_m(\theta) \sum_{n=1}^{\infty} \frac{1}{\rho_0 v_A^2 \lambda_n^2} \frac{du_n}{dr} h_n(z). \quad (1.69)$$

Now we may apply the set of boundary conditions (1.44) for an interface lying parallel to the background magnetic field, so it is required that the total pressure and radial velocity are continuous across this boundary. Matching the internal and external total pressure implies that

$$\sum_{n=1}^{\infty} u_n^i(a) h_n^i(z) = \sum_{s=1}^{\infty} u_s^e(a) h_s^e(z). \quad (1.70)$$

We now use the fact that the external solution for the z dependence can be expanded in terms of the internal solution,

$$h_s^e(z) = \sum_{n=1}^{\infty} H_{sn} h_n^i(z). \quad (1.71)$$

The reason we expand the external solution in terms of the internal solution is that part of our investigation is to examine, for the first time, the influence of structuring of the loop's environment. Using expansion (1.71), equation (1.70) can be written as

$$\sum_{n=1}^{\infty} u_n^i(a) h_n^i(z) = \sum_{s=1}^{\infty} u_s^e(a) \left[\sum_{n=1}^{\infty} H_{sn} h_n^i(z) \right]. \quad (1.72)$$

Equating terms in $h_n^i(z)$ leads to

$$u_n^i(a) = \sum_{s=1}^{\infty} H_{sn} u_s^e(a). \quad (1.73)$$

Similarly, following the same procedure for the continuity of v_r , we find

$$\frac{1}{[\lambda_n^i]^2} \frac{du_n^i}{dr} \Big|_{r=a} = \sum_{s=1}^{\infty} \frac{H_{sn}}{[\lambda_s^e]^2} \frac{du_s^e}{dr} \Big|_{r=a}. \quad (1.74)$$

Care should be taken with the sign of the $[\lambda_n^i]^2$ term as it is not always positive.

Using conditions (1.73) and (1.74) to eliminate the internal coefficients of the radial dependence

B_n in favour of the external coefficients C_n , we obtain an infinite set of linear equations:

$$\sum_{s=1}^{\infty} H_{sn} \left[\frac{1}{\lambda_n^i} I'_m(\lambda_n^i a) K_m(\lambda_s^e a) - \frac{1}{\lambda_s^e} I_m(\lambda_n^i a) K'_m(\lambda_s^e a) \right] C_s = 0 \quad (1.75)$$

for $(\lambda_n^i)^2 > 0$, and

$$\sum_{s=1}^{\infty} H_{sn} \left[\frac{1}{\{\lambda_n^i\}^*} J'_m(\{\lambda_n^i\}^* a) K_m(\lambda_s^e a) + \frac{1}{\lambda_s^e} J_m(\{\lambda_n^i\}^* a) K'_m(\lambda_s^e a) \right] C_s = 0 \quad (1.76)$$

in the case of $(\lambda_n^i)^2 < 0$. These two sets of equations are written as separate summations though the terms in them may be mixed, since $(\lambda_n^i)^2$ could change in sign after a finite number of terms. If such a change of sign occurs after l terms then the summation would be

$$\begin{aligned} & \sum_{s=1}^l H_{sn} \left[\frac{1}{\{\lambda_n^i\}^*} J'_m(\{\lambda_n^i\}^* a) K_m(\lambda_s^e a) + \frac{1}{\lambda_s^e} J_m(\{\lambda_n^i\}^* a) K'_m(\lambda_s^e a) \right] C_s + \\ & \sum_{s=l+1}^{\infty} H_{sn} \left[\frac{1}{\lambda_n^i} I'_m(\lambda_n^i a) K_m(\lambda_s^e a) - \frac{1}{\lambda_s^e} I_m(\lambda_n^i a) K'_m(\lambda_s^e a) \right] C_s = 0. \end{aligned} \quad (1.77)$$

The dispersion relation for the normal modes of a line-tied coronal loop, with radial structuring in the form of step functions but general longitudinal structuring, is given by setting the determinant of the system of equations (1.77) equal to zero. When calculating the frequency or spatial structure of the modes a truncated system is used; typically we approximate the system using between ten and fifteen terms when determining frequency, but if the spatial structure is required, then between thirty and forty terms are used. Also the coefficients H_{sn} are determined using (1.63) but for some cases $h_n^i(z)$ and $h_n^e(z)$ are not known analytically and a numerical approach (which has been outlined earlier) must be adopted to determine them. The terms λ_n^i are evaluated once the longitudinal structuring is specified; for example, in the case of a uniform loop, so only the line-tying condition must be fulfilled. The solutions for the longitudinal dependence are of the form

$$h_{2n-1}^i(z) = \frac{1}{L^{\frac{1}{2}}} \cos \sqrt{[\lambda_{2n-1}^i]^2 + \frac{\omega^2}{v_{Ai}^2}} z, \quad (1.78)$$

for even modes and to ensure $\mathbf{v}_{\perp}(z \pm L) = 0$ we choose

$$[\lambda_{2n-1}^i]^2 + \frac{\omega^2}{v_{Ai}^2} = \frac{\pi^2(2n-1)^2}{4L^2} \quad (1.79)$$

($n = 0, 1, 2, \dots$). For odd modes

$$h_{2n}^i(z) = \frac{1}{L^{\frac{1}{2}}} \sin \sqrt{[\lambda_{2n}^i]^2 + \frac{\omega^2}{v_{Ai}^2}} z, \quad (1.80)$$

again to ensure $\mathbf{v}_\perp(z \pm L) = 0$, we choose

$$[\lambda_{2n}^i]^2 + \frac{\omega^2}{v_{Ai}^2} = \frac{\pi^2(2n)^2}{4L^2}, \quad (1.81)$$

with $n = 0, 1, 2, \dots$

The separation of modes into even and odd is convenient in a configuration where there is symmetry, this being the $z = 0$ plane in this case. The apex ($z = 0$) of a loop provides a symmetric point here.

1.5 MHD waves in a homogeneous medium

In the following chapters we will discuss the propagation of MHD waves in coronal structures. Although many of these structures will appear simple, the oscillatory behaviour within them is complicated. This is seen in chapter 2 where we consider a straight uniform cylindrical loop. Consequently, knowledge of the most basic configuration to support MHD modes will be valuable.

Therefore we examine the most simple magnetized configuration, an unbounded uniform medium permeated by a homogeneous unidirectional magnetic field. We consider linear perturbations about this equilibrium, so equations (1.38) to (1.39) can be applied. All of the speeds (v_A , c_0 , c_F and c_T) and the equilibrium density (ρ_0) are constant. Assuming a Fourier form in Cartesian geometry for all the perturbation quantities,

$$P_T(\mathbf{k}, \mathbf{r}, t) = P_T \exp i(\mathbf{k} \cdot \mathbf{r} - \omega t), \quad (1.82)$$

we can derive the following relations between the magnitudes of the perturbed quantities (Roberts, 1985):

$$P_m = \left[\frac{\omega^2 - k_z^2 c_0^2}{\omega^2} \right] \left[\frac{v_A}{c_0} \right]^2 P, \quad (1.83)$$

$$P_T = \left[\frac{\omega^2 - k_z^2 c_T^2}{\omega^2} \right] \left[\frac{c_0^2 + v_A^2}{c_0^2} \right] P, \quad (1.84)$$

$$P_T = \frac{\rho_0}{\omega k_x} (\omega^2 - k_z^2 v_A^2) v_x \quad (1.85)$$

and

$$\rho c_0^2 = P = \rho_0 \left[\frac{\omega}{k_z} \right] v_z. \quad (1.86)$$

Also the magnetic tension force $\mathbf{M}_T (= \frac{1}{\mu}(\mathbf{B}_0 \cdot \nabla)\mathbf{B})$ can be written as

$$\mathbf{M}_T = ik_z \left[\frac{k_z}{\omega} \rho_0 v_A^2 v_x, \frac{k_z}{\omega} \rho_0 v_A^2 v_y, -P_m \right]. \quad (1.87)$$

These relations will be useful in interpreting differences between modes.

Eliminating the perturbation quantities from the set of Fourier analysed equations (1.83) to (1.86) yields the dispersion relation

$$(\omega^2 - k_z^2 v_A^2)[\omega^4 - \omega^2 k^2 (c_0^2 + v_A^2) + k^2 k_z^2 c_0^2 v_A^2] = 0. \quad (1.88)$$

This dispersion relation is cubic in ω^2 and therefore has three roots; it describes the three MHD modes: the Alfvén, fast and slow magnetoacoustic modes. See also Cowling (1976) and Roberts (1985).

1.5.1 Alfvén mode

Firstly we examine the Alfvén mode (Alfvén, 1942) which is described by

$$\omega^2 = v_A^2 k_z^2 = v_A^2 k^2 \cos^2 \theta, \quad (1.89)$$

a root of the dispersion relation (1.88). The angle θ is the angle between the direction of propagation (parallel to \mathbf{k}) and the applied magnetic field $B_0 \mathbf{z}$. From the relations (1.84) to (1.86) we can see that the Alfvén mode is incompressible, involving no perturbations in pressure or density; therefore this mode is driven entirely by magnetic tension. Also, considering the polarisation of the modes, it can be seen that the Alfvén mode is a transverse oscillation with velocity field

$$\mathbf{v}^{\text{Alfvén}} = \frac{v_y}{k_x} (-k_y, k_x, 0). \quad (1.90)$$

Figure 1.6, shows a polar representation of the phase speed ω/k as a function of the angle of propagation θ . The Alfvén wave is a highly anisotropic mode, which propagates along the applied field ($\theta = 0$) with its maximum phase speed v_A but is prohibited from propagating directly across field ($\theta = \pi/2$) when its phase speed falls to zero. The group velocity of the Alfvén wave $\mathbf{c}_g = \pm v_A \mathbf{z}$ is aligned with the equilibrium magnetic field and so the Alfvén mode propagates information and energy only along the magnetic field.

1.5.2 Fast and slow modes

Now we turn our attention to the solutions of dispersion relation (1.88) corresponding to the roots of

$$\omega^4 - \omega^2 k^2 (c_0^2 + v_A^2) + k^2 k_z^2 c_0^2 v_A^2 = 0. \quad (1.91)$$

This introduces two additional waves, known as the slow and fast magnetoacoustic modes, coupling magnetic aspects with the plasma pressure effects. Writing explicit solutions to equation (1.91) we find

$$2 \frac{\omega^2}{k^2} = (c_0^2 + v_A^2) \pm [(c_0^2 + v_A^2)^2 - 4c_0^2 v_A^2 \cos^2 \theta]^{\frac{1}{2}} \quad (1.92)$$

where the positive sign before the square brackets corresponds to the high frequency fast mode and the negative sign before the square brackets to the lower frequency slow mode.

When propagating along the field ($\theta = 0$), and $\omega_{\text{fast}}^2 = k^2 v_A^2$, and so the fast wave propagates with the same speed as the Alfvén wave, while $\omega_{\text{slow}}^2 = k^2 c_s^2$ and so the slow wave takes the form of a field aligned acoustic wave. When propagating perpendicular to the field ($\theta = \frac{\pi}{2}$), the fast wave achieves its greatest speed, whereas the slow wave cannot propagate. More precisely, $\omega_{\text{slow}}^2 = k^2 c_T^2 \cos^2 \theta$ as $\theta \rightarrow \frac{\pi}{2}$. Therefore, the slow wave (and the Alfvén wave) cannot propagate across field lines whereas the fast wave can. These facts can be explained by considering the forces which drive the modes. There are only two forces arising in this analysis, the pressure force (made up of contributions from the plasma and magnetic pressures) and the magnetic tension force. It can be seen that the magnetic tension force falls to zero as $\theta \rightarrow \pi/2$, for both fast and slow modes, so all propagation directly across the field is driven by pressure effects. For the fast mode the plasma pressure and magnetic pressure are in phase and therefore the total pressure takes its maximum value (with respect to plasma pressure) perpendicular to the applied magnetic field, whereas for the slow mode the plasma and magnetic pressures are out of phase becoming equal in magnitude as $\theta \rightarrow \frac{\pi}{2}$, and so the total pressure falls to zero.

It can also be shown (e.g. Roberts, 1985) that the velocity fields of both magnetoacoustic modes are of the form:

$$\mathbf{v}_{\text{fast}} = \frac{v_x}{k_x} (k_x, k_y, \lambda^F k_z), \quad \mathbf{v}_{\text{slow}} = \frac{v_x}{k_x} (k_x, k_y, \lambda^S k_z) \quad (1.93)$$

where

$$\lambda^{\text{fast}} = \frac{c_s^2 (k_x^2 + k_y^2)}{(\omega_{\text{fast}}^2 - k_z^2 c_T^2)}, \quad \lambda^{\text{slow}} = \frac{c_s^2 (k_x^2 + k_y^2)}{(\omega_{\text{slow}}^2 - k_z^2 c_T^2)}. \quad (1.94)$$

Here the slow and fast superscripts indicate the form of ω^2 from equation (1.92), i.e. fast or slow

frequency solution (where $\omega_{\text{slow}} < \omega_{\text{fast}}$).

Fig. 1.6 shows a graphical representation of the phase speeds for the three MHD modes. We can see clearly the anisotropic nature of the slow and Alfvén waves and the (almost) isotropic form of the fast mode. The speed of the Alfvén wave lies between that of the slow and fast waves, although the phase speeds for both the slow and fast waves depend upon the angle between the direction of propagation and the equilibrium magnetic field.

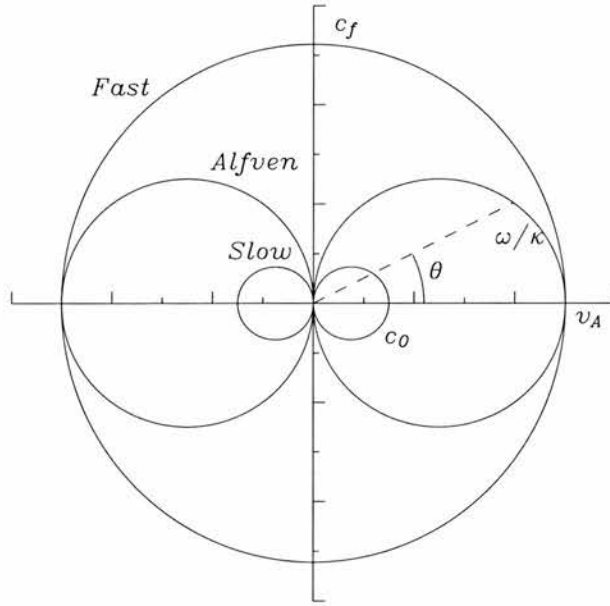


Figure 1.6: Polar plot of the phase speed diagram for the fast and slow magnetoacoustic and Alfvén modes in a homogeneous unbounded medium, for $v_A > c_s$. The equilibrium magnetic field $\mathbf{B}_0 = B_0 \mathbf{z}$ parallel to the line $\theta = 0$. The diagram shows the phase speed $c = \frac{\omega}{k}$ as a function of θ , the angle the propagation vector $\mathbf{k} = (k_x, k_y, k_z)$ makes with the equilibrium magnetic field (see, for example Cowling, 1976).

1.6 Thesis outline

In the chapters which follow we explore further the MHD modes of oscillation of several coronal structures, determining dispersion relations and eigenfunctions. Our goal is to model the behaviour of a coronal loop and the ability of this type of structure to support a wide variety of oscillatory modes.

We begin in Chapter 2 by revisiting the Edwin and Roberts (1983) model, which represents a coronal loop as a infinitely long and straight cylindrically symmetric magnetic tube, defined by sharp differences in magnetic field, density and Alfvén speed across the tube boundary. We consider the cases of a $\beta = 0$ plasma and also a $\beta \neq 0$ plasma. In the $\beta = 0$ case only fast modes are found, while in the $\beta \neq 0$ regime both fast and slow waves are present.

In Chapter 3 we study further the fast mode oscillations of a straight cylindrically symmetric magnetic tube, where the $\beta = 0$ limit has been applied. The effect of line-tying and longitudinal structuring, of both the loop interior and environment, in the form of dense uniform chromospheric layers is considered. As a result of the introduction of structuring, a modification of not only the oscillatory frequency of each mode but also the cutoff frequency arises.

In Chapter 4 we study the oscillatory nature of a 2D Cartesian arcade structure, again with $\beta = 0$. We examine the case of a uniform arcade and then introduce structuring in the density and Alfvén profiles parallel to the equilibrium magnetic field. Two density profiles are examined. The first has a gradual change in density between the arcade apex and footpoint. The second is uniform throughout a large section of the arcade but shows rapid variation through a short layer close to the footpoint, representing the rapid change from coronal conditions to photospheric conditions. A comparison with recent observations of oscillations of a coronal arcade is also made.

In Chapter 5 we return to the study of oscillations of a longitudinally structured coronal loop in a $\beta = 0$ plasma, as in Chapter 3. However, rather than consider a sharp interface between chromospheric and coronal regions we introduce continuous profiles between footpoint and apex of the loop. We study profiles of the same form as considered in Chapter 4, and in both cases make comparisons with the uniform line-tied loop (similar to that discussed in Chapter 2).

Chapter 6 contains a summary and concluding remarks.

Chapter 2

The Edwin and Roberts Model

An important feature of the solar corona is the structuring of the atmosphere by variations in density. The magnetic field and to a lesser extent the plasma pressure provide an elasticity to the coronal medium giving rise to a wide range of oscillatory behaviour. Dense coronal loops play an important role for oscillatory events as they can act as a wave guide for MHD waves.

Recent advances in solar observational technology have allowed increased spatial and temporal resolution both in space telescopes, such as TRACE (Transition Region and Coronal Explorer; Handy et al., 1999) and SoHO (Solar and Heliospheric Observatory; Wilhelm et al., 1995), and in the ground-based telescope SECIS (Solar Eclipse Corona Imaging System; Phillips et al., 2000) and radio observatory, Nobeyama Radioheliograph (Nakariakov et al., 2003, 2005). For the first time, this has provided us with instruments able to make direct detections of MHD waves in the solar corona. The first temporally resolved longitudinal waves were detected in plumes by the Ultraviolet Coronagraph Spectrometer (UVCS) on board SoHO (Ofman et al., 1997). Direct detection of transverse oscillations of coronal loops were found by TRACE and were determined to be flare excited standing waves of the fast kink mode, with a period of 280 ± 30 s (Aschwanden et al., 1999) and decay time of roughly 14.5 min (Nakariakov et al., 1999). Standing slow waves in hot coronal loops were detected by the SUMER instrument (Kliem et al., 2002, Wang et al., 2003), and identified to be slow MHD waves (Ofman and Wang, 2002, Wang et al., 2003). Standing fast waves may have been detected in microwave emissions (Nakariakov et al., 2003, 2005).

Propagating slow modes in cool coronal loops have been observed in EUV (Nakariakov et al., 2000, Robbrecht et al., 2001, De Moortel et al., 2000c). Outwardly propagating intensity fluctuations have been found to be a common occurrence in large, quiescent, coronal loop (De Moortel et al., 2002a,b,c,d) and identified as slow magnetoacoustic waves (De Moortel et al., 2002b). These modes have two distinct periods: about 3 min for those loops with footpoints above sunspots, and about 5 min for loops with footpoints above plage regions (De Moortel et al., 2002b). They

were not associated with flare-like events but excited by footpoint motions (De Moortel et al., 2002b).

Finally, oscillations of period 6 s detected in SECIS data (Williams et al., 2001) have been determined to be an impulsively generated fast magnetoacoustic wave which propagates along a coronal loop with a speed of 2100 km s^{-1} (Williams et al., 2002). A standing fast wave has been suggested to be responsible for modulation of microwave emissions, detected at Nobeyama Radio Observatory (Nakariakov et al., 2003, 2005).

The discovery of these oscillations has supported the use of simple inhomogeneity models to describe the modes of oscillation, with the model put forward by Edwin and Roberts (1983) receiving the most study. But, more importantly, the combination of a simple model with observations has opened the new avenue of coronal seismology (Roberts et al., 1984, Nakariakov et al., 1999, Nakariakov and Ofman, 2001). Coronal seismology uses the same techniques as helioseismology but rather than give a global seismology probing the solar interior, coronal seismology provides a local tool useful in the exploration of properties such as the magnetic field strength in a particular coronal loop or its spatial scale.

In this chapter we discuss the Edwin and Roberts (1983) model, giving a derivation of the dispersion relation and exploring some of the properties of the modes described by the dispersion relation. We present solutions to the dispersion relation for appropriate coronal parameters, considering zero β and non-zero β plasmas. We examine the eigenfunctions of the various modes, determining how each mode perturbs the coronal plasma. An independent study of similar features is also available on Dr. Erwin Verwichte's website at

<http://www2.warwick.ac.uk/fac/sci/physics/research/cfsa/people/erwin/>.

Recent and extensive overviews of this field have been given in Aschwanden (2004), Nakariakov and Verwichte (2005) and Roberts (2006).

2.1 Edwin and Roberts (1983)

Edwin and Roberts (1983) consider the trapped oscillations of both an isolated photospheric flux tube and a coronal tube. Of particular interest here is the case of a coronal tube or loop. Their study examines the normal modes of a static equilibrium of an untwisted magnetic flux tube under total pressure balance,

$$\frac{d}{dr} \left(P + \frac{B^2}{2\mu} \right) = 0. \quad (2.1)$$

A cylindrical (r, θ, z) geometry is used with radial structuring in r . The unperturbed magnetic flux tube is infinitely long and aligned with the z axis; the tube embedded in a coronal environment where the magnetic field is parallel to the tube. Plasma parameters from the tube interior are denoted by a subscript 'i' so density is ρ_i , plasma pressure is P_i , temperature is T_i and magnetic field strength is B_i ; their counterparts in the environment are denoted by a subscript 'e'. Gravitational effects are neglected. See Figure 2.1.

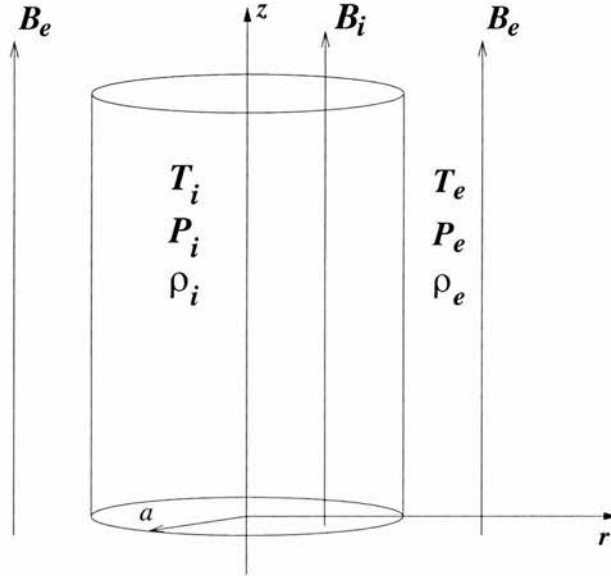


Figure 2.1: The equilibrium configuration of a magnetic flux tube, consisting of a plasma tube of radius, $r = a$ embedded in a magnetised coronal environment. (After Edwin and Roberts (1983)).

The ideal MHD equations are linearised about this equilibrium and the governing equations for the perturbations, derived for a general radially structured density profile, are equations (1.38), (1.39) and (1.40), the details of which are discussed in chapter 1. To proceed analytically it is assumed that the flux tube and its environment are uniform; it is possible to obtain analytical solutions under specific regimes for other density profiles and also numerical solutions to this problem without these assumption can be obtained (see Edwin and Roberts (1982) for the cartesian slab case). Application of appropriate boundary conditions leads to dispersion relations describing the oscillations supported by the flux tube.

2.2 Derivation of governing equations

In chapter 1 the MHD equations were linearised about the static equilibrium given in the previous section. At this stage we assume all equilibrium quantities are radially structured and denote the

velocity and magnetic perturbations by

$$\mathbf{v}_1 = (v_r, v_\theta, v_z), \quad \mathbf{B}_1 = (B_r, B_\theta, B_z). \quad (2.2)$$

The equilibrium total pressure condition is

$$P_0(r) + \frac{B_0(r)^2}{2\mu} = \text{constant}, \quad (2.3)$$

which follows from equation (2.1).

Eliminating the perturbed magnetic field from the linearised MHD equations in favour of the perturbed velocity and perturbed total pressure results in the following set of linear, second order partial differential equations (see Chapter 1):

$$\left(\frac{\partial^2}{\partial t^2} - v_A^2 \frac{\partial^2}{\partial z^2} \right) v_r = -\frac{1}{\rho_0} \frac{\partial^2 P_T}{\partial t \partial r}, \quad (2.4)$$

$$\left(\frac{\partial^2}{\partial t^2} - v_A^2 \frac{\partial^2}{\partial z^2} \right) v_\theta = -\frac{1}{\rho_0 r} \frac{\partial^2 P_T}{\partial \theta \partial t}, \quad (2.5)$$

$$\frac{\partial^2 v_z}{\partial t^2} = c_0^2 \frac{\partial}{\partial z} [\nabla \cdot \mathbf{v}_1], \quad (2.6)$$

and

$$\frac{\partial P_T}{\partial t} = -\rho_0 \left[c_0^2 \nabla \cdot \mathbf{v}_1 + \frac{v_A^2}{r} \frac{\partial (r v_r)}{\partial r} + \frac{v_A^2}{r} \frac{\partial v_\theta}{\partial \theta} \right]. \quad (2.7)$$

Here $v_A(r)$ denotes the Alfvén speed and $c_0(r)$ is the sound speed. Equations (2.4) and (2.5) follow from equation (1.38) in component form for a cylindrical geometry. Equations (2.6) and (2.7) follow from equations (1.31) and (1.32). Equations of this form have also been discussed by Roberts (1991).

Since we seek oscillatory solutions, a Fourier form is taken for the invariant azimuthal and longitudinal directions as well as the temporal dependence; the total pressure perturbation takes the form

$$P_T(r, \theta, z, t) = P_T(r) \exp i(\omega t + m\theta + kz), \quad (2.8)$$

where ω is the frequency, the integer m is the azimuthal wavenumber ($m = 0, 1, 2, \dots$), and k is the wavenumber parallel to the applied magnetic field. All perturbation quantities are now taken to represent their r -dependence. This results in the following set of ordinary differential equations

for the amplitudes of the perturbations:

$$(k^2 v_A^2 - \omega^2) v_r = \frac{-i\omega}{\rho_0} \frac{dP_T}{dr}, \quad (2.9)$$

$$(k^2 v_A^2 - \omega^2) v_\theta = \frac{m\omega}{r\rho_0} P_T, \quad (2.10)$$

$$(k^2 c_0^2 - \omega^2) v_z = \frac{ic_0^2 k}{r} \left[\frac{d(rv_r)}{dr} + imv_\theta \right], \quad (2.11)$$

and

$$i\omega P_T = -\rho_0 \left[\frac{(c_0^2 + v_A^2)}{r} \frac{d(rv_r)}{dr} + \frac{im(c_0^2 + v_A^2)}{r} v_\theta + ikc_0^2 v_z \right]. \quad (2.12)$$

Using equations (2.9)-(2.12), we derive a pair of second order ordinary differential equations which govern v_r and P_T :

$$\frac{d}{dr} \left(\frac{\rho_0(k^2 v_A^2 - \omega^2)}{r(m_0^2 + \frac{m^2}{r^2})} \frac{d(rv_r)}{dr} \right) - \rho_0(k^2 v_A^2 - \omega^2) v_r = 0, \quad (2.13)$$

$$\frac{\rho_0}{r} (k^2 v_A^2 - \omega^2) \frac{d}{dr} \left[\frac{r}{\rho_0(k^2 v_A^2 - \omega^2)} \frac{dP_T}{dr} \right] - \left(\frac{m^2}{r^2} + m_0^2 \right) P_T = 0, \quad (2.14)$$

where

$$m_0^2 = \frac{(k^2 v_A^2 - \omega^2)(k^2 c_0^2 - \omega^2)}{(c_0^2 + v_A^2)(k^2 c_T^2 - \omega^2)}. \quad (2.15)$$

It should be noted that the term in square brackets in (2.14) is proportional to rv_r ; this will be of importance later.

Equation (2.13) has been discussed in, for example, Hain and Lüst (1958), Goedbloed and Hagebeuk (1972) and Edwin and Roberts (1983). For our purposes here, we focus on equation (2.14). To proceed analytically simplification of (2.14) is required. We consider a uniform flux tube embedded in a uniform medium.

2.3 Uniform flux tube embedded in a uniform medium

So far we have considered a general radial structuring in the equilibrium. In this section we select appropriate density, magnetic field strength and pressure profiles which then determine the sound and Alfvén speeds.

We consider a uniform magnetic flux tube of radius a within a uniform coronal environment, so

the flux tube is defined by an enhancement or depletion of the density or temperature or magnetic field strength. Equilibrium quantities from the tube interior are denoted by a subscript ‘ i ’ and a subscript ‘ e ’ for environment quantities. The equilibrium total pressure balance condition (2.3) implies that

$$P_i + \frac{B_i^2}{2\mu} = P_e + \frac{B_e^2}{2\mu} \quad (2.16)$$

which, via the ideal gas law, leads to the relation

$$\frac{\rho_i}{\rho_e} = \frac{2c_e^2 + \gamma v_{Ae}^2}{2c_i^2 + \gamma v_{Ai}^2}. \quad (2.17)$$

Equation (2.17) relates the ratio of the internal density ρ_i to the external density ρ_e in terms of the internal and external sound speeds, c_i and c_e , and the Alfvén speeds, v_{Ai} and v_{Ae} , and the adiabatic constant $\gamma (= \frac{5}{3})$. For TRACE loops, the ratio ρ_i/ρ_e is typically in the range 2 to 10 (Aschwanden, 2004).

Under the above conditions, equation (2.14) for the total pressure perturbation inside the tube reduces to a Bessel or modified Bessel equation (depending on the sign of m_i^2)

$$\frac{d^2 P_T}{dr^2} + \frac{1}{r} \frac{dP_T}{dr} - \left(\frac{m^2}{r^2} + m_i^2 \right) P_T = 0, \quad (2.18)$$

with an equivalent equation holding for the environment. Here m_i^2 is the value of m_0^2 in the tube interior of the tube; specifically,

$$m_i^2 = \frac{(k^2 v_{Ai}^2 - \omega^2)(k^2 c_i^2 - \omega^2)}{(c_i^2 + v_{Ai}^2)(k^2 c_{Ti}^2 - \omega^2)}. \quad (2.19)$$

The solutions for P_T in each region are

$$P_T = \begin{cases} A_0 J_m(n_i r) + A_1 Y_m(n_i r), & -m_i^2 = n_i^2 \geq 0 \\ A_0 I_m(m_i r) + A_1 K_m(m_i r), & m_i^2 > 0 \end{cases} \quad (2.20)$$

for $r < a$, and

$$P_T = \begin{cases} A_0 J_m(n_e r) + A_1 Y_m(n_e r), & -m_e^2 = n_e^2 \geq 0 \\ A_0 I_m(m_e r) + A_1 K_m(m_e r), & m_e^2 > 0 \end{cases} \quad (2.21)$$

for $r > a$. For convenience, we have introduced the quantities $n_i^2 (= -m_i^2)$ and $n_e^2 (= -m_e^2)$.

These are purely solutions of Bessel equations. To obtain solutions of physical meaning we must apply appropriate boundary conditions. Boundary conditions have been discussed in chapter 1, leading to conditions (1.42).

We require that P_T be regular for all r but this only comes into play in two cases $r = 0$ and as $r \rightarrow \infty$. Also the radial displacement of the tube must be continuous across the tube boundary; this is based on the assumption that the plasma remains continuous. In the case of a static equilibrium, continuity of radial displacement reduces to the continuity of radial velocity v_r . As a consequence of the continuity of radial velocity, and equation (2.14) written in the form

$$\frac{\rho_0}{r}(k^2 v_A^2 - \omega) \frac{d}{dr} \left[\frac{irv_r}{\omega} \right] - \left(\frac{m^2}{r^2} + m_0^2 \right) P_T = 0, \quad (2.22)$$

the total pressure perturbation must also be continuous.

Enforcing the first condition that P_T be finite at $r = 0$ reduces the internal solution to

$$P_T = A_0 \begin{cases} J_m(n_i r), & -m_i^2 = n_i^2 \geq 0 \\ I_m(m_i r), & m_i^2 > 0. \end{cases} \quad (2.23)$$

The second condition, that $P_T \rightarrow 0$ as $r \rightarrow \infty$, corresponds to trapped modes and leads to the requirement that $m_e^2 \geq 0$ and an environment solution of the form

$$P_T = A_1 K_m(m_e r). \quad (2.24)$$

The resulting radial component of motion v_r for this P_T , for $r \leq a$, is

$$v_r = -A_0 \frac{i\omega}{\rho_i(k^2 v_{Ai}^2 - \omega^2)} \begin{cases} n_i J'_m(n_i r), & -m_i^2 = n_i^2 \geq 0 \\ m_i I'_m(m_i r), & m_i^2 > 0, \end{cases} \quad (2.25)$$

and for $r > a$

$$v_r = -\frac{i\omega}{\rho_e(k^2 v_{Ae}^2 - \omega^2)} A_1 m_e K'_m(m_e r). \quad (2.26)$$

Here a dash ($'$) denotes the derivative of the Bessel function; e.g. $J'_m(x) = \frac{dJ_m(x)}{dx}$ and $J'_m(n_i r) = \frac{dJ_m(x)}{dx}$ calculated at $x = n_i r$.

Finally the continuity of P_T and v_r at the tube boundary provide the constraints

$$A_0 I_m(m_i a) = A_1 K_m(m_e a), \quad m_i^2 > 0 \quad (2.27)$$

and

$$A_0 J_m(n_i a) = A_1 K_m(m_e a), \quad -m_i^2 = n_i^2 > 0 \quad (2.28)$$

$$\rho_e(k^2 v_{Ae}^2 - \omega^2) A_0 m_i I'_m(m_i a) = \rho_i(k^2 v_{Ai}^2 - \omega^2) A_1 m_e K'_m(m_e a). \quad (2.29)$$

For $m_i^2 < 0$ the equivalent condition is

$$\rho_e(k^2 v_{Ae}^2 - \omega^2) A_0 n_i J'_m(n_i a) = \rho_i(k^2 v_{Ai}^2 - \omega^2) A_1 m_e K'_m(m_e a). \quad (2.30)$$

From (2.27) and (2.29) the dispersion relation for modes with eigenfunctions taking a decaying behaviour in the tube interior can be derived; these modes are known as *surface* modes. From (2.28) and (2.30) the dispersion relation for modes with eigenfunctions taking an oscillatory behaviour in the tube interior, known as *body* modes, can be deduced (See Fig. 2.2).

2.4 Dispersion relation

Eliminating the constants A_0 and A_1 from conditions (2.27) and (2.29) we derive the transcendental dispersion relation

$$\rho_e(k^2 v_{Ae}^2 - \omega^2) m_i \frac{I'_m(m_i a)}{I_m(m_i a)} = \rho_i(k^2 v_{Ai}^2 - \omega^2) m_e \frac{K'_m(m_e a)}{K_m(m_e a)}. \quad (2.31)$$

This is the dispersion relation for surface ($m_i^2 > 0$) modes. For magnetic body ($m_i^2 = -n_i^2 < 0$) waves,

$$\rho_e(k^2 v_{Ae}^2 - \omega^2) n_i \frac{J'_m(n_i a)}{J_m(n_i a)} = \rho_i(k^2 v_{Ai}^2 - \omega^2) m_e \frac{K'_m(m_e a)}{K_m(m_e a)}. \quad (2.32)$$

Equations (2.31) and (2.32) were first derived in this form by Edwin and Roberts (1983). Equivalent forms have been discussed previously in Zaitsev and Stepanov (1975), Wilson (1980) and Spruit (1982); the case of a flux tube embedded in a field-free environment was given by Roberts and Webb (1978). Dispersion relations (2.31) and (2.32) both require that $m_e^2 > 0$, since they describe the trapped oscillations of a magnetic flux tube.

Equation (2.31) describes *surface* modes which are oscillations with eigenfunctions having a decaying amplitude with distance from the interface. The dispersion relation (2.32) describes *body* modes; these modes, unlike the surface modes, have an oscillatory behaviour within the tube. Both surface and body modes have decaying amplitude in the environment. Fig.2.2 illustrates the behaviour of body and surface oscillations. The integer m , which is the wavenumber associated with the θ direction, determines the mode governed by the relation; these modes can be split into three classes: $m = 0$, $m = 1$ and $m \geq 2$. The case $m = 0$ is known as the *sausage* mode, a cylindrically symmetric pulsation which causes oscillation of the tube radius while the axis of the tube remains undisturbed; $m = 1$ is the *kink* mode, a transverse global oscillation of the tube leaving the radius of the tube almost unchanged. The kink mode is the only mode which causes movement of the tube axis. For $m \geq 2$ the dispersion relation describes the *fluting* modes, which

are pulsations similar to that of the sausage modes. All three modes are illustrated in Fig.2.3. For this study our interest lies in the sausage and the kink modes, as it is thought they are most easily excited in the solar atmosphere. The dispersion curves for these modes are well known and are given in subsequent sections. The main aim here is to examine the eigenfunctions of the various modes of oscillation, which will reveal the physical behaviour of the plasma as the waves propagate.

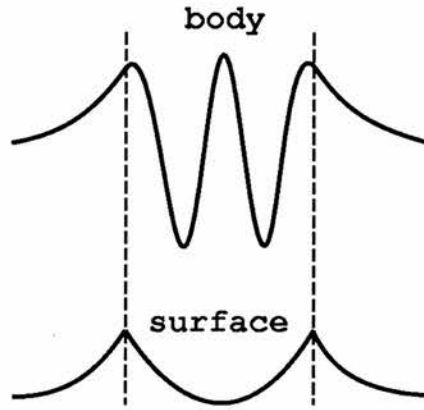


Figure 2.2: A body mode (top) has $m_i^2 < 0$, while a surface mode (bottom) has $m_i^2 > 0$; both modes have $m_e^2 > 0$.

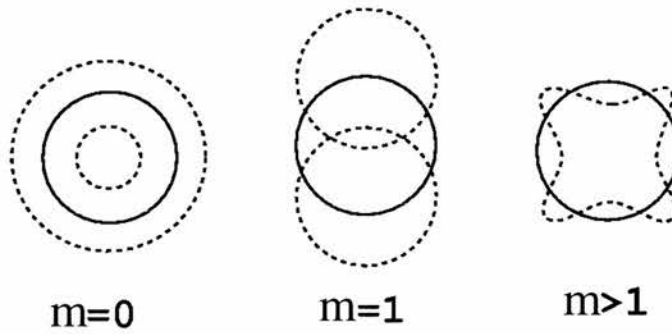


Figure 2.3: The sausage mode ($m = 0$), kink mode ($m = 1$) and fluting modes ($m > 1$; here $m = 4$) of an oscillating tube.

2.5 Eigenfunctions

In this section the eigenfunctions are presented in terms of P_T and $\frac{dP_T}{dr}$, the dimensionless wavenumber along the tube ak , and the phase speed in the z direction $c(\equiv \frac{\omega}{k})$. Inside the tube ($r < a$), the

components of the perturbed velocity are

$$v_r = \frac{-ica}{\rho_i a k (v_{Ai}^2 - c^2)} \frac{dP_T}{dr}, \quad (2.33)$$

$$v_\theta = \frac{mca}{r \rho_i a k (v_{Ai}^2 - c^2)} P_T, \quad (2.34)$$

and

$$v_z = \frac{ic_i^2 a}{r a k (c_i^2 - c^2)} \left(\frac{d(rv_r)}{dr} + imv_\theta \right). \quad (2.35)$$

An alternative form for v_z is

$$v_z = \frac{c_i^2 c}{\rho_i (c_i^2 + v_{Ai}^2) (c_{Ti}^2 - c^2)} P_T. \quad (2.36)$$

The components of the perturbed magnetic field are

$$B_r = \frac{B_i}{c} v_r, \quad (2.37)$$

$$B_\theta = \frac{B_i}{c} v_\theta, \quad (2.38)$$

and

$$B_z = \frac{B_i (c_i^2 - c^2)}{c c_i^2} v_z. \quad (2.39)$$

Finally the perturbed density ρ_1 , pressure P_1 and temperature T_1 are

$$\rho_1 = \frac{P_1}{c_i^2}, \quad (2.40)$$

$$P_1 = P_T - \frac{B_i B_z}{\mu}, \quad (2.41)$$

and

$$T_1 = T_i \left[\frac{P_1}{P_i} - \frac{\rho_1}{\rho_i} \right]. \quad (2.42)$$

It follows that

$$P_1 = -\rho_i c v_z = \frac{-c_i^2 c^2}{(c_i^2 + v_{Ai}^2) (c_{Ti}^2 - c^2)} P_T. \quad (2.43)$$

In each of equations (2.33) to (2.42) the exponential factor $\exp i(\omega t + m\theta + kz)$ has been omitted; but when incorporated (2.33) to (2.42) determine either the sine or cosine dependence in the z ,

θ and t coordinates for each function. Since we are considering a linear problem all of these eigenfunctions have an undetermined constant representing the amplitude of the wave; in order to eliminate this we can normalise P_T to 1, for the sausage mode at the tube axis and at the tube boundary for the kink mode.

We can now draw some immediate deductions from the eigenfunctions.

2.5.1 Displacement of the tube centre

Analysis of the the radial velocity perturbation v_r confirms the difference in the behaviour of the centre of the tube ($r = 0$) for the kink mode from all other modes. Only $\frac{dP_T}{dr}$ needs be examined, since $v_r \propto \frac{dP_T}{dr}$. The expansion of the derivatives of the Bessel and modified Bessel functions $J_m(z)$ and $I_m(z)$ are different for $m = 0$ and $m \geq 1$. Therefore we treat these cases separately. Firstly, for $m = 0$:

$$\frac{dP_T}{dr} = A_0 \begin{cases} -n_i J_1(n_i r), & -m_i^2 = n_i^2 \geq 0 \\ m_i I_1(m_i r), & m_i^2 > 0. \end{cases} \quad (2.44)$$

Expanding (2.44) for small arguments ($n_i r \ll 1$ or $m_i r \ll 1$)

$$\frac{dP_T}{dr} = A_0 \begin{cases} -\frac{1}{2}n_i^2 r, & -m_i^2 = n_i^2 \geq 0 \\ \frac{1}{2}m_i^2 r, & m_i^2 > 0, \end{cases} \quad (2.45)$$

therefore as $r \rightarrow 0$

$$\frac{dP_T}{dr} = A_0 \begin{cases} 0, & -m_i^2 = n_i^2 \geq 0 \\ 0, & m_i^2 > 0, \end{cases} \quad (2.46)$$

provided n_i^2 and m_i^2 remain bounded.

Now considering the second case, $m > 0$:

$$\frac{dP_T}{dr} = A_0 \begin{cases} n_i \left(-J_{m+1}(n_i r) + \frac{m}{n_i r} J_m(n_i r) \right), & -m_i^2 = n_i^2 \geq 0 \\ m_i \left(I_{m+1}(m_i r) + \frac{m}{m_i r} I_m(m_i r) \right), & m_i^2 > 0. \end{cases} \quad (2.47)$$

For small arguments ($n_i r \ll 1$ or $m_i r \ll 1$)

$$\frac{dP_T}{dr} = A_0 \begin{cases} n_i \left(-\frac{(\frac{1}{2}n_i r)^{m+1}}{(m+1)!} + \frac{1}{2} \frac{(\frac{1}{2}n_i r)^{m-1}}{(m-1)!} \right), & -m_i^2 = n_i^2 \geq 0 \\ m_i \left(\frac{(\frac{1}{2}m_i r)^{m+1}}{(m+1)!} + \frac{1}{2} \frac{(\frac{1}{2}m_i r)^{m-1}}{(m-1)!} \right), & m_i^2 > 0. \end{cases} \quad (2.48)$$

Setting $m = 1$ and allowing $r \rightarrow 0$ yields

$$\frac{dP_T}{dr} = \frac{A_0}{2} \begin{cases} n_i, & -m_i^2 = n_i^2 \geq 0 \\ m_i & m_i^2 > 0, \end{cases} \quad (2.49)$$

but if $m \neq 1$ and $r \rightarrow 0$

$$\frac{dP_T}{dr} = \begin{cases} 0, & -m_i^2 = n_i^2 \geq 0 \\ 0 & m_i^2 > 0. \end{cases} \quad (2.50)$$

Therefore the centre of the tube is unmoved for all $m \neq 1$; the kink mode, $m = 1$, is the only oscillation causing the centre of the tube to be displaced.

2.5.2 Shear motions

Inspection of v_θ shows that under certain circumstances it is possible for the interior of the tube to be rotating out of phase with the environment. Consider for example, a fast wave propagating with a phase speed c lying between the internal and external Alfvén speeds, $v_{Ai} < c < v_{Ae}$. Then

$$v_\theta = \begin{cases} \frac{mca}{r\rho_i ak(v_{Ai}^2 - c^2)} P_T, & r < a \\ \frac{mca}{r\rho_e ak(v_{Ae}^2 - c^2)} P_T, & r > a. \end{cases} \quad (2.51)$$

Since m, c, a, r, k, P_T and the densities in (2.51) have the same sign across $r = a$ whereas $(v_{Ai}^2 - c^2)$ and $(v_{Ae}^2 - c^2)$ are of opposite sign in the tube interior to the exterior, a shearing effect arises due to the sharp change in sign of v_θ at the interface.

2.5.3 Relations between pressures

For the embedded flux tube model there are three different pressures we can define. The first and most important is the total pressure perturbation, giving the net effect of the plasma and magnetic pressures. However, it is interesting to examine the relationships between the different pressures for fast and slow modes.

Firstly, the plasma pressure perturbation P_1 and the total pressure perturbation P_T can be related by

$$P_1 = \frac{-c_i^2 c^2}{(c_i^2 + v_{Ai}^2)(c_{Ti}^2 - c^2)} P_T. \quad (2.52)$$

We can see that for both slow and fast modes in the loop and environment these pressures are in

phase, since the phase speed of these modes satisfy $c > c_{Ti}, c_{Te}$. Also equation (2.52) reveals that in a cold plasma ($\beta = 0, c_i = 0$) there is no perturbation to the plasma pressure (as expected).

The linearised magnetic pressure ($P_m = \frac{B_0 B_z}{\mu}$) can be related to the total pressure P_T via

$$P_m = \frac{c_{Ti}^2(c_i^2 - c^2)}{c_i^2(c_{Ti}^2 - c^2)} P_T, \quad (2.53)$$

where we can see, assuming a typical ordering of speeds in the corona, that P_m and P_T are out of phase for the slow modes, but in phase for the fast modes inside the loop; however, they are in phase for fast and slow modes in the environment of the loop.

Finally, we discuss the relation between the plasma and magnetic pressures (which can be combined to produce the total pressure). P_1 and P_m are related by

$$P_1 = \frac{-c_i^2 c^2}{v_{Ai}^2(c_i^2 - c^2)} P_m. \quad (2.54)$$

Therefore, for the slow mode which has $c_e < c < c_i$, P_1 and P_m are out of phase inside the loop and in phase in the environment. By contrast, the fast mode has these pressures in phase both inside and outside the loop.

2.5.4 Forces

There are two forces acting upon the plasma: the total pressure force and the magnetic tension force acting along field lines. We can write the total pressure force as

$$-\nabla P_T = -ik \frac{c_i^2(c_{Ti}^2 - c^2)}{c_{Ti}^2(c_i^2 - c^2)} \left(\frac{\rho_i v_{Ai}^2 m_i^2}{ck^2} v_r, \frac{\rho_i v_{Ai}^2 m_i^2}{ck^2} v_\theta, P_m \right) \quad (2.55)$$

and the magnetic tension force as

$$\mathbf{M}_T = ik \left(\frac{\rho_i v_{Ai}^2}{c} v_r, \frac{\rho_i v_{Ai}^2}{c} v_\theta, P_m \right). \quad (2.56)$$

Using these expressions we compare the driving forces and their phase for fast and slow modes and also surface and body modes. Unfortunately, these expressions do not allow distinctions to be made between sausage and kink modes.

For the slow surface modes inside the tube we find each component of the total pressure force and the magnetic tension force are in phase and so act together. However, for the slow body modes the transverse components are out of phase, so oppose each other, while the longitudinal components continue to act in unison. This indicates a predominantly longitudinal nature for the slow body

modes. In the environment it is found that all components of these two forces act against each other, resulting in a decay in oscillation power with increasing distance from the tube boundary (as expected for trapped modes).

When considering fast surface modes it is now seen that all components of these two forces act out of phase inside the tube, rather than together as in the case of the slow surface modes. This may account for the decay in oscillation amplitude away from the tube boundary for the surface mode. However, the transverse components of the forces are in phase for the fast body modes while the longitudinal forces oppose each other. This suggests that the fast body modes are predominantly transverse oscillations. This fact can also be observed in the zero β limit when the net longitudinal force is seen to fall to zero. Similarly to the slow modes, all the components of the total pressure force and magnetic tension force act against each in the environment of the tube, causing a decay in oscillation power away from the tube.

2.6 Cold plasma

The solar corona is a magnetically dominated environment with a small plasma β ($\equiv \frac{2\mu P_0}{B_0^2}$), corresponding to in Alfvén speeds greatly exceeding sound speeds. Therefore examining the cold plasma ($\beta = 0$) limit is not only a useful simplification of the model, eliminating the slow modes, but is also a close approximation to the low β ($\approx 10^{-3} - 10^{-4}$, see Chapter 1) corona and so describes adequately the fast waves.

Notice that the $\beta = 0$ equilibrium has a uniform magnetic field throughout ($B_i = B_e$) so the flux tube is defined purely by a density enhancement (or contrast), which translates to an Alfvén speed depression. From the total pressure balance condition (2.16), it can be seen that the ratio of external to internal density is related to the ratio of the square of the internal to external Alfvén speeds by

$$\frac{\rho_e}{\rho_i} = \frac{v_{Ai}^2}{v_{Ae}^2}; \quad (2.57)$$

this ratio typically lies in the range 0.1 - 0.5 for TRACE coronal loops. The sound speeds are zero in both the tube and environment regions ($c_i = c_e = 0$), hence the effective radial wavenumber squared reduces to

$$m_i^2 = \frac{k^2(v_{Ai}^2 - c^2)}{v_{Ai}^2} \quad (2.58)$$

with an equivalent form in the environment.

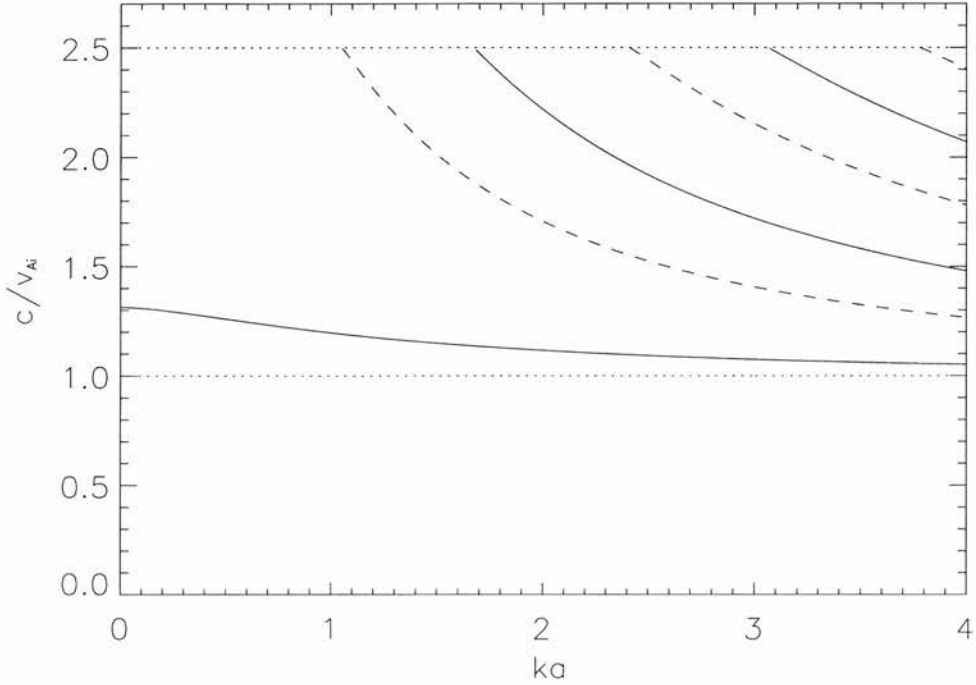
2.6.1 Dispersion diagram $\beta = 0$ 

Figure 2.4: Dispersion diagram for the $\beta = 0$ case, with $v_{Ae} = 2.5v_{Ai}$. The diagram shows the non-dimensional phase speed $\frac{c}{v_{Ai}} (= \frac{\omega}{kv_{Ai}})$ as a function of ka . The solid curves are the kink modes ($m = 1$) and the dashed curves sausage modes ($m = 0$). The curves cutoff at $\omega = kv_{Ae}$.

We will now examine the solutions of dispersion relations (2.31) and (2.32). Due to the transcendental nature of these dispersion relations a numerical approach must be applied to obtain solutions. We use a combination of the bisection method and the Newton-Raphson method, but estimating the derivative term via a high order finite difference method. The dispersion curves are found as a function of ka starting from large values of ka and working towards smaller values of ka . The bisection method is used to find initial points on the dispersion curves; thereafter the Newton-Raphson method is used with the initial guess obtained by a linear extrapolation on previous points on the dispersion curve.

This method is very efficient in finding solutions in the $\beta = 0$ case, when only the fast modes are present and there are large separations between the dispersion curves. However, when $\beta \neq 0$ the presence of a slow mode band containing an infinite number of modes does not prove straightforward, although there are still no difficulties solving the dispersion relations for the fast modes.

Fig. 2.4 shows the dispersion diagram for the solutions of dispersion relations (2.32) in the zero β case, for Alfvén speeds of $v_{Ae} = 2.5v_{Ai}$. For this case, $\rho_e = 0.16\rho_i$. We have plotted the non-

dimensional phase speed c/v_{Ai} in the longitudinal direction against longitudinal dimensionless wavenumber ka . Note that no surface modes occur under these parameters. There are no slow modes present but there is a band of fast modes with phase speeds lying in the range between the internal and external Alfvén speeds. Within this band of fast modes there are many classes of modes for each value of m . However, our main interest here is in the sausage modes ($m = 0$), plotted as dashed curves, and the kink modes ($m = 1$) plotted as solid curves. The interleaving of a single sausage mode lying between each pair of consecutive kink harmonics and never crossing is a universal property of this model, but it will be seen in subsequent models (Chapter 3 and 5) that the addition of longitudinal structuring may break this pattern. The ability of the loop to support trapped modes is as a result of its density enhancement over its environment, and increasing the density enhancement (increasing ρ_i/ρ_e) improves the efficiency of the loop to act as a waveguide and results in a reduction in the phase speeds of the modes, making it possible for more harmonics to arise lying below the cutoff frequency, for a give range of ka . The cutoff frequency (which can also be cast in terms of phase speed) is defined by the properties of the loop's environment and take a value of $c = c_{cut} = v_{Ae}$ (plotted in Fig. 2.4 as the upper dotted line) in this case. However, in more structured models this can take a modified value (see Chapter 3 and 5). The cutoff curve is important as it marks the transition between a mode propagating as a trapped mode or a leaky mode, corresponding to m_e^2 positive or negative respectively. Fig. 2.4 shows that all but the *fundamental* kink mode reaches this cutoff and therefore propagate as leaky modes in the long wavelength limit. A *fundamental* mode of any structure, be it a coronal loop or a length of string, implies that the entire structure is oscillating in phase and the only nodes (points where the position of the structure is fixed) are situated at the ends of the structure. The values of ka at which each mode becomes leaky can be evaluated using the formula (Edwin and Roberts, 1983)

$$ka = j_{0i} \left(\frac{v_{Ai}^2}{(v_{Ae}^2 - v_{Ai}^2)} \right)^{\frac{1}{2}}, \quad (2.59)$$

for the i^{th} sausage mode ($m = 0$), where j_{0i} is the i^{th} zero of the Bessel function J_0 . In the same way, for the $(i + 1)^{th}$ kink modes ($m = 1$) the cutoff values of ka are found to be

$$ka = j_{1i} \left(\frac{v_{Ai}^2}{(v_{Ae}^2 - v_{Ai}^2)} \right)^{\frac{1}{2}} \quad (2.60)$$

where j_{1i} is the i^{th} zero of the Bessel function J_1 . The importance of these cutoffs is discussed in Roberts et al. (1984).

The fundamental kink mode propagates as a trapped mode for all values of ka . Also it can be seen from Fig. 2.5 that in the long wavelength limit $ka \rightarrow 0$ the kink mode propagates with the kink

speed c_k , defined by

$$c_k = \left(\frac{\rho_0 v_A^2 + \rho_e v_{Ae}^2}{\rho_0 + \rho_e} \right)^{\frac{1}{2}}. \quad (2.61)$$

The kink mode possesses the property that its phase speed is insensitive to ka in the small ka range so the gradient of the dispersion curve is shallow for small values of ka and its phase speed remains approximately c_k ; this is in contrast to the sausage modes and harmonics of the kink mode which have a strongly dispersive nature with respect to ka .

The fact that the fundamental kink mode has this special property of weak dispersion for small and moderate ka makes it ideal for use in coronal seismology. Provided the loop length (which is inversely proportional to the wavenumber of a standing mode) is much longer than the loop radius, a , then the phase speed of the fundamental kink mode can be accurately approximated by the kink speed c_k without actually knowing the loop radius. Coronal seismology is a useful tool in the extrapolation of parameters, such as the coronal magnetic field strength which cannot be observed directly. The use of coronal seismology of loops was first put forward by Roberts et al. (1984). The method has been successfully used with TRACE data by Nakariakov et al. (1999) and Nakariakov and Ofman (2001). In Nakariakov et al. (1999), an observation of the fundamental kink mode was made with frequency $\omega = 1.47 \pm 0.05 \text{ rad min}^{-1}$ or $\frac{\omega}{2\pi} = 3.90 \pm 0.13 \text{ mHz}$ in a loop of length $L = (130 \pm 6) \times 10^6 \text{ m}$. Assuming the loop can be represented by this model, the frequency is related to phase speed and wavelength (twice the loop length) by

$$\omega = \frac{\pi c_k}{L}. \quad (2.62)$$

From this a kink speed of $c_k = 1040 \pm 50 \text{ km s}^{-1}$ can be deduced. Now if we assume a uniform magnetic field the kink speed and internal Alfvén speed v_{Ai} can be related by

$$c_k = \left(\frac{2}{1 + \rho_e/\rho_i} \right)^{\frac{1}{2}} v_{Ai}, \quad (2.63)$$

and if we suppose the loop has an order of magnitude density enhancement over its environment we can then determine the internal Alfvén speed to be $v_{Ai} \approx 770 \pm 40 \text{ km s}^{-1}$. Combining equations (2.62) and (2.63) we obtain an expression for the coronal magnetic field strength (Nakariakov and Ofman, 2001)

$$B_0 = (2\mu)^{\frac{1}{2}} (\rho_i)^{\frac{1}{2}} \left(1 + \frac{\rho_e}{\rho_i} \right)^{\frac{1}{2}} L \frac{\omega}{2\pi}. \quad (2.64)$$

Note the dependence of the field strength on the square root of the density so reducing the error due to a poor estimation of the density. Densities of $10^{9.3 \pm 0.3} \text{ cm}^{-3}$ at the loop apex and $10^{9.2 \pm 0.3} \text{ cm}^{-3}$ leads to a coronal magnetic field of $B_0 = 13 \pm 9 \text{ G}$ (Nakariakov and Ofman, 2001).

It should be noted that the fundamental kink mode is not the only mode to propagate as a trapped mode in the thin tube limit with a phase speed close to c_k ; the fluting modes ($m \geq 2$) also possess this property. Therefore, the fundamental modes for all $m \neq 0$ propagate as a trapped mode in the long wavelength limit. This suggests that it may be more appropriate to view the fundamental sausage mode ($m = 0$) as a special case, propagating only as a leaky mode in the long wavelength limit. Unfortunately it is difficult to see how it is possible to take advantage of this special property of the sausage mode as there is no convenient expression for its behaviour in this limit and also any observation of the fundamental sausage mode in this limit will be rapidly damped through leakage of energy into the loop's environment (see, for example, Brady and Arber, 2005).

In the other extreme, as ka becomes large (corresponding to the short wavelength limit) all modes have phase speeds which tend to the internal Alfvén speed, v_{Ai} .

2.6.2 Eigenfunctions $\beta = 0$

The eigenfunctions are evaluated analytically, although the frequency of the mode must still be determined numerically. It is also possible to solve equation (2.13) or (2.14) numerically in order to obtain solutions for the eigenfunctions. This is the method used if more complicated Alfvén profiles are to be considered (Goossens et al., 2002).

2.6.3 Long wavelength limit

In this section we discuss the perturbations produced in the propagation of the kink mode. It is important to remark that as this is a linear problem all eigenfunctions have an unspecified multiplicative constant, which we fix by setting the maximum value of the non-dimensionalised total pressure perturbation, $P_T/\rho_i v_{Ai}^2$, to unity. In some cases this results in other perturbations that are large, but this indicates that the initial normalisation was inappropriate rather than a failure of linear theory.

In Figure 2.5 we plot: (a) the non-dimensional total pressure perturbation, (b) the radial velocity (v_r/v_{Ai}); (c) the azimuthal velocity (v_θ/v_{Ai}); and (d) the longitudinal velocity (v_z/v_{Ai}), each as a function of the radial coordinate r/a for the case $v_{Ae} = 2.5v_{Ai}$ and a longitudinal wavenumber $ka = 0.2$. For $ka = 0.2$, it can be seen from the dispersion diagram that only the fundamental kink mode is trapped and it takes a phase speed close to c_k . Fig. 2.5(a) shows the total pressure perturbation has one extrema, occurring at the tube radius $r = a$, and otherwise decays to zero at the centre of the loop and also as $r \rightarrow \infty$. This behaviour is similar to that shown by a surface mode; however, this is a body mode (since $m_i^2 < 0$) (Zhugzhda, 2004). Inside the tube, the

growth of the total pressure perturbation is linear in r , as a result of the small value of ka . Also, for the same reason, the penetration of this perturbation into the environment is very high (the smaller m_e , the higher the penetration), having only decayed by a factor of five after four tube radii (comparisons with other modes are made later). Fig. 2.5(b) shows the radial component of the velocity has its maximum value of $v_r/v_{Ai} = 9.5$ at the centre of the tube and is approximately uniform across the tube; this indicates that the oscillation of the tube is like that of a solid body. Outside the tube the radial velocity falls off rapidly, decaying by a factor of eight by a distance of four tube radii. Fig. 2.5(c) shows the azimuthal velocity has an almost uniform value $v_\theta/v_{Ai} = 9$ across the tube but, as evident directly from the analytical expressions for the eigenfunction, has a discontinuous jump in phase at the tube boundary. Therefore the tube interior and exterior oscillate out of phase, causing a shearing effect across the tube boundary. Finally, if we assume that the oscillation had a radial velocity of 50 km s^{-1} (which is one twentieth of a typical coronal internal Alfvén speed of 1000 km s^{-1}), then we would expect this mode to cause a maximum perturbation in the total pressure of 0.5% of the background. The small value of the total pressure perturbation is consistent with this mode being almost incompressible.

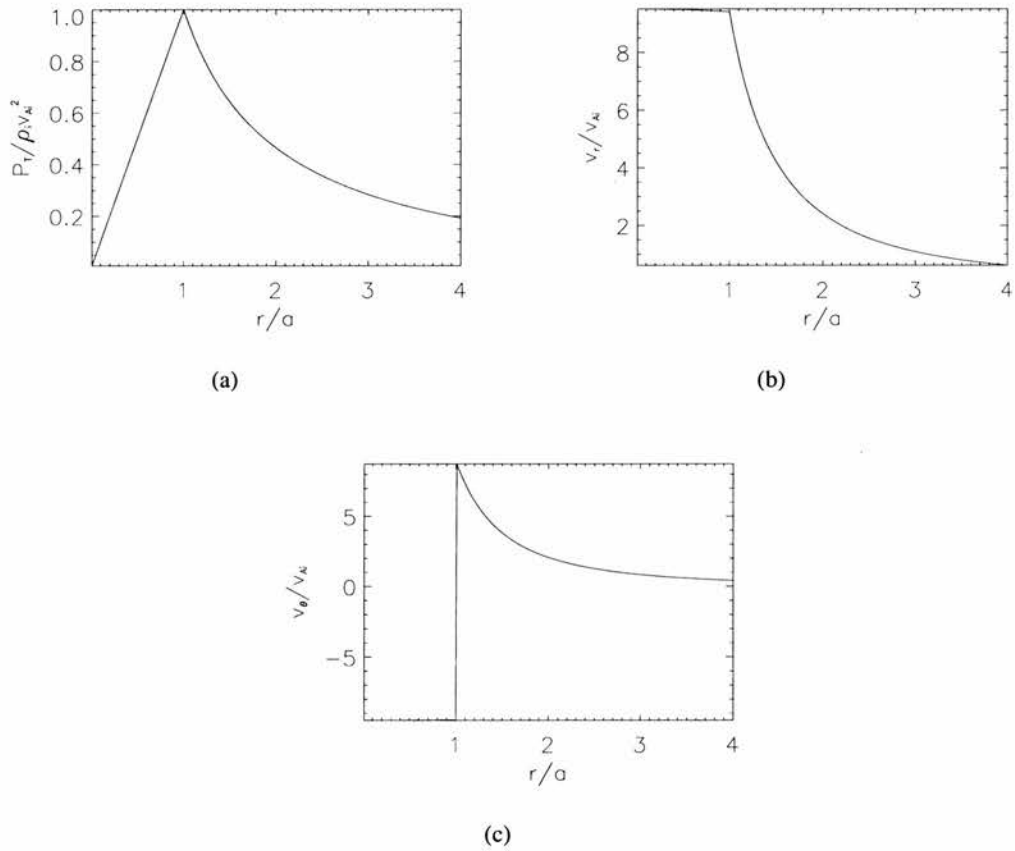


Figure 2.5: Eigenfunctions of the fundamental kink mode in the $\beta = 0$ limit, for $v_{Ae} = 2.5v_{Ai}$ and $ka = 0.2$. Plotted are the non-dimensional (a) total pressure $P_T / \rho_i v_{Ai}^2$, (b) radial velocity v_r / v_{Ai} and (c) azimuthal velocity v_θ / v_{Ai} , each as a function of the dimensionless radial coordinate r/a .

2.6.4 Short wavelength kink modes

Next we discuss the behaviour of the perturbation for a larger value of ka , taking $ka = 3.8$, where not only the fundamental but also the first and second harmonics of the kink mode are trapped. See Figures 2.6, 2.7 and 2.8, which display the equivalent quantities as Fig. 2.5.

Fig. 2.6(a) shows that for this larger value of ka the total pressure perturbation has retained its surface mode like behaviour. However, inside the tube it no longer has the same linear growth as seen previously, and the fall off in the environment from its maximum value at the tube radius is very rapid, with the perturbation having all but disappeared by $r = 2.5a$. Fig. 2.6(b) shows that allowing the eigenfunction to evolve from a value of $ka = 0.2$ to $ka = 3.8$ results in the tube no longer oscillating as a solid body, but has large variations in radial velocity across the tube, having decayed from its maximum value at the tube centre to half this value by the tube boundary. In the tube exterior the radial velocity, like the total pressure, falls off rapidly. It is notable that the maximum radial velocity produced in this case has been significantly reduced when compared with the case $ka = 0.2$. Similarly, the azimuthal velocity shown in Fig. 2.6(c) now shows greater variation across the tube radius but as the eigenfunction evolves from a value of $ka = 0.2$ to $ka = 3.8$, it retains the property that the interior and exterior oscillate out of phase. Again, if we suppose there is a 50 km s^{-1} maximum radial velocity we can estimate that this will result in a maximum perturbation to the total pressure of 1.6% compared to its background; this is three times larger than seen in the case of $ka = 0.2$ and so the fundamental kink mode for $ka = 3.8$ shows a higher level of compressibility than it does for $ka = 0.2$.

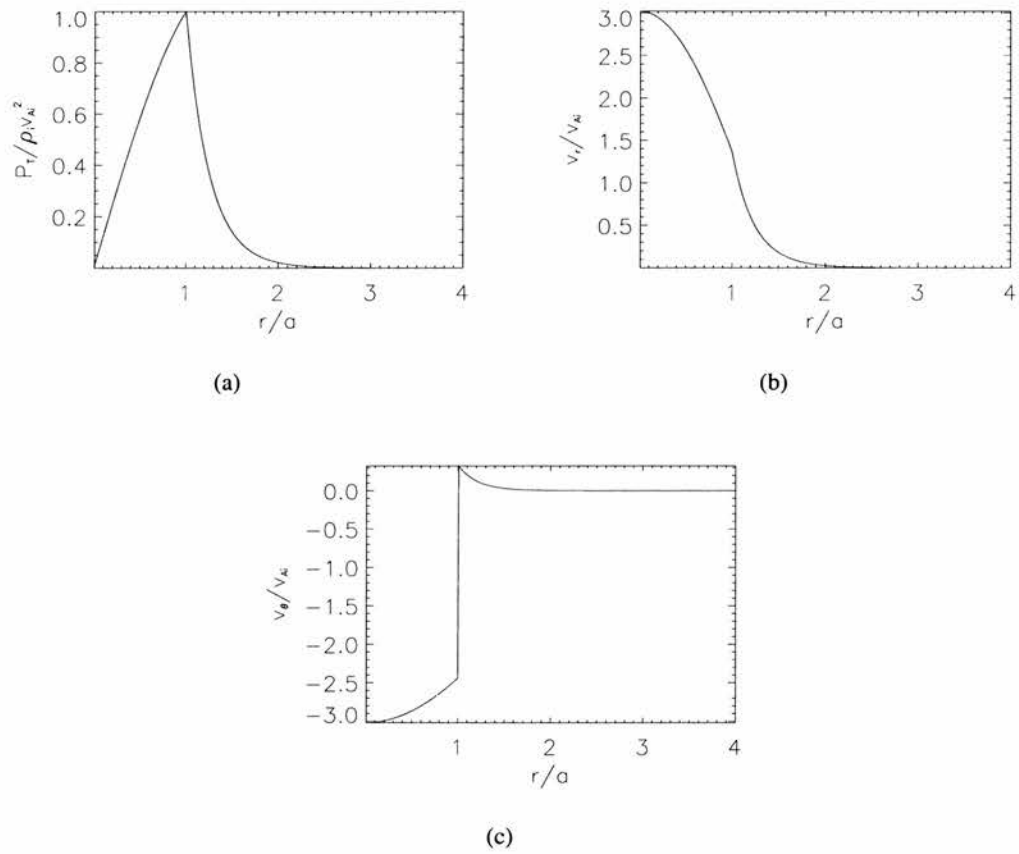


Figure 2.6: Eigenfunctions of the fundamental kink mode in the $\beta = 0$ case, for $v_{Ae} = 2.5v_{Ai}$ and $ka = 3.8$. The figures show the non-dimensional (a) total pressure $P_T / \rho_i v_{Ai}^2$, (b) radial velocity v_r / v_{Ai} , and (c) azimuthal velocity v_θ / v_{Ai} as functions of the dimensionless radius r/a .

For $ka = 3.8$ the first harmonic of the kink mode also propagates as a trapped mode and in Fig. 2.7 we examine the eigenfunctions for the first harmonic. For the first harmonic, each eigenfunction is seen to have two extrema inside the tube rather than the single extrema found in the case of the fundamental mode.

Fig. 2.7(a) shows that the total pressure perturbation is again zero at the tube centre and now takes a maximum value at approximately $r/a = 0.5$, rather than on the tube boundary; after this maxima, it goes through another extrema at $r/a = 1$ and then decays rapidly in the environment. This mode is recognisable as a body mode, as it has oscillations in amplitude throughout the tube. The radial velocity (Fig. 2.7(b)) again takes its maximum value at the tube centre but goes through an oscillatory decay into the environment. Therefore, examining a slice of the tube at a fixed value of z , would show some of the plasma inside the loop oscillating outwards while some is oscillating inwards, so causing a stagnation point ($v_r = 0$) in the radial direction which corresponds to the extrema in the total pressure perturbation. Also the maximum value of v_r/v_{Ai} produced by the total pressure perturbation is smaller than in previous cases. Fig. 2.7(c) shows the azimuthal velocity takes its maximum value (in absolute terms) at the centre of the tube and rapidly increases across the tube until it takes a positive value at the tube boundary, so again inside the tube there is a stagnation point on either side of which the plasma is oscillating out of phase. There is also a discontinuous jump in phase at the tube boundary, as discussed previously, causing a shearing. If again we suppose the radial velocity is 50 km s^{-1} at its maximum value, then this mode would result in a maximum perturbation to the total pressure of 4.5% of the equilibrium value. Hence this mode causes a significant level of compressibility when compared with the fundamental mode.

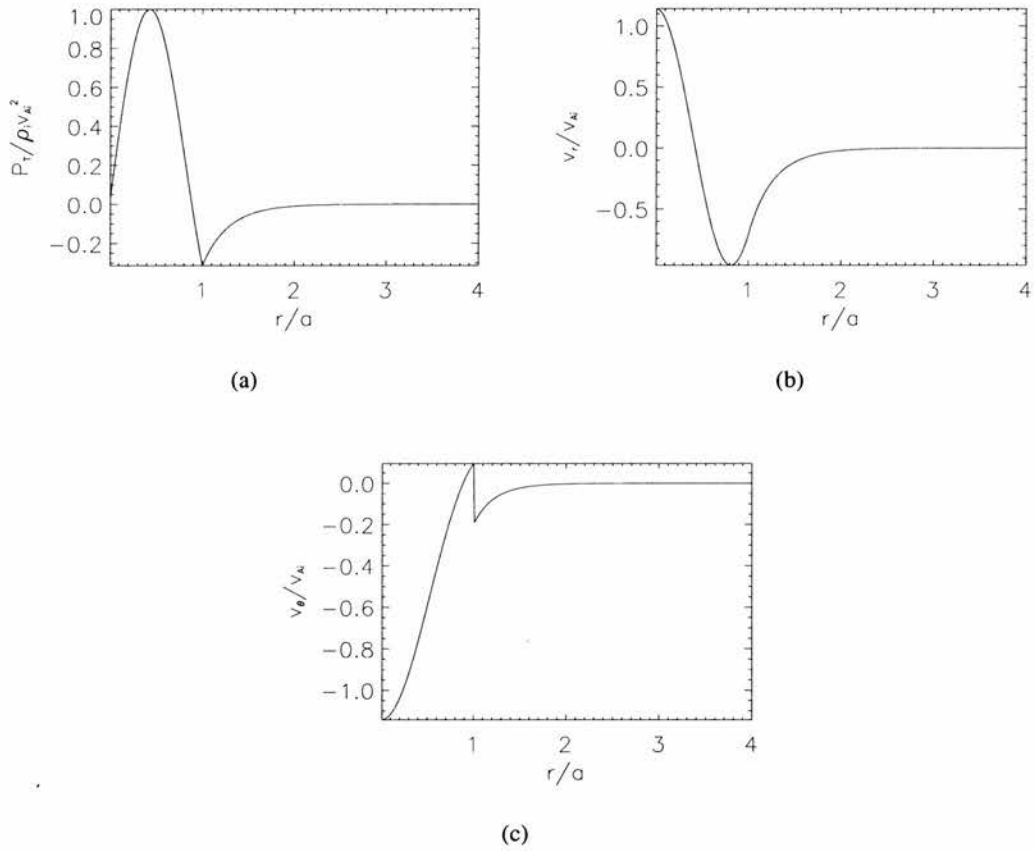


Figure 2.7: Eigenfunctions of the first kink harmonic in the $\beta = 0$ limit for $v_{Ae} = 2.5v_{Ai}$ and $ka = 3.8$. The figure shows the (a) total pressure $P_T / \rho_i v_{Ai}^2$, (b) radial velocity v_r / v_{Ai} , and (c) azimuthal velocity v_θ / v_{Ai} as functions r/a .

The last kink mode to be trapped when $ka = 3.8$ is the second harmonic, with eigenfunctions shown in Fig. 2.8. We see that the number of extrema inside the tube for each eigenfunction has now increased to three.

Fig. 2.8(a) displays the total pressure perturbation which is zero at the tube centre but grows rapidly to its first extrema, where it takes its largest value: thereafter, an oscillation in magnitude is seen along with a decay in absolute terms until the tube boundary. In the environment the perturbation rapidly decays away from the tube. Again this mode is instantly recognisable as a body mode. The radial velocity (Fig. 2.85(b)) takes its largest value at the tube axis and oscillates through a maximum and minimum before decaying away in the tube exterior. As with the total pressure, the maxima with the largest absolute value occurs closest to the tube axis. Also there are two stagnation points, which are seen to correspond to the maxima of the total pressure perturbation. Finally, the azimuthal velocity is seen to take its largest value in absolute terms at the tube centre and oscillates until the tube boundary, so parts of the loop interior have a rotational oscillation which is out of phase with other parts but there is a continuous variation between regions of differing phase. However, on the tube boundary there is a discontinuous jump in phase, resulting in shear flows near the tube boundary. If we suppose a typical radial velocity of 50 km s^{-1} we can estimate that this results in a 5.2% change in total pressure compared with its equilibrium value. Therefore the higher harmonics of the kink mode are more compressive than the fundamental mode, if we assume they have comparable radial velocities. A 5.2% variation in total pressure would be easily detected but the second harmonic has not yet been observed, so it maybe that the fundamental and its harmonics are not in fact generated with comparable amplitudes, or it maybe that dissipation acts more efficiently on higher harmonics.

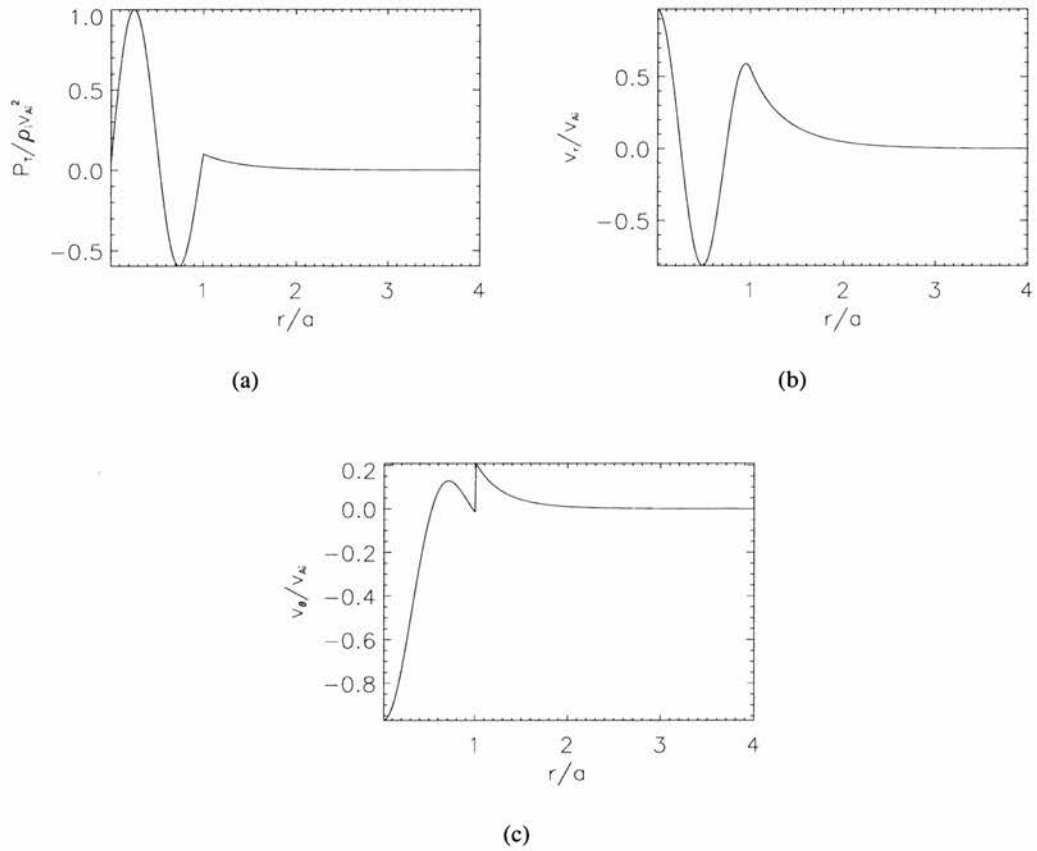


Figure 2.8: Eigenfunctions of the second kink harmonic in the $\beta = 0$ limit for $v_{Ae} = 2.5v_{Ai}$ and $ka = 3.8$. The figures show the non-dimensional (a) total pressure $P_T / \rho_i v_{Ai}^2$, (b) radial velocity v_r / v_{Ai} , and (c) azimuthal velocity v_θ / v_{Ai} as functions r/a .

2.6.5 Short wavelength sausage modes

We now examine the eigenfunctions of the sausage mode which has been described earlier as a cylindrically symmetric pulsation and therefore does not produce an azimuthal velocity. Since there are no trapped sausage modes in the long wavelength limit ($ka \ll 1$) we consider a wavenumber of $ka = 3.8$; at this value both the fundamental and first harmonic of the sausage mode propagate as trapped modes. Again we apply the normalisation of the maximum value of the non-dimensional total pressure to one. Fig. 2.9(a) shows that the total pressure perturbation takes its largest value at the tube centre and falls off across the loop to a second extrema lying on the tube boundary and then decays rapidly in the loop exterior. Fig. 2.9(b) shows the radial velocity; as discussed earlier, the sausage mode does not perturb the position of the tube axis and therefore there is a stagnation point at $r = 0$, which again corresponds to a maximum value in the total pressure perturbation. From the stagnation point the centre of the tube the radial velocity grows to a maximum at the point where the total pressure goes through zero and it then decays rapidly to zero (by a radius of $r/a = 2.5$, it is negligible). Supposing a maximum radial velocity of 50 km s^{-1} , this would result in a maximum total pressure perturbation of 5.5% of its equilibrium value. The fundamental sausage mode is a compressive mode.

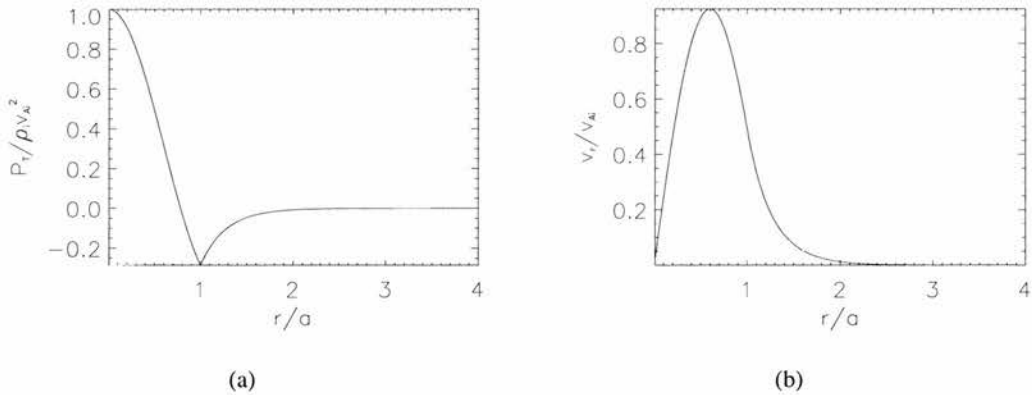


Figure 2.9: Eigenfunctions of the fundamental sausage mode in the $\beta = 0$ limit for $v_{Ae} = 2.5v_{Ai}$ and $ka = 3.8$. (a) total pressure $P_T/\rho_i v_{Ai}^2$, and (b) radial velocity v_r/v_{Ai} , given as functions of r/a .

Fig. 2.10 shows the eigenfunctions for the first harmonic of the sausage mode. We see in Fig. 2.10(a) that the total pressure perturbation takes its maximum value at the tube centre and oscillates through a second minimum (which is smaller in absolute terms than the first) before reaching another maximum at $r = a$ and decaying rapidly thereafter in the environment. The radial velocity shown in Fig. 2.10(b) has a stagnation point at the tube centre, oscillates through a maximum and a minimum and then decays rapidly in the environment. If we assume a maximum radial velocity of 50 km s^{-1} , then we would expect to see a perturbation of 7.1% in total pressure on the tube axis.

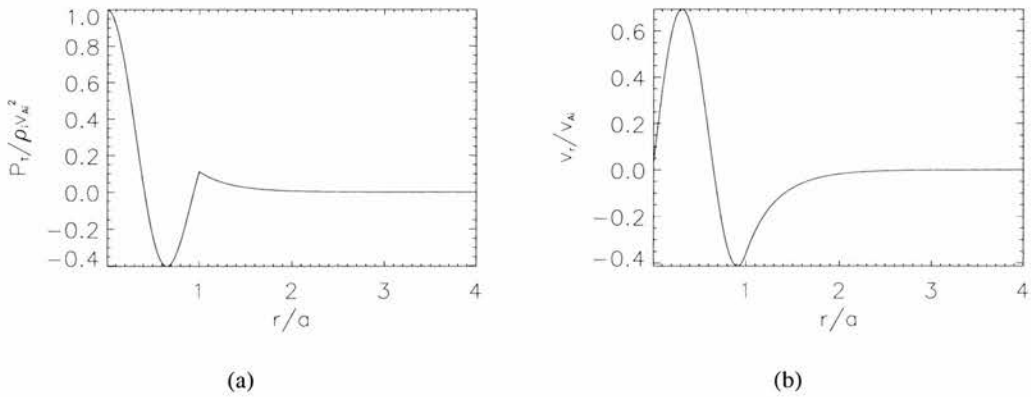


Figure 2.10: Eigenfunctions of the first sausage harmonic in the $\beta = 0$ limit for $v_{Ae} = 2.5v_{Ai}$ and $ka = 3.8$. (a) total pressure $P_T / \rho_i v_{Ai}^2$, and (b) radial velocity v_r / v_{Ai} , as functions of r/a .

2.6.6 Characterizing the sausage and kink modes

The kink mode is characterized by an oscillation of the tube axis and a shear azimuthal velocity across the tube boundary. The radial and azimuthal velocities are comparable for the kink mode. Also, in comparison to the sausage mode, the kink mode exhibits low levels of plasma compression. In the long wavelength limit ($ka \ll 1$) it is seen that the kink mode causes an almost solid body oscillation of the tube, and resultant plasma perturbations penetrate a significant depth into the environment of the tube. At shorter wavelengths, more harmonics are present and do not show a solid body oscillation; there are higher levels of compression with each harmonic and lower levels of penetration into the environment.

The sausage mode is characterized by a cylindrically symmetric oscillation leaving the tube axis unmoved and no azimuthal flows. The mode is trapped only for shorter wavelengths and shows much higher levels of compression than the kink mode. However, the penetration of the sausage mode into the tube environment is comparable with that of the kink mode at similar wavelengths.

2.7 $\beta \neq 0$

Although the $\beta = 0$ model produces a useful coronal model for the fast modes it eliminates some features such as the slow modes which it may be interesting to comment on. Therefore we now reintroduce pressure effects and study the case where β is small but non-zero in order to examine the effects of $\beta \neq 0$ on the fast modes. We also consider the slow mode oscillations which are absent in the $\beta = 0$ case.

Fig. 2.11 show the dispersion diagram for the non-zero beta case, plotting the non-dimensional phase speed c/v_{Ai} against ka for the case $v_{Ae} = 2.5v_{Ai}$, $c_i = 0.5v_{Ai}$, $c_e = 0.3v_{Ai}$, with the sausage modes ($m = 0$) and kink modes ($m = 1$) plotted as dashed and solid curves respectively. We can see that, as in the zero β case, a band of fast modes lying in the range $[v_{Ai}, v_{Ae}]$ which show very similar behaviour to what has already been observed in the $\beta = 0$ case. Again, only the fundamental kink mode propagates for all ka , showing a weakly dispersive nature; in the long wavelength limit ($ka \rightarrow 0$), the kink mode has a phase speed c_k . All other sausage and kink modes reach their cutoff speed at $c = v_{Ae}$ where modes become leaky. The value of ka for which each sausage mode becomes leaky is given by (Roberts et al., 1984)

$$ka = j_{0i} \left(\frac{(c_i^2 + v_{Ai}^2)(c_{Ti}^2 - v_{Ae}^2)}{(v_{Ae}^2 - c_i^2)(v_{Ai}^2 - v_{Ae}^2)} \right)^{\frac{1}{2}}. \quad (2.65)$$

In the same way, for the $(i + 1)^{th}$ kink modes ($m = 1$) the cutoff values of ka are given by

$$ka = j_{1i} \left(\frac{(c_i^2 + v_{Ai}^2)(c_{Ti}^2 - v_{Ae}^2)}{(v_{Ae}^2 - c_i^2)(v_{Ai}^2 - v_{Ae}^2)} \right)^{\frac{1}{2}}. \quad (2.66)$$

Here j_{0i} denotes the zeros of the Bessel function J_0 and j_{1i} denotes the zeros of J_1 . All sausage and kink fast modes are seen to be highly dispersive with $c \rightarrow v_{Ai}$ as $ka \rightarrow \infty$. Notice that each harmonic has a larger phase speed than the previous mode. Therefore the introduction of a non-zero β has not resulted in a structural change to the fast mode band, though there are some modifications to the phase speed.

Having a non-zero β makes a significant difference though introducing a slow mode band. This occurs in the phase speed range $[c_{Ti}, c_i]$, where an infinite number of slow modes are contained with each harmonic having a smaller phase speed than lower harmonics (note this is the opposite behaviour to fast modes). It is seen that all slow sausage and slow kink modes propagate for all values of ka , with phase speeds tending to c_{Ti} in the long wavelength limit and c_i in the short wavelength limit. Since these modes propagate for all values of ka they never become leaky. Also with the slow modes being confined to such a narrow band of phase speeds, $[c_{Ti}, c_i]$, the slow modes are only weakly dispersive in nature.

2.7.1 Fast mode eigenfunctions

We examine the eigenfunctions of the fast modes in the finite β case. However, as there is no structural change in behaviour only slight modifications to the results from the zero β case occur. We will not comment on the total pressure, radial and azimuthal velocities, although they are still plotted. We will, however, comment on the longitudinal velocity since this is zero in the $\beta = 0$ case. The perturbed pressure and density have the same behaviour as the longitudinal velocity, apart from a different scaling. Throughout this section we have chosen the speeds to be $v_{Ae} = 2.5v_{Ai}$, $c_i = 0.5v_{Ai}$, $c_e = 0.3v_{Ai}$, which is a typical ordering for the corona.

Fig. 2.12 shows the fundamental kink mode in the long wavelength range with $ka = 0.2$; it is the only mode to propagate for this value. Again we see the solid body oscillation with the radial and azimuthal velocities inside the tube being of comparable magnitude. Fig. 2.12(a) and (d) show that the total pressure and the longitudinal velocity, grow linearly with radius r from 0 at the tube centre to a maximum value on the boundary of the tube. The longitudinal flow v_z displays a discontinuous drop from its maximum in the environment, so the plasma inside the tube oscillates more rapidly than in the environment. For increasing r , the longitudinal velocity decays to zero; but (as with the other perturbations) in this case it penetrates a significant depth into the environment.

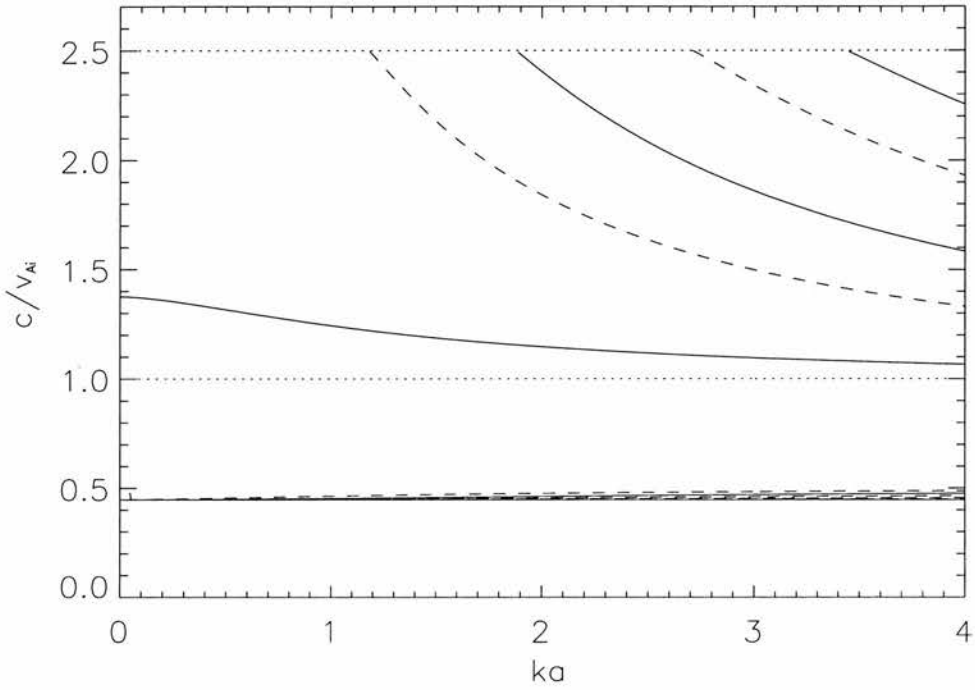


Figure 2.11: The dispersion diagram for $v_{Ae} = 2.5v_{Ai}$, $c_i = 0.5v_{Ai}$ and $c_e = 0.3v_{Ai}$, showing the non-dimensional phase speed $\frac{c}{v_{Ai}} (= \frac{\omega}{kv_{Ai}})$ a function of ka . The solid curves are the kink modes and the dashed curves sausage modes. There is a band of fast waves with $v_{Ai} < c < v_{Ae}$ and a band of slow waves in $c_{Ti} < c < c_i$.

If we suppose a typical maximum radial velocity of 50 km s^{-1} and an internal Alfvén speed of 1000 km s^{-1} , this will result in a small 0.6% total pressure perturbation and a negligible longitudinal velocity of 1 km s^{-1} . This indicates that the fast fundamental kink mode is predominantly a transverse mode, for this wavenumber.

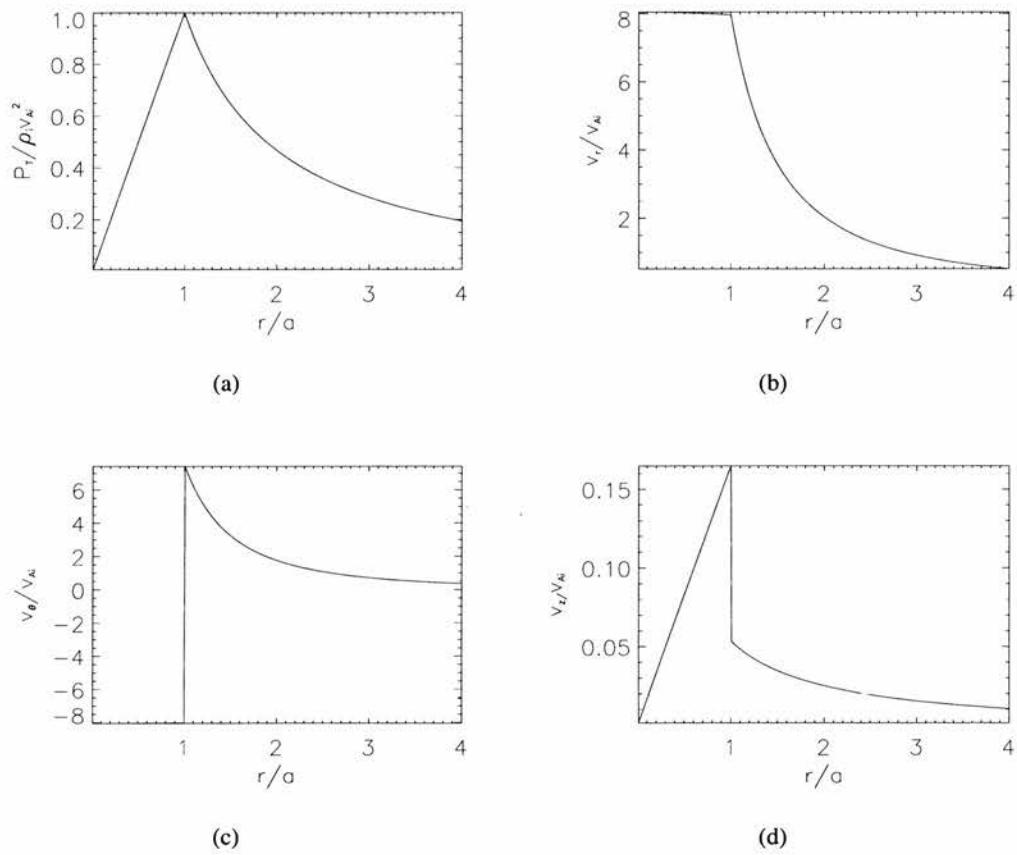


Figure 2.12: Eigenfunctions of the fundamental kink mode for $v_{Ae} = 2.5v_{Ai}$, $c_i = 0.5v_{Ai}$, $c_e = 0.3v_{Ai}$ and $ka = 0.2$. (a) total pressure $P_T / \rho_i v_{Ai}^2$, (b) radial velocity v_r / v_{Ai} , (c) azimuthal velocity v_θ / v_{Ai} , and (d) longitudinal velocity v_z / v_{Ai} as functions of r/a .

Next we examine the fundamental fast kink mode in the short wavelength range, at a value of $ka = 3.8$; see Fig. 2.13. Again much the same behaviour is found for the total pressure, radial and azimuthal velocities as in the zero beta limit. Since the longitudinal velocity is a scaling of the total pressure in each region we see it shares similar properties with growth across the tube but this is not linear for this case. As the scaling for the interior and exterior are different, there is a discontinuity in longitudinal velocity at the tube boundary and thereafter it decays rapidly in the environment. A maximum radial velocity of 50 km s^{-1} and internal Alfvén speed of 1000 km s^{-1} leads to a 2.1% change in total pressure and a maximum longitudinal velocity of 4.7 km s^{-1} . Therefore, the fundamental fast kink mode has remained predominately transverse and incompressible for this choice of wavenumber.

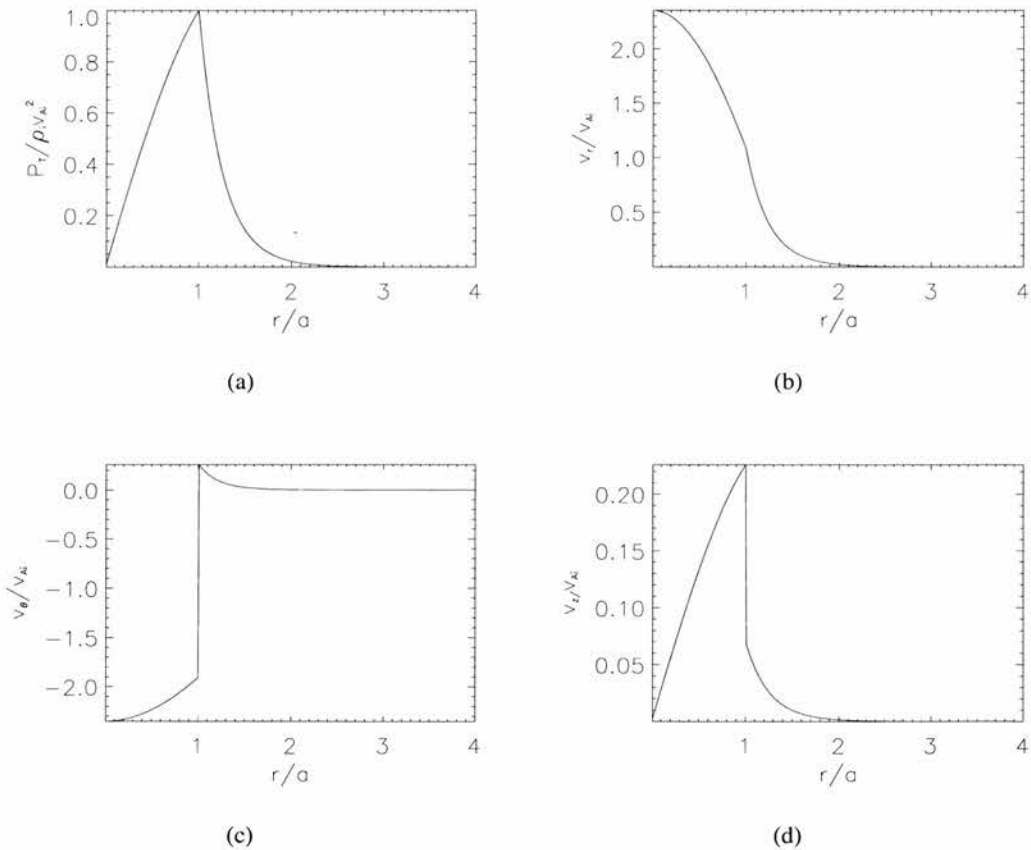


Figure 2.13: Eigenfunctions of the fundamental kink mode for $v_{Ae} = 2.5v_{Ai}$, $c_i = 0.5v_{Ai}$, $c_e = 0.3v_{Ai}$ and $ka = 3.8$. (a) total pressure $P_T / \rho_i v_{Ai}^2$, (b) radial velocity v_r / v_{Ai} , (c) azimuthal velocity v_θ / v_{Ai} , and (d) longitudinal velocity v_z / v_{Ai} as functions of r/a .

Also at this wavenumber of $ka = 3.8$ the first harmonic of the fast kink modes propagates as a trapped mode. In Fig. 2.14 we plot the eigenfunctions for this mode. It can be seen from Fig. 2.14(a), (b) and (c) that the behaviour of the total pressure, radial and azimuthal velocities is the same as found for the zero β case, apart from slight modifications to the magnitudes. However, a non-zero β introduces a longitudinal component to the velocity as shown in Fig. 2.14(d). We can see this perturbation shares many of the same properties as the total pressure, being zero at the tube centre but it takes its maximum value inside the tube at the same radius that v_r goes through zero. After this maximum it decays to another extrema on the tube boundary, where it suffers a discontinuity on moving into the environment, resulting in a small perturbation that quickly decays with distance from the tube.

Assuming the same radial velocity and internal Alfvén speed as previously, the first of the fast kink mode produces a moderate level of compression of 5.5% change in total pressure and longitudinal velocities of 7.2 km s^{-1} ; these values are below current detection limits, so this mode could only be seen as a transverse one.

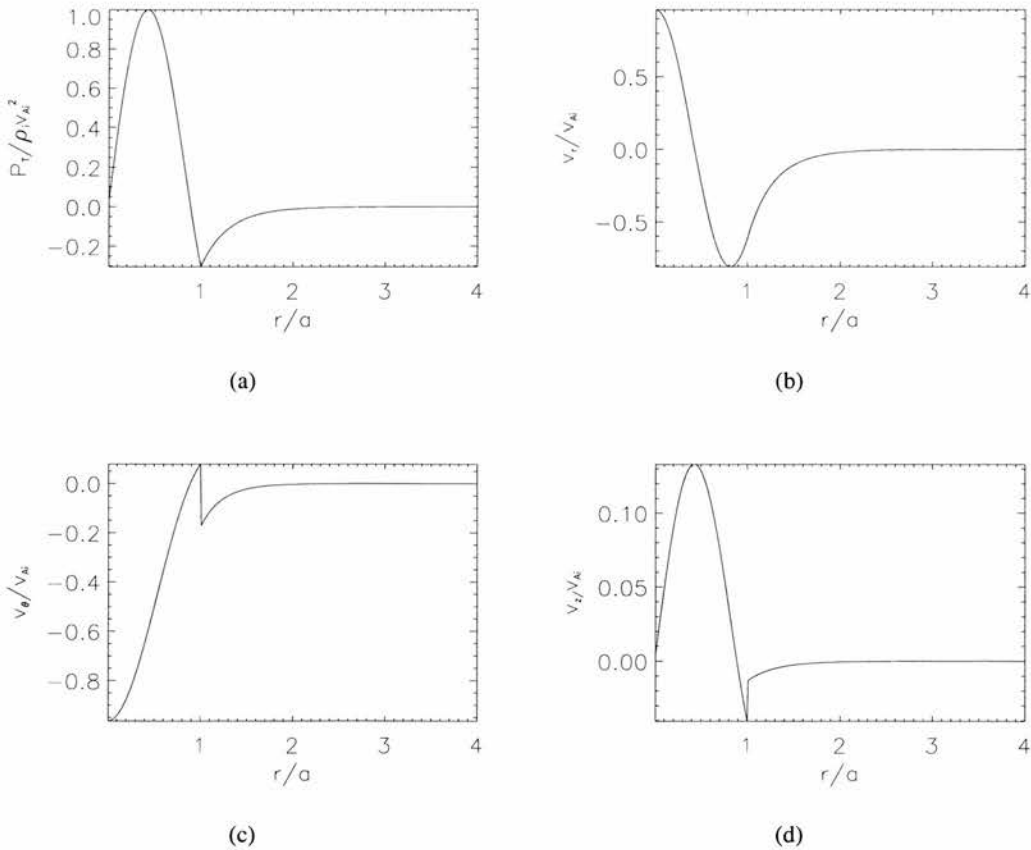


Figure 2.14: Eigenfunctions of the first fast kink harmonic for $v_{Ae} = 2.5v_{Ai}$, $c_i = 0.5v_{Ai}$, $c_e = 0.3v_{Ai}$ and $ka = 0.2$. (a) total pressure $P_T/\rho_i v_{Ai}^2$, (b) radial velocity v_r/v_{Ai} , (c) azimuthal velocity v_θ/v_{Ai} , and (d) longitudinal velocity v_z/v_{Ai} as functions r/a .

Next we examine the fundamental fast sausage mode. As with the kink mode, the behaviour of the total pressure and transverse velocity is the same as that described in the zero β case. The longitudinal velocity (Fig. 2.5(d)), which is not present in the zero β case, shows a maximum value on the tube axis so the largest plasma jets occur at the centre of the tube. Across the tube radius the longitudinal velocity falls to a minimum at the tube boundary, suffers a discontinuous jump on moving into the environment but causes only small perturbations there. Under the earlier assumed conditions, this oscillation would produce a perturbation to total pressure of 6.6% and longitudinal velocities of 11 km s^{-1} .

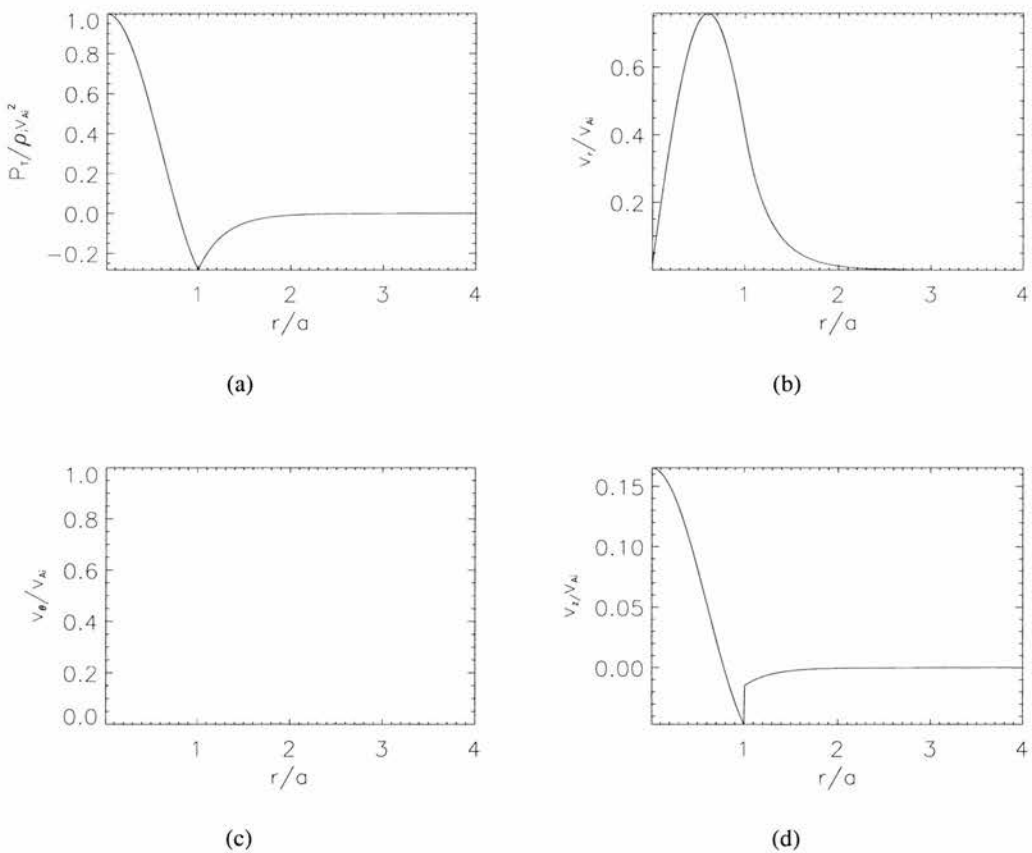


Figure 2.15: Eigenfunctions of the fundamental sausage mode for $v_{Ae} = 2.5v_{Ai}$, $c_i = 0.5v_{Ai}$, $c_e = 0.3v_{Ai}$ and $ka = 3.8$. (a) total pressure $P_T / \rho_i v_{Ai}^2$, (b) radial velocity v_r / v_{Ai} , (c) azimuthal velocity v_θ / v_{Ai} (zero for this mode), and (d) longitudinal velocity v_z / v_{Ai} as functions of r/a .

The second harmonic of the fast sausage mode can also be observed as a trapped mode for this value of ka . In Fig. 2.16 we plot the eigenfunctions of this mode; total pressure and the radial velocity have the same behaviour as in the zero β case. Therefore we describe the behaviour of the longitudinal velocity, shown in Fig. 2.16(d), where it is apparent that the largest flows along the tube occur at its centre. Across the tube it oscillates in magnitude, so there are flows within the tube which oscillate out of phase, while in the environment this mode causes negligible perturbations. We would expect to find an 8% change in total pressure and longitudinal velocities of 8.3 km s^{-1} . Therefore this mode produces a high level of compression for a fast mode and (as expected) small velocities along the tube.

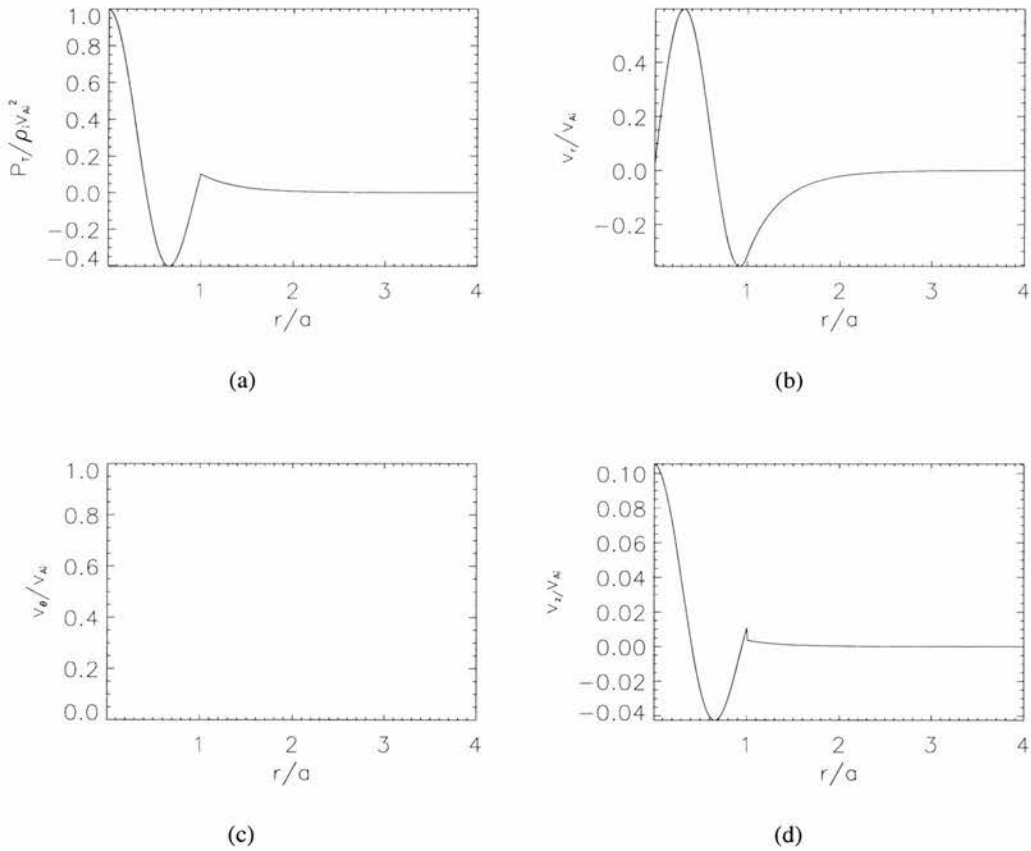


Figure 2.16: Eigenfunctions of the first sausage harmonic for $v_{Ae} = 2.5v_{Ai}$, $c_i = 0.5v_{Ai}$, $c_e = 0.3v_{Ai}$ and $ka = 0.2$. (a) total pressure $P_T / \rho_i v_{Ai}^2$, (b) radial velocity v_r / v_{Ai} , (c) azimuthal velocity v_θ / v_{Ai} (absent for this mode), and (d) longitudinal velocity v_z / v_{Ai} as functions r/a .

2.7.2 Slow modes

As discussed previously, in addition to the band of fast waves in the finite β case there is also a band of slow modes lying between the internal tube and sound speeds. All of these slow modes, of which there are an infinite number, propagate as trapped modes for all values of ka . We now examine the perturbations in the fundamental and first harmonic of the slow mode.

Fig. 2.17 displays plots equivalent to Fig. 2.13, but here for the fundamental slow mode with $ka = 3.8$. Fig. 2.17(a) shows that the total pressure perturbation is again zero on the tube axis and grows to a maximum, which lies inside the tube, but then decays rapidly from this value into the environment, having fallen to zero by $r/a = 2.5$. Fig. 2.17(b) shows that the radial velocity takes its maximum (value in absolute terms) on the tube axis. It then decreases and goes through a stagnation point, which corresponds to the maximum in the total pressure; thereafter v_r reaches a maximum on the tube boundary. So there are two layers inside the tube which oscillate out of phase. Therefore, for this case there is no similarity to the oscillation of a solid body. In the environment the oscillation quickly decays to zero. Fig. 2.17(c) shows the azimuthal velocity has a maximum value at the tube centre, which is of the same magnitude as the maximum value at the tube centre of the radial velocity. The azimuthal component then decays across the radius of the tube and undergoes a discontinuous decrease on the tube boundary. The interior and exterior remain in phase, unlike the fast modes. Fig. 2.17(d) shows the longitudinal velocity, which is simply a scaling of the total pressure for the interior and exterior (the scaling is different in these regions). The most interesting feature of the longitudinal velocity is its magnitude being about nine times larger than the other velocity components. If we suppose a maximum radial velocity of 5 km s^{-1} and internal Alfvén speed of 1000 km s^{-1} we see this oscillation produces a 1.2% perturbation to total pressure and 46.5 km s^{-1} longitudinal velocity. This illustrates the longitudinal nature of the slow mode.

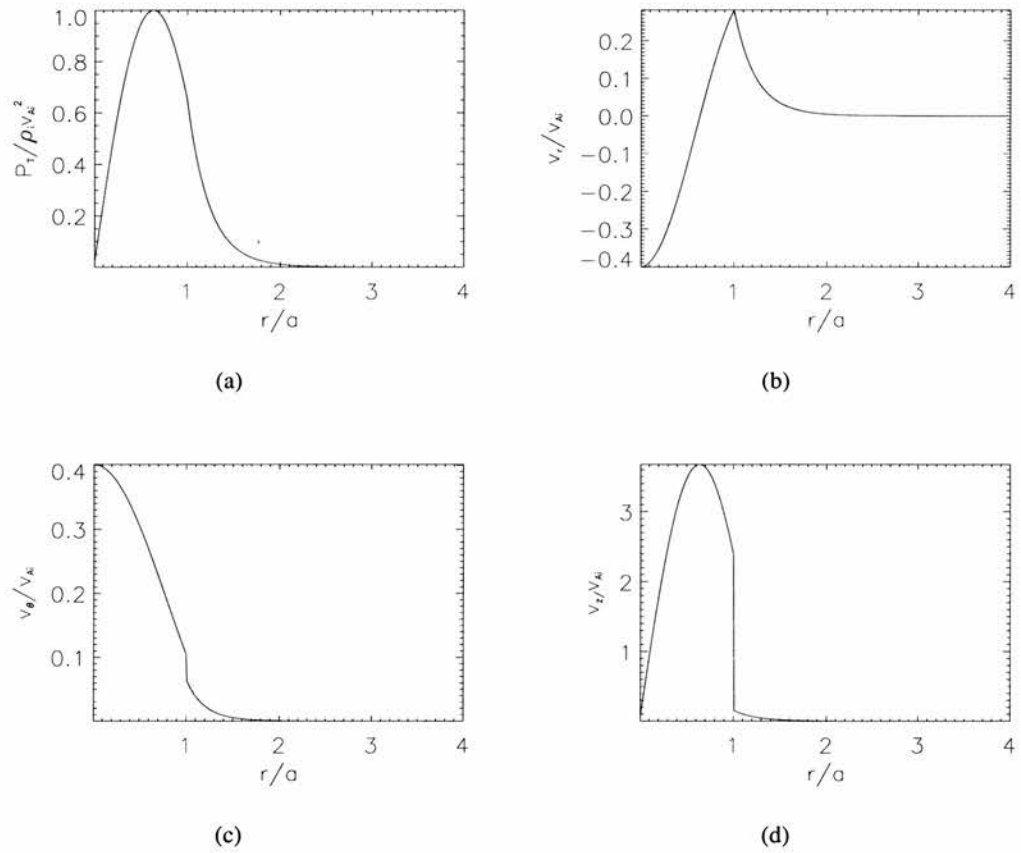


Figure 2.17: Eigenfunctions of the slow fundamental kink mode for $v_{Ae} = 2.5v_{Ai}$, $c_i = 0.5v_{Ai}$, $c_e = 0.3v_{Ai}$ and $ka = 3.8$. (a) total pressure $P_T / \rho_i v_{Ai}^2$, (b) radial velocity v_r / v_{Ai} , (c) azimuthal velocity v_θ / v_{Ai} , and (d) longitudinal velocity v_z / v_{Ai} as functions of r/a .

Next we examine the first harmonic of the slow kink mode. The eigenfunctions of this mode are shown in Fig. 2.18. As expected, the eigenfunctions all have one more extremum than the equivalent eigenfunction of the fundamental mode. Fig. 2.18(a) shows the total pressure perturbation. In common with all other kink modes, there is no perturbation to the total pressure at the tube centre but the pressure perturbation oscillates through two extrema inside the tube before decaying rapidly in the environment. It can be seen that the extremum closer to the tube axis has the largest absolute value. Fig. 2.18(b) shows the radial velocity taking its maximum perturbation on the loop axis and then has another two extrema inside the loop, so two stagnation points arise (which again correspond to the extrema of the total pressure). The perturbation then decays in the exterior. Fig. 2.18(c) shows the azimuthal velocity is largest at the tube centre, going through a zero at a point inside the tube at $r/a \approx 0.7$. A discontinuity occurs on the tube boundary but the interior and exterior regions still oscillate in phase on either side. The perturbation to the exterior is very small in comparison with that at the centre of the tube. Finally, we have the longitudinal velocity (Fig. 2.18(d)) which mimics the behaviour of the total pressure. However, it is discontinuous on the tube boundary. Again, the longitudinal perturbation is much larger than the radial and azimuthal velocities inside the tube. However, there is almost no longitudinal perturbation in the environment; the longitudinal flow is strongly confined to the tube.

Again, supposing a maximum radial velocity of 5 km s^{-1} and an internal Alfvén speed of 1000 km s^{-1} results in a total pressure perturbation of 0.8% and a longitudinal velocity of 66.5 km s^{-1} . This indicates that the higher harmonics of the slow mode show less compression but have a strongly longitudinal nature.

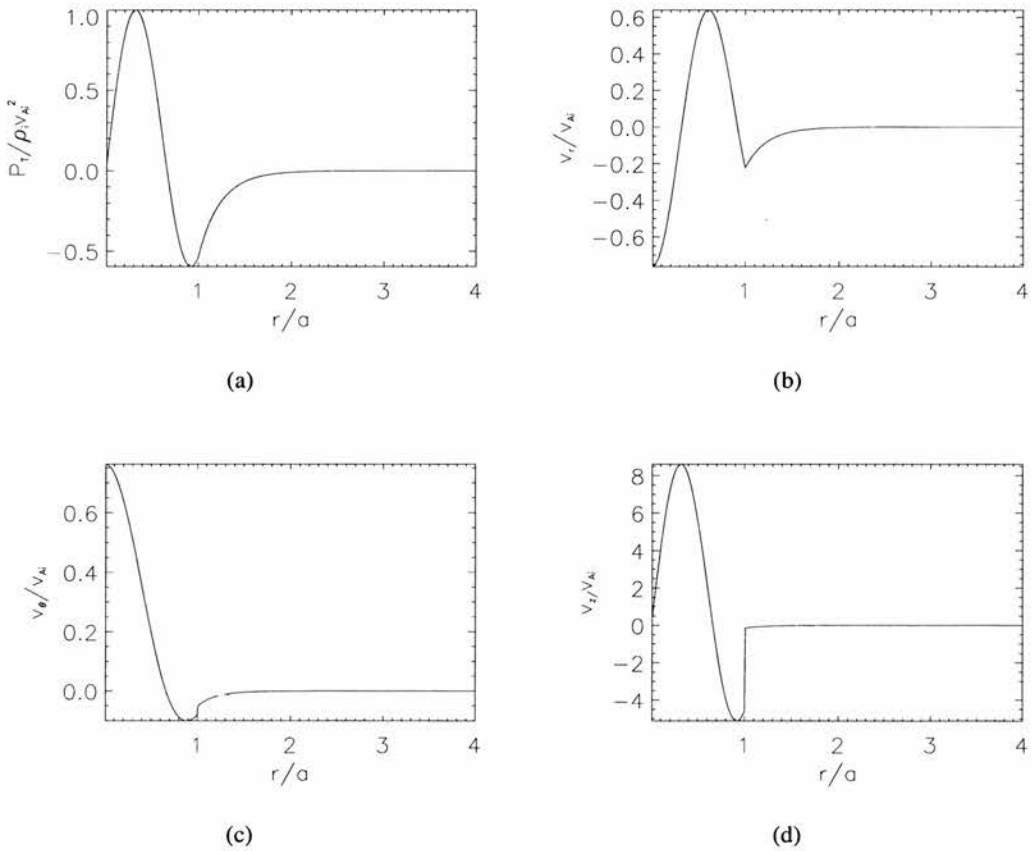


Figure 2.18: Eigenfunctions of the first harmonic of the slow kink mode for $v_{Ae} = 2.5v_{Ai}$, $c_i = 0.5v_{Ai}$, $c_e = 0.3v_{Ai}$ and $ka = 3.8$. (a) total pressure $P_T / \rho_i v_{Ai}^2$, (b) radial velocity v_r / v_{Ai} , (c) azimuthal velocity v_θ / v_{Ai} , and (d) longitudinal velocity v_z / v_{Ai} .

2.7.3 Sausage mode

We now consider the fundamental slow sausage mode. This is expected to be a highly compressible mode which does not perturb the position of the tube axis and causes no azimuthal velocities. Fig. 2.19 shows plots of the eigenfunctions for this mode at a wavenumber of $ka = 3.8$. Fig. 2.19(a) shows that the total pressure perturbation has its largest value at the tube centre. The decay across the tube is rapid, falling in magnitude by a factor of 2.5 at the tube boundary. But the decay in the environment is even faster, with the perturbation falling to a negligible value by $r/a = 2.5$. So this mode has a low level of penetration into its environment. Turning to the radial velocity (Fig. 2.19(b)), v_r is zero at the tube centre (this mode does not perturb the position of the tube axis). The radial velocity then grows in magnitude, with an almost linear behaviour for small r/a , reaching an extremum at the tube-environment interface. In the environment, the decay is very rapid close to $r = a$ but this reduces with distance from the tube as the radial velocity decays to zero. Finally, the longitudinal velocity is shown in Fig. 2.19(d). This is simply a scaling of the total pressure perturbation, so takes its maximum value at the centre of the tube and falls off towards the boundary of the tube, where it has a strong discontinuity as it moves into the environment. In the environment, the perturbations are very small in comparison with those occurring in the tube, suggesting that as the tube expands and contracts plasma is shoot back and forth along the tube. The magnitude of v_z compared with v_r shows that the slow sausage mode is predominantly a longitudinal mode.

For a maximum radial velocity of 5 km s^{-1} and an internal Alfvén speed of 1000 km s^{-1} , the slow sausage mode results in a perturbation in total pressure of 2.9% and a longitudinal velocity of 76.4 km s^{-1} , some fifteen times larger than the transverse velocity.

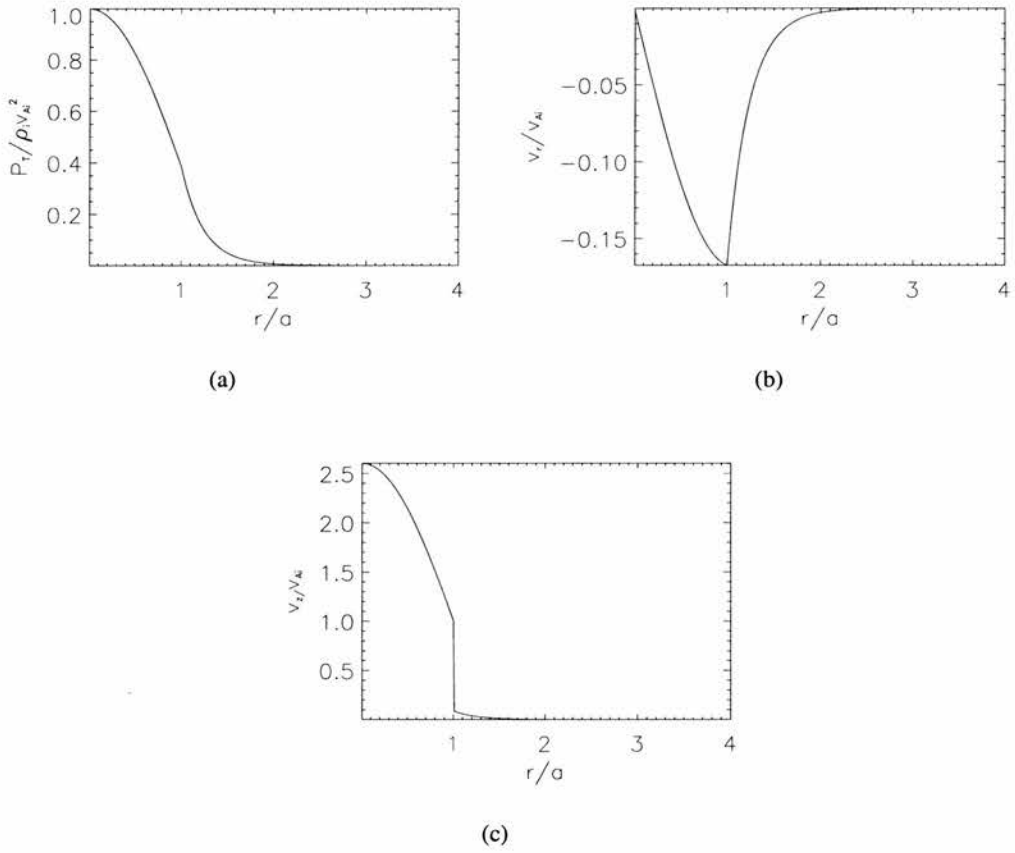


Figure 2.19: Eigenfunctions of the fundamental slow sausage mode for $v_{Ae} = 2.5v_{Ai}$, $c_i = 0.5v_{Ai}$, $c_e = 0.3v_{Ai}$ and $ka = 3.8$. (a) total pressure $P_T / \rho_i v_{Ai}^2$, (b) radial velocity v_r / v_{Ai} , and (c) longitudinal velocity v_z / v_{Ai} . The azimuthal velocity is identically zero for this mode.

We also examine the behaviour of the first harmonic of the slow sausage mode. If the slow sausage mode follows the same trend as exhibited in the slow kink mode, then it will be less compressive than the fundamental mode. Fig. 2.20(a) shows the total pressure perturbation and, as expected, it has two extrema (i.e. one more than the fundamental mode). The first extremum occurs at the centre of the tube and has larger magnitude than the second extremum close to the tube boundary; thereafter, the mode decays to zero. Again, the radial velocity (Fig. 2.20(b)) shows that the position of the tube axis is unperturbed; v_r then oscillates through a minimum inside the tube and reaches a local maximum on the tube boundary. There is a stagnation point between the two extrema which correspond to an extremum of the total pressure perturbation. Therefore this oscillation consists of two concentric layers inside the tube which oscillate out of phase. A rapid decay occurs in the environment. Finally, the longitudinal velocity (which is a scaling of the total pressure) has a similar behaviour, apart from a discontinuity at the tube boundary. Also this oscillation causes almost no longitudinal flow in the environment. In the tube, the magnitude of the longitudinal component of velocity is more than ten times that of the transverse component. Assuming a maximum radial velocity of 5 km s^{-1} and an internal Alfvén speed of 1000 km s^{-1} , this would result in a perturbation to total pressure of 1.25% which (as expected for the slow mode) is less than that arising in the fundamental mode; the maximum longitudinal velocity is 68.7 km s^{-1} , which is more than seven times larger than the transverse velocity.

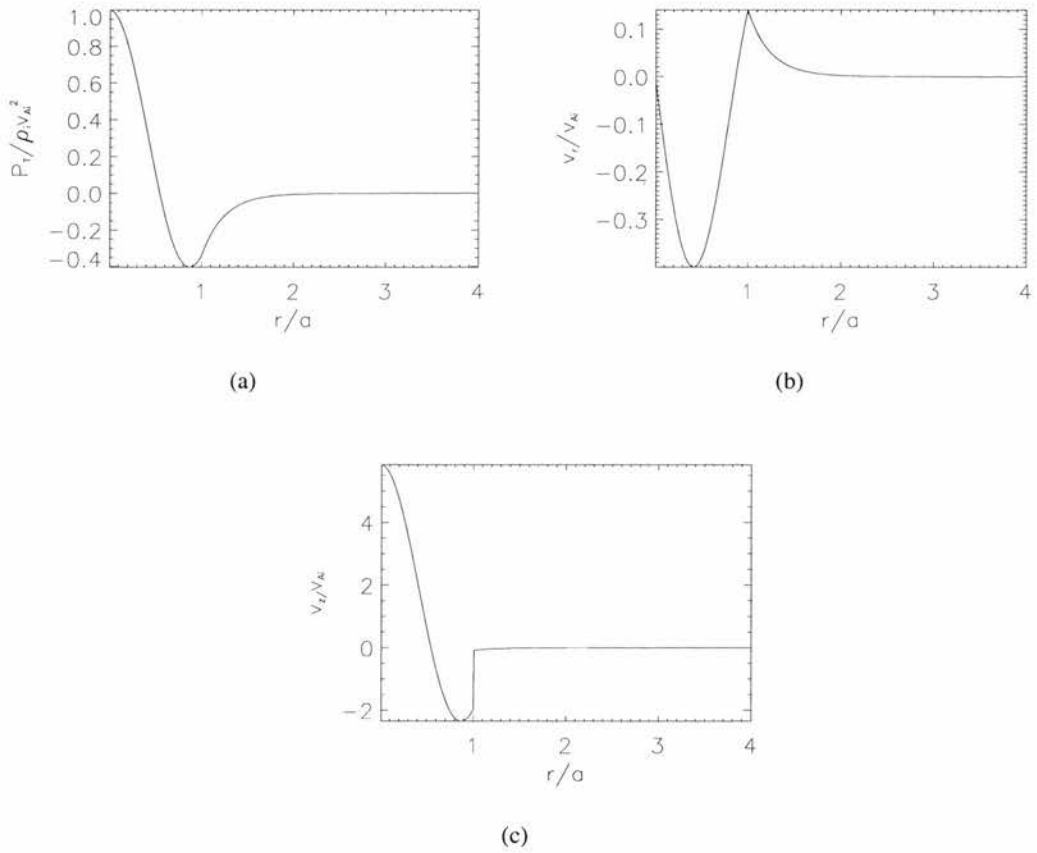


Figure 2.20: Eigenfunctions of the first harmonic of the slow sausage mode for $v_{Ae} = 2.5v_{Ai}$, $c_i = 0.5v_{Ai}$, $c_e = 0.3v_{Ai}$ and $ka = 3.8$. (a) total pressure $P_T / \rho_i v_{Ai}^2$, (b) radial velocity v_r / v_{Ai} , and (c) longitudinal velocity v_z / v_{Ai} .

2.8 Conclusions

We want to answer the following questions:

1. What is the difference between a slow sausage mode and a slow kink mode?
2. What is the difference between fast and slow modes for sausage or kink modes?

2.8.1 What is the difference between a slow sausage or kink mode?

It is interesting to ask: how can we distinguish between a slow sausage mode and a slow kink mode? The answer is not easily given. The sausage and kink definitions focus on transverse behaviour but the slow modes are predominantly longitudinal and therefore this distinction is not easily made. Also both modes share a highly compressive nature in their fundamental and lower harmonics; however, the compressibility of each harmonic becomes less than the previous ones. Therefore we must look at the eigenfunctions themselves and the difference between these modes is most apparent along the tube axis. The sausage mode produces the largest total pressure perturbation and longitudinal velocity on the tube axis, while there is no perturbation to the position of the tube axis. By contrast, the kink mode causes no change in total pressure or longitudinal velocity along the axis but takes its largest radial velocity on the axis.

2.8.2 What is the difference between fast and slow modes for sausage or kink modes?

The main difference between fast and slow modes, both sausage and kink, is in the polarisation of the mode: in a low β plasma fast modes are predominantly transverse, while the slow modes show mainly longitudinal velocities. Also the most obvious difference is in the phase speed, with slow modes in the range $[c_{Ti}, c_i]$ and fast modes in the range $[v_{Ai}, v_{Ae}]$. In the long wavelength limit only the fundamental fast kink mode is trapped; this mode has a solid body oscillation causing low levels of compression, while all harmonics of the slow sausage and kink modes are present and do not result in solid body oscillations. For the fundamental modes, a high level of compression occurs. Therefore it is straightforward to determine the difference between fast kink and sausage modes or fast and slow modes but it is not straightforward to distinguish between fast and slow sausage or kink modes.

Chapter 3

Line Tying and Longitudinal Structuring

3.1 Introduction

An important feature of the solar corona is the wide variety of structures which occur as a result of the Sun's complex magnetic field (e.g. Golub and Pasachoff, 1997). Many of these structures share the feature that they have a density enhancement (high plasma density compared with the surrounding plasma), allowing them to act as a MHD wave guide. They may also have temperature or magnetic field enhancements or depletions, but in the low β corona it is density (and through this the Alfvén speed) that plays the major role.

The excellent observational ability of spacecraft such as TRACE and SOHO has provided us with an array of detections of both standing (Aschwanden et al., 1999, 2002, Nakariakov et al., 1999, Schrijver and Brown, 2000, Schrijver et al., 2002, Ofman and Wang, 2002, Wang et al., 2002a,b,c, 2003) and propagating (Berghmans and Clette, 1999, De Moortel et al., 2000c, 2002a,d,c,b, Robbrecht et al., 2000) waves occurring in coronal loops. Despite these capabilities it is still difficult to make direct observations of fundamental quantities such as the magnetic field strength. However, the technique of coronal seismology (Roberts et al., 1984, Roberts, 1986, Nakariakov et al., 1999, Nakariakov and Ofman, 2001, De Moortel et al., 2002a) allows information carried by MHD waves to be extracted from observations of oscillatory events and the results interpreted using theoretical models.

There have been several theoretical models of coronal loops. The first models considered only the simplest aspects of magnetic structuring, using a Cartesian slab (Roberts, 1981, Edwin and Roberts, 1982) or a cylindrical geometry (Spruit, 1982, Edwin and Roberts, 1983). In the cylindri-

cal models the coronal loop is represented by an infinitely long and straight uniform magnetic flux tube. The loop has a plasma density enhancement compared with its environment, and the magnetic field is directed along the loop. This configuration produces a rich array of wave behaviour and is widely used in coronal seismology. Edwin and Roberts (1983) gave a detailed description of the model's dispersion diagram (see also Chapter 2). From this model several additional features may be added, such as the presence of magnetic twist (Bennett et al., 1999, Sakai et al., 2000), the inclusion of a co-axial shell (Solov'ev et al., 2002), the presence of field-aligned flows (Nakariakov and Roberts, 1995a, Somasundaram et al., 1999, Terra-Homem et al., 2003), the role of line-tying effects (Díaz et al., 2004) and stratification (Nakariakov et al., 2000, Nakariakov and Ofman, 2001, James, 2003, Mendoza-Briceño et al., 2004, Roberts, 2006). Also investigations into wave damping through phase mixing (Heyvaerts and Priest, 1976, De Moortel et al., 2000a,b) and mode coupling as a result of resonant absorption (Steinolfson and Davila, 1993, Ofman et al., 1994a,b, Ruderman and Roberts, 2002, Goossens et al., 2002) are available.

Despite extensive work there are still many aspects of coronal loop oscillations and coronal seismology to be explored. Here we consider the role of footpoint structuring on the modes of oscillation. We consider a uniform line-tied loop with longitudinal structuring in the loop's environment by incorporating a dense chromospheric layer. The chromospheric layer produces a cutoff frequency which depends upon the depth of the layer, producing a different cutoff frequency for each mode. In an unbounded homogeneous loop of radius a , the fundamental kink mode propagates as a trapped mode for all wavenumbers ka , with a phase speed equal to the kink speed c_k in the thin tube limit (Chapter 2). However, for a suitable depth of chromospheric layer, we find that the kink mode no longer propagates as a trapped mode. Also, in the case where it is trapped in the thin tube limit, it now propagates at the kink speed that is modified by the presence of the chromospheric layer.

Many results of coronal seismology, such as the deduction of the coronal magnetic field strength from the TRACE loop oscillations (Nakariakov and Ofman, 2001), use the fact that the fundamental kink mode is trapped in the thin tube limit and is propagating at the kink speed. The result that the fundamental kink mode is not trapped in the thin tube limit may thus have important implications for coronal seismology.

3.2 Equilibrium and basic equations

In this study we consider a spatially structured static equilibrium of a cylindrically symmetric line-tied coronal loop or magnetic flux tube (lying parallel to the z axis) of length $2L$ and radius a . The magnetic field $\mathbf{B}_0 = B_0\mathbf{z}$ is assumed to be uniform throughout the medium and aligned with the loop. The equilibrium density $\rho_0(r, z)$ is structured in both the radial and longitudinal

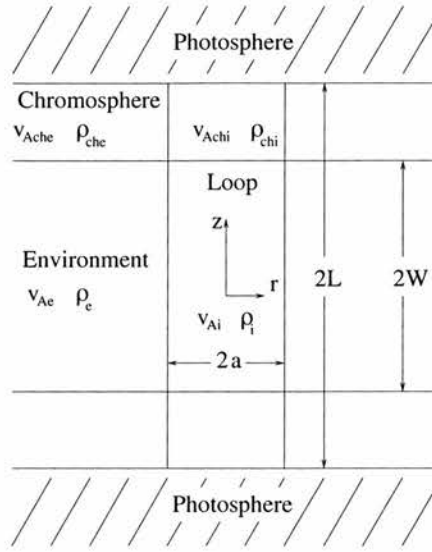


Figure 3.1: A sketch of the equilibrium configuration showing a slice (in r and z) of the cylindrically symmetric uniform coronal loop, of length $2L$ and radius a . The density in the tube interior is ρ_i and the coronal region is of density ρ_e . In the chromospheric layers (of depth $L - W$), the density is ρ_{che} in the external chromosphere and ρ_{chi} in the internal chromosphere. The magnetic field is everywhere uniform and directed parallel to the loop. The footpoints of the loop are fixed at the chromospheric/photospheric base ($z = \pm L$).

directions. Gravitational effects are ignored. Small amplitude oscillations about this equilibrium are introduced. The ideal adiabatic MHD equations (neglecting gravitational effects) reduce to the following system of coupled partial differential equations (see, for example, Roberts, 1991, Díaz et al., 2002)

$$\frac{\partial P_T}{\partial t} = \rho_0 v_A^2 \frac{\partial v_z}{\partial z} - \rho_0 c_f^2 \nabla \cdot \mathbf{v}, \quad (3.1)$$

$$\rho_0 \left[\frac{\partial^2}{\partial t^2} - v_A^2 \frac{\partial^2}{\partial z^2} \right] \mathbf{v}_\perp = -\nabla_\perp \left[\frac{\partial P_T}{\partial t} \right], \quad (3.2)$$

and

$$\rho_0 \left[\frac{\partial^2}{\partial t^2} - c_T^2 \frac{\partial^2}{\partial z^2} \right] v_z = -\frac{c_0^2}{c_f^2} \frac{\partial^2 P_T}{\partial z \partial t}, \quad (3.3)$$

where $v_A = B_0 / \sqrt{\mu \rho_0}$ and $c_0 = \sqrt{\gamma P_0 / \rho_0}$ are the Alfvén and sound speeds, $c_T^{-2} = v_A^{-2} + c_0^{-2}$ determines the tube speed c_T , and $c_f^2 = v_A^2 + c_0^2$. The subscript ‘ \perp ’ denotes components perpendicular to the equilibrium magnetic field, so the perturbed flow is $\mathbf{v} = \mathbf{v}_\perp + v_z \mathbf{e}_z$. The perturbed total pressure is P_T .

The low β or cold plasma approximation ($\beta = 0$) is now taken so we neglect the effect of plasma pressure; this is a good approximation in the corona where the plasma-beta is small. Consequently,

the slow mode is removed from the system. See Chapter 2. Some care should be taken making this approximation to other regions of the solar atmosphere, such as the chromosphere or photosphere, as pressure effects and gravitational stratification play a greater role in these layers (see Roberts, 2004, for a recent discussion). The implication of the $\beta \rightarrow 0$ limit on the speeds of the system are that $c_0 \rightarrow 0$, $c_T \rightarrow 0$ and $c_f \rightarrow v_A$ so acoustic aspects are lost and the fast modes are decoupled from the Alfvén waves; hence the zero β assumption allows a study of fast modes to be undertaken.

We allow for a general longitudinal and transverse structuring in the form of step functions, the equilibrium plasma density profile taking the form

$$\rho_0(r, z) = \begin{cases} \rho_i(z), & r < a \\ \rho_e(z), & r > a \end{cases} \quad (3.4)$$

where we denote internal and external equilibrium values by a subscript ‘i’ and ‘e’ respectively. Making these steps reduces equations (3.1) and (3.2) to the wave equation for P_T (Díaz et al., 2002)

$$\left[\frac{\partial^2}{\partial t^2} - v_{Ai}^2(z) \nabla^2 \right] P_T = 0, \quad (3.5)$$

and equation (3.2) is retained in the same form but with appropriate density and Alfvén profiles depending on whether it is being applied internally or externally to the tube. There is no perturbed flow along the loop ($v_z = 0$).

We consider trapped modes for which there is no propagation of energy towards or away from the loop. This is achieved by imposing $\mathbf{v}_\perp \rightarrow 0$ and $P_T \rightarrow 0$ as $r \rightarrow \infty$. The loop is line-tied with the footpoints fixed in the dense photosphere where it is expected that coronal perturbations will be so small that they are incapable of perturbing the dense photospheric plasma; this leads to the condition $\mathbf{v}_\perp(z = \pm L) = 0$. In this model we have interfaces over which the equilibrium plasma properties jump discontinuously so we must know how the perturbations behave across such surfaces. There are two types of interface: those parallel to the applied equilibrium magnetic field and those which are not parallel to the equilibrium magnetic field. In the case where the interface is parallel to the equilibrium field, the boundary conditions are (see Chapter 1 and Díaz, 2004)

$$\hat{\mathbf{n}} \cdot [\mathbf{v}_1] = \hat{\mathbf{n}} \cdot [\mathbf{B}_1] = 0, \quad [P_T] = 0. \quad (3.6)$$

Thus, only the components of the perturbed velocity and magnetic field perpendicular to the interface are required to be continuous along with the total pressure.

For interfaces which are not parallel to the equilibrium magnetic field, the boundary conditions

are (Chapter 1)

$$[\mathbf{v}_1] = [\mathbf{B}_1] = [P_T] = 0; \quad (3.7)$$

in this case all components of the velocity and the magnetic field (as well as the total pressure) must be continuous at the interface.

3.3 Analytical method

We study oscillatory solutions to equations (3.5) in cylindrical coordinates. We follow Díaz (2004) and assume a solution which is separable in space and Fourier analysing in time, writing P_T in the form

$$P_T(r, \theta, z, t) = u(r) \Phi(\theta) h(z) \exp(i\omega t), \quad (3.8)$$

with ω the frequency. This form for the total pressure perturbations P_T produces a set of ordinary differential equations (for $r < a$):

$$\frac{d^2 u}{dr^2} + \frac{1}{r} \frac{du}{dr} - \left(\lambda^2 + \frac{m^2}{r^2} \right) u = 0, \quad (3.9)$$

$$\frac{d^2 \Phi}{d\theta^2} + m^2 \Phi = 0, \quad (3.10)$$

and

$$\frac{d^2 h}{dz^2} + \left(\frac{\omega^2}{v_{Ai}^2(z)} + \lambda^2 \right) h = 0, \quad (3.11)$$

where m^2 and λ^2 are the separation constants.

Solving equation (3.10) for Φ gives

$$\Phi(\theta) = \Phi(0) \exp(im\theta). \quad (3.12)$$

This solution applies for both the tube interior and the exterior, since the total pressure must be continuous across the tube boundary.

Equation (3.9) for $u(r)$ inside the loop has the form of a Bessel (or modified Bessel) equation of order m for $(\lambda^i)^2 > 0$ (or $(\lambda^i)^2 < 0$); we write

$$u^i(r) = A \begin{cases} I_m(\lambda^i r), & (\lambda^i)^2 > 0, \\ J_m(\{\lambda^i\}^* r), & (\{\lambda^i\}^*)^2 = -(\lambda^i)^2 > 0. \end{cases} \quad (3.13)$$

We have required the solution to be finite in the region $r < a$.

In the environment of the tube the equation for $u(r)$ takes the form of a modified Bessel equation; since we consider only trapped modes, it is required that all perturbations decline to zero as $r \rightarrow \infty$, with the implication that $(\lambda^e)^2 > 0$ and then

$$u^e(r) = CK_m(\lambda^e r), \quad (\lambda^e)^2 > 0. \quad (3.14)$$

The fact that $(\lambda^e)^2 > 0$ for trapped modes is significant; the frequency that $(\lambda^e)^2$ changes sign at defines the cutoff frequency, marking the transition between *trapped* and *leaky* behaviour.

Finally, we consider the equation for $h(z)$, which defines the longitudinal structuring. We can proceed generally, without specifying the equilibrium density profile, by noting that for certain choices of Alfvén profile the differential operator

$$\frac{d^2}{dz^2} + \frac{\omega^2}{v_A^2(z)} + \lambda^2 \quad (3.15)$$

is self-adjoint. If this is the case and $h(z = \pm L) = 0$, which is equivalent to the line-tying condition $\mathbf{v}_\perp(z = \pm L) = 0$, then the Sturm-Liouville (Arfken, 1985) theorem can be applied with the implication that the set of solutions to equation (3.11) form a complete set on $-L \leq z \leq L$. Hence there exists an infinite set of solutions to equation (3.11), and accordingly we label $h(z)$ and $u(r)$ by a subscript n . This gives an orthonormal set for $h_n^i(z)$. The function $h_1^i(z)$ is the solution of equation (3.11) when $n = 1$ and $\lambda^2 = \lambda_1^2$. This allows the external solutions $h_n^e(z)$ to be expanded in terms of the complete set of internal solutions $h_m^i(z)$:

$$h_n^e(z) = \sum_{m=1}^{\infty} H_{nm} h_m^i(z), \quad (3.16)$$

where the coefficients H_{nm} are given by

$$H_{nm} = \int_{-L}^L h_n^e(z) h_m^i(z) dz. \quad (3.17)$$

In order to satisfy the continuity of P_T and v_r on the tube interface $r = a$, we write the solution for P_T as a linear combination of all solutions (Díaz et al., 2001):

$$P_T(r, \theta, z) = \Phi(\theta) \begin{cases} \sum_{n=1}^{\infty} u_n^i(r) h_n^i(z), & r < a, \\ \sum_{n=1}^{\infty} u_n^e(r) h_n^e(z), & r > a. \end{cases} \quad (3.18)$$

Assuming that v_r has the same separable form as P_T , we find

$$v_r(r, \theta, z) = -i\omega\Phi(\theta) \begin{cases} \sum_{n=1}^{\infty} \frac{1}{\rho_i v_{Ai}^2 (\lambda_n^i)^2} \frac{du_n^i}{dr} h_n^i(z), & r < a, \\ \sum_{n=1}^{\infty} \frac{1}{\rho_e v_{Ae}^2 (\lambda_n^e)^2} \frac{du_n^e}{dr} h_n^e(z), & r > a. \end{cases} \quad (3.19)$$

From the continuity of P_T and v_r we can derive the set of linear equations for the amplitude coefficients C_s present in solution (3.14):

$$\sum_{s=1}^{\infty} H_{sn} \left[\frac{1}{\lambda_n^i} I'_m(\lambda_n^i a) K_m(\lambda_s^e a) - \frac{1}{\lambda_s^e} I_m(\lambda_n^i a) K'_m(\lambda_s^e a) \right] C_s = 0 \quad (3.20)$$

for $(\lambda_n^i)^2 > 0$, and

$$\sum_{s=1}^{\infty} H_{sn} \left[\frac{1}{\{\lambda_n^i\}^*} J'_m(\{\lambda_n^i\}^* a) K_m(\lambda_s^e a) + \frac{1}{\lambda_s^e} J_m(\{\lambda_n^i\}^* a) K'_m(\lambda_s^e a) \right] C_s = 0 \quad (3.21)$$

in the case of $(\lambda_n^i)^2 < 0$. These two sets of equations are written as separate summations though the terms in them may in fact be mixed as $(\lambda_n^i)^2$ could change in sign after a finite number of terms. Suppose this change of sign occurs after l terms. Then the appropriate summation would be

$$\begin{aligned} \sum_{s=1}^l H_{sn} \left[\frac{1}{\{\lambda_n^i\}^*} J'_m(\{\lambda_n^i\}^* a) K_m(\lambda_s^e a) + \frac{1}{\lambda_s^e} J_m(\{\lambda_n^i\}^* a) K'_m(\lambda_s^e a) \right] C_s + \\ \sum_{s=l+1}^{\infty} H_{sn} \left[\frac{1}{\lambda_n^i} I'_m(\lambda_n^i a) K_m(\lambda_s^e a) - \frac{1}{\lambda_s^e} I_m(\lambda_n^i a) K'_m(\lambda_s^e a) \right] C_s = 0. \end{aligned} \quad (3.22)$$

The dispersion relation for the trapped modes of oscillation of a line-tied coronal loop with arbitrary longitudinal environmental structuring and step functions in the radial coordinate is satisfied when the determinant of the system of equations (3.22) vanishes. This dispersion relation (not displayed) describes the sausage ($m = 0$), kink ($m = 1$) and fluting ($m \geq 2$) modes. An interesting aspect of the dispersion relation is that, due to the summation over all harmonics, each mode is a combination of both surface and body modes whereas in simpler models (see Chapter 2 and below) these may be considered separately.

3.4 Uniform loop

In order to investigate the effect of chromospheric layers on the oscillations of a coronal loop we consider first the special case of an entirely uniform loop. In this case the chromospheric layer is confined to the loop's environment. This allows a more straightforward discussion of the new effects. Later, in section 3.5, we return to the more realistic model in which the chromospheric

layers occur both inside and outside the loop. Consider, then, equilibrium configuration (3.1) but here assuming an entirely uniform loop profile, of density $\rho_i = \rho_{chi}$. The chromospheric inhomogeneity is then confined entirely to the loop's environment, so that for $r > a$ the density profile is

$$\rho_e(z) = \begin{cases} \rho_{che}, & W < |z| < L, \\ \rho_e, & |z| \leq W, \end{cases} \quad (3.23)$$

where ρ_{che} and ρ_e are the densities in the chromospheric and coronal regions. The symmetry of the equilibrium means that waves can be split into *odd* (having a node at the loop apex $z = 0$) or *even* (with an anti-node at the loop apex) modes. Hence the solution to equation (3.11) (noting that we may neglect the interfaces at $z = \pm W$ inside the loop) for the loop interior (for $r < a$) is

$$h_n^i(z) = \frac{1}{L^{1/2}} \begin{cases} \cos(M_n^i z), & \text{even}, \\ \sin(M_n^i z), & \text{odd}. \end{cases} \quad (3.24)$$

In the exterior (for $r > a$), the equivalent solution for the even modes is

$$h_n^e(z) = \Lambda_{ev} \begin{cases} \cos(M_n^e W) \sin(M_n^{che}(z + L)), & -L < z < -W, \\ \sin(M_n^{che}(L + W)) \cos(M_n^e z), & -W < z < W, \\ \cos(M_n^e W) \sin(M_n^{che}(L - z)), & W < z < L. \end{cases} \quad (3.25)$$

The multiplicative factors $\frac{1}{L^{1/2}}$ and Λ_{ev} have been chosen to normalise the functions $h_n^i(z)$ and $h_n^e(z)$ which satisfy

$$\int_{-L}^L [h_n^i(z)]^2 dz = \int_{-L}^L [h_n^e(z)]^2 dz = 1. \quad (3.26)$$

This leads to a Λ_{ev} defined by

$$\Lambda_{ev}^{-2} = (L - W) \cos^2(M_n^{che} W) + W \sin^2[M_n^e(L - W)] - \frac{1}{2M_n^e} \cos^2(M_n^{che} W) \sin[2M_n^e(L - W)] + \frac{1}{2M_n^{che}} \sin(2M_n^{che} W) \sin[M_n^e(L - W)] \quad (3.27)$$

with an equivalent expression for the odd coefficients, Λ_{od} . The terms M_n^i , M_n^{che} and M_n^e are defined by

$$(M_n^i)^2 = (\lambda_n^i)^2 + \frac{\omega^2}{v_{Ai}^2}, \quad (M_n^{che})^2 = (\lambda_n^e)^2 + \frac{\omega^2}{v_{Ache}^2}, \quad (M_n^e)^2 = (\lambda_n^e)^2 + \frac{\omega^2}{v_{Ae}^2}, \quad (3.28)$$

where λ_n^i and λ_n^e are the separation constants for the interior and exterior regions, respectively.

The line tying condition $h_n(z = \pm L) = 0$ is automatically satisfied by our choice of solution

(3.25) in the loop environment, but M_n^i is restricted to be

$$M_n^i = \frac{n\pi}{2L}; \quad (3.29)$$

if n is odd then this is an even mode, and if n is even then this is an odd mode. There are an infinite set of solutions to equations (3.9) and (3.10) and therefore the systems of equations (3.20) and (3.21) are infinite sets. For the environment region we must apply the boundary conditions for an interface perpendicular to the equilibrium magnetic field at $z = \pm W$, which requires the total pressure, magnetic field and velocity to be continuous across this boundary. This leads to the conditions (via the ideal induction equation) that $h_n^e(z)$ and $\frac{dh_n^e}{dz}$ be continuous across this surface. The result is the transcendental equation

$$M_n^{che} \cot [M_n^{che}(L - W)] = M_n^e \tan [M_n^e W] \quad (3.30)$$

for the even modes, and

$$M_n^{che} \cot [M_n^{che}(L - W)] = -M_n^e \cot [M_n^e W] \quad (3.31)$$

for the odd modes. It has been assumed that $\frac{\omega^2}{v_{Ache}^2} + (\lambda_n^e)^2 > 0$ and $\frac{\omega^2}{v_{Ae}^2} + (\lambda_n^e)^2 > 0$. There are equivalent forms for the case of one or both of $\frac{\omega^2}{v_{Ache}^2} + (\lambda_n^e)^2$ and $\frac{\omega^2}{v_{Ae}^2} + (\lambda_n^e)^2$ being negative; these can be obtained simply by observing that $\sin(ix) = -i \sinh(x)$ and $\cos(ix) = \cosh(x)$.

Equations (3.30) and (3.31) have an infinite number of solutions. In Fig. 3.2 the first three solutions of each equation are plotted as a function of $\omega L/v_{Ai}$. There are an infinite set of solutions to equation (3.11) in the exterior as well as for the interior.

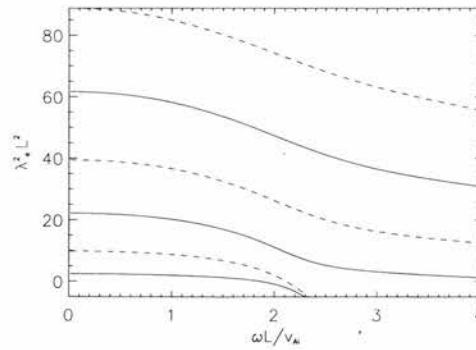


Figure 3.2: Plot of $[\lambda_e]^2 L^2$ against $\omega L/v_{Ai}$, for $v_{Ae} = 2.5v_{Ai}$, $v_{Ache} = 0.25v_{Ai}$ and $W/L = 0.8$. The solid curves are for the even modes (solutions of equation (3.30)) and the dashed curves are for the odd modes (solutions of equation (3.31)).

The final coefficient we require, in order to evaluate the determinant of the system of equations

(3.22) and obtain our dispersion relation, are the values of H_{nm} . Coefficients H_{nm} are evaluated using equation (3.15), which is straightforward but tedious. It is found that for the even modes

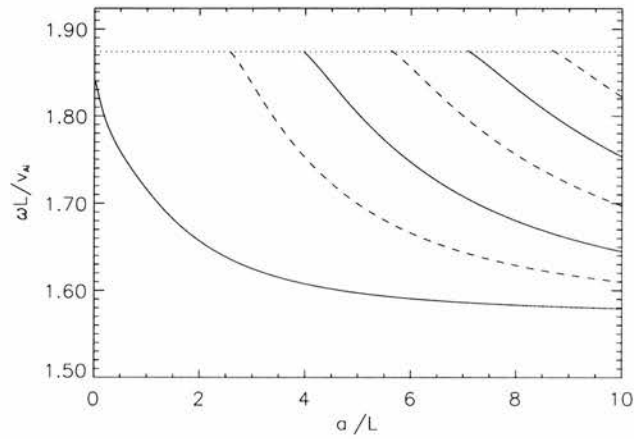
$$H_{2n-1,2m-1} = \Lambda_{ev} L^{-0.5} \left[\sin[M^{che}(L-W)] \left\{ \frac{\sin[(M^i-M^e)W]}{[M^i-M^e]} + \frac{\sin[(M^i+M^e)W]}{[M^i+M^e]} \right\} - \right. \\ \left. \cos[M^e W] \left\{ \frac{\cos[M^i W + M^{che}(W-L)]}{M^i + M^{che}} + \frac{\cos[M^i W + M^{che}(L-W)]}{M^{che} - M^i} \right\} \right]. \quad (3.32)$$

Again, in writing (3.32) it has been assumed that $[M^i]^2$, $[M^{che}]^2$ and $[M^e]^2$ are all positive but equivalent forms can be obtained when this is not the case. Also there is a similar form for the H_{nm} coefficient in the case of the odd modes.

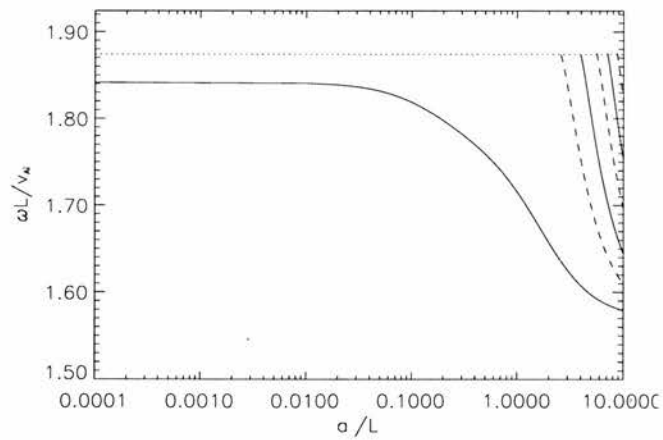
3.4.1 Dependence on loop radius a

We first study the dispersive nature of the modes as the ratio a/L of the loop radius to the loop half-length varies. Fig. 3.3 shows the dispersion diagram for the even modes, for appropriate coronal parameters. The dispersion diagram shows is a band of dispersive fast modes, similar in behaviour to those of Edwin and Roberts (1983). There is only one sausage or kink mode propagating in the thin tube limit $a/L \ll 1$, which is the fundamental kink mode with frequency $\omega L/v_{Ai} = 1.84$. This differs from the typical frequency of the fundamental kink mode in a homogeneous environment, which gives $\omega L/v_{Ai} = 2.06$ for these parameters. The sausage modes and the higher harmonics of the kink modes all have cutoff frequencies, so none propagate in the thin tube limit.

The cutoff curve is marked by the dotted line showing the cutoff frequency $\omega = \omega_{cut}$, with $\omega_{cut}L/v_{Ai} = 1.87$. Therefore we have observed an immediate consequence of the chromospheric layer, which causes the cutoff frequency to differs from its value $\frac{\omega_{cut}L}{v_{Ai}} = \frac{\pi v_{Ae}}{2v_{Ai}} \approx 3.92$ in a homogeneous environment, independently of the internal structure of the loop. It has been found that the internal structure of the loop only causes slight modification to the frequencies of the modes (Díaz, 2004). Fig. 3.3(b) shows a log plot of the dispersion diagram displayed in Fig. 3.3(a), demonstrating the insensitivity of the frequency for the fundamental kink mode to the loop radius for realistically small values of $a/L (\approx 10^{-4} - 10^{-1})$. This is a useful property for coronal seismology, since errors due to inaccuracy in determining the loop radius are minimal if the mode observed is the fundamental kink mode.



(a)



(b)

Figure 3.3: (a) Dispersion diagram for $v_{Ae} = 2.5v_{Ai}$, $v_{Ache} = 0.25v_{Ai}$ and $W/L = 0.8$, showing $\omega L/v_{Ai}$ as a function of a/L . The solid and dashed curves are kink and sausage modes. Case (b) shows the results of (a) using a log scale, displaying more clearly the behaviour for small a/L . The cutoff curve is displayed in (a) and (b) by the dotted line.

3.4.2 Dependence on chromospheric depth

In addition to the parameter a/L there is a second free parameter, W/L , representing the coronal depth. There are two extreme cases involved in this model, $W/L \rightarrow 0$ and $W/L \rightarrow 1$, when the loop's environment becomes uniform. In both cases a structure similar to that of the Edwin and Roberts (1983) model discussed in chapter 2 is obtained. The first case, $W/L \rightarrow 0$, consists of a uniform loop embedded in a dense chromospheric plasma. Therefore the loop has an enhancement in Alfvén speed over its environment and is incapable of supporting trapped modes of oscillation. The second case, of $W/L \rightarrow 1$, now consists of a loop embedded in fine coronal material. In this case the loop has a depression in Alfvén speed compared with its environment, which is exactly the structure Edwin and Roberts (1983) found to support trapped modes of oscillation.

It is interesting to examine the effect of letting $W/L \rightarrow 1$, on the system of equations (3.22). The first thing to note is that the solutions to equation (3.9) inside and outside the loop become identical for $n = m$, and hence these solutions are orthogonal; therefore,

$$H_{nm} = \begin{cases} 0, & n \neq m, \\ 1, & n = m, \end{cases} \quad (3.33)$$

so the system of equations (3.22) becomes diagonal. The diagonal terms are equivalent to the dispersion relation for the trapped modes of oscillation of a magnetic tube with magnetic environment (in the $\beta = 0$ limit) when line-tying is imposed, so a longitudinal dependence of the form (3.23) is assumed. Then the n^{th} term on the diagonal represents the dispersion relation for modes of oscillation with n extrema in the longitudinal direction (Díaz et al., 2004). Hence each diagonal term represents a family of modes with a particular longitudinal wavenumber and each family has its own cutoff frequency $\omega_{cut} = \pi v_{Ae}/2L$. These families are decoupled from each other. Note that when longitudinal structure is incorporated the modes of oscillation become a superposition of these different families, and so have varying longitudinal wavenumbers.

Fig. 3.4 shows the dispersion diagram for $v_{Ae} = 2.5v_{Ai}$, $v_{Ache} = 0.25v_{Ai}$ and $a/L = 10$, displaying the non-dimensional frequency against W/L . A large value of a/L has been chosen to make clearer the main effects introduced in this case. It can be seen there are many trapped sausage and kink modes present for a relatively small range of chromospheric depths ($W/L \approx 0.8 - 1.0$), as would be expected from Fig. 3.3(a) for a large value of a/L . The frequencies appear to be almost independent of chromospheric depth, provided they lie below the cutoff curve.

The most striking difference between this diagram and those against a is that the cutoff curve exhibits a non-uniform variation, varying from $\omega_{cut} = \pi v_{Ache}/2L$ as $W/L \rightarrow 0$ to $\omega_{cut} = \pi v_{Ae}/2L$ as $W/L \rightarrow 1$. This variability in the cutoff frequency is perhaps expected from the presence of the parameter W in equations (3.30) and (3.31) and is independent of a (as previously

noted). As a result of the non-uniform cutoff curve, each mode has a cutoff frequency and value of W/L for which the mode becomes leaky and this is specific to that mode; this is in contrast to the uniform tube, where all cutoff frequencies are the same. Another point to be stressed about the dispersion diagram Fig. 3.4 is that it reveals that the fundamental kink mode also has a cutoff frequency for small W/L , even in the case $a/L = 10$, and also has a cutoff frequency in the thin tube limit, where this mode is typically thought of as a trapped mode.

Fig. 3.5 displays the case of a thin tube, $a/L = 0.1$, so essentially plots the variation of the modified kink speed, c_k , as a function of W/L . We see that in the limit $W/L \rightarrow 1$ only the fundamental kink mode is trapped; this is similar to the case in Fig. 3.3. The dispersive effect of W/L has increased but the range for which this mode remains trapped has been reduced. Also it can be seen from Fig. 3.4 and Fig. 3.5 that the cutoff frequency is strongly dependent on the chromospheric depth.

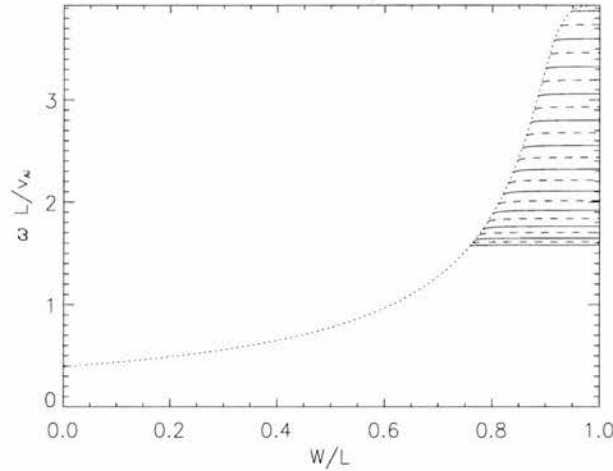


Figure 3.4: Dispersion diagram for $v_{Ae} = 2.5v_{Ai}$, $v_{Ache} = 0.25v_{Ai}$ and $a = 10L$, showing $\omega L/v_{Ai}$ as a function of W/L . The solid and dashed curves are kink and sausage modes respectively. The dotted curve shows the dimensionless cutoff frequency as a function of W/L .

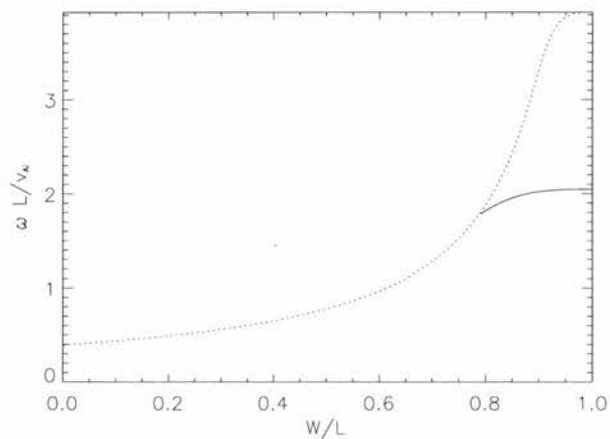


Figure 3.5: Dispersion diagram for $v_{Ae} = 2.5v_{Ai}$, $v_{Ache} = 0.25v_{Ai}$ and $a = 0.1L$, showing $\omega L/v_{Ai}$ as a function of W/L . The solid curve is the fundamental kink mode, and the dotted curve shows the dimensionless cutoff frequency as a function of W/L .

In order to investigate the effect of the chromospheric layers on the nature of the fundamental kink mode we plot a superposition of the dispersion curves and cutoff curves on a single diagram, Fig. 3.6. Four cases are displayed: $v_{Ache} = 0.125v_{Ae}$, and $\rho_{che} = 64\rho_e$; $v_{Ache} = 0.25v_{Ae}$, and $\rho_{che} = 16\rho_e$; $v_{Ache} = 0.5v_{Ae}$, and $\rho_{che} = 4\rho_e$; and $v_{Ache} = v_{Ae}$, $\rho_{che} = \rho_e$. Thus, we evolve the diagram from the case of the chromosphere being 64 times denser than the coronal region to the case of an entirely uniform environment (no chromosphere). The cutoff curves evolve from one of steep gradients to a flat curve. Also the range of W/L allowing the loop to trap the fundamental kink mode increases from the relatively small range of $W/L \approx 0.8 - 1.0$ when $v_{Ache} = 0.125v_{Ae}$ to being trapped for all values of W/L in the final two cases, when $v_{Ache} = 0.5v_{Ae}$ and $v_{Ache} = v_{Ae}$. The dispersion becomes less pronounced as the curves move towards a uniform environment model.

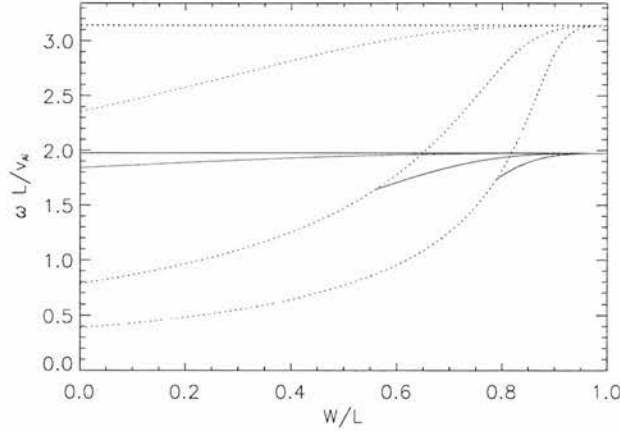


Figure 3.6: Superposition of dispersion diagrams with $v_{Ae} = 2v_{Ai}$ and $a = 0.1L$, for $v_{Ache} = 0.125v_{Ae}$ (green), $v_{Ache} = 0.25v_{Ae}$ (blue), $v_{Ache} = 0.5v_{Ae}$ (red) and $v_{Ache} = v_{Ae}$ (black), showing $\omega L/v_{Ai}$ as a function of W/L . The solid and dotted curves are dispersion and cutoff curves respectively.

Previous work has shown that in a cylindrical geometry the eigenfunctions of such trapped modes do not penetrate deeply into the environment of the loop (Díaz et al., 2001, 2004) and so would have no strong interaction with neighbouring structures, although as the mode propagates close to its cutoff frequency its eigenfunctions are expected to penetrate further into the environment. However, this is not the behaviour here. Fig. 3.7 gives the evolution of the non-dimensionalised total pressure perturbation at the loop apex ($z = 0$) as a function of radial coordinate along the dispersion curve displayed in Fig. 3.5. There is little difference in the penetrations of the eigenfunctions between a point close to the cutoff frequency (Fig. 3.7(a)) and a point far from it (Fig. 3.7(c)). This suggests that the interaction of neighbouring loops is weak, unless the loops are in a tightly packed group. It is evident from Fig. 3.7, which show surface plots of the $P_T/\rho_i v_{Ai}^2$ against r/a and z/L , that the structure of the eigenfunction evolves along the dispersion curve. At $W/L = 0.99$, P_T behaves much as expected for the fundamental kink mode having, one extremum in both the radial and longitudinal directions. However, for $W/L = 0.79$ the eigenfunction has developed three extrema in the longitudinal direction, although it retains the single extrema in the radial direction.

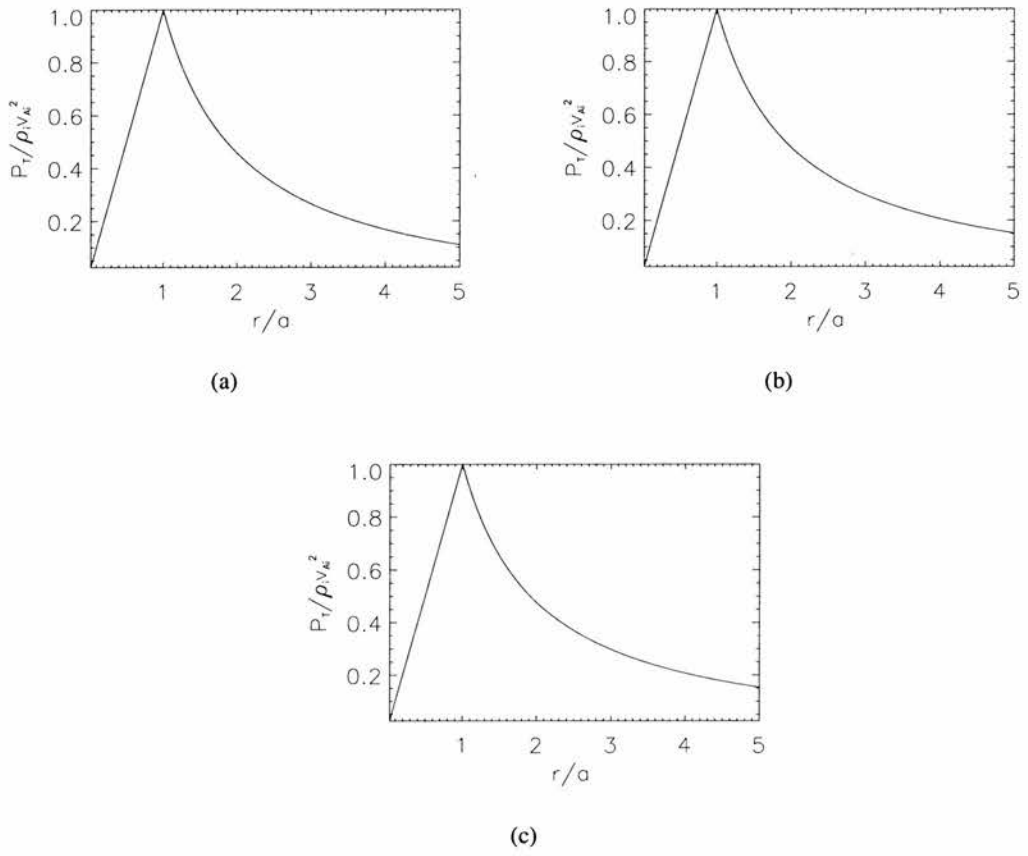


Figure 3.8: Plots of $P_T / \rho_i v_{Ae}^2$ as a function of the radial coordinate r/a , for the loop apex $z/L = 0$ and $v_{Ae} = 2.5v_{Ai}$, $v_{Ache} = 0.25v_{Ai}$ and $a = 0.1L$. The following parameters were used: (a) $W/L = 0.79$, (b) $W/L = 0.89$, and (c) $W/L = 0.99$.

3.4.3 Unrealistic chromospheric densities

For certain parameter sets it is found that more kink oscillations other than the fundamental mode may be trapped in the thin tube limit. This is the case in Fig. 3.9, which shows two kink modes, the fundamental and its first harmonic; both lie below the new cutoff curve as $a/L \rightarrow 0$. The dispersive effect of the loop radius on the fundamental kink mode has been significantly reduced so its frequency is quite insensitive to the parameter a/L . We can also see the effect of mode coupling, introduced between the first and second harmonics at an avoided crossing. However, it should be noted that this happens for an unrealistically thick loop. As an avoided crossing is approached, the frequency of the two modes interacting rapidly converge after reaching the point where the curves are closest; this point is the avoided crossing, and thereafter the frequencies rapidly diverge. Also the spatial structure of their eigenfunctions are exchanged across the avoided crossing. This mode coupling is only possible between modes having properties which can be exchanged. For example, a mode having two extrema in the radial direction may couple with a mode with two extrema in the z direction, resulting in each mode still having two extrema but in the other coordinate. Therefore, generally the fundamental modes only having one extrema cannot undergo this mode coupling. However, Figure (3.8)(b) show the fundamental kink mode to have more than one extrema and therefore may interact with other modes under certain circumstances.

We should note too that the structure shown in Fig. 3.3, of a sausage mode lying between each pair of neighbouring kink modes, has not been preserved in Fig. 3.9; as we can see, the dispersion curves of the fundamental sausage mode and first kink harmonic cross. Note that this is only possible in a linear treatment since the dispersion relations for the sausage and kink modes are decoupled. However, if a non-cylindrically symmetric equilibrium were considered then we may expect a coupling between the sausage ($m = 0$) and kink ($m = 1$) modes. The dispersion curves of coupled modes are not able to cross but the modes would interact at an avoided crossing. The fact that this structure has not been preserved suggests that the sausage modes may not propagate in the thin tube limit for all sets of parameters.

As the density contrast ρ_i/ρ_e increases, more modes will be present in the dispersion diagram. We have concentrated on the even modes since the odd modes have a similar behaviour. But it should be noted that the cutoff frequency of the odd modes is dependent on the change in sign of $[\lambda_1^e]^2$ while the cutoff frequency of the even modes is dependent on the change in sign of $[\lambda_2^e]^2$. This results in the cutoff frequency of the odd modes always being greater than that of the even modes. If both even and odd modes are plotted on the same dispersion diagram it is seen that an odd mode lies between each pair of consecutive even modes, for the range of frequencies that both even and odd modes propagate for.

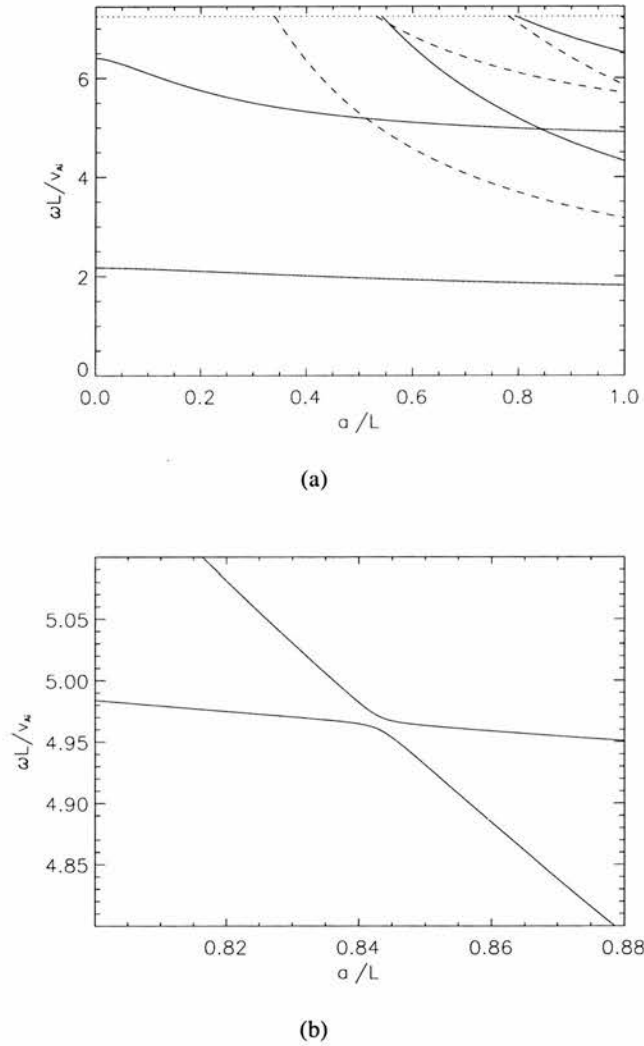


Figure 3.9: (a) Dispersion diagram for $v_{Ae} = 5v_{Ai}$, $v_{Ache} = 1.5v_{Ai}$ and $W/L = 0.8$, showing $\omega L/v_{Ai}$ as a function of a/L . The solid and dashed curves are kink and sausage modes respectively. Note the avoided crossing between the first and second kink harmonic, shown in (b) for the region $0.81 < a/L < 0.88$.

3.5 Non-uniform loop

In the previous sections we discussed the simplified case of a uniform loop lying within an environment structured by the presence of chromospheric layers. We now turn to the more realistic case in which chromospheric layers arise both inside and outside the loop (Fig. 3.1).

We consider a longitudinally structured loop of length $2L$ and radius a . The structuring in the environment region is the same as previously. The loop has a uniform region of depth W and a uniform chromospheric region of depth $(L - W)$. These four regions are denoted by subscripts 'e', 'che', 'i' and 'chi' respectively. The same general procedure is followed as previously, resulting in a solution $h_n^i(z)$ in the region $r < a$ which is of the same form as $h_n^e(z)$ discussed earlier. Note that the sign of $[\lambda_n^i]^2$ is unrestricted as we may consider both body and surface modes; this results in hyperbolic, rather than trigonometric, behaviour. The solutions $h_n^e(z)$ in the environment ($r > a$) remain as before. The same boundary conditions are applied at each interface, with the addition of the interface perpendicular to the magnetic field inside the loop. We make use of the Sturm-Liouville theorem which states that the solutions of an eigenvalue equation such as (3.11) in self-adjoint form with boundary conditions $h_m(z = \pm L) = 0$ form a complete set on the region $z = [-L, L]$. Also the Sturm-Liouville theorem guarantees that the the eigenvalues of this equation are ordered and are countable. Therefore, we may apply the Sturm-Liouville theorem to expand the external solution $h_n^e(z)$ in terms of the internal solutions $h_m^i(z)$.

These steps lead to a dispersion relation taking identical form to equations (3.22) from the previous case. However, the modification of $h_n^i(z)$ due to the internal structure of the loop results in changes to the set of λ_n^i s, which are solutions of

$$M_n^{chi} \cot [M_n^{chi}(L - W)] = M_n^i \tan [M_n^i W] \quad (3.34)$$

for the even modes, and

$$M_n^{chi} \cot [M_n^{chi}(L - W)] = -M_n^i \cot [M_n^i W] \quad (3.35)$$

for the odd modes. Here

$$[M_n^{chi}]^2 = \frac{\omega^2}{v_{Achi}^2} + (\lambda_n^i)^2, \quad [M_n^i]^2 = \frac{\omega^2}{v_{Ai}^2} + (\lambda_n^i)^2 \quad (3.36)$$

have been assume to be positive, with equivalent relations for other cases. The coefficients H_{nm} dependent on $h_m^i(z)$ and $h_n^e(z)$, being evaluated using equation (3.17), so are different in this case.

3.5.1 Case 1

There are two main cases of interest: the case where the loop footpoint is denser than the surrounding chromosphere (resulting in the footpoint having a depression in Alfvén speed compared with its surroundings), so $v_{Achi} < v_{Ache}$ (discussed in section 3.5.2); and the case when the loop footpoint is less dense than the surrounding chromosphere (giving a footpoint with an enhancement in Alfvén speed compared with its surroundings), so $v_{Achi} > v_{Ache}$ (see Fig. 3.16). If $v_{Achi} < v_{Ache}$, we expect trapped modes to propagate in the limit $W/L \rightarrow 0$ since the loop still has a density enhancement over its surroundings, so the loop may still act as a waveguide. This is illustrated by Fig. 3.10, showing the dispersion diagram for $v_{Ae} = 2.5v_{Ai}$, $v_{Achi} = 0.25v_{Ai}$ and $v_{Ache} = 0.35v_{Ai}$, with $a/L = 0.1$. The dispersion curve shown is the fundamental kink mode. The kink mode now propagates as a trapped mode for all W/L . Also in Fig. 3.10 we can see the cutoff frequency which varies with W/L and is the same as in Fig. 3.5; as expected, the cutoff frequency is independent of the internal structure of the loop.

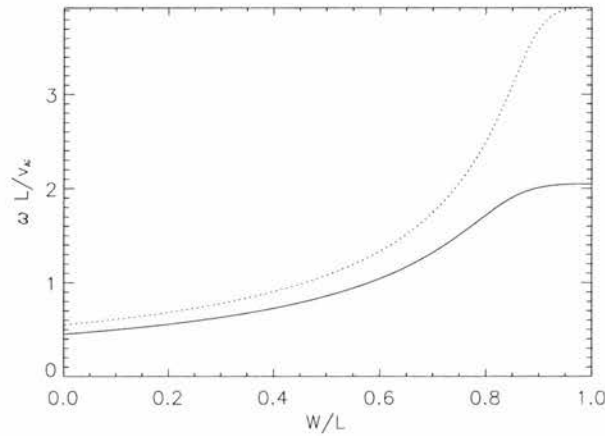


Figure 3.10: Dispersion diagram for $v_{Ae} = 2.5v_{Ai}$, $v_{Achi} = 0.25v_{Ai}$, $v_{Ache} = 0.35v_{Ai}$ and $a/L = 0.1$, showing $\omega L/v_{Ai}$ as a function of W/L . The solid curve is the fundamental kink mode, and the dotted curve shows the dimensionless cutoff frequency as a function of W/L .

To understand a mode of oscillation it is important to examine the perturbations it causes to the plasma through which it propagates, as discussed in Chapter 2. Here we consider the eigenfunctions associated with the fundamental kink mode shown in Fig. 3.10 for values of $W/L = 0.1$, $W/L = 0.5$ and $W/L = 0.99$. Fig. 3.11 shows surface plots of the total pressure perturbation. For $W/L = 0.99$, the total pressure perturbation has one extremum for the fundamental kink mode, but this structure evolves along the dispersion curve producing two extrema in the z direction. In turn, these extrema move closer together as W/L is reduced until $W/L = 0$, where again one extremum arises. This can also be seen in Fig. 3.12, showing contour plots of P_T .

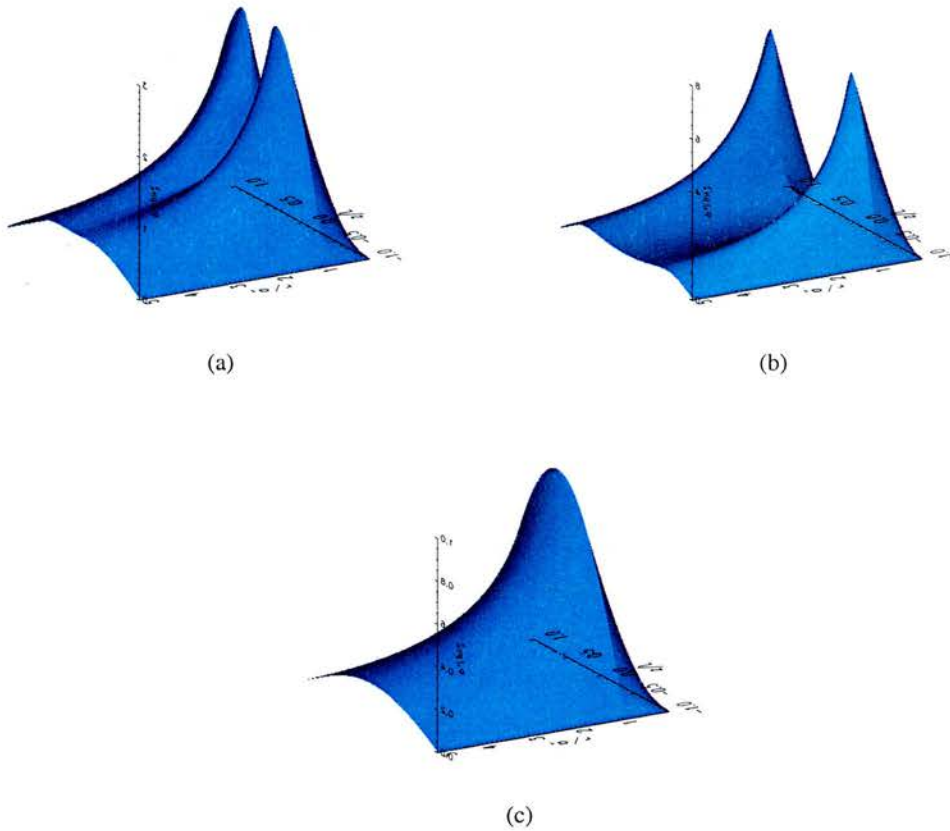


Figure 3.11: Surface plots of $P_T / \rho_i v_{Ai}^2$ as a function of the radial and longitudinal coordinates r/a and z/L . The following parameters were used: (a) $W/L = 0.1$, (b) $W/L = 0.5$, (c) $W/L = 0.99$, with $v_{Ae} = 2.5v_{Ai}$, $v_{Aci} = 0.25v_{Ai}$, $v_{Ache} = 0.35v_{Ai}$ and $a/L = 0.1$.

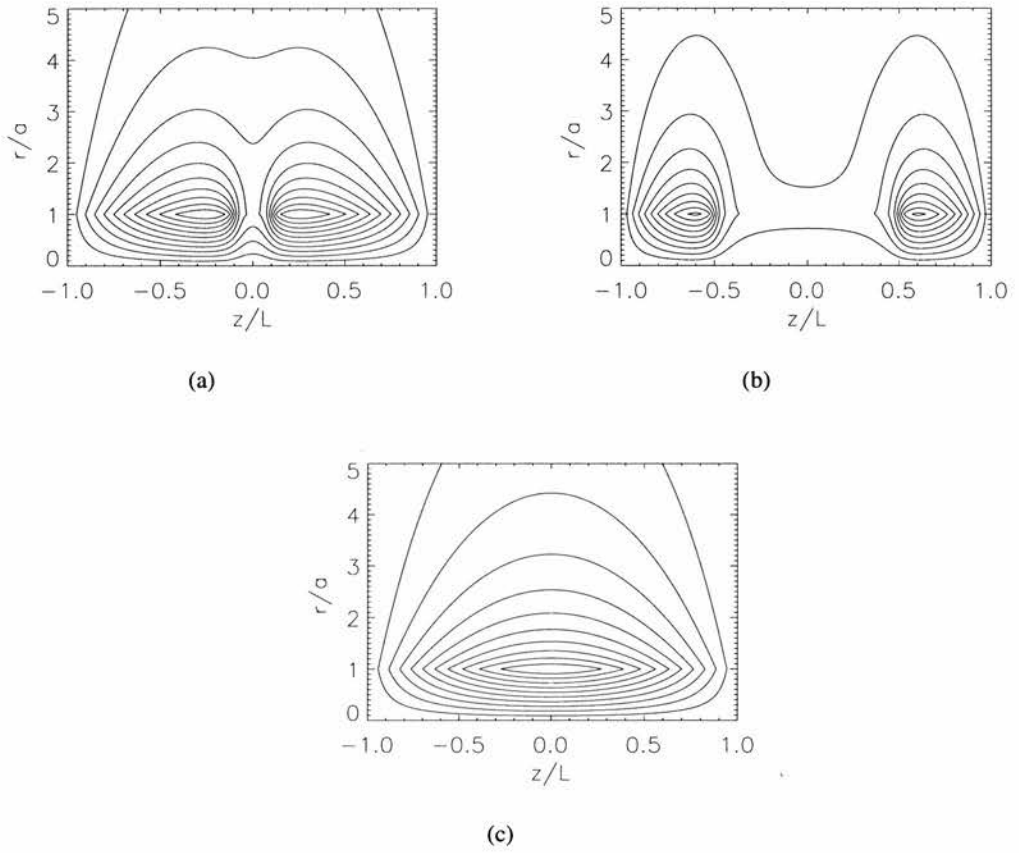


Figure 3.12: Contour plots of $P_T/\rho_i v_{Ai}^2$ as a function of radial coordinate r/a and longitudinal coordinate z/L . The following parameters were used: (a) $W/L = 0.1$, (b) $W/L = 0.5$, and (c) $W/L = 0.99$, with $v_{Ae} = 2.5v_{Ai}$, $v_{Achi} = 0.25v_{Ai}$, $v_{Ache} = 0.35v_{Ai}$ and $a/L = 0.1$.

Another property of interest is the penetration of an eigenfunction into the environment, which can give a indication of the importance of the interaction of neighbouring loops. Fig. 3.13 shows cuts of P_T as a function of r/a , with $z/L = 0$. From these plots of P_T at the loop apex it is clear that penetration is greater for smaller values of W/L . However, for the realistic range $W/L \approx 0.8 - 0.9$, interaction of neighbouring loops is not important.

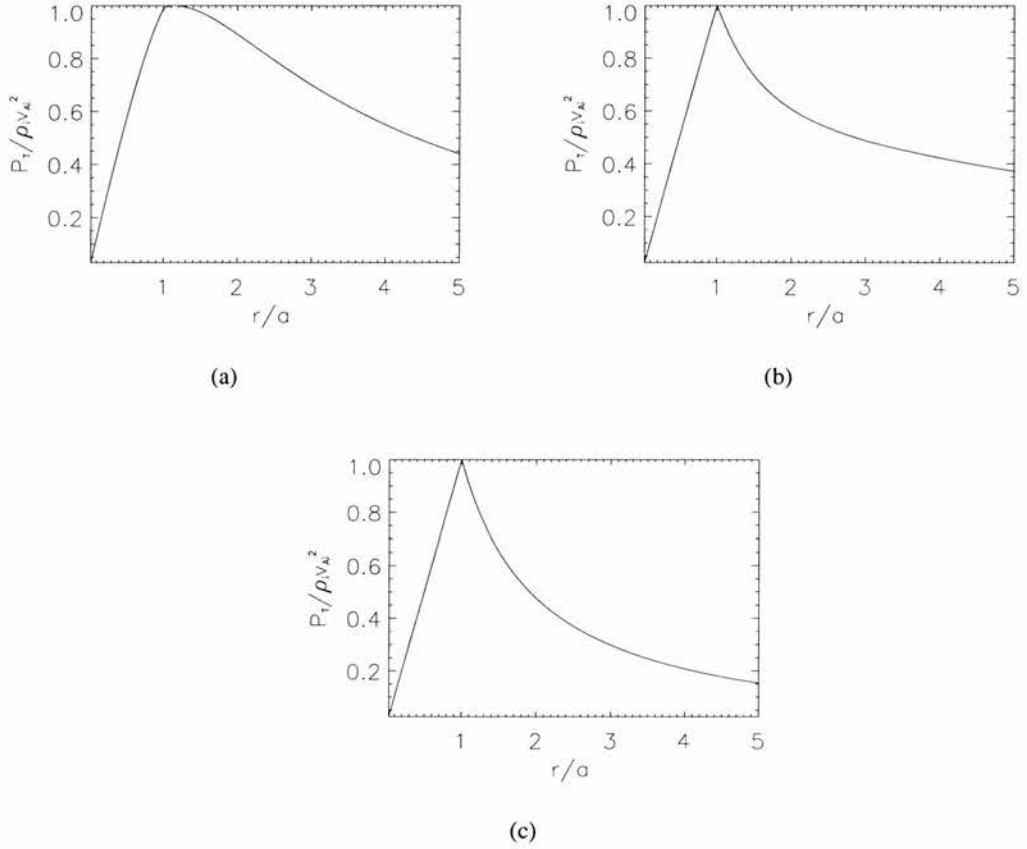


Figure 3.13: Plots of $P_T / \rho_i v_{Ai}^2$ as a function of the radial coordinate r/a , for the loop apex $z/L = 0$. The following parameters were used: (a) $W/L = 0.1$, (b) $W/L = 0.5$, and (c) $W/L = 0.99$, with $v_{Ae} = 2.5v_{Ai}$, $v_{Aci} = 0.25v_{Ai}$, $v_{Ache} = 0.35v_{Ai}$ and $a/L = 0.1$.

Fig. 3.14 show surface plots of the radial velocity component, illustrating that v_r has little radial variation across the radius of the loop for all values of W/L ; this is apparent from Fig. 3.15 displaying cuts of v_r as a function of r/a at $z/L = 0$. Also the magnitude of v_r is larger for $W/L = 0.5$ and has a more rapid decline in the footpoint region than for other values of W/L plotted.

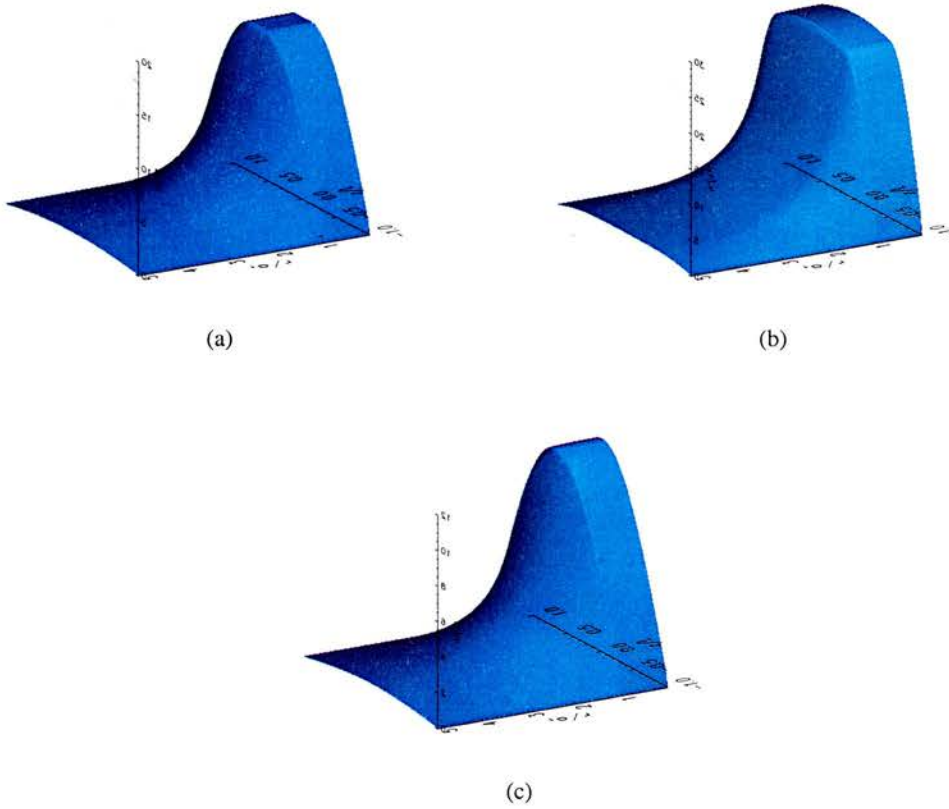


Figure 3.14: Surface plots of v_r/v_{Ai} as a function of r/a and z/L . Here (a) $W/L = 0.1$, (b) $W/L = 0.5$, and (c) $W/L = 0.99$, with $v_{Ae} = 2.5v_{Ai}$, $v_{Aci} = 0.25v_{Ai}$, $v_{Ache} = 0.35v_{Ai}$ and $a/L = 0.1$.

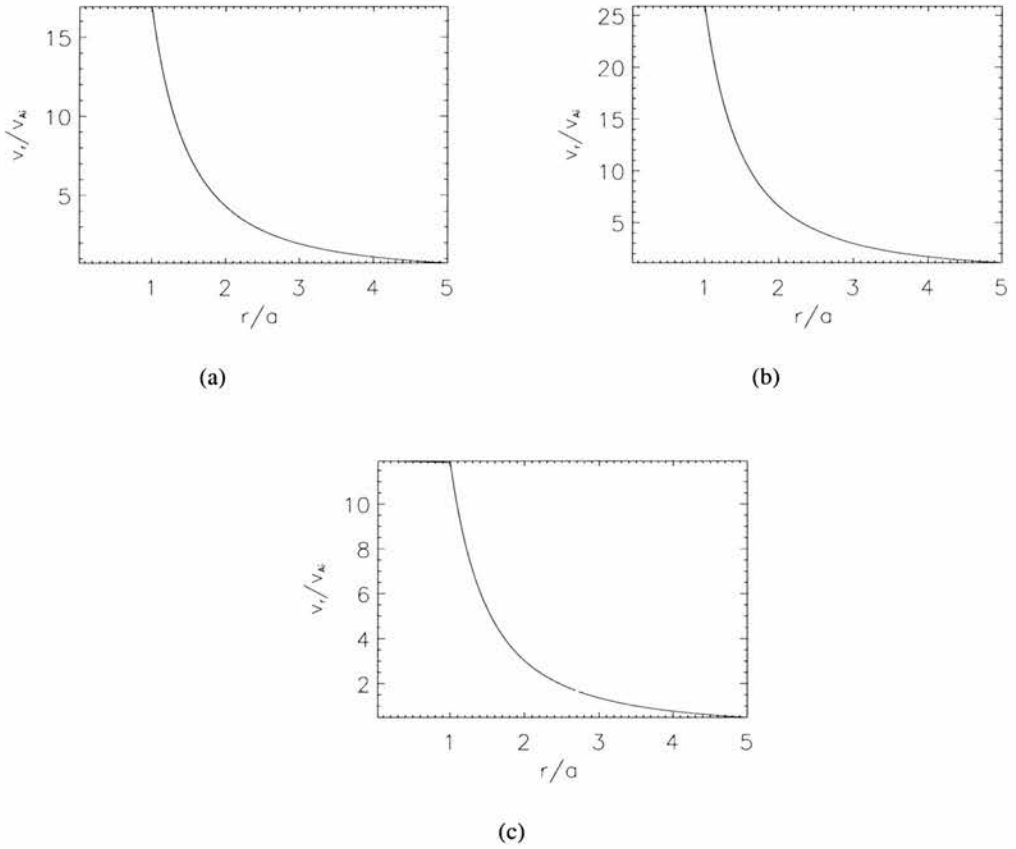


Figure 3.15: Plots of v_r/v_{Ai} at the apex $z = 0$ as a function of the radial coordinate r/a . for $z/L = 0$. Here (a) $W/L = 0.1$, (b) $W/L = 0.5$, and (c) $W/L = 0.99$, with $v_{Ae} = 2.5v_{Ai}$, $v_{Achi} = 0.25v_{Ai}$, $v_{Ache} = 0.35v_{Ai}$ and $a/L = 0.1$.

3.5.2 Case 2

The second case of mathematical interest is when $v_{Achi} > v_{Ache}$, so that the loop footpoint is less dense than the surrounding chromosphere. This case may in fact be more realistic than the previous case as the magnetic field in the photosphere and chromosphere is confined to focused tubes which would result in $v_{Achi} > v_{Ache}$ if the density is approximately constant at this level. However, it should be noted that there is no variation magnetic field in this model therefore, changes in Alfvén speed are produced by variations in density. Hence, in the limit of $W/L \rightarrow 0$, we expect leaky modes. Fig. 3.16 shows the dispersion diagram for the case $v_{Ae} = 2.5v_{Ai}$, $v_{Achi} = 0.35v_{Ai}$, and $v_{Ache} = 0.25v_{Ai}$, with $a/L = 0.1$. The dispersion curve shown is the fundamental kink mode, which behaves similarly to the case of a uniform loop discussed earlier and has a cutoff frequency. The cutoff curve, shown as a dotted curve, is unchanged from Fig. (3.5), despite the different internal structure of the loop.

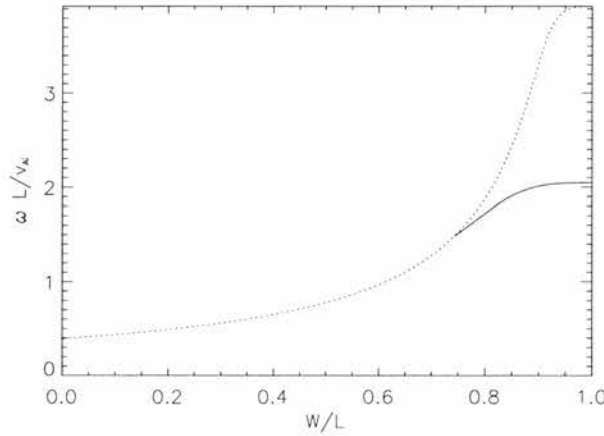


Figure 3.16: Dispersion diagram for $v_{Ae} = 2.5v_{Ai}$, $v_{Achi} = 0.35v_{Ai}$, $v_{Ache} = 0.25v_{Ai}$ and $a/L = 0.1$, showing $\omega L/v_{Ai}$ as a function of W/L . The solid and dashed curves are kink and sausage modes, respectively, and the dotted curve shows the dimensionless cutoff frequency as a function of W/L .

We now examine the evolution of the eigenfunctions for the three cases $W/L = 0.8$, $W/L = 0.9$ and $W/L = 0.99$. The surface plots of P_T shown in Fig. 3.17 show a change from the expected structure for the fundamental kink mode with one extremum, but as W/L is reduced structures in the form of depressions are produced in the footpoints, with their magnitude increasing as W/L is reduced. Hence, for smaller values of W/L the oscillation power in the loop footpoint is greater, possibly making detection in this region more likely. This is also illustrated by the contour plots in Fig. 3.18. The total pressure eigenfunction does not penetrate more deeply into the loop's environment, even as the cutoff frequency is approached. Fig. 3.19 showing cuts of P_T as a function of r/a for $z/L = 0$.

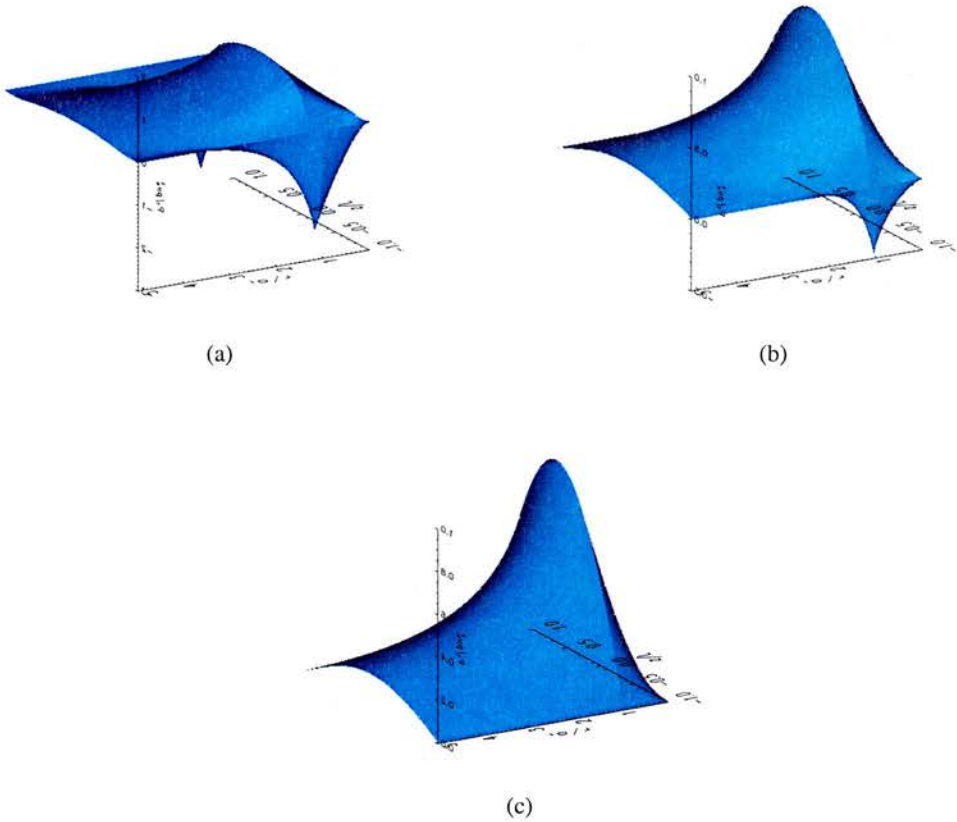


Figure 3.17: Surface plots of $P_T/\rho_i v_{Ai}^2$ as a function of the radial coordinate r/a and longitudinal coordinate z/L . Here (a) $W/L = 0.8$, (b) $W/L = 0.9$, and (c) $W/L = 0.99$, with $v_{Ae} = 2.5v_{Ai}$, $v_{Achi} = 0.35v_{Ai}$, $v_{Ache} = 0.25v_{Ai}$ and $a/L = 0.1$.

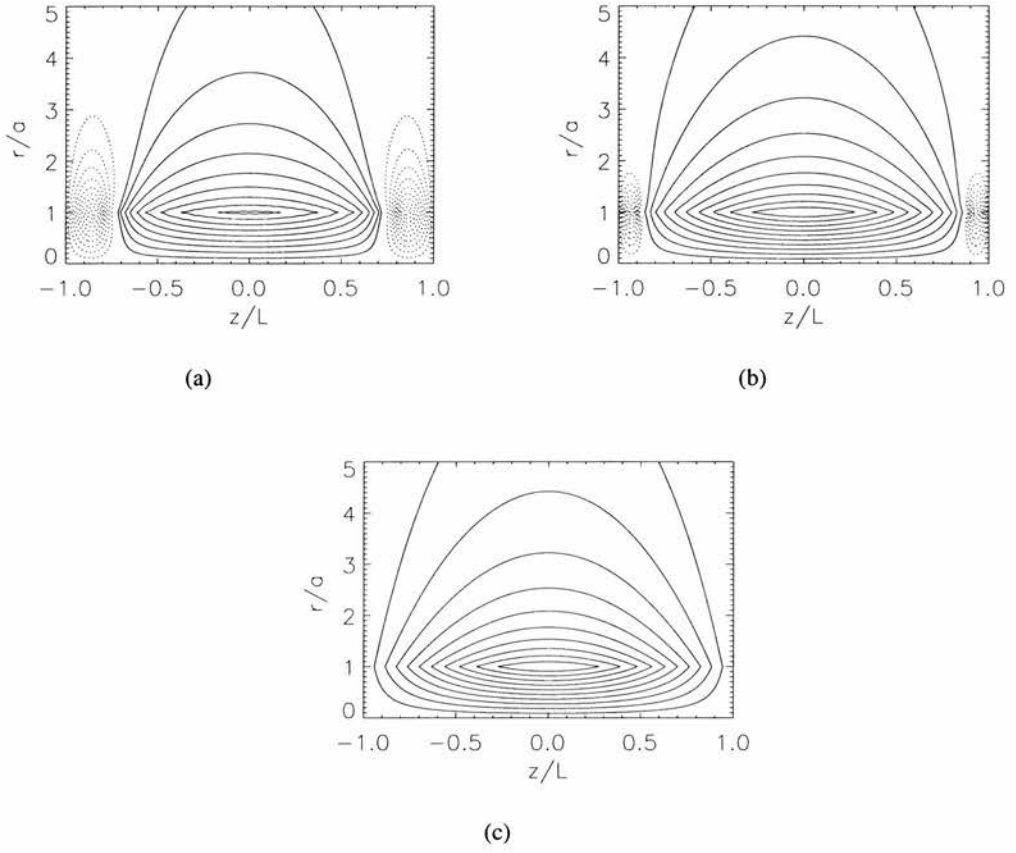


Figure 3.18: Contour plots of $P_T/\rho_i v_{Ai}^2$ as a function of the radial and longitudinal coordinates r/a and z/L . Solid and dotted contours signify positive and negative values of P_T respectively. Here (a) $W/L = 0.8$, (b) $W/L = 0.9$, and (c) $W/L = 0.99$, with $v_{Ae} = 2.5v_{Ai}$, $v_{Achi} = 0.35v_{Ai}$, $v_{Ache} = 0.25v_{Ai}$ and $a/L = 0.1$.

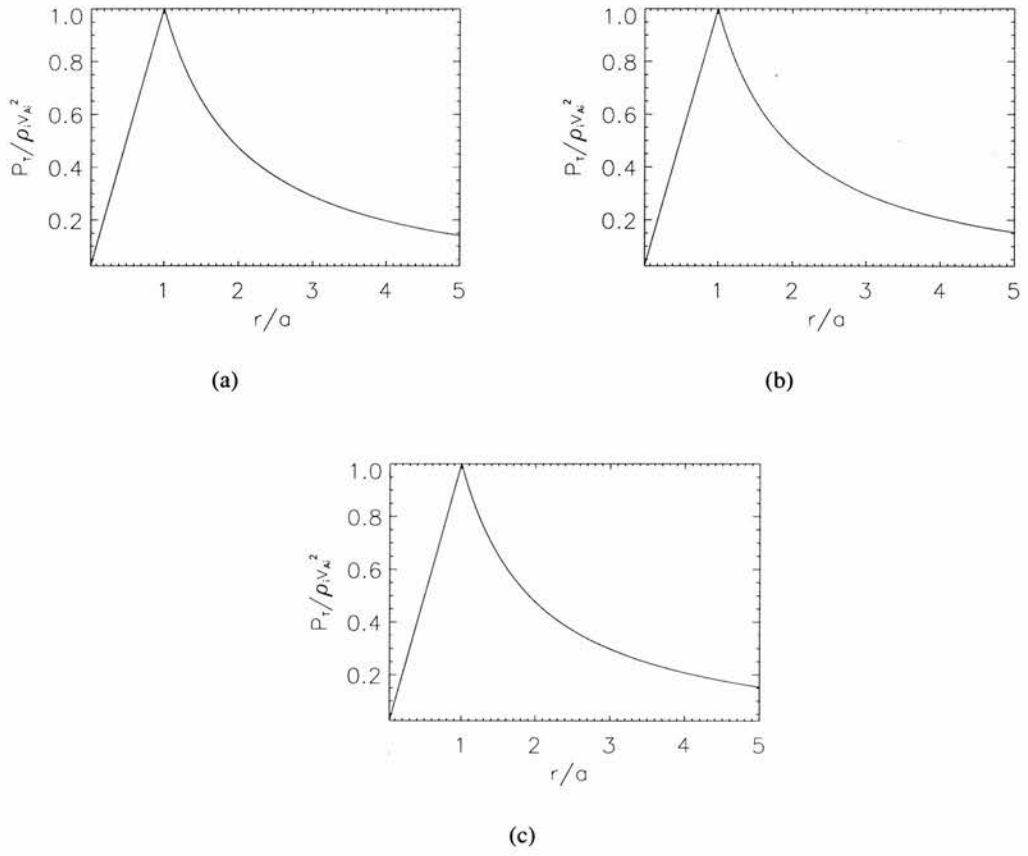


Figure 3.19: Plots of $P_T / \rho_i v_{Ai}^2$ as a function of the radial coordinate r/a , for $z/L = 0$. Here (a) $W/L = 0.8$, (b) $W/L = 0.9$, and (c) $W/L = 0.99$, with $v_{Ae} = 2.5v_{Ai}$, $v_{Achi} = 0.35v_{Ai}$, $v_{Ache} = 0.25v_{Ai}$ and $a/L = 0.1$.

The structure of v_r is unchanged along the dispersion curve although its maximum amplitude again shows an increase as W/L decreases (Fig. 3.20). Since a/L is small, v_r is almost constant across the loop; see Fig. 3.21.

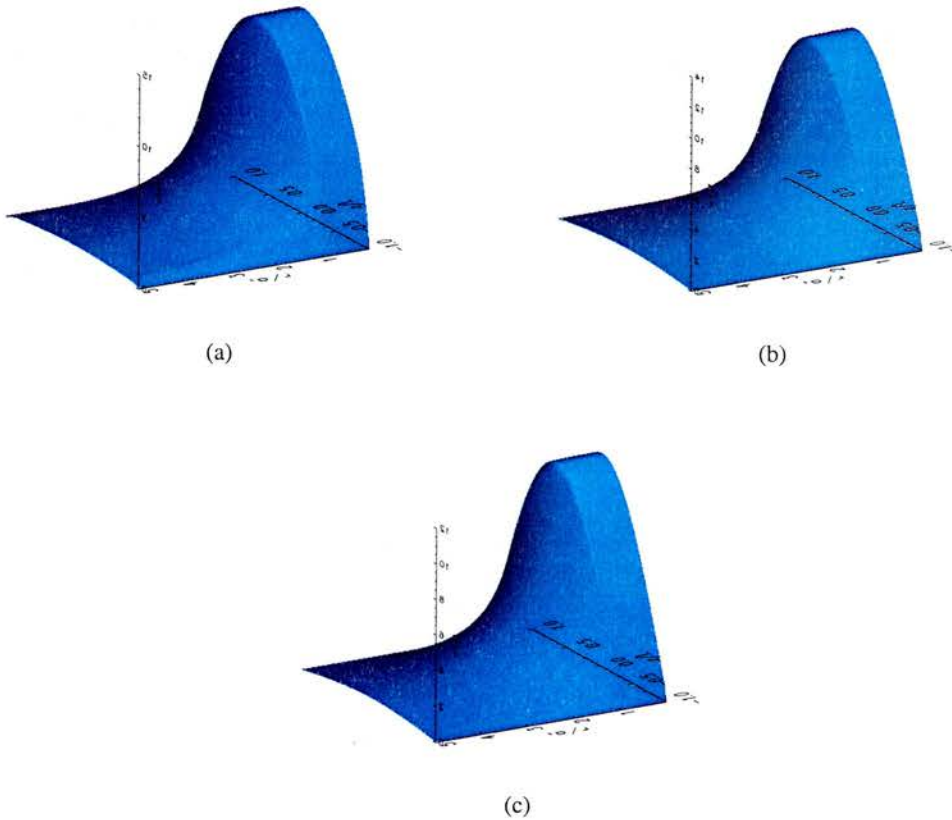


Figure 3.20: Surface plots of v_r/v_{Ai} as a function of r/a and z/L , with (a) $W/L = 0.8$, (b) $W/L = 0.9$, and (c) $W/L = 0.99$. Here $v_{Ae} = 2.5v_{Ai}$, $v_{Aci} = 0.35v_{Ai}$, $v_{Ache} = 0.25v_{Ai}$ and $a/L = 0.1$.

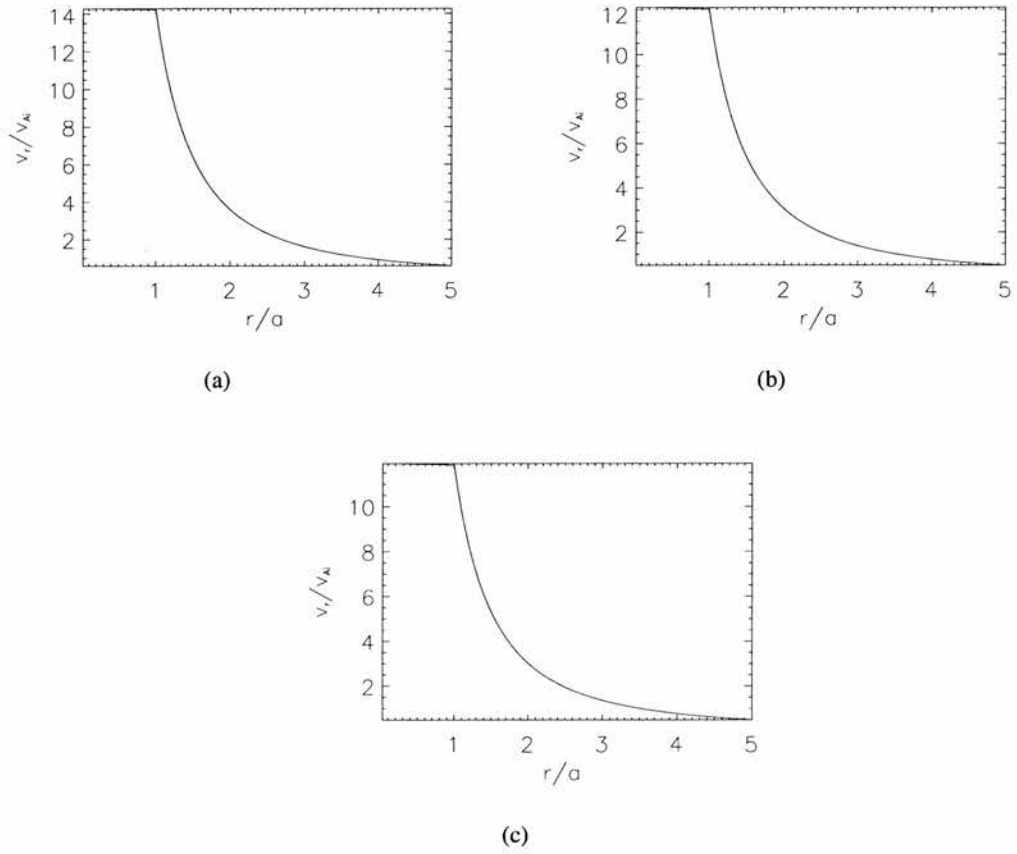


Figure 3.21: Plots of v_r/v_{Ai} as a function of the radial coordinate r/a , for $z/L = 0$. Here (a) $W/L = 0.8$, (b) $W/L = 0.9$, and (c) $W/L = 0.99$, $v_{Ae} = 2.5v_{Ai}$, with $v_{Achi} = 0.35v_{Ai}$, $v_{Ache} = 0.25v_{Ai}$ and $a/L = 0.1$.

3.6 Conclusions

We have discussed the trapped oscillations of a coronal loop with a complex footpoint structure. The loop was modelled as a cylindrically symmetric magnetic flux tube with a uniform or non-uniform structured density profile embedded in a longitudinally structured environment. The zero β approximation was employed. We derived the dispersion relation for a generally structured profile. We studied the effect of uniform dense chromospheric layers, firstly in the environment and then both inside and outside the loop; the interior and exterior structures are different.

The most important effect is that environmental structuring produces a mode cutoff frequency which depends upon the parameters of the chromospheric layer but is independent of the loop interior; the cutoff curve is the same for both uniform and structured loops, provided the environmental structuring is unchanged. In the case of a thin chromospheric layer, there is a single trapped kink mode with all higher harmonics and sausage modes possessing the same cutoff frequency. However, for certain parameters both the fundamental and first harmonic kink mode can be trapped. Importantly, no sausage modes lie under the cutoff for the thin tube, for any case examined, suggesting that the sausage mode is always leaky in the thin tube limit.

All previous models have had a uniform cutoff curve so all modes have the same cutoff frequency. The introduction of the dispersive effect produced by the chromospheric layers yields a non-uniform cutoff curve: no two modes possess the same cutoff frequency. As a result of the non-uniform cutoff, it is found that the fundamental kink mode of a uniform loop does not propagate as a trapped mode in the thin tube limit for certain chromospheric depths (typically $W/L < 0.7$; see Fig. 3.16). This also happens in the case of a structured loop, if the footpoint is denser than the surrounding chromosphere. The observation that the fundamental kink mode is no longer trapped in the thin tube limit could have important consequences for coronal seismology. However, this result is lost in the structured loop if the chromospheric region is denser than the footpoint. It is possible that modes may propagate close to their cutoff frequency in this model, but penetration of the eigenfunctions into the loop's environment is no greater here than any other point on the dispersion curve; this indicates that the interaction between neighbouring loops is not significant for the case where the fundamental kink mode has a cutoff frequency. If the fundamental kink mode propagates as a trapped mode for small W/L , we find that the total pressure penetrates more deeply into the environment. But in the realistic range of $W/L \approx 0.8 - 0.9$ penetration is low, indicating interaction between neighbouring loops is not significant.

The evolution of P_T along the dispersion curve of the fundamental kink mode shows the development of structure in the loop's dense footpoints, and also a greater amplitude of oscillation in these regions for both the uniform and structured loop cases. Hence, these modes may be more readily detected in the footpoint regions of coronal loops.

Chapter 4

Arcade

4.1 Introduction

Thus far we have discussed the structuring of the corona into isolated flux tubes. Examining the oscillatory properties of these structures which have been clearly observed in TRACE (Aschwanden et al., 1999, Nakariakov et al., 1999), SoHO (Wang et al., 2002a,b,c, 2003) and SECIS (Williams et al., 2001, 2002, Katsiyannis et al., 2003) data. These observations have been observed and interpreted using theoretical models (Edwin and Roberts, 1983, Bennett et al., 1999, Sakai et al., 2000, Nakariakov et al., 2000, Nakariakov and Ofman, 2001, James, 2003, Mendoza-Briceño et al., 2004).

However, it is evident from observations that flux tubes often occur in groups, forming structures such as coronal arcades. These arcades are often formed in the aftermath of a flare event. In the simplest form a coronal arcade consists of a set of closed homogeneous loops of equal length which run parallel to each other connecting two points in the photosphere. In reality a coronal arcade may be made up of loops which do not lie parallel to each other, the loops possessing differing plasma properties from each other while being independently inhomogeneous. The arcade may also be comprised of loops differing in length, thickness and radius of curvature (see Fig. 4.1).

As with the majority of coronal structures, coronal arcades have been observed to support MHD oscillations (Reeves et al., 2001, Aschwanden et al., 2002, Verwichte et al., 2004, 2005). Of particular interest (as we will make comparisons with this observation later in this chapter) are the observations of oscillations of a post-flare loop arcade detected in TRACE data on the 15th of April 2001 (Verwichte et al., 2004, 2005). The analysis of oscillatory properties of nine loops within the arcade were made, finding the loops lie in the height range 65 – 76 Mm. The periods



Figure 4.1: TRACE image showing a coronal loop arcade.

of oscillations in the loops were found to lie in the range 200 – 450 s, and were determined using both a wavelet analysis and also a curve fitting method which provide consistent results. The damping times were found to be in the range 800 – 1800 s, which is consistent with previous studies (Reeves et al., 2001). Examination of periods and loop displacement has shown that not only the fundamental mode but also the first harmonic has been observed in two of the loops examined within the arcade. The ratio of the periods of the fundamental and the first harmonic have been discussed and suggested as a useful tool in coronal seismology (Andries et al., 2005, McEwan et al., 2006). The oscillation periods and the transverse nature of the loop displacement is consistent with that of the kink mode.

Recent theoretical studies of arcade structures have considered a curved magnetic field shedding light on new modes of oscillation *vertical*, *swaying* (longitudinal), and *rocking* modes alongside the usual sausage and kink modes (Díaz et al., 2006). An independent study of this nature is also available in Verwichte et al. (2006). It is our intention to discuss the rocking mode which is a transverse oscillation of the arcade. We will carry out this study using a 2D cartesian geometry in a straightened arcade and examine the influence of longitudinal structuring on these modes of oscillation. Finally, we compare this model against the observed periods (Verwichte et al., 2004, 2005).

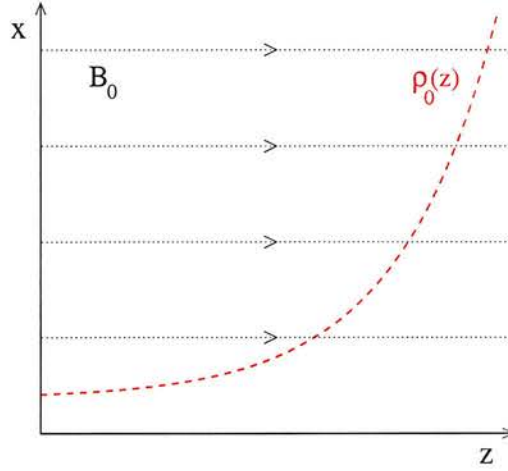


Figure 4.2: The equilibrium configuration for a coronal arcade. The magnetic field across the arcade is assumed to be uniform and parallel to the z axis with density stratification along the arcade, increasing from a low value at the arcade summit ($z = 0$) to a high value at the base ($z = L$).

4.2 Equilibrium and basic equations

We consider a spatially structured static equilibrium of a 2D Cartesian line-tied coronal arcade with field lines of length $2L$ parallel to the z axis and infinite in the transverse (x) direction. We study modes of oscillation which are line-tied in the z direction but we allow free propagation in the transverse direction. The equilibrium magnetic field $\mathbf{B}_0 = B_0 \mathbf{z}$ lies parallel to the z axis and is assumed to be uniform throughout the medium. The equilibrium density $\rho_0(z)$ is structured along the magnetic field lines. We consider small deviations from this equilibrium, applying the ideal adiabatic MHD equations in linearised form. Gravitational effects are neglected. The resulting set of equations can then be written as a set of four couple partial differential equations for the primary variables; total pressure perturbation $P_T (= P + \frac{B_0 B_z}{2\mu})$, the two components of the perpendicular velocity \mathbf{v}_\perp , and the longitudinal velocity v_z :

$$\frac{\partial P_T}{\partial t} = \rho_0(z) v_A^2(z) \frac{\partial v_z}{\partial z} - \rho_0(z) c_f^2(z) \nabla \cdot \mathbf{v}, \quad (4.1)$$

$$\rho_0(z) \left[\frac{\partial^2}{\partial t^2} - v_A^2(z) \frac{\partial^2}{\partial z^2} \right] \mathbf{v}_\perp = -\nabla_\perp \left[\frac{\partial P_T}{\partial t} \right], \quad (4.2)$$

and

$$\rho_0(z) \left[\frac{\partial^2}{\partial t^2} - c_T^2(z) \frac{\partial^2}{\partial z^2} \right] v_z = -\frac{c_0^2(z)}{c_f^2(z)} \frac{\partial^2 P_T}{\partial z \partial t}. \quad (4.3)$$

Here $v_A = B_0/\sqrt{\mu\rho_0}$ and $c_0 = \sqrt{\gamma P_0/\rho_0}$ are the Alfvén and sound speeds, $c_T^{-2} = v_A^{-2} + c_0^{-2}$ determines the tube speed c_T and $c_f^2 = v_A^2 + c_0^2$ defines a typical fast speed c_f . The subscript ‘ \perp ’ denotes that v_\perp perpendicular to the equilibrium magnetic field. Equations of this form have been discussed in Chapter 1; see also Roberts (1991) and Díaz (2004).

As discussed in Chapter 1 the corona is magnetically dominated with a low plasma β . Using the limit of $\beta = 0$ eliminates the acoustic effects (including the slow mode), but allows a clearer investigation into the behaviour of the fast waves, unhindered by the complexities introduced by acoustic effects. In this geometry the Alfvén mode is decouple allowing us to carry out a study of the fast mode. It is important to note that we make this approximation down to the chromosphere/photospheric level, where it is less appropriate and gravitational effects are also important. We allow an exponential longitudinal density profile to represent the rapid change from the dense photosphere to the rarefied corona, while the density is invariant in the transverse direction. In the current model we assume symmetry of the equilibrium about the x axis and invariance in the y axis.

With $\beta = 0$, so that $c_0, c_T = 0$ and $c_f = v_A$ equations (4.1) and (4.2) may be reduced to the wave equation for P_T (Díaz et al., 2002)

$$\left[\frac{\partial^2}{\partial t^2} - v_A^2(z) \nabla^2 \right] P_T = 0, \quad (4.4)$$

and we retain equation (4.2) in the form

$$\rho_0(z) \left[\frac{\partial^2}{\partial t^2} - v_A^2(z) \frac{\partial^2}{\partial z^2} \right] v_x = -\frac{\partial^2 P_T}{\partial x \partial t}. \quad (4.5)$$

There is no perturbation flow along the field lines ($v_z = 0$).

It is clear that motions of the arcade footpoints as a result of the oscillation within the corona are minimal (Hood, 1986). This is because of the low coronal density (in comparison with the photosphere) results in coronal oscillations carrying relatively little momentum into the photosphere, so leaving it unperturbed. This leads us to the line-tying boundary condition $v_x(z = \pm L) = 0$. Thus, there are no transverse oscillations at the footpoints ($z = \pm L$) of the arcade.

4.3 Analytical method

We study solutions to equations (4.4) and (4.5) which are oscillatory in time so a Fourier form is taken for the time component. The modes we are interested in are freely propagating perpendicular to the magnetic field and so a Fourier analysis in the x direction can be made. This leads to P_T

having the form

$$P_T(x, z, t) = h(z) \exp[i(\omega t + kx)], \quad (4.6)$$

with ω the frequency and k the wavenumber in the x direction. The amplitude function $h(z)$ is dependent on the z coordinate in which the arcade density is stratified. Substituting (4.6) into equation (4.4) results in the ordinary differential equation

$$\frac{d^2 h}{dz^2} + \left(\frac{\omega^2}{v_A^2(z)} - k^2 \right) h = 0, \quad (4.7)$$

where $v_A(z)$ is the z -dependent Alfvén speed.

Assuming the transverse velocity has the same z dependence as the total pressure perturbation, then v_x and P_T are related by

$$v_x = \frac{-c}{\rho_0(z)v_A^2(z)} P_T \quad (4.8)$$

where $c(= \omega/k)$ is the phase speed along the arcade. Note that $\rho_0(z)v_A^2(z) = B_0^2$, so $\rho_0(z)v_A^2(z)$ is uniform throughout the medium.

4.4 Results

4.4.1 Homogeneous medium

We begin our discussion by considering the simplest case: a homogeneous medium. In a uniform medium the Alfvén profile $v_A(z) = v_{A0}$ (constant), so there is no variation in density or Alfvén speed in either the parallel or perpendicular directions with respect to the magnetic field. Hence we may write equation (4.7) as

$$\frac{d^2 h}{dz^2} + M_0^2 h = 0, \quad (4.9)$$

where M_0 is defined by $M_0^2 = \frac{\omega^2}{v_{A0}^2} - k^2$ and is a constant.

In order to satisfy the line-tying boundary conditions $h(z = \pm L) = 0$ the solutions to equation (4.9) must be oscillatory in nature; hence $M_0^2 > 0$. This immediately draws our attention to the presence of a lower floor for the frequency such that $\omega > v_{A0}k$ (or in terms of the phase speed $c > v_{A0}$). If we separate solutions for $h(z)$ into modes which result in even or odd disturbances

about the x axis, then

$$h(z) = A \begin{cases} \sin(M_0 z), & \text{odd} \\ \cos(M_0 z), & \text{even.} \end{cases} \quad (4.10)$$

Application of the line-tying conditions at $z = L$ implies that

$$\sin(M_0 L) = 0 \quad (4.11)$$

for odd modes and

$$\cos(M_0 L) = 0 \quad (4.12)$$

for even modes. Hence

$$M_0 L = n\pi \quad \text{or} \quad M_0 L = \frac{(2n+1)\pi}{2}, \quad n = 0, 1, 2, \dots \quad (4.13)$$

for odd and even modes respectively, writing the even and odd modes together we obtain

$$M_0 L = \frac{(n+1)\pi}{2}, \quad n = 0, 1, 2, \dots \quad (4.14)$$

Hence using the definition of M_0^2 we can write

$$\left(\frac{\omega^2}{v_{A0}^2} - k^2 \right) = \left(\frac{(n+1)\pi}{2L} \right)^2, \quad n = 0, 1, 2, \dots \quad (4.15)$$

from this we can easily derive an explicit dispersion relation for the phase speed $c = c_n$:

$$\left(\frac{c_n}{v_{A0}} \right)^2 = \left(\frac{(n+1)\pi}{2kL} \right)^2 + 1, \quad n = 0, 1, 2, \dots \quad (4.16)$$

Equation (4.16) encompasses both even and odd modes, with the even modes corresponding to even values of the integer n and odd modes corresponding to odd values of n . From dispersion relation (4.16) we see that both even and odd modes asymptote to the floor value of $c/v_{A0} = 1$ in the short wavelength limit $kL \rightarrow \infty$. Fig.4.3(a) illustrates the behaviour of (4.16).

Very recently the importance of the ratio P_1/P_2 of the periods of the fundamental mode (P_1) and its first harmonic (P_2) has been discussed in the field of coronal seismology (see Goossens et al., 2006, Andries et al., 2005, McEwan et al., 2006). In this simple case we can write an explicit formula for P_n/P_m :

$$\left(\frac{P_n}{P_m} \right)^2 = \left(\frac{\omega_m}{\omega_n} \right)^2 = \frac{(m\pi)^2 + 4(kL)^2}{(n\pi)^2 + 4(kL)^2}. \quad (4.17)$$

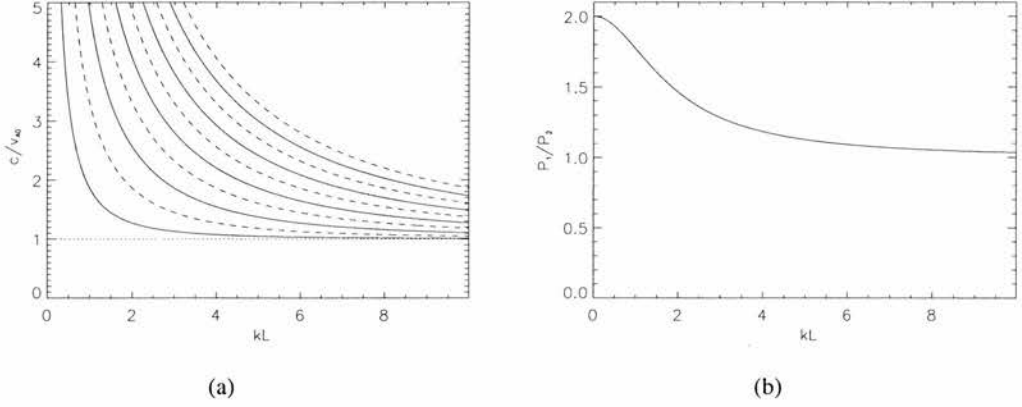


Figure 4.3: (a) Dispersion diagram plotting the non-dimensional phase speed c/v_{A0} against the non-dimensional perpendicular wavenumber kL for a homogeneous arcade. The even and odd modes are plotted as solid and dashed curves respectively, while the dotted line $c/v_{A0} = 1$ marks the cutoff curve. (b) Ratio of the fundamental even and odd modes, P_1/P_2 , plotted against kL for a homogeneous arcade.

Hence, setting $n = 1$ and $m = 2$,

$$\left(\frac{P_1}{P_2}\right) = \left[\frac{(2\pi)^2 + 4(kL)^2}{(\pi)^2 + 4(kL)^2}\right]^{\frac{1}{2}}, \quad (4.18)$$

and therefore in the limit $kL \rightarrow 0$, $P_1/P_2 \rightarrow 2$ and as $kL \rightarrow \infty$, $P_1/P_2 \rightarrow 1$. These trends can be observed in Fig.4.3 (b), which plots P_1/P_2 as a function of kL .

4.4.2 Case: 1 an exponential profile

Next we examine the influence of an exponentially structured environment. In the corona, this structuring could be as a result of gravity or temperature inhomogeneities; however, we do not consider a self consistent model, so although we incorporate the structuring of the environment in the equilibrium model we neglect the dynamical effects of the mechanisms which produces the structuring in the wave analyses. Hence we consider an Alfvén profile of the form

$$v_A(z) = v_{A0} \exp(-\alpha|z|/L), \quad (4.19)$$

which gives $v_A(z)$ decaying exponentially from the loop apex ($z = 0$) towards the photospheric footpoint ($z = \pm L$). Although we have continuous equilibrium profiles they are not continuously differentiable having an unphysical sharp peak in the Alfvén profile at the loop apex and so we must understand how the perturbations behave across this interface. Another essential point about these interfaces within this model is that they are perpendicular to the equilibrium magnetic field.

The boundary conditions at such an interface are given in (1.43) of Chapter 1:

$$[\mathbf{v}_1] = [\mathbf{B}_1] = [P_T] = 0, \quad (4.20)$$

which implies that all velocity and magnetic field components, as well as the total pressure, must be continuous at such an interface.

Using the Alfvén profile (4.19), equation (4.7) takes the form

$$\frac{d^2 h}{dz^2} + \left(\frac{\omega^2}{v_{A0}^2} \exp(2\alpha z/L) - k^2 \right) h = 0, \quad (4.21)$$

in the positive z region. Now equation (4.21) is of the form

$$\frac{d^2 y}{dx^2} + (\gamma^2 \exp 2\alpha x - \nu^2) y = 0, \quad (4.22)$$

which has general solution (Abramowitz and Stegun, 1964)

$$y(x) = A_1 J_{\frac{\nu}{\alpha}} \left(\frac{\gamma}{\alpha} \exp(\alpha x) \right) + B_1 Y_{\frac{\nu}{\alpha}} \left(\frac{\gamma}{\alpha} \exp(\alpha x) \right). \quad (4.23)$$

Therefore the general solution to equation (4.21) is

$$h(z) = A J_{\frac{kL}{\alpha}} \left(\frac{\omega L}{\alpha v_{A0}} \exp(\alpha z/L) \right) + B Y_{\frac{kL}{\alpha}} \left(\frac{\omega L}{\alpha v_{A0}} \exp(\alpha z/L) \right), \quad z \geq 0. \quad (4.24)$$

There are several important features to note about the solution (4.24). Firstly it does not apply for $\omega = 0$, $L = 0$ or $\alpha = 0$ although it will be seen later that the solution displays the correct limiting behaviour as $\alpha \rightarrow 0$. The second point is that the Bessel functions generally are of non-integer order but here this order is a function of kL and α . Finally we note that in the bounded region $[-L, L]$ neither Bessel function is singular, since their arguments are exponential functions of z (hence $Y_{kL/\alpha}(0)$ is never attained); therefore, both Bessel functions are incorporated into the solution for $h(z)$ and P_T .

Due to the symmetry of the equilibrium it is possible to separate solutions into *even* and *odd* modes, depending on the disturbances they give rise to about the line $z = 0$. The boundary conditions for the complete problem are

$$h(z = \pm L) = 0, \quad \lim_{z \rightarrow 0^-} h(z) = \lim_{z \rightarrow 0^+} h(z), \quad \lim_{z \rightarrow 0^-} \frac{dh}{dz} = \lim_{z \rightarrow 0^+} \frac{dh}{dz}. \quad (4.25)$$

The first condition is because of the line-tying; condition, the second condition is derived from the continuity of P_T (or v_x) across the apex $z = 0$. The third condition is a consequence of the continuity of the perturbed magnetic field and the x component of the induction equation which

imply $\frac{dv_x}{dz}$, and therefore $\frac{dh}{dz}$, are continuous across $z = 0$. Once we have separated solutions into even and odd modes, the boundary conditions are reduced in each case since some are identically satisfied (since the point of symmetry is the same as the interface) due to the fact that

$$\lim_{z \rightarrow 0} h(z) = 0 \quad (4.26)$$

for odd modes,

$$\lim_{z \rightarrow 0} \frac{dh}{dz} = 0 \quad (4.27)$$

for even modes. Conditions (4.26) and (4.27) are in addition to the line-tying condition $h = 0$ at $z \pm L$.

Application of these boundary condition yield the following dispersion relations:

$$J_{\frac{kL}{\alpha}} \left(\frac{ckL}{\alpha v_{A0}} \exp(\alpha) \right) Y_{\frac{kL}{\alpha}} \left(\frac{ckL}{\alpha v_{A0}} \right) - J'_{\frac{kL}{\alpha}} \left(\frac{ckL}{\alpha v_{A0}} \right) Y_{\frac{kL}{\alpha}} \left(\frac{ckL}{\alpha v_{A0}} \exp(\alpha) \right) = 0 \quad (4.28)$$

for the odd modes, and

$$J_{\frac{kL}{\alpha}} \left(\frac{ckL}{\alpha v_{A0}} \exp(\alpha) \right) Y'_{\frac{kL}{\alpha}} \left(\frac{ckL}{\alpha v_{A0}} \right) - J'_{\frac{kL}{\alpha}} \left(\frac{ckL}{\alpha v_{A0}} \right) Y_{\frac{kL}{\alpha}} \left(\frac{ckL}{\alpha v_{A0}} \exp(\alpha) \right) = 0 \quad (4.29)$$

for the even modes. Here the dash denotes the derivative of the Bessel function. These transcendental equations for the phase $c = \omega/k$ speed perpendicular to the equilibrium magnetic field (in the x direction) and free parameter k describe the modes of oscillation exhibited by a coronal arcade stationary in the longitudinal direction but freely propagating in the transverse component, with an exponential density profile. The dispersion relations (4.28) and (4.29) are similar in form. They are closely related to those found by McEwan et al. (2006) and Díaz and Roberts (2006) for standing slow modes in stratified loops.

We now present plots of the dispersion curves and eigenfunctions P_T , choosing the density profile shown in Fig.4.4. There is a density enhancement of a factor of 100 between the photospheric plasma at the footpoint ($z = \pm L$) and the loop apex ($z = 0$).

Fig. 4.5(a) displays the dispersion diagram for the fundamental mode and first nine harmonics, showing both even (solid) and odd (dashed) modes. Notice that since the Alfvén profile is invariant in the x direction there is no upper cutoff frequency; hence all modes propagate for all kL . Modes asymptote to a lower cutoff. As a result, in the long wavelength limit no mode propagates with finite phase speed in the way the fundamental kink modes found by Edwin and Roberts (1983) do (see also Chapter 2). It can be seen that the phase speeds of consecutive even and odd modes rapidly converge when kL is increased. As in the homogeneous case there is a lower limit to which the phase speed asymptotes. It can be argued from equation (4.21) that the lower limit

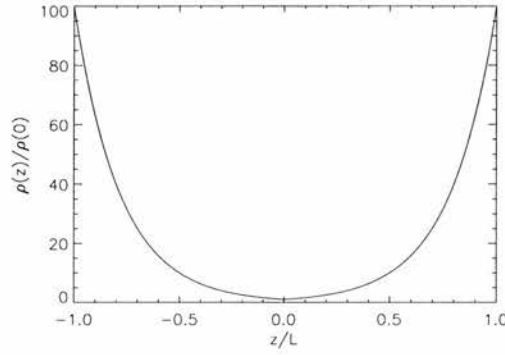


Figure 4.4: Non-dimensional density profile $\rho(z)/\rho_0$ as a function of the perpendicular coordinate z/L for an exponentially stratified arcade with $\rho(L)/\rho_0 = 100$.

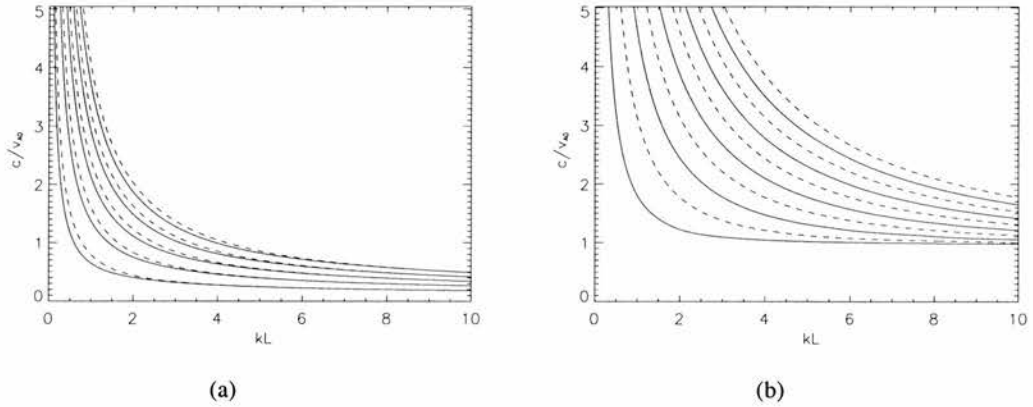


Figure 4.5: Dispersion diagrams plotting non-dimensional phase speed c/v_{A0} against kL , non-dimensional perpendicular wavenumber, for an exponentially stratified arcade with (a) $\rho(L)/\rho_0 = 100$ and (b) $\rho(L)/\rho_0 = 1.2$. The even modes are plotted as solid curves, and the odd modes as dashed curves.

lies in the range $[\exp(-\alpha), 1]$, since the solution to equation (4.21) must have a region where it exhibits oscillatory behaviour in $[0, L]$, in order to satisfy the line-tying boundary condition. This oscillatory behaviour can only occur when the quantity in parentheses in equation (4.21) is positive so that

$$\frac{\omega^2}{v_{A0}^2} \exp(2\alpha z/L) - k^2 > 0; \quad (4.30)$$

in terms of phase speed, this leads to

$$\frac{c}{v_{A0}} > \exp(-\alpha z/L). \quad (4.31)$$

Hence the ends of this interval $z = 0$ and $z = L$ give the most extreme values that the cutoff

could possibly take. Note we recover the homogeneous limit by allowing $\alpha \rightarrow 0$. It will be demonstrated later that $c/v_{A0} \rightarrow \exp(-\alpha)$ as $kL \rightarrow \infty$.

An important feature, which has recently been discussed by Andries et al. (2005), is that the ratio of the periods of the fundamental and first harmonic differ from 2. The trend is evident in this model, as shown in Fig.4.6(a) with P_1/P_2 plotted as a function of kL . Note that P_1/P_2 involve a comparison between the first even mode (which is classically known as the fundamental mode) and the first odd mode (which is classically known as the first harmonic). We see that for $P_1/P_2 < 2$ for all kL . Here, with $\alpha = 2.3$, we find that $P_1/P_2 \leq 1.35$ with the value of $P_1/P_2 = 1.35$ attained in the long wavelength limit and is a decreasing function of kL , tending to 1 in the short wavelength limit ($kL \rightarrow \infty$). If we allow $\alpha \rightarrow 0$ we recover the results for a uniform medium as seen in Fig.4.5(a). Also $P_1/P_2 \approx 2$ in the long wavelength limit and falls off towards 1 as kL is increased (Fig.4.6(b)).

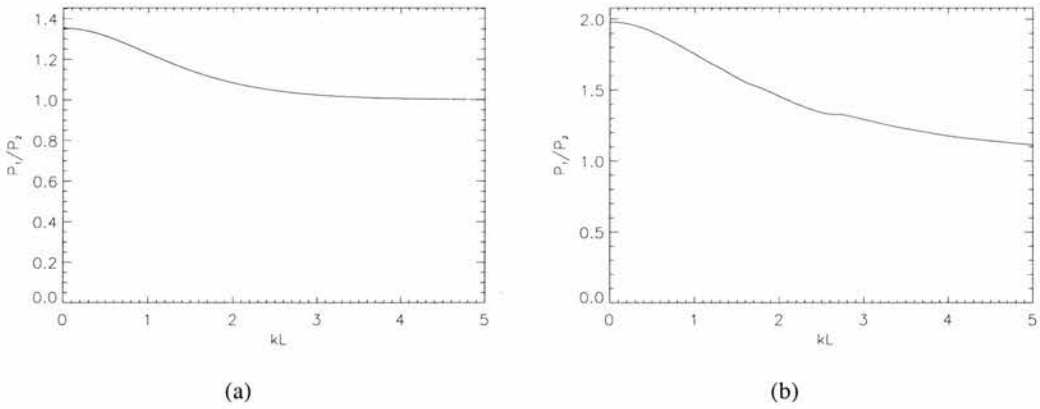


Figure 4.6: The ratio P_1/P_2 of the fundamental even modes of period P_1 and odd mode of period P_2 , plotted against kL for an exponentially stratified arcade with (a) $\rho(L)/\rho_0 = 100$ (which results in a value of $\alpha = 2.3$) and (b) $\rho(L)/\rho_0 = 1.2$ (which results in $\alpha = 0.09$).

Fig. 4.7 shows the dispersion diagram plotting the non-dimensional frequency $\omega L/v_{A0}$ against kL , for an exponential density stratification of $\rho(L)/\rho_0 = 100$. The frequency is a monotonic increasing function of kL with frequency taking a finite non-zero value as $kL \rightarrow 0$; therefore all modes have a finite non-zero period as $kL \rightarrow 0$. It can again be seen that the frequency of consecutive even and odd modes rapidly converge and also that the dispersion curves appear to become linearly dependent on kL ; for large kL , this points to the fact that the phase speed asymptotes to its cutoff value for large kL .

Fig. 4.8 shows plots of the total pressure perturbation (in units of $\rho_0 v_{A0}^2$), $P_T/(\rho_0 v_{A0}^2)$, against z/L for the fundamental mode and the first 8 harmonics of the even modes; here $kL = 2.0$. We can see that the fundamental modes does not display the expected behaviour as it has three extrema rather than a single extremum which would occur in the uniform arcade case. We can

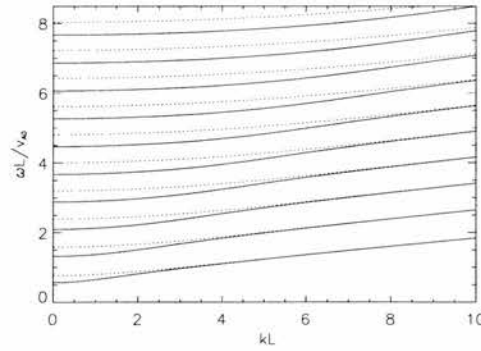


Figure 4.7: The dispersion diagram showing the non-dimensional frequency $\omega L/v_{A0}$ as a function of kL , for a density stratification of $\rho(L)/\rho_0 = 100$. The even modes are plotted as solid curves, and the odd modes as dotted curves.

see in figures 4.8(a) and (b) that the total pressure perturbation has a minimum at the loop apex ($z = 0$); this appears to be a characteristic of a mode which has phase speed less than the maximum Alfvén speed, $c < v_{A0}$. This trend is also followed by all of the modes plotted in Fig. 4.9 which are equivalent to those of Fig. 4.8 for a value of $kL = 8$. Also from the fundamental mode plotted in Fig. 4.8(a) the oscillation power has been restricted to a lower region of the loop and the effect is seen more strongly for the case $kL = 8$ shown in Fig. 4.9(a), with the oscillation causing almost no perturbation to the loop apex.

Finally, we see growing numbers of rapid oscillations near the footpoints, for both $kL = 2$ and $kL = 8$; the amplitude of these oscillations falls from the apex to the footpoints.

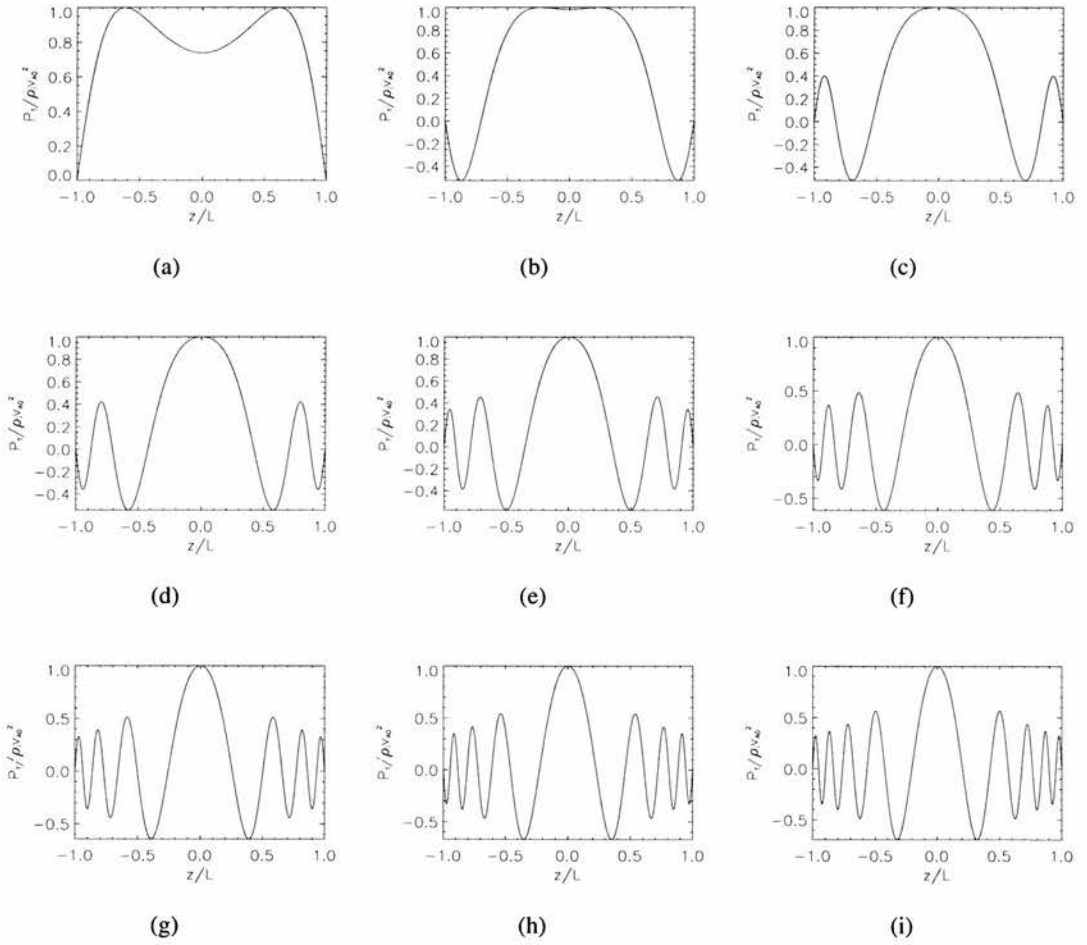


Figure 4.8: Plots of the non-dimensional total pressure perturbation $P_T/(\rho_0 v_{A0}^2)$ against z/L for the fundamental and first 8 even harmonics, at a value of $kL = 2$. An exponential density profile is used with density enhanced by a factor of 100 between the loop apex and the footpoints.

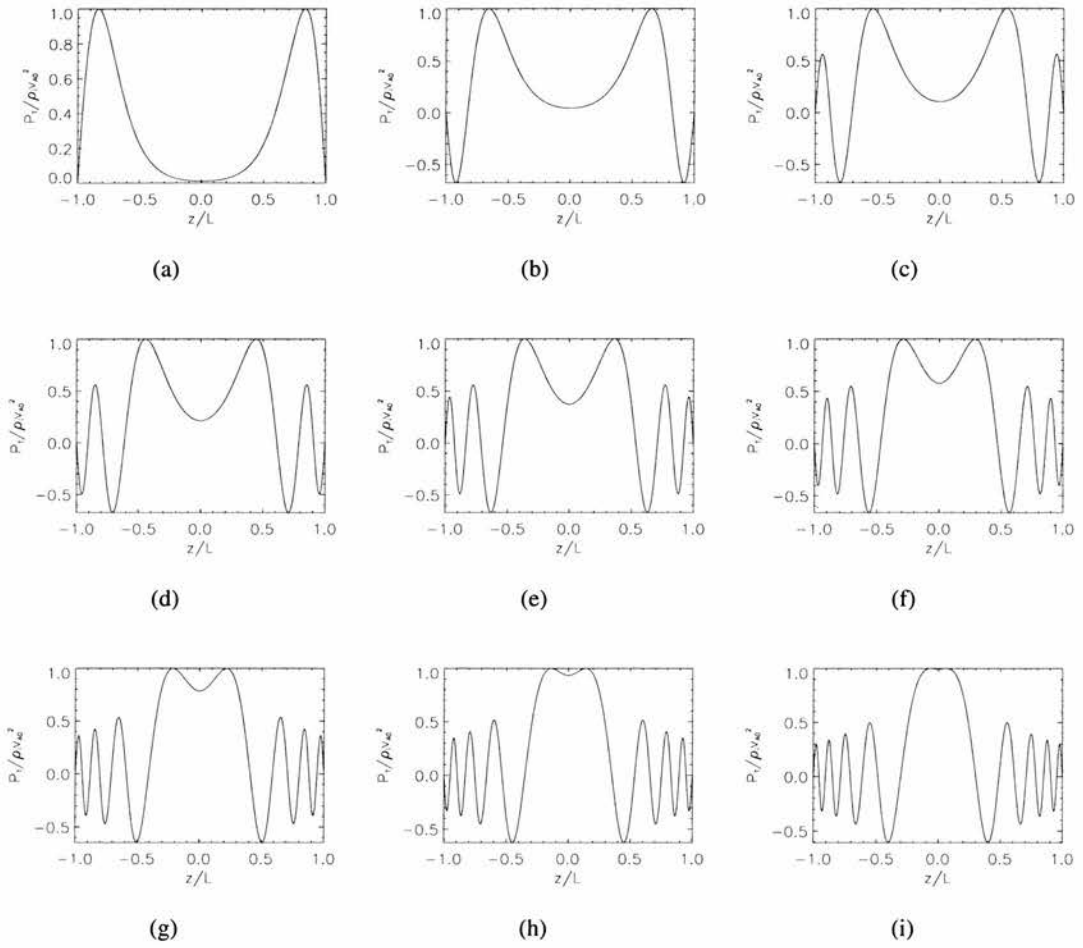


Figure 4.9: Plots of the non-dimensional total pressure perturbation $P_T / (\rho_0 v_{A0}^2)$ against z/L for the fundamental and first 8 harmonics, at a value of $kL = 8$. An exponential density profile is used with density enhanced by a factor of 100.

4.4.3 Numerical results

The unexpected result that the fundamental mode has three extrema rather than one provided encouragement for us to solve equation (4.21) numerically in order to verify this result. In Fig. 4.10 we show the dispersion diagram for both the solution of the analytical dispersion relations (4.28) and (4.29) and also the dispersion curves determined numerically from equation (4.21). There is excellent agreement between the numerical and analytical solutions for both the dispersion curves and the total pressure eigenfunction (Fig. 4.11), confirming the unexpected result concerning the extrema of this perturbation. It is interesting to note that the unusual occurrence of the fundamental mode having more than one extrema seems to develop as the phase speed falls below the maximum Alfvén speed. This is only possible due to the longitudinal structure of the arcade, since this behaviour is never seen in the uniform case where the phase speed is restricted to $c > v_{A0}$.

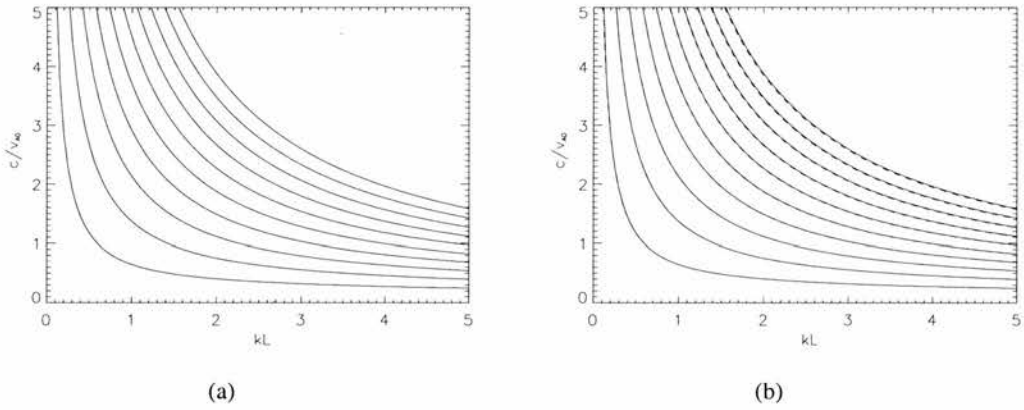


Figure 4.10: Dispersion diagrams showing the non-dimensionalised phase speed c/v_{A0} against the transverse wavenumber kL for exponential longitudinal structuring with $\rho(L)/\rho_0 = 100$. (a) the numerical results and (b) a comparison of numerical (solid curves) and analytical (dashed curves) dispersion curves.

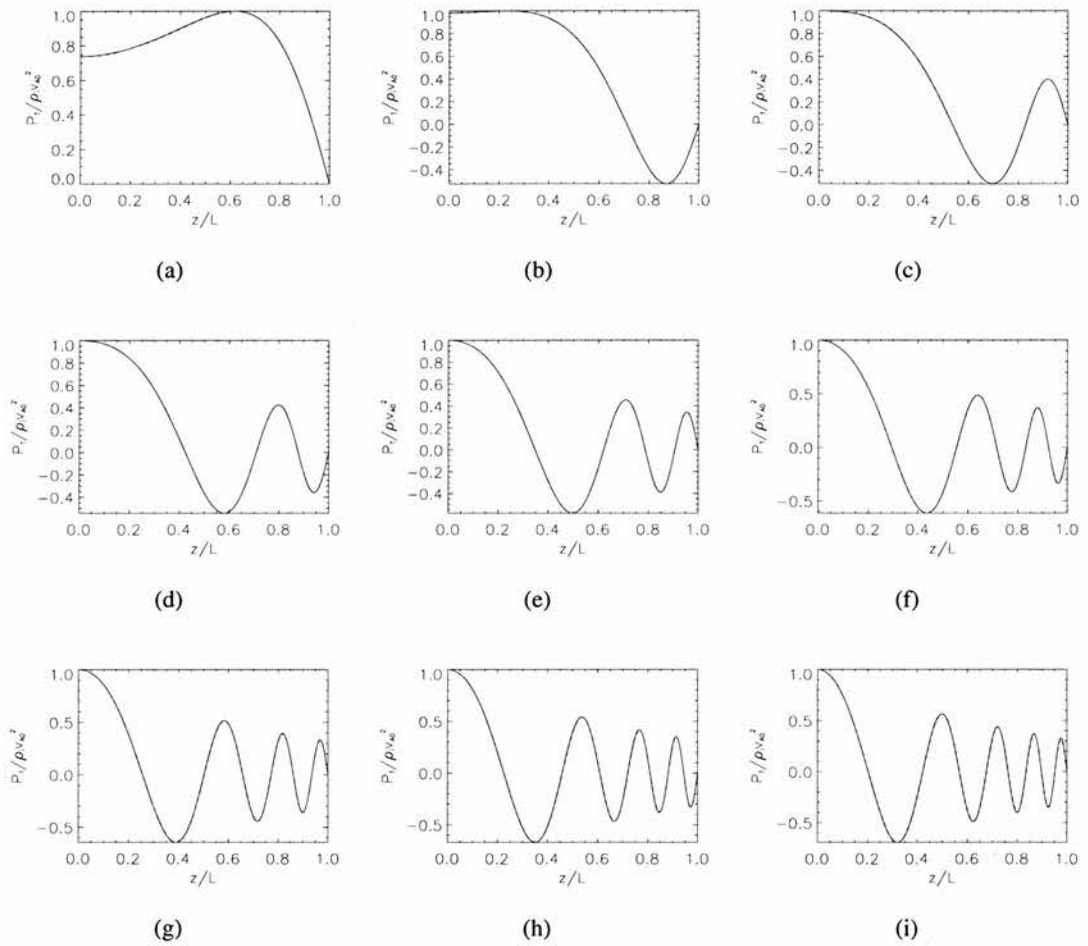


Figure 4.11: Plots of the non-dimensional total pressure perturbation, $P_T/(\rho_0 v_{A0}^2)$, against z/L for the fundamental and first 8 even harmonics, and $kL = 2$. An exponential density profile is used with density enhanced by a factor of 100. Both analytical (dashed curves) and numerical (solid curves) are plotted.

4.4.4 Analytical work

We now examine dispersion relations (4.28) and (4.29) analytically. Firstly using the expansions for the $(s + 1)^{th}$ zeros of an expression of the form

$$J_\nu(z)Y_\nu(\lambda z) - J_\nu(\lambda z)Y_\nu(z) \quad (4.32)$$

we can derive an approximate solution to dispersion relation (4.28) for the odd modes (see Appendix B)

$$\frac{c}{v_{A0}} = \frac{\alpha(s + 1)\pi}{kL(\exp(\alpha) - 1)} \left[1 + \frac{(4k^2L^2 - \alpha^2)(\exp(\alpha) - 1)^2}{8\alpha^2 \exp(\alpha)(s + 1)^2\pi^2} + \dots \right] \quad (4.33)$$

for the s^{th} harmonic (with $s = 0$ corresponding to the fundamental mode). Fig. 4.12(b) gives the dispersion diagram plotting the non-dimensional phase speed c/v_{A0} against kL , showing the approximate solution as solid curves and the full solution as dashed curves; there is excellent agreement for all harmonics, for kL less than two.

We can derive a similar approximation for the even modes using the expansion for the zeros of

$$J'_\nu(z)Y_\nu(\lambda z) - J_\nu(\lambda z)Y'_\nu(z). \quad (4.34)$$

We find (see Appendix B)

$$\frac{c}{v_{A0}} = \frac{\alpha(s - \frac{1}{2})\pi}{kL(\exp(\alpha) - 1)} \left[1 + \frac{[k^2L^2(4\exp(\alpha) - 1) + \alpha^2(\exp(\alpha) + \alpha^2)](\exp(\alpha) - 1)}{8\alpha^2 \exp(\alpha)(s - \frac{1}{2})^2\pi^2} + \dots \right], \quad (4.35)$$

with $s = 0, 1, 2, \dots$. It should be noted that this is not necessarily for the s^{th} even harmonic since expansion (4.35) is for a large zero of (4.29). We can see in Fig. 4.12(a) that this provides a good approximation to all harmonics, but not the fundamental mode, for larger values of c/v_{A0} .

Large kL

In the limit of large kL the order and argument of the Bessel functions in the dispersion relations (4.28) and (4.29) become large. Therefore these dispersion relations can be replaced by their leading order expansion (see Appendix C), giving

$$\frac{kL}{\alpha} \left[\sqrt{\frac{c^2 \exp(2\alpha)}{v_{A0}^2} - 1} - \sec^{-1} \left(\frac{c \exp(\alpha)}{v_{A0}} \right) \right] = \frac{(4n - 1)\pi}{4}, \quad n = 1, 2, 3, \dots \quad (4.36)$$

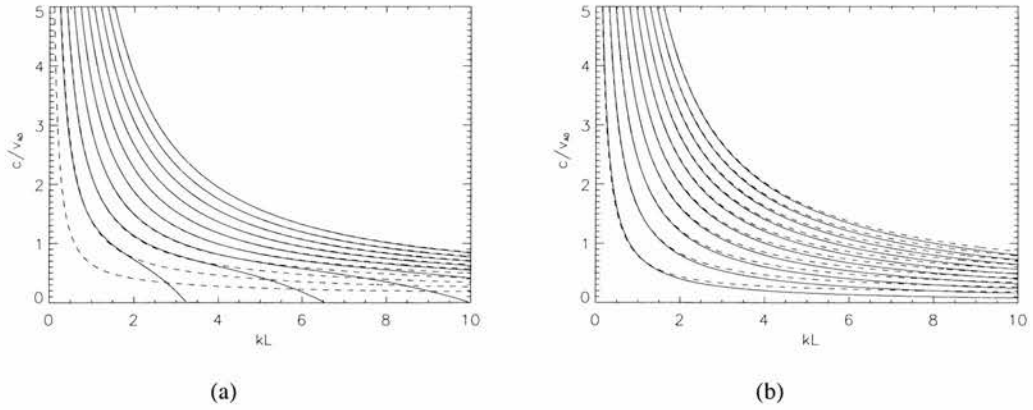


Figure 4.12: Dispersion diagrams showing the non-dimensionalised phase speed c/v_{A0} against the transverse wavenumber kL for exponential longitudinal structuring with $\rho(L)/\rho_0 = 100$. Both the full solution (dashed) and approximate (solid) solutions for (a) even modes and (b) odd modes.

for both even and odd modes. The fact that the even and odd modes both have the same asymptotic expansion in this limit is to be expected since their dispersion curves are seen to rapidly converge for increasing kL . Since kL/α is becoming large, the term in parentheses must become small since the right-hand side is finite, which happens as $c \exp(\alpha)/v_{A0}$ approaches 1. Therefore, using a series expansion for the term in parentheses about $c \exp(\alpha)/v_{A0} = 1$, we find

$$\frac{kL}{\alpha} \left[\frac{2}{3} \sqrt{2} \left(\frac{c \exp(\alpha)}{v_{A0}} - 1 \right)^{\frac{3}{2}} \right] = \frac{(4n-1)\pi}{4}, \quad n = 1, 2, 3, \dots \quad (4.37)$$

and therefore

$$\frac{c}{v_{A0}} = \exp(-\alpha) \left[\frac{3(4n-1)\pi}{8\sqrt{2}} \frac{\alpha}{kL} \right]^{\frac{2}{3}} + \exp(-\alpha). \quad (4.38)$$

From equation (4.38) it is apparent that the phase speed $c \rightarrow v_{A0} \exp(-\alpha)$ as $kL \rightarrow \infty$. Note that this produces the correct limiting behaviour of $c \rightarrow v_{A0}$ as $\alpha \rightarrow 0$. Fig. 4.13 shows a plot of the full solution (even modes plotted as solid curves and odd modes plotted as dotted curves) and the approximate solution for large kL plotted as dashed curves. We see good agreement for the fundamental and first harmonic and the approximate solution. As a result of the accuracy of the approximation being dependent on $(4n-1)\pi/4$ for higher harmonics, a much larger value of kL would be necessary to observe the same level of agreement as for the fundamental and first harmonic.

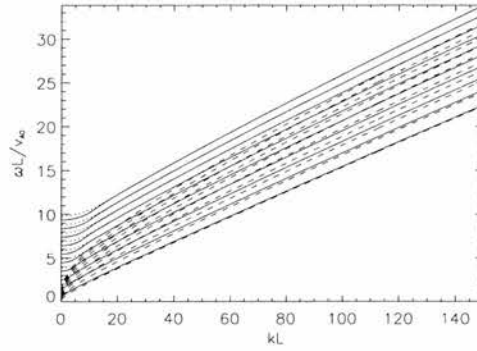


Figure 4.13: The dispersion diagram showing the non-dimensional frequency $\omega L/v_{A0}$, as a function of kL for a density stratification of $\rho(L)/\rho_0 = 100$. The even modes, odd modes and approximately determined modes are shown in solid, dotted and dashed curves, respectively.

4.4.5 Case 2 an exponential profile with uniform region

Finally we consider an Alfvén profile having a similar form to that of the time-averaged profile produced Mendoza-Briceño et al. (2004). investigates the heating of a coronal loop, modelled by a 1D hydrodynamic semicircular simulation. This structure is then subjected to impulsive localized heating near the loop footpoints. This results in a continuously varying temperature profile, when time averaged a temperature profile which corresponds to a density profile of similar properties to that shown in Figure 4.14 is obtained. This profile, unlike the previous case has the exponential behaviour confined to the footpoints of the structure, where the density changes rapidly from a photospheric level to a coronal level over the height of the chromosphere, and the central coronal region is uniform and this seemed to be the natural step forward from the previous case considered in this Chapter. Fig. 4.14 shows a plot of the normalised density profile used in this case. We have chosen the chromospheric depth to be $(L - W) = L/10$, so it is one twentieth of the loop length, and we have chosen a density contrast of $\rho(L)/\rho_0 = 100$ between the footpoint and coronal region.

This density structuring leads to an Alfvén profile of the form

$$v_A(z) = \begin{cases} v_{A0} \exp(\alpha(z + W)/L), & -L < z < -W \\ v_{A0}, & -W < z < W \\ v_{A0} \exp(-\alpha(z - W)/L), & W < z < L. \end{cases} \quad (4.39)$$

A value of $\alpha = 23.0$ results in a change to the Alfvén speed between the footpoint and the loop apex by a factor of 10.

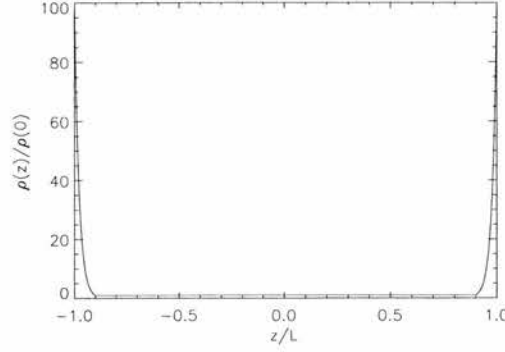


Figure 4.14: Non-dimensional density profile $\rho(z)/\rho_0$ as a function of the perpendicular coordinate z/L for a uniform coronal region $|z| < W$ where $\rho(z) = \rho_0$ and an exponentially stratified chromosphere $W < |z| < L$. The density contrast between footpoint and apex is $\rho(L)/\rho_0 = 100$ and the coronal depth $W = L/10$.

Hence equation (4.7) takes the form

$$\frac{d^2 h}{dz^2} + \left(\frac{\omega^2}{v_{A0}^2} \exp(2\alpha(z - W)/L) - k^2 \right) h = 0, \quad (4.40)$$

in the photospheric region $W < z < L$, with solution

$$h(z) = AJ_{\frac{kL}{\alpha}} \left(\frac{\omega L}{\alpha v_{A0}} \exp(\alpha(z - W)/L) \right) + BY_{\frac{kL}{\alpha}} \left(\frac{\omega L}{\alpha v_{A0}} \exp(\alpha(z - W)/L) \right). \quad (4.41)$$

Solution (4.41) possesses similar properties as (4.24) with non-integer order and no singularity in the applicable region $[W, L]$ so both Bessel functions are retained in the solution. However, the arguments are now exponential functions shifted by the coronal depth W . In the homogeneous coronal region, $-W < z < W$, equation (4.7) takes the form

$$\frac{d^2 h}{dz^2} + M_0^2 h = 0, \quad (4.42)$$

which is the same as equation (4.9) that arises in the entirely homogeneous arcade. However, the boundary conditions we apply at $z = \pm L$ in the homogeneous case are not equivalent to the boundary conditions (4.20) to be applied at $z = \pm W$. As a result M_0^2 is not restricted to be positive; hence both oscillatory and hyperbolic functions are admissible solutions under these conditions. Also, as a result of this, the normalised phase speed may fall below $c/v_{A0} = 1$ which was the floor value for the entirely uniform case. Therefore the solution has the form

$$h(z) = \begin{cases} C^+ \sin(M_0 z) + D^+ \cos(M_0 z), & M_0^2 \geq 0 \\ C^+ \sinh(N_0 z) + D^+ \cosh(N_0 z), & M_0^2 = -N_0^2 < 0. \end{cases} \quad (4.43)$$

Application of the appropriate boundary conditions (4.26) and (4.27) along the line of symmetry $z = 0$ allows us to separate the discussion into even and odd modes. In this case there is also an interface at $z = \pm W$, where the continuity of both $h(z)$ and $\frac{dh}{dz}$ must be enforced. This leads us to the following transcendental dispersion relations (see Appendix E)

$$\begin{aligned} \frac{c}{v_{A0}} \tan \left(kW \sqrt{\frac{c^2}{v_{A0}^2} - 1} \right) = \\ \frac{W \sqrt{\frac{c^2}{v_{A0}^2} - 1} \left(J_{\frac{kL}{\alpha}} \left(\frac{ckL}{\alpha v_{A0}} \exp(\alpha(L-W)/L) \right) Y_{\frac{kL}{\alpha}} \left(\frac{ckL}{\alpha v_{A0}} \right) - Y_{\frac{kL}{\alpha}} \left(\frac{ckL}{\alpha v_{A0}} \exp(\alpha(L-W)/L) \right) J_{\frac{kL}{\alpha}} \left(\frac{ckL}{\alpha v_{A0}} \right) \right)}{\left(J_{\frac{kL}{\alpha}} \left(\frac{ckL}{\alpha v_{A0}} \exp(\alpha(L-W)/L) \right) Y'_{\frac{kL}{\alpha}} \left(\frac{ckL}{\alpha v_{A0}} \right) - Y'_{\frac{kL}{\alpha}} \left(\frac{ckL}{\alpha v_{A0}} \exp(\alpha(L-W)/L) \right) J'_{\frac{kL}{\alpha}} \left(\frac{ckL}{\alpha v_{A0}} \right) \right)} \end{aligned} \quad (4.44)$$

for the odd modes and

$$\begin{aligned} -\frac{c}{v_{A0}} \cot \left(kW \sqrt{\frac{c^2}{v_{A0}^2} - 1} \right) = \\ \frac{W \sqrt{\frac{c^2}{v_{A0}^2} - 1} \left(J_{\frac{kL}{\alpha}} \left(\frac{ckL}{\alpha v_{A0}} \exp(\alpha(L-W)/L) \right) Y_{\frac{kL}{\alpha}} \left(\frac{ckL}{\alpha v_{A0}} \right) - Y_{\frac{kL}{\alpha}} \left(\frac{ckL}{\alpha v_{A0}} \exp(\alpha(L-W)/L) \right) J_{\frac{kL}{\alpha}} \left(\frac{ckL}{\alpha v_{A0}} \right) \right)}{\left(J_{\frac{kL}{\alpha}} \left(\frac{ckL}{\alpha v_{A0}} \exp(\alpha(L-W)/L) \right) Y'_{\frac{kL}{\alpha}} \left(\frac{ckL}{\alpha v_{A0}} \right) - Y'_{\frac{kL}{\alpha}} \left(\frac{ckL}{\alpha v_{A0}} \exp(\alpha(L-W)/L) \right) J'_{\frac{kL}{\alpha}} \left(\frac{ckL}{\alpha v_{A0}} \right) \right)} \end{aligned} \quad (4.45)$$

for the even modes. We have assumed $M_0^2 > 0$; equivalent relations arise in the case $M_0^2 < 0$. Notice there is no upper cutoff frequency but we find that there is a lower cutoff value to which the dispersion curves asymptote in the short wavelength limit. This cutoff lies in the range $[\exp(\alpha(W/L - 1)), 1]$; the same argument as the previous case can be made once $c/v_{A0} < 1$. Notice this cutoff value returns to the case of a uniform medium, when $\alpha \rightarrow 0$ or $W \rightarrow L$.

Fig. 4.15(a) shows the dispersion diagram plotting non-dimensional phase speed c/v_{A0} in the transverse direction against non-dimensional wavenumber kL . The fundamental mode and first nine harmonics are shown. Even and odd modes are plotted as solid and dashed curves respectively. We have taken $\alpha = 23$, which results in a density contrast of 100 between the loop apex and footpoint. As in the previous case, we can see no mode propagates with finite phase speed in the limit $kL \rightarrow 0$. The spacing of the dispersion curves has been modified from Fig. 4.3(a). This influences the ratio of periods P_1/P_2 , causing it to be less than the expected value of two as $kL \rightarrow 0$. See Fig. 4.16(a).

The phase speed of the odd and even modes are identical on crossing the curve $c/v_{A0} = 1$. This is because $\tanh(x) \approx \coth(x)$ for large x , and hence the dispersion relations are very similar for $c/v_{A0} < 1$ but for $c/v_{A0} > 1$ the phase speed of the even and odd modes are distinct. Also there

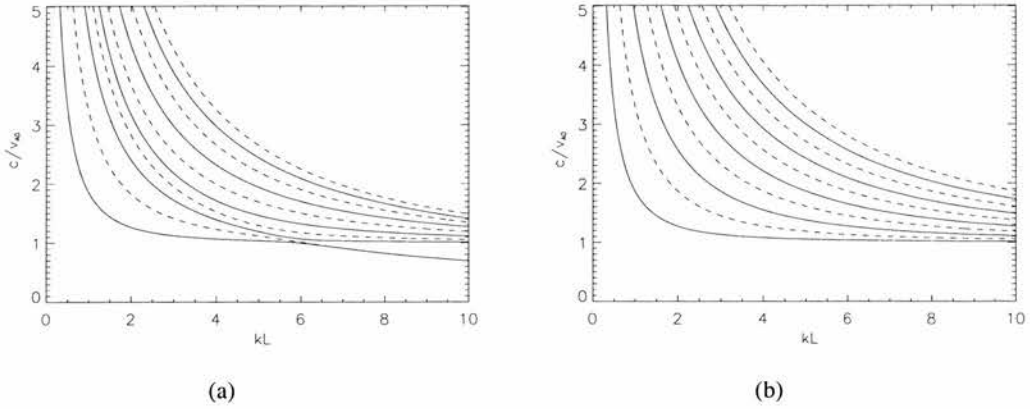


Figure 4.15: Dispersion diagrams plotting non-dimensional phase speed c/v_{A0} against kL for the Alfvén profile (4.39) with $W = L/10$ and density contrasts (a) $\rho(L)/\rho_0 = 100$ and (b) $\rho(L)/\rho_0 = 1.2$. The even and odd modes are plotted as solid and dashed curves, respectively.

is an avoided crossing between the first two even modes at the point where the fundamental mode crosses $c/v_{A0} = 1$. This is because on crossing this curve the eigenfunctions can have at most one extrema in the region $0 < z < W$ (at the origin), due to their hyperbolic dependence; hence if more extrema are present before crossing this curve they must be transferred to the region $W < z < L$ via an avoided crossing. As a result of this avoided crossing, local minima and maxima can be found in the ratio P_1/P_3 (see Fig. 4.16(b)) so it is no longer a monotonic decreasing function of kL , as occurred in the homogeneous case when $P_1/P_3 = 2.85$ as $kL \rightarrow 0$. However, setting $\alpha = 0.1$ we find that we recreate the uniform medium case as seen in Fig. 4.15(b), where the curves asymptote to $c/v_{A0} = 1$; this fact is also evident from the ratios P_1/P_2 (Fig. 4.17(b)) or P_1/P_3 (Fig. 4.18(b)), both now monotonic decreasing functions of kL and equal to 2 and 3 respectively as $kL \rightarrow 0$, as expected.

Fig. 4.19 and Fig. 4.20 show plots of the total pressure perturbation (non-dimensionalised against $\rho_0 v_{A0}^2$ and normalised to 1 at its maximum value) as a function of z/L , for the fundamental and first 8 even harmonics for values of $kL = 2$ (Fig. 4.19) and $kL = 8$ (Fig. 4.20). For all of the modes plotted at $kL = 2$, we find that $c/v_{A0} > 1$ so $M_0^2 > 0$, and hence the behaviour of the total pressure perturbation is oscillatory in the central region $|z| < W$. Hence M_0^2 increases as you look at each higher harmonic therefore more oscillations in amplitude are found to occur in the region $|z| < W$ for each harmonic compared with the previous harmonic. The fundamental mode takes a similar form to that of a uniform arcade, with one extrema for a value of $kL = 2$ (Fig. 4.19(a)). But comparing this to the fundamental mode at a value of $kL = 8$ (Fig. 4.20(a)) after the avoided crossing between this modes and first harmonic, we see it now has three extrema while the first harmonic (Fig. 4.20(b)) has adopted a very similar behaviour to the fundamental mode at $kL = 2$ (Fig. 4.19(a)). In the regions $W < |z| < L$, the solutions have smaller but more

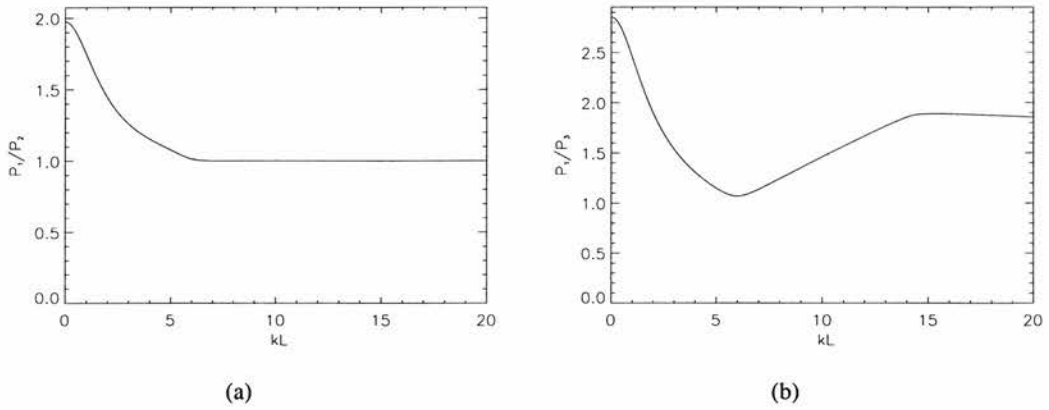


Figure 4.16: (a) Ratio P_1/P_2 of the fundamental even and odd modes (a) P_1/P_2 and (b) ratio P_1/P_3 of fundamental and first harmonic of the even modes, plotted against kL for Case 2 with $\rho(L)/\rho_0 = 100$.

rapid amplitude oscillations, for both $kL = 2$ and $kL = 8$. This is similar to the findings of Díaz and Roberts (2006), where a similar governing equation was derived for the slow modes.

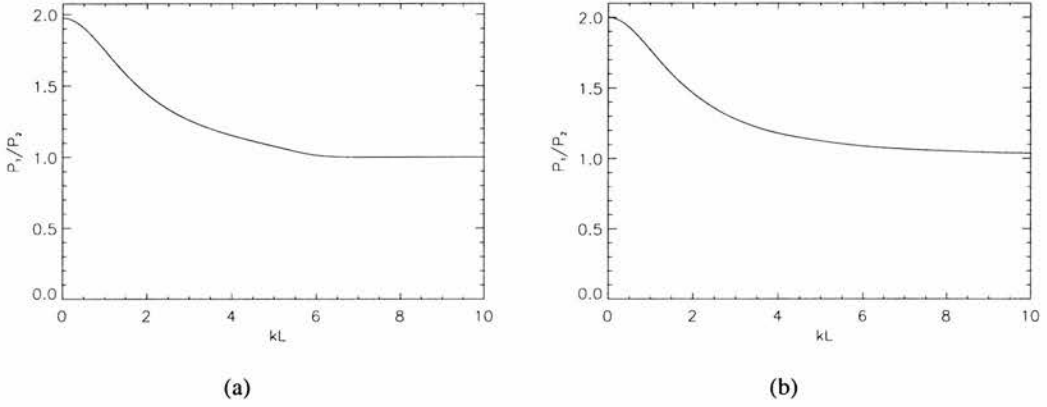


Figure 4.17: Ratio P_1/P_2 of the fundamental even and odd modes, plotted against kL for Case 2 with (a) $\rho(L)/\rho_0 = 100$ and (b) $\rho(L)/\rho_0 = 1.2$.

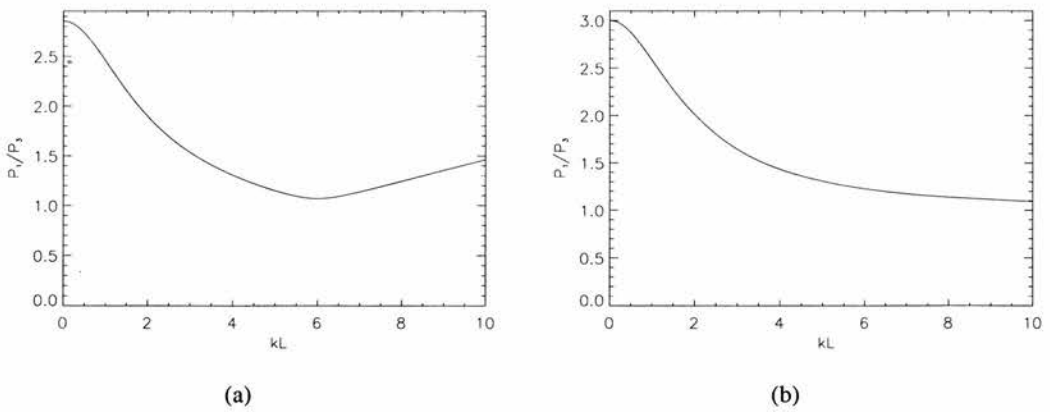


Figure 4.18: Ratio P_1/P_3 of fundamental and first harmonic of the even modes plotted against kL for Case 2 with (a) $\rho(L)/\rho_0 = 100$ and (b) $\rho(L)/\rho_0 = 1.2$.

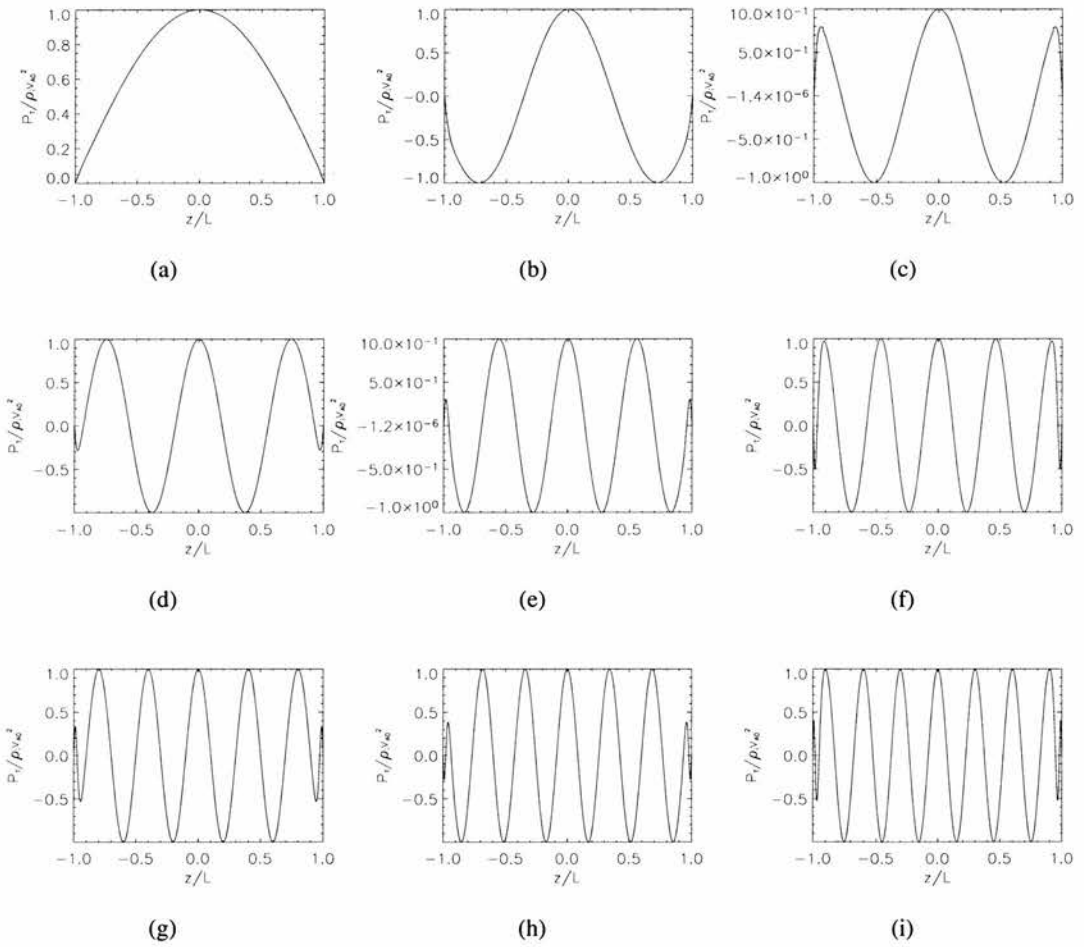


Figure 4.19: Plots of the non-dimensional total pressure perturbation $P_T/(\rho_0 v_{A0}^2)$ against z/L for the fundamental and first 8 even harmonics, at a value of $kL = 2$ for Case 2. The density contrast between the loop apex and footpoint is $\rho(L)/\rho(0) = 100$ and the coronal depth $W = 0.1L$.

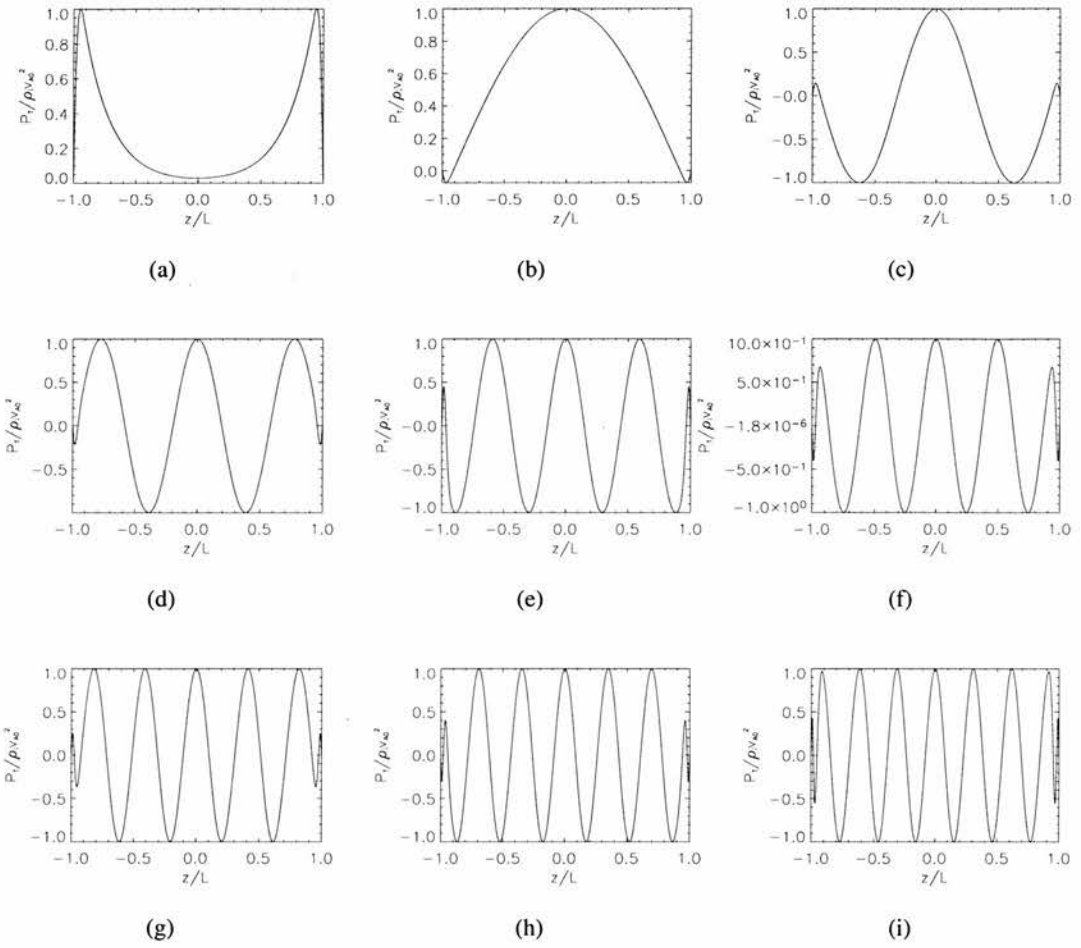


Figure 4.20: Plots of the non-dimensional total pressure perturbation $P_T/(\rho_0 v_{A0}^2)$ against z/L for the fundamental and first 8 even harmonics, at a value of $kL = 8$ for Case 2. The density contrast between the loop apex and footpoint is $\rho(L)/\rho_0 = 100$ and the coronal depth $W = 0.1L$.

4.4.6 Changing W

It is of interest to investigate the influence of the chromospheric depth ($L - W$) on the phase speed of these modes. Plots of phase speed against W/L are shown in Fig. 4.21 for a density ratio of $\rho(L)/\rho_0 = 100$. To achieve this for different values of W/L we vary α , these quantities being related by

$$\alpha = \frac{1}{2(1 - \frac{W}{L})} \ln \frac{\rho(L)}{\rho_0}. \quad (4.46)$$

The plots provide us the opportunity to compare the phase speeds of the uniform medium (case $W/L = 1$) and the exponentially stratified case $W/L = 0$. We see that stratification results in a reduction of phase speed.

Fig. 4.21(a) shows a plot of c/V_{A0} for $kL = 2$. Immediately we notice a large number of interactions between adjacent modes, as a result of the many small amplitude oscillations in the chromospheric region being transferred from the coronal region. It can also be seen that although there is a general decreasing trend in phase speed from the homogeneous structure ($W/L = 1$) to an entirely exponential profile density ($W/L = 0$). There is an increase in phase speed caused by the introduction of a small chromospheric layer (this may indicate competing effects, one causing an increase in phase speed and the other causing a decrease in phase speed, such as the effective shortening of the loop and the increase of overall density) the effect occurring for thinner chromospheres for higher harmonics (The other option is that this is a numerical error). Finally, the fundamental mode shows little dependence on the chromospheric depth. The right hand plot of Fig. 4.21(b) is for $kL = 8$, where we can see many of the same features though now the fundamental mode is strongly dependent on the chromospheric depth in the range $W/L = 0.3 - 0.9$, outside this region, so in the realistic thin chromosphere region, again the phase speed does not depend on W/L .

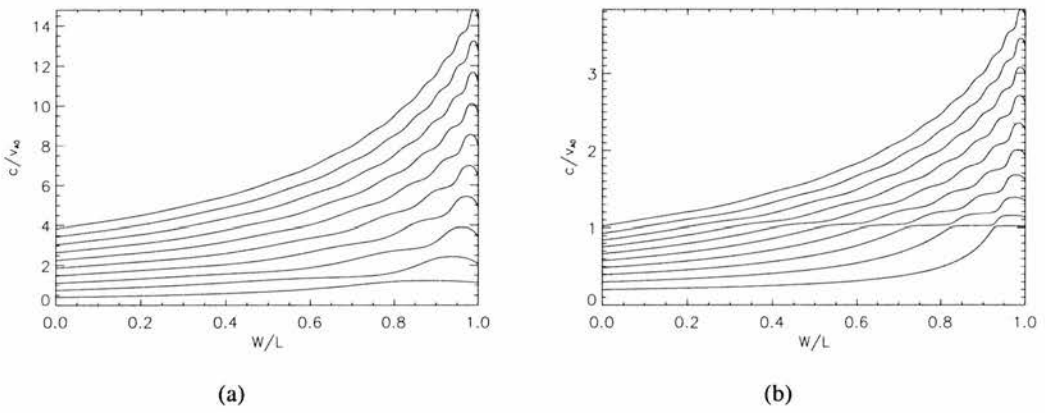


Figure 4.21: Dispersion diagrams plotting non-dimensional phase speed c/v_{A0} against W/L for Case 2 with density contrasts $\rho(L)/\rho_0 = 100$ and values of (a) $kL = 2$ and (b) $kL = 8$.

4.5 Comparison with observations

Observations of a flare excited oscillation in a coronal arcade have been recently discussed in Verwichte et al. (2004). Finding a coherent oscillation of many coronal loops, forming an arcade structure in some parts of the structure, there is strong evidence in oscillation period and also displacement profile in the plane of the loop that not only the fundamental but the first harmonics are being observed. It is our intention here to test the model presented in Case 2 with the observational data in Verwichte et al. (2004) by using the first harmonic to fix then parameters of the model and then deduce the period of the first harmonic and compare this to the observed value.

The height of the loop arcade has been found to be in the range 65 – 76 Mm (Verwichte et al. 2004). We choose a value of 70 Mm and assume the loop arcade is semicircular, leading to a field line length of 70π Mm = 220 Mm. It has also been assumed that the density profile along the loop is the same as presented previously, where the chromosphere has been taken to be one twentieth of the loop length and a density stratification of 100 occurs across the chromosphere and the coronal structure, where we take a coronal Alfvén speed of 1000 km s^{-1} (assumed uniform).

Taking the observed period to be 400 s (Verwichte et al., 2004) we find this corresponds to a non-dimensional frequency of $\omega L/v_{A0} = 1.72$ for the fundamental mode. Reading the wavenumber from Fig. 4.22 it is found that this mode is propagating with a wavenumber of $kL = 0.72$. Assuming that the first harmonic (this has previously been referred to as the fundamental odd mode) has a similar wavenumber (which is reasonable assumption because kL is the wavenumber in the direction the wave packet is propagating and so is independent of the longitudinal direction which determines whether a mode is the fundamental or the i^{th} harmonic by the number of nodes along this axis) allows us to read the frequency of the first harmonic from Fig. 4.22. It is found that $\omega L/v_{A0} = 3.16$ from Fig. 4.22 which leads to a deduced period of 218s for the first harmonic, which is in good agreement with observed value of 242 ± 31 s (Verwichte et al., 2004).

4.6 Conclusions

Our aim here was to model the oscillations of a coronal arcade with footpoints fixed in the photospheric surface but allowing for free propagation along the arcade. To achieve this we considered a 2D arcade aligned with the x axis of a uniform magnetic field directed across the arcade in the z direction. We considered three density profiles $\rho_0(z)$ so we have structuring along the magnetic field but invariant along the arcade. We solved the linearised MHD equations in the zero beta limit, so only the fast modes are present. The modes of oscillation are governed by the wave equation with propagation speed dependent on the density stratification.

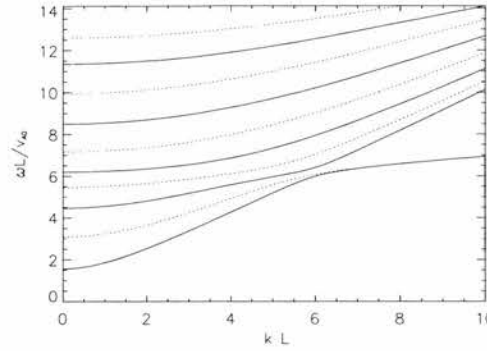


Figure 4.22: Dispersion diagram plotting non-dimensional frequency $\omega L/v_{A0}$ against kL for the Alfvén profile (4.39) with $W = L/10$ and density contrasts $\rho(L)/\rho_0 = 100$. The even and odd modes are plotted as solid and dashed curves, respectively.

The reference case we use is a homogeneous arcade which allows us to derive an explicit dispersion relation (equation (4.16)). From this dispersion relation we find that the dispersion curves asymptote to the limit $c/v_{A0} = 1$ (see Fig. 4.3(a)). Andries et al. (2005) identified the ratio P_1/P_2 of periods of the fundamental mode to first harmonic to be potentially important in the field of coronal seismology. In the homogeneous case we find the ratio P_1/P_2 follows the same trend as previously found, equal to 2 in the long wavelength limit and monotonic decreasing to 1 in the short wavelength limit (see Fig. 4.3(b)).

The second case examined here is that of an exponentially stratified density profile, with the loop footpoints denser than the apex. We have taken the density enhancement to be a factor of 100 which is in line with the difference between photosphere and coronal values. It is found that the addition of the density structures results in a transcendental dispersion relations (4.28) and (4.29) for odd and even modes respectively. From this, we find a reduction in the phase speed compared with the homogeneous case. Also the phase speed of consecutive even and odd modes converge for larger values of kL , which has been demonstrated analytically. As in the homogeneous case, there is a floor value for the phase speed. However, the floor value does not lie at $c/v_{A0} = 1$ but at $c/v_{A0} \rightarrow \exp(-\alpha)$. The fact that the dispersion curves are differently spaced influences the ratio P_1/P_2 , causing it to be less than 2 in the limit $kL \rightarrow 0$ but as $kL \rightarrow \infty$ it still tends to a value of 1. In this case the eigenfunctions exhibit different behaviour to the homogeneous case, developing many oscillations in the footpoint regions and also in some cases the fundamental mode has more than one extrema. Finally, we regain the properties of the homogeneous case in the limit $\alpha \rightarrow 0$.

The drawback of this density profile is that in reality the change from photospheric to coronal densities occurs more rapidly. However, the final profile we considered does not have this drawback, since it has exponential behaviour in the chromospheric region $W < |z| < L$ and is uniform in

the corona $|z| < W$. Again the stratification results in a decrease in phase speed compared with the homogeneous case, but it is not as extreme as the previous case. It is found that crossing the curve $c/v_{A0} = 1$, the phase speeds of consecutive even and odd modes rapidly converge. Also, on crossing this curve we found an interaction between the fundamental and first harmonic of the even modes in the form of an avoided crossing. As expected, the floor value is altered by the stratification and now lies in the range $[\exp(-\alpha(W/L - 1)), 1]$. The influence of this case on the ratio P_1/P_2 is the same as the previous case. It is also interesting to consider P_1/P_3 , which is less than 3 as $kL \rightarrow 0$. This case also has a local minimum, as a result of the avoided crossing between these two modes; this type of behaviour would be possible in P_1/P_2 in a model where these modes did not decouple (such as a non-symmetric equilibrium). The eigenfunctions display oscillatory behaviour in the region $|z| < W$ and a more rapid oscillation in $W < |z| < L$, and the exchange of extrema between these two regions can account for the large number of avoided crossings seen in Fig. 4.21 as W/L varies. Importantly, testing this model as $\alpha \rightarrow 0$ or $W \rightarrow L$, it reduces to the homogeneous case and also as $W \rightarrow 0$ to the exponential profile case. This model has been shown to compare well with observations of an impulsively excited arcade oscillation; when given the period of the fundamental mode, the period of the first harmonic has been predicted and is found to be in line with observed values.

Therefore it is clear that the influence of stratification, regardless of the effect producing it, yields an important influence on both the frequency of modes and their eigenfunctions. Due to the shift in frequency caused by the stratification, the seismological tool P_1/P_2 is also altered. This may be important in future coronal seismology developments.

Chapter 5

Exponential Loop Profile

5.1 Introduction

In Chapters 1 and 2 we have given a brief overview of observational evidence for coronal loop oscillations. It is clear from the abundance of observations that this is a commonly occurring behaviour for a coronal loop. As with any wave mode, oscillations of coronal loops carry information about the medium in which the wave propagates. If we understand the wave mode and its effect on the plasma as it propagates we can extract the information the wave possesses about the plasma, this is known as coronal seismology. An example of results obtained using coronal seismology is given in Chapter 2 (Nakariakov et al., 1999, Nakariakov and Ofman, 2001). In order to carry out coronal seismology a good understanding of the oscillatory modes of a structure is necessary. This understanding comes from the development of theoretical models. Current models generally consist of a straight cylindrical flux tube which is either infinitely long or line-tied (finite length) (Edwin and Roberts, 1983). When line-tying has been studied it is also possible to study the effect of longitudinal structuring (Díaz et al., 2002), and in Chapter 3 this structuring has been in the form of step functions. In Chapter 3 step functions are used to represent dense chromospheric layers both inside and outside the loop. However, the use of step functions is only a first approximation and in an actual coronal loop a continuously varying density profile is expected. In this chapter it is our intention to include continuous density profiles in the longitudinal direction to the model and to compare with the uniform line-tied loop. As the z dependence of the oscillation is governed by a similar equation to (4.7), discussed in Chapter 4, it is convenient to consider the same density profiles, the first with exponential behaviour along the full length of the loop and the second with uniform coronal region and exponential behaviour restricted to chromospheric regions close to the footpoints. For the first profile the influence of the loop radius as well as the level of stratification between the loop apex and footpoint is studied. In the second case the effect of the loop radius is still studied and also the effect of the depth of chromospheric

layers, while the level of stratification between footpoint and apex is held constant.

The same method is adopted as used in Chapter 3 which is easily adapted to permit different longitudinal dependence of the density and Alfvén profiles. Also, since these profiles are continuous, a numerical approach may be of use solve equation (1.58). If a numerical solution to equation (1.58) is to be found, either a fifth or eighth order Runge-Kutta method is employed. A general outline of the Runge-Kutta method and an example of the fourth order method is given in Chapter 1.

5.2 Case 1: the exponentially stratified corona

We consider the fast wave in a zero β plasma with magnetic field lying parallel to the z axis. The z dependence of the fast mode is governed by the equation (see Chapter 1)

$$\frac{d^2 h}{dz^2} + \left(\frac{\omega^2}{v_A^2(z)} + \lambda_n^2 \right) h = 0 \quad (5.1)$$

which incorporates all of the dependence on the longitudinal stratification of the equilibrium. Here we introduce longitudinal stratification of the loop using an exponential Alfvén profile of the form

$$v_A(z) = v_{A0} \exp(-\alpha_0 |z|/L), \quad (5.2)$$

where $v_{A0} = v_A(z = 0)$ is the Alfvén speed at the loop apex ($z = 0$) and α_0 governs the stratification rate between the apex and the loop footpoint ($z = L$). It should be noted that this profile has some unphysical features, having a sharp peak in the Alfvén profile at the loop apex and the variation in density is gradual. Internal ($r < a$) quantities are denoted by a subscript ‘ i ’ and external ($r > a$) quantities are denoted by a subscript ‘ e ’, so we have internal and external Alfvén profiles of the form

$$v_{Ai}(z) = v_{Ai}(0) \exp(-\alpha_i |z|/L), \quad v_{Ae}(z) = v_{Ae}(0) \exp(-\alpha_e |z|/L). \quad (5.3)$$

In the region $0 < z < L$, the exponential Alfvén profile (5.2) results in equation (5.1) taking the form

$$\frac{d^2 h}{dz^2} + \left(\frac{\omega^2}{v_{A0}^2} \exp(2\alpha_0 z/L) + \lambda_n^2 \right) h = 0. \quad (5.4)$$

We may transform equation (5.4) to a Bessel equation for either purely real or purely imaginary order (depending upon whether $\lambda_n^2 \geq 0$ or $\lambda_n^2 < 0$, respectively) using the change of variable

$$x = \frac{L\omega}{\alpha_0 v_{A0}} \exp(\alpha_0 z/L). \quad (5.5)$$

The result is

$$\frac{d^2h}{dx^2} + \frac{1}{x} \frac{dh}{dx} + \left(1 + \frac{\lambda_n^2 L^2}{\alpha_0^2 x^2}\right) h = 0. \quad (5.6)$$

Equation (5.6) has solutions

$$h(z) = \begin{cases} AJ_{\frac{\lambda_n L}{\alpha_0}}(x) + BY_{\frac{\lambda_n L}{\alpha_0}}(x), & \lambda_n^2 \geq 0 \\ AJ_{i\left|\frac{\lambda_n L}{\alpha_0}\right|}(x) + BY_{i\left|\frac{\lambda_n L}{\alpha_0}\right|}(x), & \lambda_n^2 < 0. \end{cases} \quad (5.7)$$

Notice that these solutions are a linear combination of ordinary Bessel functions; however, their order is generally non-integer and indeed may be purely imaginary (which implies that the Bessel functions are not necessarily real-valued). We are interested in real valued solutions to equation (5.6). Therefore in the case $\lambda_n^2 < 0$ we define two linearly independent real-valued solutions to equation (5.6) as

$$F_{i\nu}(x) = \frac{1}{2} \sec\left(\frac{i\nu\pi}{2}\right) \{J_{i\nu}(x) + J_{-i\nu}(x)\} \quad (5.8)$$

and

$$G_{i\nu}(x) = \frac{1}{2} \operatorname{cosec}\left(\frac{i\nu\pi}{2}\right) \{J_{i\nu}(x) - J_{-i\nu}(x)\}, \quad (5.9)$$

where $\nu = \left|\frac{\lambda_n L}{\alpha_0}\right|$. The functions $F_{i\nu}$ and $G_{i\nu}$ can be used to write down appropriate analytical solutions to equation (5.6) in the case of $\lambda_n^2 < 0$ otherwise the Bessel solutions $J_{\frac{\lambda_n L}{\alpha_0}}$ and $Y_{\frac{\lambda_n L}{\alpha_0}}$ are satisfactory.

Although the ordinary Bessel function has been extensively explored in the case of real orders the properties and methods of calculation of Bessel functions of purely imaginary order are not well known and the use of recurrence relations or integral representations is not straight forward. We find the use of numerical methods to solve the equation directly a more appropriate approach for determining solutions of (5.4). The numerical method is appealing when it is noted that the equilibrium is symmetric about the z axis and so boundary conditions

$$\frac{dh}{dz}(z=0) = 0 \quad \text{or} \quad h(z=0) = 0 \quad (5.10)$$

arise and allow us to separate solutions into even and odd modes, respectively. Also the fact that the equilibrium density and Alfvén profiles are continuous in the z direction.

In the following sections we examine the influence of exponential stratification on the frequency of the trapped modes of oscillation of a line-tied coronal loop for four different cases: (1) both loop and environment homogeneous; (2) a stratified loop and homogeneous environment; (3) a

homogeneous loop and stratified environment; and (4) both loop and environment stratified.

5.2.1 Uniform loop and environment

In the subsequent sections we investigate the effect of longitudinal stratification on the trapped modes of oscillation of a line-tied coronal loop. We consider the influence of external and internal stratification separately and finally combine the effects to produce a more realistic coronal loop model than is currently available. But first it is useful to calculate the modes of oscillation of a uniform loop embedded in a uniform environment. This affords a useful basis for later comparisons.

For a $\beta = 0$ plasma, the modes of oscillation of a uniform loop embedded in a uniform environment are governed by the dispersion relation (see Chapter 2)

$$\frac{1}{\lambda_n^e} \frac{K'_m(\lambda_n^e a)}{K_m(\lambda_n^e a)} = \frac{1}{\lambda_n^i} \frac{J'_m(\lambda_n^i a)}{J_m(\lambda_n^i a)} \quad (5.11)$$

where

$$[\lambda_n^i]^2 = M_n^2 - \frac{\omega^2}{v_{Ai}^2}, \quad [\lambda_n^e]^2 = M_n^2 - \frac{\omega^2}{v_{Ae}^2}; \quad (5.12)$$

for even modes,

$$M_n^2 = \frac{(2n-1)\pi}{2L} \quad n = 1, 2, 3, \dots \quad (5.13)$$

The longitudinal wavenumber M_n is determined by imposing the line-tying condition $\mathbf{v}_\perp(z = \pm L) = 0$. Modes of different longitudinal wavenumbers are denoted by a subscript 'n', with the set or family of modes with one extrema in the z direction corresponding to $n = 1$. Note that since we have written (5.13) for the even modes the $n = 2$ family corresponds to the family with three extrema in the longitudinal direction. In the absence of longitudinal stratification families with different longitudinal wavenumbers are decoupled. The cutoff frequency is different for each family and corresponds to $[\lambda_n^e]^2 = 0$, occurring when

$$\omega = \omega_{cut} = \frac{(2n-1)\pi v_{Ae}}{2L}. \quad (5.14)$$

We will only be concerned with modes lying below the first ($n = 1$) cutoff frequency $\omega = \omega_{cut} = \frac{\pi v_{Ae}}{2L}$ as the introduction of longitudinal structuring results in the tube supporting a superposition of these families and the resulting set of modes has a cutoff frequency corresponding to $[\lambda_1^e]^2 = 0$. Note that in some cases the uniform loop model will support a second family (having 3 extrema in the z direction) with frequencies less than the cutoff frequency of the first family in the range

of $a/L = 0 - 4$ we consider. This will become important in the stratified case as it appears to give an indication of when mode coupling can occur.

Fig. 5.1 shows the dispersion diagram plotting non-dimensional frequency $\omega L/v_{Ai}$ against a/L for a uniform loop and uniform environment, with $v_{Ae} = 2.5v_{Ai}$; the loop is 6.25 times denser than its surroundings. Also plotted in Fig. 5.1 are the dispersion curves for a uniform loop and uniform environment calculated using the numerical code which will be employed later in the stratified loop and environment cases. Here, setting $\rho_i(L)/\rho_i(0) = \rho_e(L)/\rho_e(0) = 1$, provides a test of the code. The black curves are calculated directly via dispersion relation (5.11). The red curves are obtained from the uniform environment stratified loop code, the yellow curves from the stratified environment uniform loop code, and the green curves for the stratified environment and loop code. We see that in all cases there is excellent agreement. We see the dispersion diagram for the first family of modes which have only one extrema in the z direction. We see this diagram is similar to the fast mode band of the coronal case considered by Edwin and Roberts (1983), with the fundamental kink mode the only mode to propagate for all a/L ; all other modes reach the cutoff frequency $\omega_{cut}L/v_{Ai} = \pi v_{Ae}/2v_{Ai}$ (see Chapter 2). We have plotted modes causing even disturbances about the $z = 0$ plane; the odd modes cause odd disturbances about the $z = 0$ plane and have a different cutoff frequency which is twice that of the even modes (in the situation where the environment is uniform), $\omega_{cut}L/v_{Ai} = \pi v_{Ae}/v_{Ai}$. Notice that the cutoff frequency is determined entirely by the loop exterior. Sausage ($m = 0$) and kink ($m = 1$) modes are plotted as dashed and solid lines respectively, and are interlaced. Fluting modes ($m \geq 2$) are also described by the dispersion relation but have not been plotted in Fig. 5.1. All the modes are seen to be highly dispersive. Apart from the fundamental kink mode in the realistic thin tube region of the diagram, $a/L = 10^{-3} - 10^{-1}$ where its frequency is insensitive to the loop ratio a/L .

Fig. 5.2(a) and (b) shows examples of dispersion diagrams where the first and second families appear below the cutoff frequency of the first family. The first family which also appears in Fig. 5.1 has one extremum in the longitudinal direction while the second even family has three extrema in the longitudinal direction, so they represent different longitudinal harmonics. Notice the effect of reducing the internal Alfvén speed compared with the external Alfvén speed results in a decrease in the frequency across all modes of oscillation. The reduction in frequency has now permitted the second family of even modes having three extremum in the longitudinal direction to propagate below the cutoff frequency of the first family. As there is no longitudinal structuring of the loop or the environment each family with different longitudinal wavenumbers are decoupled; this permits the crossing of their dispersion curves. It will be seen later that these actual crossings correspond to avoided crossings.

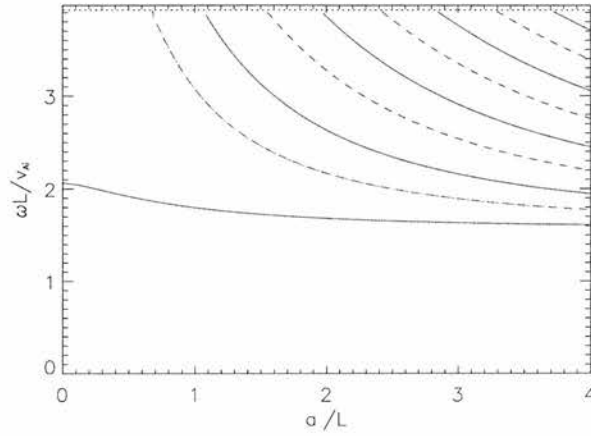


Figure 5.1: Dispersion diagram for a $\beta = 0$ plasma plotting non-dimensional frequency $\omega L/v_{Ai}$ against the non-dimensional loop radius a/L for a uniform loop and uniform environment, with $v_{Ae} = 2.5v_{Ai}$, showing sausage and kink modes as dashed and solid curves respectively. The colours indicate the method by which the curve has been calculated: black curves from dispersion relation (5.11); red curves from the uniform environment stratified loop numerical code; yellow curves from the stratified environment uniform loop code; and green curves for the stratified environment and loop code.

5.2.2 Stratified loop

We may isolate the effect of loop stratification. Previous studies in this area have considered loop profiles using step functions (Díaz et al. 2004) to approximate a coronal region above a dense chromospheric layer with a homogeneous environment. We extend these models by approximating the longitudinal density structure by a continuous exponential profile. We choose the Alfvén speeds at the apex to be related by $v_{Ae}(z = 0) = 2.5v_{Ai}(z = 0)$, leading to the apex of the loop having a density enhancement of 6.25 times its environment, while the density of the loop increases continuously towards the footpoints lying in the photospheric surface. Since we are effectively adding density to the loop compared with the case of a uniform loop and uniform environment considered in Fig. 5.1, we expected that the loop will become a more efficient waveguide and therefore support a greater number of trapped modes with reduced frequencies in a given range of a/L . Previous studies have shown that stratification of the loop results in a modification of the oscillation frequency (Díaz et al. 2004). Since the cutoff frequency depends purely on the stratification of the external medium it remains at $\omega_{cut}L/v_{Ai} = \pi v_{Ae}/2v_{Ai}$; see Figs. 5.1 and 5.2.

In the next sections we consider the effect of environmental stratification, taking $\rho_e(L)/\rho_e(0) = 10$ or 50 and a uniform loop. Finally, we consider stratification of both the loop and its environment in which we choose a uniform photospheric level leading to $\rho_e(L) = \rho_i(L)$. Therefore in the current section, while considering only a stratified loop, we choose $\rho_i(L)/\rho_i(0)$ to correspond to

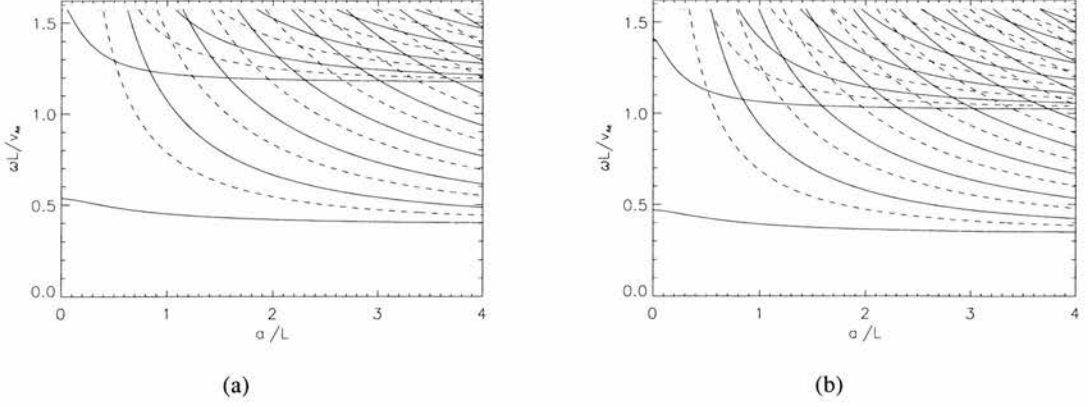


Figure 5.2: Dispersion diagram plotting non-dimensional frequency $\omega L/v_{Ae}$ (note that this is v_{Ae} and not v_{Ai}) against the non-dimensional loop radius a/L for a uniform loop and a uniform environment with (a) $v_{Ae} = 4.03v_{Ai}$ and (b) $v_{Ae} = 4.62v_{Ai}$. Sausage modes are shown as dashed curves, kink modes as solid curves.

current section, while considering only a stratified loop, we choose $\rho_i(L)/\rho_i(0)$ to correspond to the values of $\rho_e(L)/\rho_e(0) = 10$ or 50 which will be used later; we calculate these values by the $\beta = 0$ relation

$$\frac{\rho_i(L)}{\rho_i(0)} = \left(\frac{v_{Ai}(0)}{v_{Ae}(0)} \right)^2 \frac{\rho_e(L)}{\rho_e(0)}. \quad (5.15)$$

Fig. 5.4(a) shows the dispersion diagram for the case $\rho_i(L)/\rho_i(0) = 1.6$ (which will correspond to an environmental stratification of $\rho_e(L)/\rho_e(0) = 10$ in later sections), plotting the non-dimensional frequency against a/L and showing sausage and kink modes as dashed and solid lines respectively. The diagram is similar in structure to that of Edwin and Roberts (1983) with only the fundamental kink mode propagating for all values of a/L and all other modes reaching the cutoff frequency where these modes become leaky. All modes are highly dispersive and sausage and kink modes are distributed alternately; in the thin tube limit the frequency of the fundamental kink mode is insensitive to a/L . Fig. 5.4(b) shows the same dispersion diagram as Fig. 5.4(a) but with addition that the curves for the case shown in Fig. 5.1, for uniform loop and environment, are plotted (the dot dash lines are the kink curves and the triple dot dash lines are the sausage modes). As expected, we see the internal stratification has resulted in a modification to the frequency of each mode. This is illustrated by the modification of the kink mode from $\omega L/v_{Ai} = 2.1$ in the uniform case to $\omega L/v_{Ai} = 1.9$ as a result of the stratification. However the modification of the frequency appears to be a uniform scaling of the dispersion curves as seen in Fig. 5.3(a), where the dispersion curves of a uniform loop embedded in a uniform environment with $v_{Ae} = 2.5v_{Ai}$ and the dispersion curves of a stratified loop embedded in a uniform environment have been overlaid for $\rho_i(L)/\rho_i(0) = 1.6$.

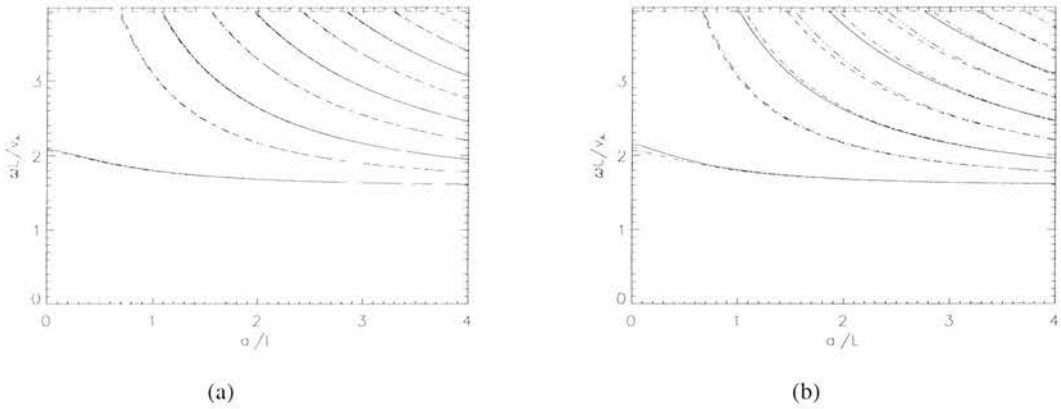


Figure 5.3: Dispersion diagram plotting $\omega L/v_{Ai}$ against a/L for a uniform loop embedded in a uniform environment with $v_{Ae} = 2.5v_{Ai}$. In each plot a uniform scaling of the dispersion curves of a stratified loop embedded in a uniform environment have been overlaid for: (a) $\rho_i(L)/\rho_i(0) = 1.6$ and (b) $\rho_i(L)/\rho_i(0) = 8$.

We also consider a density stratification of $\rho_i(L)/\rho_i(0) = 8$ which corresponds to the case of $\rho_e(L)/\rho_e(0) = 50$. It should be noted that a density stratification of 8 over the length of the loop is very modest but it nonetheless proves instructive and provides a useful illustration. Fig. 5.5(a) shows the dispersion diagram for this case. It can be seen that the structure of the dispersion diagram has been significantly altered, with many more modes now propagating in a given range of a/L . Not only the fundamental kink mode but also its first harmonic now propagate as trapped modes for all a/L ; the frequency of the fundamental mode has retained its insensitivity to a/L in the thin tube limit but the first harmonic does not share this property; all other modes reach the cutoff frequency. The structure of one sausage mode lying between consecutive kink modes has now been broken as a result of many mode interactions at avoided crossings (the spatial structure across an avoided crossing will be discussed later) between like curves. Also, the presence of avoided crossings seems to allow sausage and kink modes to cross, and so having the same frequency for a particular loop dimension.

Fig. 5.5(b) shows the same dispersion diagram as Fig. 5.5(a) together with and curves from the uniform loop and uniform environment which have been over-plotted. Although this diagram appears very complicated we can see that the frequency of all the modes have been significantly altered. This is most notable from the kink speed of $\omega L/v_{Ai} = 2.1$ in the uniform case but takes a value of $\omega L/v_{Ai} = 1.6$ once a stratification of $\rho_i(L)/\rho_i(0) = 1.6$ has been introduced. The dispersion diagram (Fig. 5.5) is again seem to be a uniform scaling (seen in fig.5.3(b)) of the homogeneous loop and environment case with $v_{Ae} = 2.5v_{Ai}$.

Fig. 5.6(a) shows part of the dispersion diagram of Fig. 5.5(a), but here focusing on the avoided crossings between the first and third kink harmonics. Also shown in Fig. 5.6(b)-5.6(d) are cuts

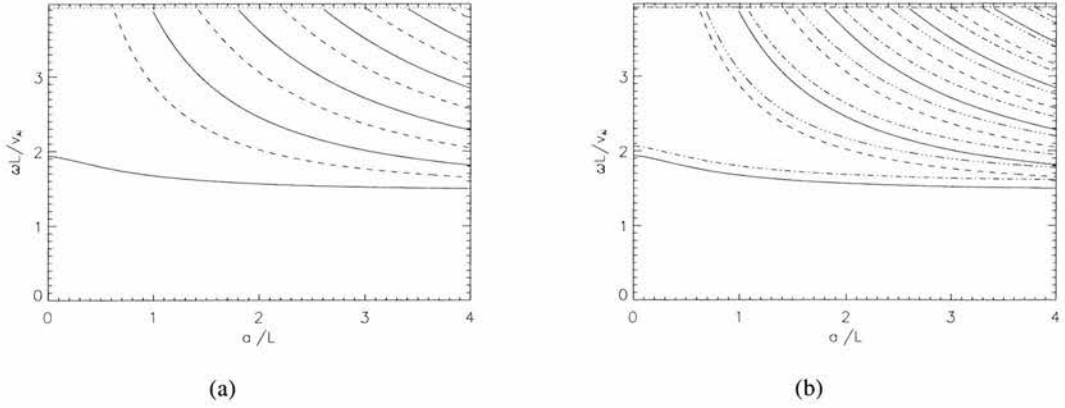


Figure 5.4: Dispersion diagram plotting non-dimensional frequency $\omega L/v_{Ai}$ against the non-dimensional loop radius a/L for (a) an exponentially stratified loop with $\rho_i(L)/\rho_i(0) = 10v_{Ai}^2(z=0)/v_{Ae}^2(z=0)$ and homogeneous environment $v_{Ae}(z=0) = 2.5v_{Ai}(z=0)$. (b) as in (a) but with the dispersion curves for a uniform loop and environment (with $v_{Ae} = 2.5v_{Ai}$) added.

of the non-dimensional total pressure as a function of z/L at $r/a = 0.85$ (inside the loop), for the three points marked along each dispersion curve. The solid and dashed lines correspond to the lower and upper dispersion curves respectively. We can see that there are two types of mode in this model; those modes which take their largest amplitude in P_T at the apex and those which have their largest amplitude nearer the footpoints. This amplitude effect changes as we move through the avoided crossing, the property being exchanged between this interacting modes.

It is clear from Fig. 5.5(b) that the uniform loop does not produce a good approximation to the stratified loop even for moderate levels of stratification ($\rho_i(L)/\rho_i(0) = 8$) for this density profile. Thus, to determine the loop parameters at either the footpoints or apex (as in Fig. 5.5(b)) and use these values in a uniform loop approximation will not produce good agreement with the stratified loop. Therefore, to make this uniform loop approximation taking the uniform value to be that of the footpoint or apex of an observed coronal loop and carry out coronal seismology based on these assumptions will produce significant errors if the actual coronal loop has density profile of the form taken here. To improve this situation we compare a stratified loop and a uniform loop containing the same integrated density, leaving the environment unchanged. Fig. 5.7(a) shows the dispersion diagram for Alfvén speeds at the apex related by $v_{Ae}(z=0) = 2.5v_{Ai}(z=0)$ and $\rho_i(L)/\rho_i(0) = 1.6$. In the previous comparison between a loop having a stratification of $\rho_i(L)/\rho_i(0) = 8$ and considering a uniform loop, chosen to match the stratified loop at the apex, there was poor agreement (see Fig. 5.5(b)). Now comparing a stratified loop with a uniform loop chosen so that the mass contained in both loops are equal shows a significantly improved agreement. This improvement is illustrated by examining the modification of the kink mode from a value of $\omega L/v_{Ae} = 0.53$ without stratification to $\omega L/v_{Ae} = 0.59$ with stratification.

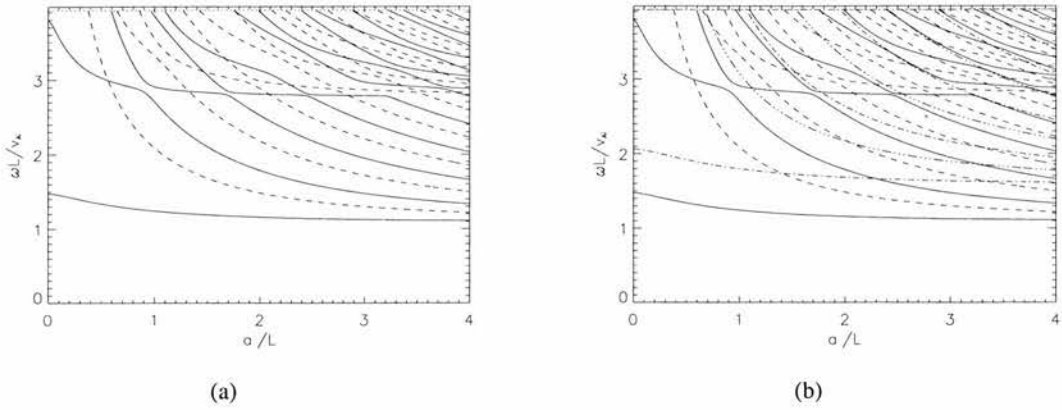


Figure 5.5: Dispersion diagram plotting non-dimensional frequency $\omega L/v_{Ai}$ against the non-dimensional loop radius a/L for (a) an exponentially stratified loop with $\rho_i(L)/\rho_i(0) = 8$ and a homogeneous environment with $v_{Ae}(z) = 2.5v_{Ai}(z = 0)$; (b) as in plot (a) but with the dispersion curves for the uniform loop and environment (for $v_{Ae} = 2.5v_{Ai}$) overlaid.

Another interesting point is how the actual crossings of the dispersion curves of the uniform loop correspond to the avoided crossings in the stratified case. This suggests that for avoided crossings to occur in the stratified loop the loop must have a large enough density enhancement so that a uniform loop of equivalent mass supports more than just the first family of modes below the cutoff frequency of the first family. As the oscillatory modes of a stratified loop are a superposition of all families of the uniform loop, one family will generally be dominant; but at an avoided crossing the dominant family is changed, resulting in a change in spatial structure of the mode.

In conclusion the uniform loop is a reasonable approximation to the stratified loop provided an appropriate density is used. However, if loop parameters are determined from one point on the loop, especially an extreme point such as the apex or the footpoint, and the rest of the loop is assumed to be the same value, this will give a poor approximation since some sort of averaging is necessary. If a higher accuracy is required, then the stratified model should be employed rather than the uniform model, if the model is to capture all features such as modified frequencies and spatial structure of the eigenfunctions and also interactions between modes at avoided crossings.

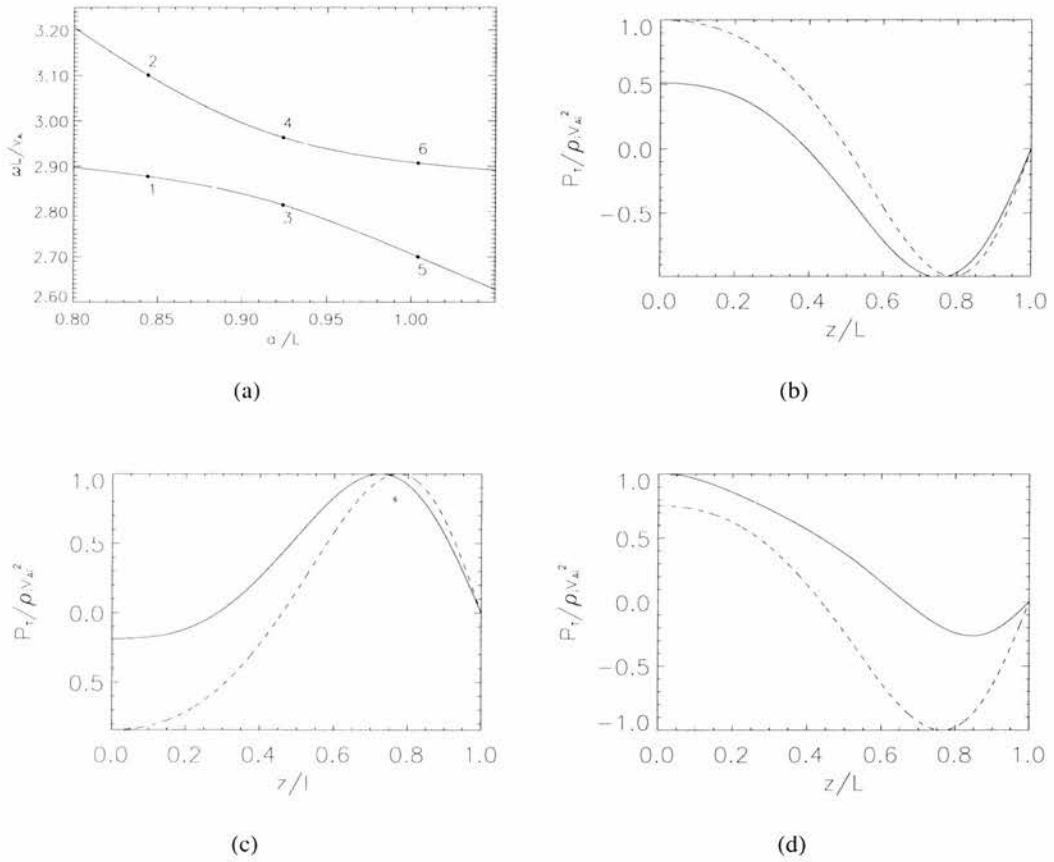


Figure 5.6: (a) Dispersion diagram plotting $\omega L/v_{Ai}$ against a/L for an exponentially stratified loop and homogeneous environment satisfying $\frac{\rho_i(L)}{\rho_i(0)} = 8$ and $v_{Ae}(z=0) = 2.5v_{Ai}(z=0)$. (b), (c) and (d) show the non-dimensional total pressure perturbation as a function of z/L at a value of $r/a = 0.85$. In plot (b) the solid and dashed line corresponds to the points marked 1 and 2 in (a) respectively. In plot (c) the dashed and solid lines corresponds to points 3 and 4 in (a) respectively, and in plot (d) the dashed and solid line corresponds to points 5 and 6 in (a) respectively.

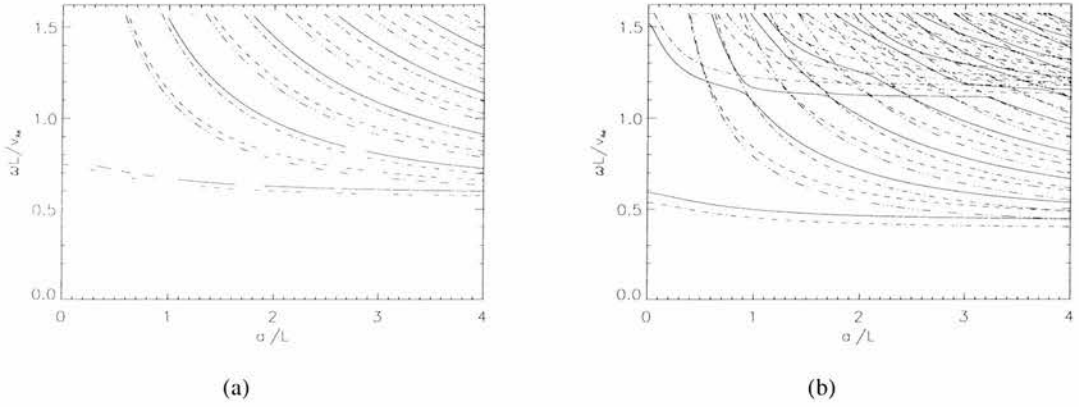


Figure 5.7: Dispersion diagram plotting non-dimensional frequency $\omega L/v_{Ae}$ against the non-dimensional loop radius a/L for an exponentially stratified loop and homogeneous environment and the dispersion curves of uniform loop containing the same mass as the stratified loop are overlaid. In (a) stratified loop with $v_{Ae}(z=0) = 2.5v_{Ai}(z=0)$ and $\rho_i(L)/\rho_i(0) = 1.6$ and uniform loop with $v_{Ae} = 4.03v_{Ai}$ is displayed; and in (b) stratified loop with $v_{Ae}(z=0) = 2.5v_{Ai}(z=0)$ and $\rho_i(L)/\rho_i(0) = 8$ and uniform loop with $v_{Ae} = 4.62v_{Ai}$ is displayed.

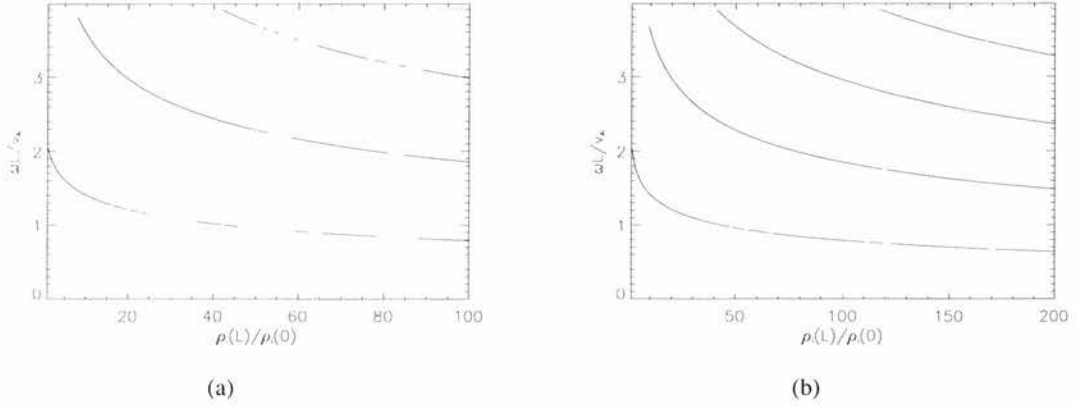
5.2.3 Changing $\rho_i(L)/\rho_i(0)$ 

Figure 5.8: Dispersion diagram plotting non-dimensional frequency $\omega L/v_{Ai}(0)$ against the internal density stratification $\rho_i(L)/\rho_i(0)$ for $v_{Ae}(z=0) = 2.5v_{Ai}(z=0)$ and a loop radius of $a/L = 0.001$. Case (a) is for an internal density stratification in the range $\rho_i(L)/\rho_i(0) = 1 - 100$, and (b) shows the range $\rho_i(L)/\rho_i(0) = 1 - 200$. Note that the second harmonic does not reach $\rho_i(L)/\rho_i(0) = 1$ or the cutoff frequency but this is as a result of a failure in the numerical method, the curve should reach either $\rho_i(L)/\rho_i(0) = 1$ or the cutoff frequency.

The final aspect of the internal stratification to be investigated is the dependence of the oscillation frequency on the strength of the stratification. This is displayed in Fig. 5.8, showing dispersion diagrams of the non-dimensional frequency as a function of $\rho_i(L)/\rho_i(0)$ for a thin tube, $a/L = 0.001$, which is in line with the value used by Nakariakov et al. (1999). We can see in the uniform loop case, $\rho_i(L)/\rho_i(0) = 1$, that in the thin tube limit only the fundamental kink mode propagates as a trapped mode. For moderate levels of stratification ($\rho_i(L)/\rho_i(0) = 1 - 20$) it is seen that the frequency of the fundamental kink mode is strongly dependent on the density stratification, causing the frequency to decrease rapidly, but this decrease becomes slower as $\rho_i(L)/\rho_i(0)$ becomes large and there is not show a strong dependence on this parameter in the realistic range of $\rho_i(L)/\rho_i(0) = 100 - 200$.

Since the addition of density to the loop results in a reduction in oscillation frequency eventually many of the kink harmonics as well as the fundamental will propagate as trapped modes in the thin tube limit. As seen in Fig. 5.8(b), at a value of $\rho_i(L)/\rho_i(0) = 200$ four kink modes are seen to propagate below the cutoff in this case of a thin tube. However, this is not the case for the sausage mode which is never found to propagate as a trapped mode in the thin tube limit; this feature is common across all models (see also chapters 2 and 3). Since the environment remains unchanged while the loop structure is varied, so the cutoff frequency is uniform and takes the same value as for all other cases in this section: $\omega_{cut}L/v_{Ai} = \pi v_{Ae}/2v_{Ai}$.

5.2.4 Stratified environment

In order to isolate the effect of stratification in the environment of a coronal loop we consider an exponentially stratified environment surrounding a homogeneous loop. In this case the density of the environment increases towards the chromospheric-photospheric base and so can become denser than the loop. As the overall density of the environment has increased relative to the loop, the loop becomes a less efficient waveguide supporting fewer trapped modes. As previously noted, environmental stratification will modify the cutoff frequency (see Chapter 3) of the trapped modes, with additional density causing a reduction in the cutoff frequency, and so leakage will be enhanced.

In some cases we will consider a variation in density from the loop apex $z = 0$ in the corona to the footpoint $z = L$ with $\rho_e(L)/\rho_e(0) = 100$. However, in this case we find no trapped modes with such strong stratification so we will look at smaller density variations of $\rho_e(L)/\rho_e(0) = 10$ and $\rho_e(L)/\rho_e(0) = 50$, where trapped modes are still present for the range $a/L \leq 4$. Fig. 5.9(a) shows the dispersion diagram for a homogeneous loop in a stratified environment with $\rho_e(L)/\rho_e(0) = 10$, giving the non-dimensional frequency $\omega L/v_{Ai}$ as a function of a/L . Sausage ($m = 0$) and kink ($m = 1$) modes are plotted as solid and dashed curves, respectively. The cutoff curve is plotted with a dotted line. The diagram shows similarities with that of the uniform loop in a uniform environment, with the fundamental kink mode being the only mode to propagate for all a/L ; all other modes reach a uniform cutoff frequency beyond which the modes become leaky. The kink and sausage modes are interspersed with one sausage mode between consecutive kink modes. All modes have a dispersive nature so their frequency is strongly dependent on the loop radius or length. However, in the realistic thin tube region ($a/L = 10^{-3} - 10^{-1}$), only the fundamental kink mode propagates and then $\omega L/v_{Ai}$ is insensitive to the loop radius. Fig. 5.9(b) shows the same dispersion curves as Fig. 5.9(a) but with the dispersion curves for the uniform environment, $v_{Ae}(z) = v_{Ae}(0)$, over plotted; this allows us to see directly the effect of the stratified environment. The first point to note is that there is a significant reduction in the cutoff frequency from $\omega_{cut}L/v_{Ai} \approx 3.9$ for a uniform environment to $\omega_{cut}L/v_{Ai} \approx 2.6$ for the case with exponential environment stratification of $\rho_e(L)/\rho_e(0) = 10$. As a result of the reduced cutoff frequency, the value of a/L for which modes become leaky is increased. Another interesting point is that the modification to the frequency in the range where both sets of modes are trapped is relatively small, especially for larger values of a/L . Notice also that the stratification has resulted in a reduction in the dispersive effect of a/L when compared with the uniform environment.

We also examine the case of $\rho_e(L)/\rho_e(0) = 50$ which helps to point out the general trend as we move towards more realistic density ratios. Fig. 5.10(a) and (b) are equivalent to Fig. 5.9(a) and (b) but for $\rho_e(L)/\rho_e(0) = 50$. From Fig. 5.10(a) we see only the fundamental kink and first sausage mode propagate as trapped modes in the range $a/L \leq 4$, which shows the loop has

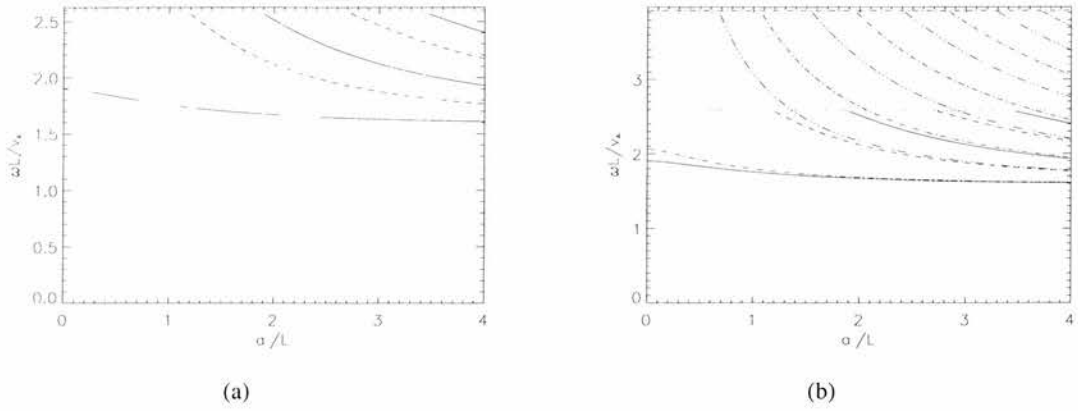


Figure 5.9: Dispersion diagram plotting non-dimensional frequency $\omega L/v_{Ai}$ against the non-dimensional loop radius a/L for (a) an exponentially stratified environment and homogeneous loop with $v_{Ae}(z = 0) = 2.5v_{Ai}(z = 0)$ and $\frac{\rho_e(L)}{\rho_e(0)} = 10$. (b) as in (a) but also here the dispersion curves for a uniform loop in a uniform environment, with $v_{Ae} = 2.5v_{Ai}$.

become a less efficient waveguide. Also the dispersive effect of a/L has been drastically reduced, even compared with the case of $\rho_e(L)/\rho_e(0) = 10$. Fig. 5.10(b) shows the difference between the stratified case $\rho_e(L)/\rho_e(0) = 50$ and the uniform case $\rho_e(L)/\rho_e(0) = 1$. The cutoff curve has been reduced from the value of $\omega_{cut}L/v_{Ai} = \pi v_{Ae}/v_{Ai} = 3.9$ for the uniform environment to a value of $\omega_{cut}L/v_{Ai} = 1.7$ for a stratification of $\rho_e(L)/\rho_e(0) = 50$ so there is now only a small overlap region where trapped modes of the uniform and stratified environments both propagate. However, in this small overlap region the frequencies of both sets of modes are very similar, especially in the short loop limit ($a/L \rightarrow \infty$).

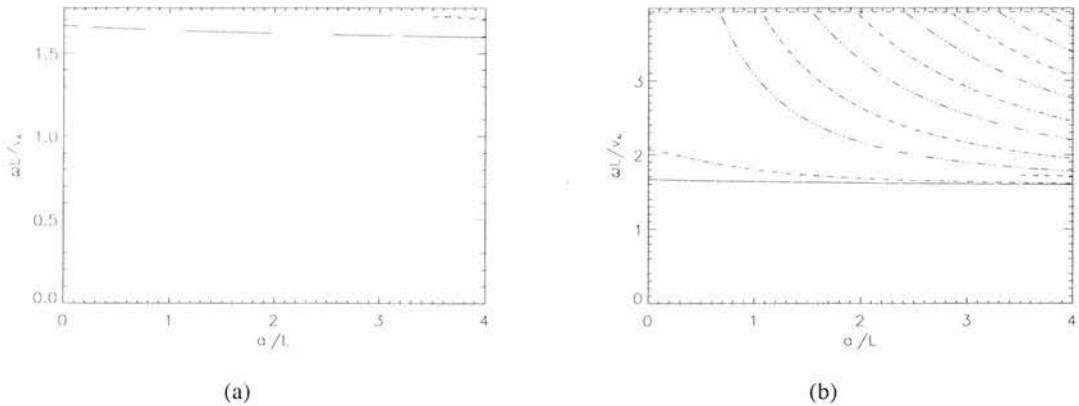


Figure 5.10: Dispersion diagram plotting $\omega L/v_{Ai}$ against a/L for (a) an exponentially stratified environment and homogeneous loop with $v_{Ae}(z = 0) = 2.5v_{Ai}(z = 0)$ and $\frac{\rho_e(L)}{\rho_e(0)} = 50$. (b) as in plot (a) but the dispersion curves of a uniform loop and uniform environment with $v_{Ae} = 2.5v_{Ai}$ are overlaid.

Again it is of interest to compare these cases for a stratified environment with the case of a uniform environment, taking the integrated densities for the stratified and uniform cases to be equal. Fig. 5.11(a) shows the dispersion curves for $\rho_e(L)/\rho_e(0) = 10$ and the equivalent uniform values of $v_{Ae} = 1.48v_{Ai}$. We can see a significantly improved approximation of the cutoff frequency and a slight improvement in the approximation of the frequency compared with the cases considered in Fig. 5.9(b) and Fig. 5.10(b), where the uniform and stratified environments are matched at the apex. However, in the more strongly stratified case $\rho_e(L)/\rho_e(0) = 50$, plotted in Fig. 5.11(b) together with the equivalent uniform case, we see the cutoff frequencies are almost identical and there in very good agreement in frequency for this case.

Therefore, we conclude that environmental stratification results in a small modification to the oscillation frequency and a reduction in the dispersive nature of the modes. The most significant alteration to the modes caused by environmental stratification occurs in the cutoff frequency: adding density results in a reduction in the cutoff frequency and so leakage is enhanced. Again, making comparisons with the uniform case shows that matching the densities of the two cases at a single point does not produce close agreement whereas matching the integrated densities does so. It should be noted density stratifications of $\rho_e(L)/\rho_e(0) = 10$ or 50 are modest compared with a more realistic value of $\rho_e(L)/\rho_e(0) = 100$, but we do not find any trapped modes for the realistic stratification and the loop parameters we consider.

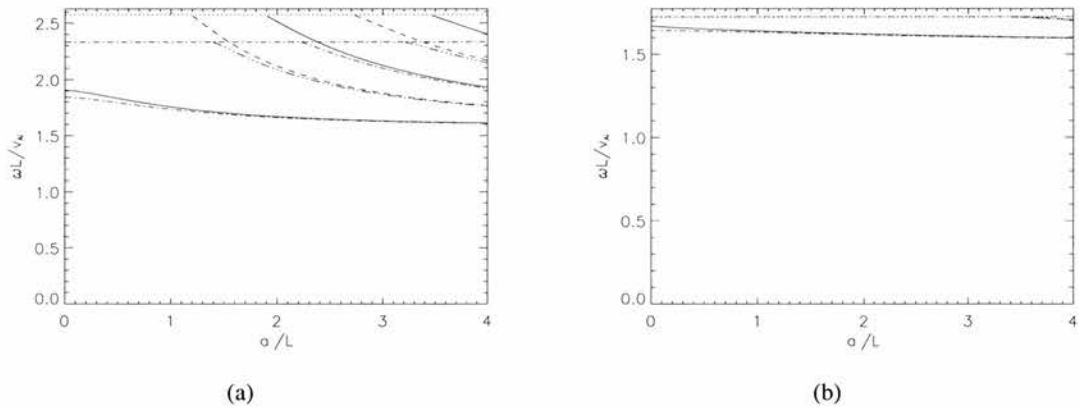


Figure 5.11: Dispersion diagram plotting $\omega L/v_{Ai}$ against the a/L for an exponentially stratified environment and also the dispersion curves of a uniform loop and environment which matches the mass contained in the stratified case. (a) Stratified environment with $\frac{\rho_e(L)}{\rho_e(0)} = 10$ and $v_{Ae}(z=0) = 2.5v_{Ai}(z=0)$ and a uniform loop and environment with $v_{Ae} = 1.48v_{Ai}$; (b) stratified environment with $\frac{\rho_e(L)}{\rho_e(0)} = 50$ and $v_{Ae}(z=0) = 2.5v_{Ai}(z=0)$ and a uniform loop and environment with $v_{Ae} = 1.09v_{Ai}$.

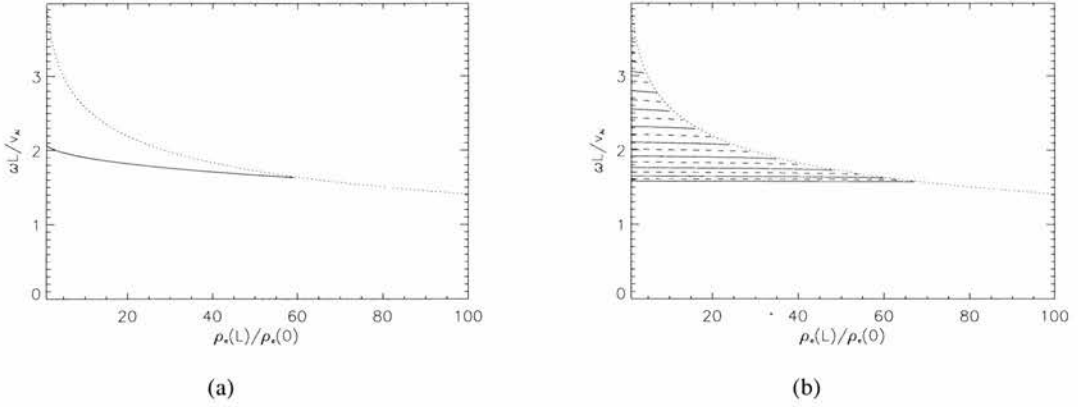
5.2.5 Changing $\rho_e(L)/\rho_e(0)$ 

Figure 5.12: Dispersion diagram plotting $\omega L/v_{Ai}(0)$ against the external density stratification $\rho_e(L)/\rho_e(0)$, for $v_{Ae}(0) = 2.5v_{Ai}(0)$ and a loop radius of (a) $a/L = 0.001$ and (b) $a/L = 10.0$.

As in the stratified loop case, we now consider the influence of varying the level of stratification in the environment to examine the effect on the oscillation frequency and also the cutoff frequency. We can see these effects in Fig. 5.12(a) and (b), showing dispersion diagrams for the non-dimensional frequency against external stratification $\rho_e(L)/\rho_e(0)$ for thin ($a/L = 0.001$) and fat ($a/L = 10.0$) tubes respectively.

As previously noted, the external stratification has little influence on the oscillation frequency in the thin tube case, as seen in Fig. 5.12(a). In the fat tube case shown in Fig. 5.12(b), we see many more kink and sausage modes trapped by the tube but their frequencies vary little with respect to the external stratification.

The main impact of the external stratification is on the cutoff frequency (see Chapter 3), in that the addition of density to the environment in comparison with the loop results in a reduction in the cutoff frequency as the loop becomes a less efficient wave guide. In Fig. 5.12(a) and (b) we can see a significant reduction in cutoff frequency from a value of $\omega_{cut}L/v_{Ai} = 3.9$ in the uniform case to a value of $\omega_{cut}L/v_{Ai} = 1.4$ for a stratification of $\rho_e(L)/\rho_e(0) = 100$. Notice the most rapid reduction in cutoff frequency occurs as low levels of stratification are introduced, $\rho_e(L)/\rho_e(0) = 1 - 10$, and the gradient becomes shallower as $\rho_e(L)/\rho_e(0)$ becomes larger. Another feature of the cutoff frequency is that it is independent of the loop radius; this can be seen in Fig. 5.12(a) for a thin tube and (b) for a fat tube, where the cutoff curves are identical. As a result of the reduction in the cutoff frequency, modes that have previously been considered to propagate as a trapped mode, such as the fundamental kink mode in the thin tube limit, are now seen to reach the cutoff frequency and become leaky. Also in thicker loops, where many sausage and kink modes are expected to propagate as trapped modes, for large enough environmental

stratification (say $\rho_e(L)/\rho_e(0) \geq 70$) all modes become leaky.

5.2.6 Stratification in both loop and environment

Having seen separately the effects of stratification in the loop or in the environment, we now come to the point where we combine the effects of stratification both inside and outside the loop, thus producing a more realistic model for a coronal loop. We have seen earlier that the main influence of the internal stratification is to modify the oscillation frequency and the main influence of the external stratification is in production of a modification in the cutoff frequency. We consider a realistic density ratio in the environment of $\rho_e(L)/\rho_e(0) = 100$ between the coronal and chromospheric-photospheric levels, and assume the photosphere to be uniform so that $\rho_e(L) = \rho_i(L)$. Although this may not always be accurate, we do not expect significant changes to the results due to variations in density in the lower atmosphere, especially since the perturbations fall to zero at the footpoints to satisfy the line tying condition. Hence, choosing the density stratification by the relation (5.15) and again choosing $v_{Ae}(0) = 2.5v_{Ai}(0)$ results in $\frac{\rho_i(L)}{\rho_i(0)} = 16$.

The dispersion diagram shown in Fig. 5.13(a) for this case is very similar in structure and appearance to the uniform loop and uniform environment, as we see only the fundamental kink mode propagating for all a/L and other modes reach the cutoff frequency. Also kink and sausage modes are again distributed alternately and there are no avoided crossings present. The most interesting aspects are seen most clearly when we make direct comparison between this case and the homogeneous loop and environment, where we have simply matched the densities at the loop apex; see Fig. 5.13(b). We see immediately that the fast mode bands for these two different coronal loop structures do not overlap. The stratification of the corona has reduced the cutoff frequency to a dimensionless value of 1.4 (also see Fig. 5.12(a)), which is below the lower limit of the frequency for the uniform loop and environment. Also the value of a/L for which modes reach the cutoff frequency has increased as a result of the reduction in the cutoff frequency. Previously, when we implemented such a large environmental stratification around a uniform loop, we found that the loop did not support any trapped modes. However, as noted earlier, the introduction of internal stratification results in a modification to the oscillation frequency and in this case the loop again supports many trapped modes.

In Fig. 5.14 we compare the stratified case with a uniform loop and environment, where we have chosen the parameters such that the integrated densities of the stratified and uniform cases in appropriate regions are equal. We see in Fig. 5.14 that the oscillatory frequency is increased by the introduction of stratification compared with the uniform case. However, stratification reduces dispersion compared with the uniform case with respect to a/L . Finally, as a result of the external stratification the cutoff frequency is reduced to a value of $\omega_{cut}L/v_{Ai} = 2.6$ to be compared with the cutoff frequency for the uniform case of $\omega_{cut}L/v_{Ai} = 2.8$.

Therefore we conclude exponential stratification of the form (5.2) is an important factor for the cutoff frequency but more importantly for the oscillation frequency and period of the modes. If a loop of uniform interior and exterior is to be used to approximate a stratified structure, it is important that the parameters chosen for the uniform case reflect the overall structure along the loop rather than simply matching the densities at a single point (such as the apex or the footpoint). In fact the apex or the footpoints are the worst points to choose for a comparison since they are most extreme in the model. A more effective method of representing the stratified case by a uniform case is to match the total integrated densities in each of the appropriate regions.

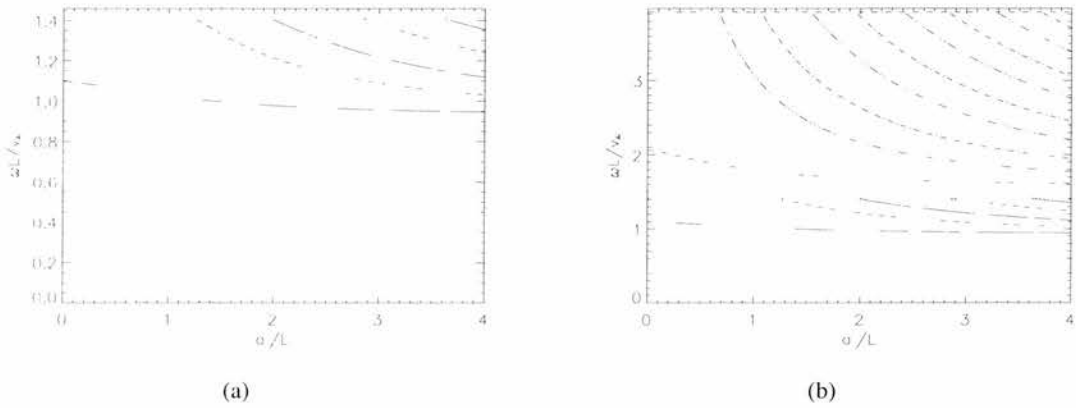
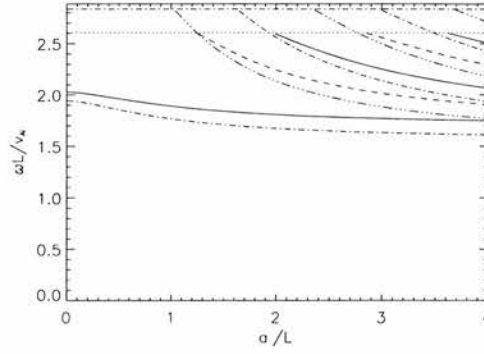


Figure 5.13: Dispersion diagram plotting $\omega L/v_{Ai}$ against the a/L for (a) an exponentially stratified loop and environment with $v_{Ae}(z=0) = 2.5v_{Ai}(z=0)$, $v_{Ae}(z=L) = v_{Ai}(z=L)$ and $\rho_e(L)/\rho_e(0) = 100$; (b) the same as in plot (a) but with the dispersion curves for the uniform loop and uniform environment, with $v_{Ae} = 2.5v_{Ai}$, overlaid.

5.3 Varying the magnitude of stratification

Here we consider the case of stratification in both loop and environment and we allow the external density stratification to vary, but retain the assumption that the photospheric surface ($z = \pm L$) is uniform (so $\rho_e(L) = \rho_i(L)$). The internal stratification is modified appropriately. For this case the loop always has a density enhancement over its environment.

Fig. 5.15(a) and (b) show the dispersion diagrams plotting non-dimensional frequency against $\rho_e(L)/\rho_e(0)$ for $a/L = 0.001$ and $a/L = 10.0$ respectively. In both diagrams the cutoff curve is identical to that of Fig. 5.12, since it is independent of the internal structure and loop radius. We can see that in both cases modes remain trapped for a larger range of density stratification compared with the case displayed in Fig. 5.12(a) and (b). This is due to the modification of the oscillation frequency as a result of the internal loop structure, where we can see the fundamental kink mode remains trapped for all values of stratification shown in Fig. 5.15(a) for the thin



(a)

Figure 5.14: Dispersion diagram plotting $\omega L/v_{Ai}$ against a/L for an exponentially stratified loop and environment with $v_{Ae}(z=0) = 2.5v_{Ai}(z=0)$, $v_{Ae}(z=L) = v_{Ai}(z=L)$ and $\frac{\rho_e(L)}{\rho_e(0)} = 100$. Overlaid are the dispersion curves for the uniform loop and environment which have same mass inside and outside the loop as in the stratified case. For the uniform case, $v_{Ae} = 1.80v_{Ai}$. The normalisation for both sets of curves is made against the internal Alfvén speed for the uniform loop.

tube limit. Therefore in this case the effect of internal stratification in modifying the oscillatory frequency is greater than the effect of the external stratification in reducing the cutoff frequency.

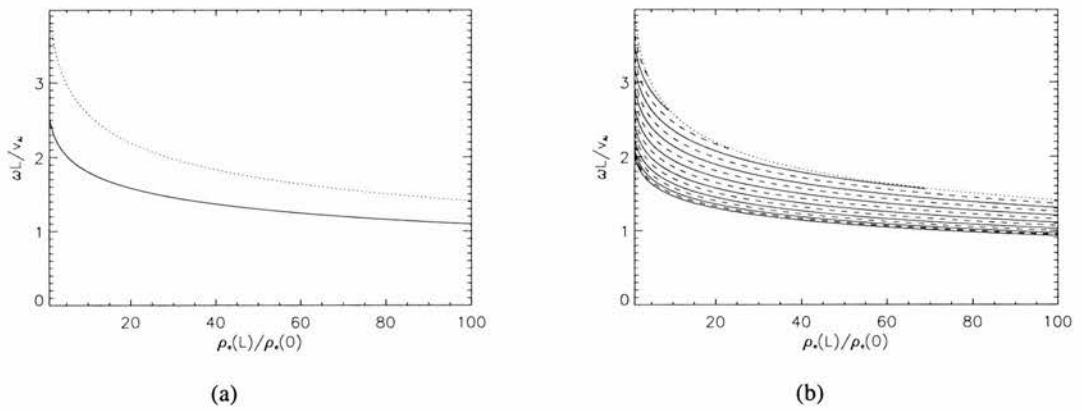


Figure 5.15: Dispersion diagram plotting $\omega L/v_{Ai}$ against density stratification $\rho_e(L)/\rho_e(0)$ for $v_{Ae}(z=0) = 2.5v_{Ai}(z=0)$ and a uniform photosphere $\rho_e(L) = \rho_i(L)$, for (a) $a/L = 0.001$ and (b) $a/L = 10.0$.

5.4 Case 2: the exponentially stratified chromosphere

In the previous case we took a step forward in that the density stratification of the loop is continuous, whereas in Chapter 3 step functions were used to represent the density profile changing from the coronal to photospheric material. However, our use of an exponential density profile poorly represents the rapid change from the corona to the photosphere over the depth of the chromosphere. The final profile we consider attempts to represent this feature while still using a continuous profile. We consider a uniform coronal region but allow an exponential density profile in the chromospheric layers near the footpoints. The chromospheric layer has thickness of $L - W$ (see Chapters 3 and 4). Thus, the profile of the Alfvén speed is

$$v_A(z) = \begin{cases} v_{A0} \exp(\alpha(z + W)/L), & -L < z < -W \\ v_{A0}, & -W < z < W \\ v_{A0} \exp(-\alpha(z - W)/L), & W < z < L. \end{cases} \quad (5.16)$$

As an example for the case of $W/L = 0.8$ stratifications of $\rho(L)/\rho(0) = 16$ and $\rho(L)/\rho(0) = 100$ have corresponding values of $\alpha = 6.93$ and $\alpha = 11.51$ respectively.

5.4.1 Stratified loop

Now we have a third parameter in the model, this being the extent ($L - W$) of the chromospheric layer. But before examining this new parameter we first investigate the importance of loop radius for a stratified loop within a uniform environment.

5.4.2 Changing a

We consider a density profile inside the loop of the form (5.16), with $\frac{\rho_i(L)}{\rho_i(0)} = 16$ and $W/L = 0.8$, and assume a uniform environment. Therefore we expect to see a modification in the oscillation frequency but not the cutoff frequency. The dispersion diagram for this case is plotted in Fig. 5.16(a) with the dispersion curves of the uniform case also plotted in Fig. 5.16(b). We have chosen the Alfvén speeds for the uniform case to match that of the stratified loop at the apex, and the environment regions are identical. We see that the introduction of stratification across the chromospheric region has resulted in a slight correction to the frequency of the uniform loop. Hence the use of a uniform loop, such as that in Edwin and Roberts (1983), will produce a reasonably accurate representation of a coronal loop for seismology, provided the loop apex is considered rather than the footpoint where the parameters are very different.

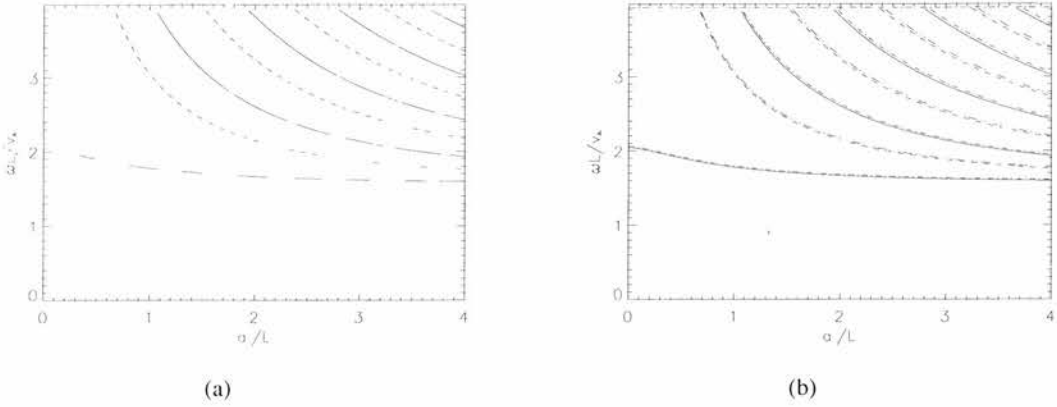


Figure 5.16: (a) Dispersion diagram plotting $\omega L/v_{Ai}$ against a/L for an exponentially stratified loop and homogeneous environment, with $v_{Ae}(z = 0) = 2.5v_{Ai}(z = 0)$ and $\frac{\rho_i(L)}{\rho_i(0)} = 16$; (b) as in plot (a) but with the dispersion curves for the uniform loop and uniform environment overlaid, with $v_{Ae} = 2.5v_{Ai}$.

5.4.3 Changing W

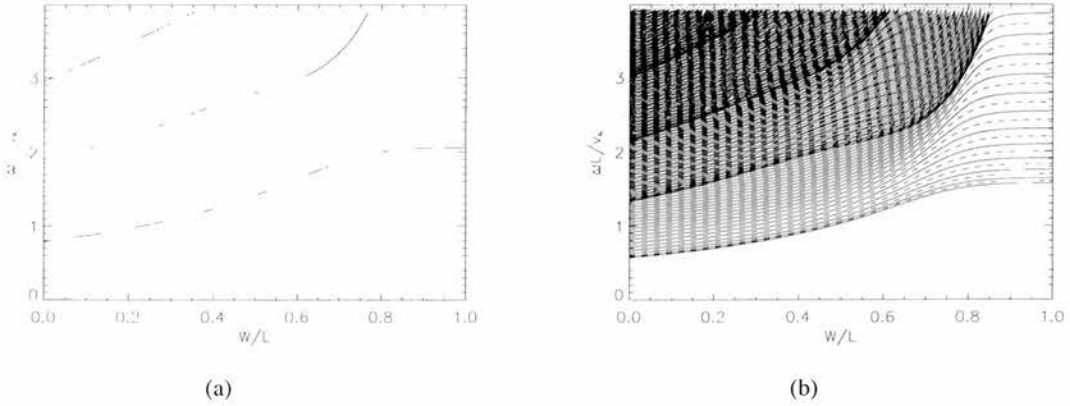


Figure 5.17: Dispersion diagram plotting $\omega L/v_{Ai}$ against the fractional coronal depth W/L for (a) a loop radius $a/L = 0.001$, and (b) a loop radius $a/L = 10.0$. Here $v_{Ae}(0) = 2.5v_{Ai}(0)$ and $\frac{\rho_i(L)}{\rho_i(0)} = 16$.

We consider the impact of varying the chromospheric depth ($L - W$) while holding the internal density ratio fixed at $\rho_i(L)/\rho_i(0) = 16$. Fig. 5.17(a) and (b) show dispersion diagrams of non-dimensional frequency against W/L for $a/L = 0.001$ and $a/L = 10.0$. In determining some sections of this diagram, the number of terms in the sum is not large enough so only the first ten or fifteen curves are reliable. The case $W/L = 0$ corresponds to the exponential loop profile (5.2) considered earlier and $W/L = 1$ is the uniform loop, so we will be able to observe the evolution from the stratified case to to the uniform case. Fig. 5.17(a), for the thin loop, shows that

only the fundamental kink mode is able to propagate as a trapped mode for all values of W/L , and its frequency increases as we evolve from the exponential stratification to the uniform loop. Also, for smaller values of W/L we find the first and second kink harmonics are trapped in the thin tube limit but are seen to reach the cutoff frequency before the realistic range of values of $W/L \approx 0.8 - 1.0$. Importantly, for a realistic range of chromospheric depth, the frequency of the fundamental mode is insensitive to the chromospheric depth. This explains why there is such good agreement between the stratified dispersion curves and uniform dispersion curves in Fig. 5.16(b). Fig. 5.17(b) shows these trends are carried forward in the case of fat loops, with an increase in frequency from the exponential stratification to the uniform loop; all modes which remain trapped for a realistic range of chromospheric depth show only a very weak dependence on depth. Note that due to the truncation of the linear system of equations, only the first twelve curves are reliable.

We conclude that loop stratification of the form (5.16) does not cause significant changes to the frequency for realistic parameters $W/L = 0.8 - 1.0$. In fact, it is reasonable to assume a uniform loop provided it is chosen to match the stratified loop at the apex.

5.4.4 Stratified environment

As before we now isolate the effect of stratification of the form (5.16) in the environment by considering a uniform loop. Again we examine the role of chromospheric depth but first we must understand the dependence on the loop radius.

5.4.5 Changing a

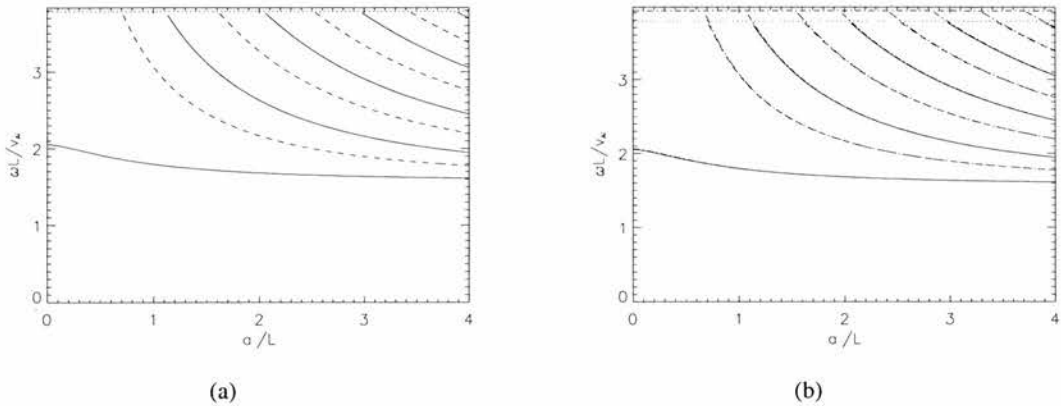


Figure 5.18: (a) Dispersion diagram plotting $\omega L/v_{Ai}$ against a/L for an exponentially stratified environment and homogeneous loop with $v_{Ae}(z=0) = 2.5v_{Ai}(z=0)$ and $\frac{\rho_e(L)}{\rho_e(0)} = 100$; (b) as in plot (a) but with the dispersion curves for the uniform loop and environment, with $v_{Ae} = 2.5v_{Ai}$, overlaid.

We consider an environmental stratification of the form (5.16) with $\rho_e(L)/\rho_e(0) = 100$ surrounding a uniform loop. We expect a modification to the cutoff frequency in this case but only a small correction to the oscillatory frequency. Fig. 5.18(a) and (b) show dispersion diagrams for this case, plotting non-dimensional frequency against loop radius; in Fig. 5.18(b) the dispersion curves for the case of a uniform environment which matches the stratified case at the apex are plotted. We see an almost exact agreement between the calculated oscillation frequencies in the two cases of a stratified environment and a uniform environment in the region where both sets of curves lie below the lower cutoff frequency (determined by the stratified environment). The reduction in the cutoff frequency as a result of the environmental stratification can be seen clearly; the modes of the uniform environment propagate through this cutoff and reach their own cutoff frequency. Therefore a consideration of environment stratification may be of importance when the fundamental sausage mode has been identified observationally and used for coronal seismology.

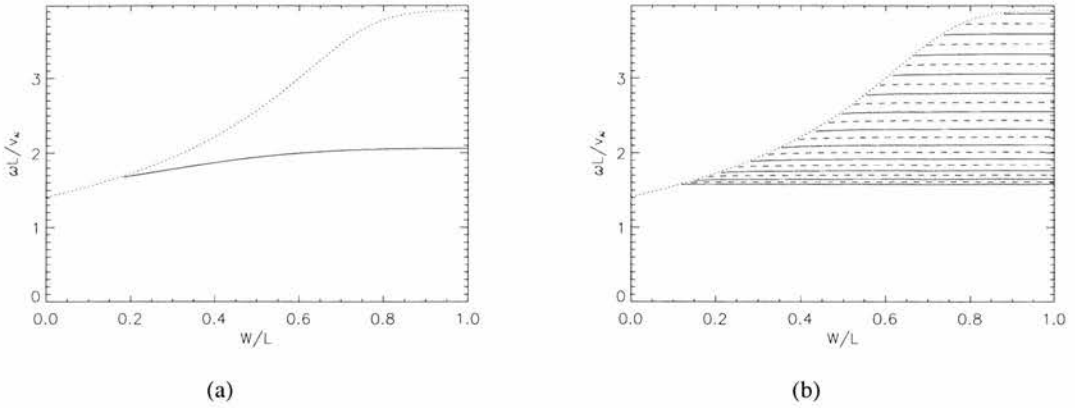


Figure 5.19: Dispersion diagram plotting $\omega L/v_{Ai}$ against the non-dimensional coronal depth W/L for (a) loop radius $a/L = 0.001$ and (b) loop radius $a/L = 10.0$. Here $v_{Ae}(0) = 2.5v_{Ai}(0)$ and $\frac{\rho_e(L)}{\rho_e(0)} = 100$.

5.4.6 Changing W

Again we investigate the influence of the parameter W/L on the oscillation and cutoff frequencies. We expect that as W/L increases, the loop will become a more efficient wave guide, causing the cutoff frequency to increase and a greater number of trapped modes to lie below it. This is evident from Fig. 5.19(a) and (b), plotting the non-dimensional frequency against W/L for loop radii of $a/L = 0.001$ and $a/L = 10.0$ respectively. The cutoff curves are the same in both diagrams since the cutoff is independent of the loop radius. Fig. 5.19(a) shows that for $W/L \geq 0.2$ only the fundamental kink mode propagates as a trapped mode in the thin tube limit for values of $W/L \geq 0.2$ so does have a cutoff frequency. The oscillation frequency of the fundamental kink mode shows only a slight dependence on W/L , especially in the realistic range of $W/L = 0.8 - 1.0$.

Consider the broad loop dispersion diagram shown in Fig. 5.19(b) where, in comparison with Fig. 5.19(a), many more sausage and kink modes are permitted to propagate as trapped modes. The curves shown in Fig. 5.19(b) vary only slightly with respect to W/L ; therefore, the only effect W/L has on these modes is to reduce the cutoff frequency below the oscillation frequency and so they cannot propagate as a trapped mode.

5.5 Stratification in both loop and environment

So far we have explored the effects of stratification in density by looking separately at its role in the loop interior or in the loop environment. In reality, of course, the effects will arise in a combined way. Here we consider the combined effects of loop and environment stratification.

5.5.1 Changing a

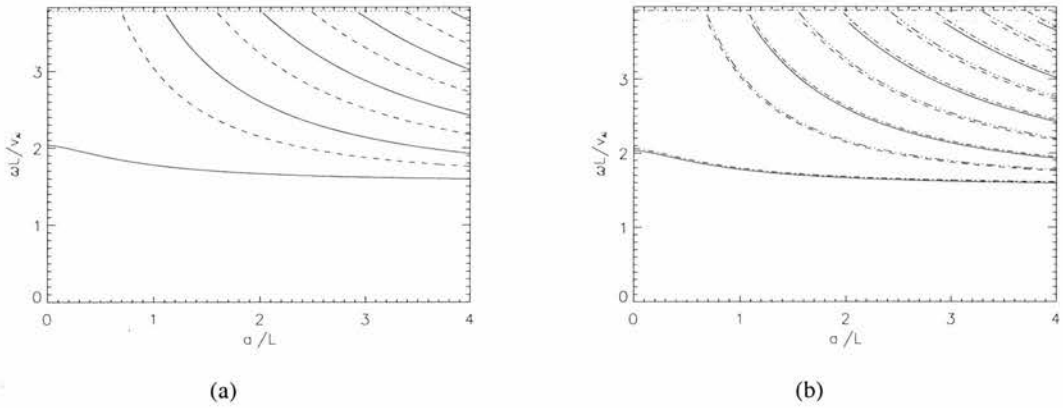


Figure 5.20: (a) Dispersion diagram plotting $\omega L/v_{Ai}$ against a/L for an exponentially stratified loop and environment for a uniform photospheric level, with $v_{Ae}(z=0) = 2.5v_{Ai}(z=0)$ and $\frac{\rho_e(L)}{\rho_e(0)} = 100$; (b) as in plot (a) but with the dispersion curves for the uniform loop and uniform environment included, with $v_{Ae} = 2.5v_{Ai}$.

Stratification is again taken to be of the form (5.16), now applied in both regions. In the environment $\rho_e(L)/\rho_e(0) = 100$. However, we assume a uniform photospheric surface, so $\rho_e(L) = \rho_i(L)$. The implication of this is that the density stratification of the loop across the chromosphere depth is less than that of the environment.

Fig. 5.20(a) and (b) shows the dispersion curves for the case of an external stratification of $\frac{\rho_e(L)}{\rho_e(0)} = 100$. With the assumption of a uniform photospheric surface, this corresponds to an internal stratification of $\frac{\rho_i(L)}{\rho_i(0)} = 16$ for a density contrast at the apex of 6.25 and a chromospheric depth $W/L = 0.2$. The curves for the uniform loop and environment matching the apex values of the stratified loop are displayed in Fig. 5.20(b). We see in Fig. 5.20(b) that the stratification has resulted in a small correction to the oscillation frequency, which is mainly due to the internal stratification. However, the reduction in the cutoff frequency is entirely a result of the external stratification. Again, the uniform case provides an adequate representation of this loop structure and would thus serve adequately for the purpose of coronal seismology, but care should be taken in using modes close to the cutoff.

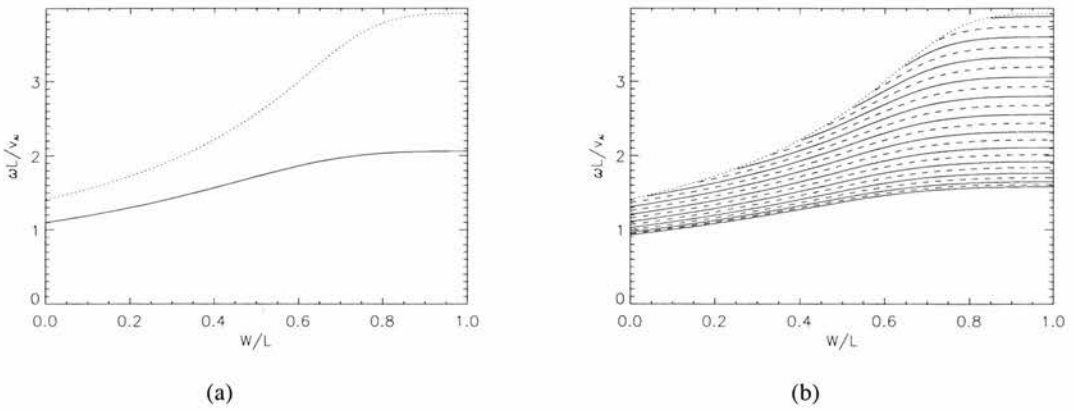
5.5.2 Changing W 

Figure 5.21: Dispersion diagram plotting $\omega L/v_{Ai}$ against the non-dimensional coronal depth W/L for (a) loop radius $a/L = 0.001$ and (b) loop radius $a/L = 10.0$, with $v_{Ae}(0) = 2.5v_{Ai}(0)$ and $\frac{\rho_e(L)}{\rho_e(0)} = 100$.

It is also important to examine the influence of the chromospheric depth on the oscillation frequency and the cutoff frequency. The cutoff frequency is influence as discussed earlier. However, in this case the fundamental kink mode does not reach the cutoff frequency in the thin tube case (Fig. 5.21(a)). This is due to the reduction in its frequency as a result of the internal stratification as $W/L \rightarrow 0$. This modification in frequency is also seen in fat loops, for which many kink and sausage modes propagate as trapped modes. However, in both the thin and fat tubes, the frequency of all trapped modes in the realistic range where $W/L = 0.8 - 1.0$ is found to be independent of W/L . This again points to the fact that the uniform loop and uniform environment provides a robust model.

5.6 Conclusions

In this chapter we have studied the effect of a longitudinally stratified density profiles in either the loop interior or its exterior, or combined in both. The first of these profiles was a purely exponential one and so the transition between the maximum density at the loop footpoint and minimum at the apex is gradual, and therefore does not reflect the more realistic rapid change from the photosphere to the corona over the height of the chromosphere. For this profile it was found that the frequency of the oscillation was strongly dependent on $\frac{\rho_i(L)}{\rho_i(0)}$, the ratio of the loop apex density to density at the footpoints. This strong dependence reflects the large addition of mass in the loop associated with the exponential profile. Comparisons with a uniform loop showed poor agreement in frequency when the uniform loop parameters were chosen to match the apex of the stratified loop. However, a much better agreement was observed when the mass contained by the two loops, stratified or unstratified, was equal. When stratification of the environment is included there results a modification of the cutoff frequency but comparatively small changes in the oscillation frequency occur, when compared with the effect of internal stratification. Drawing comparison with the uniform loop in the case of the internal stratification, good agreement is found when the profiles of the stratified and uniform environments are in mass balance.

The second density profile was chosen to represent more accurately the rapid transition between the photosphere and the corona. In this profile a uniform coronal region of extent $2W$ is assumed to be grounded by an exponentially stratified chromosphere. For this case there is excellent agreement between the uniform loop and stratified loop which are matched at the apex. These results demonstrate the robust nature of the Edwin and Roberts (1983) model and gives confidence to the results of coronal seismology (see, for example, Nakariakov and Ofman 2001) based on this model. Nonetheless, if observational data of sufficient accuracy were available, it should prove possible to probe stratification effects through the use of more complex models such as that investigated here.

Chapter 6

Conclusions

Throughout this thesis we have attempted to produce theoretical models which display oscillatory behaviour, as inspired by recent observational findings. In order to set the scene we return to the starting point for many coronal loop models, the Edwin and Roberts (1983) model. This model consists of an infinitely long magnetic flux tube embedded in a homogeneous environment. Dispersion relations for both surface and body modes are derived. However, under typical coronal conditions (Alfvén speeds greatly exceeding the sound speeds) only body modes are permitted to propagate. The modes of oscillation can additionally be classified into either sausage, kink or fluting modes, based on how they deform the tube cross-section. The main focus of our study in Chapter 2 is not the dispersion relation but the eigenfunctions of the sausage and kink modes, in both the fast and slow mode bands. It is apparent that the sausage mode results in no azimuthal flows, while the kink mode displays azimuthal flows. These flows show a discontinuity at the tube boundary, resulting in a shearing effect on the tube boundary. Also we can note a difference between fast and slow modes concerning these azimuthal flows, with fast modes resulting in the tube interior and exterior to be oscillating out of phase while slow modes allow the interior and exterior to oscillate in phase. The kink mode is the only mode which results in the displacement of the tube centre; sausage and fluting modes leave its position unperturbed. Both sausage and kink modes are found to be predominately transverse when occurring as fast modes in a low β plasma. Both are almost entirely longitudinal in the slow mode band. In the fast mode band, higher harmonics are found to be more compressible than the fundamental mode, while in the slow mode band higher harmonics are less compressible than the fundamental mode. We have also examined the fast modes in the $\beta = 0$ limit, where it is noted that the slow modes are eliminated and no longitudinal flows occur.

In Chapter 3 we examine the trapped modes of oscillation of a coronal loop but line-tying and longitudinal structure were introduced. The aim of introducing longitudinal structure is to simulate the effect of a dense chromospheric layer close to the loop footpoints. The loop is modelled as a

cylindrically symmetric magnetic flux tube, using the $\beta = 0$ approximation. Previous studies of oscillatory properties of this structure have been primarily interested in the effect of non-uniform longitudinal loop structures and homogeneous environment (Díaz et al. 2004). These studies show that there is a first order correction on oscillatory frequency when compared with a uniform line-tied loop. We discussed the influence of a longitudinally structured loop environment with either a uniform or non-uniform loop structure. In this first step we took the plasma properties, as well as the depth of the chromospheric layers, to be uniform.

The most striking effect introduced by longitudinal structuring is a modification in the cutoff frequency, which has not been considered in previous studies as the cutoff frequency is independent of the internal loop structure. The introduction of dense layers in the environment, so increasing the average density of the environment, produces a decrease in the cutoff frequency. The modification of the cutoff frequency is important as it reflects the ability of the loop to support trapped modes. In the case of a thin chromospheric layer it is found, in much the same way as the mode discussed in Chapter 2, that the loop supports only the fundamental kink mode as a trapped mode in the thin tube limit. However, it now propagates in this limit with a modified kink speed. All higher harmonics and sausage modes propagate as trapped modes for wider loops and all reach a modified cutoff frequency. It has also been found that for certain loop parameters the loop may support both the fundamental and first harmonic of the kink mode in the thin tube limit. If this case were to be discovered observationally it would be extremely useful from the point of view of coronal seismology as the fundamental mode could then be used to obtain the loop dimensions and the first harmonic could be used to deduce plasma parameters. Although plasma parameters within the model can be altered to obtain more kink modes below the cutoff in the thin tube limit, this is not the case for the sausage mode which is never found to propagate as a trapped mode in the thin tube limit. This suggests that the fast sausage mode only occurs as a leaky mode in the thin tube limit, resulting in the rapid damping of this mode.

As previously mentioned the cutoff frequency is dependent on the environmental structure and hence examining the influence of the oscillatory frequency on the chromospheric depth also introduces a non-uniform cutoff frequency. This non-uniform cutoff frequency results in each mode which becomes leaky having a unique cutoff frequency. Also, as a result of this non-uniform cutoff frequency, in a uniform loop the fundamental kink mode can be found to reach the cutoff frequency. This can also be seen for a structured loop when the loop footpoint is denser than the surrounding chromospheric layers. However, in the case of the loop footpoint being less dense than the chromospheric layers this effect is lost as a result of the modification to the oscillatory frequency of the fundamental mode. This result, of the fundamental mode no longer propagating as a trapped mode, may be important for coronal seismology.

Previous studies (see Chapter 2) suggest that when a mode propagates with a frequency close to its cutoff, the eigenfunctions of the mode will penetrate more deeply into the loop's environment

as the mode makes the transition from trapped to leaky; however, this is not apparent in this model with penetration approximately the same as the eigenfunctions evolve along the dispersion curve and its frequency becomes closer to the cutoff frequency. The fact that the eigenfunctions do not penetrate deeply into the environment of the loop indicates that the interaction between neighbouring loops is not significant, so justifying the study of an isolated magnetic flux tube.

Also it is seen in the case that the perturbed total pressure shows greater structure and larger amplitude in the region of the dense footpoints. As in Chapter 2, the radial velocity of the fundamental kink mode is found to be approximately uniform across the radius of the loop, so retaining the property of oscillating as a solid body.

The introduction of longitudinal structuring has allowed the interaction of modes, resulting in avoided crossings. At avoided crossings, modes exchange spatial structures. As a result it becomes difficult to determine which mode is present purely from examining its spatial structure. Also, the fundamental mode may possess more than one extrema, although it does not interact with another mode. Therefore, the presence of more than one extrema in the eigenfunctions of the fundamental kink mode is as a result of the weighting of the density profile. The fact that the fundamental kink mode may also have more than one extrema means it is no longer straightforward to identify it purely based on its spatial structure.

In Chapter 4 we moved away from the study of an isolated flux tube, as considered in Chapters 2 and 3, and considered a coronal arcade. A coronal arcade consists of many coronal loops and often occur in the aftermath of a flaring event. As these structures are born in a highly dynamical region they often display oscillatory behaviour and this has been noted observationally (Verwichte et al. 2004). The aim of Chapter 4 was to model the fast mode oscillations of a coronal arcade with footpoints fixed in the photospheric surface, but allowing free propagation along the arcade (transverse to the magnetic field).

In order to carry out this study we create a simplified arcade-like structure, consisting of a 2D Cartesian arcade aligned with the x axis with a uniform magnetic field directed across the arcade in the z direction. As in Chapter 3, we were interested in the influence of longitudinal structuring of the equilibrium density profile, while the arcade is invariant in the transverse direction. Linear perturbations are introduced about this equilibrium and the linear MHD equations in the zero β limit are applied. From the MHD equations we derived the equations which governed the total pressure perturbation for a general density stratification. In our study we consider three density profiles, the first for a homogeneous arcade, the second considering an exponential stratification over the full longitudinal length, and the third profile has both uniform and stratified regions.

The homogeneous arcade is considered in order to understand its basic modes of oscillation. In this case we derive an explicit dispersion relation and the eigenfunctions have a simple sine or cosine dependence. The dispersion relation's explicit form makes it straightforward to see that

the phase speed of all modes asymptote to the Alfvén speed in the short wavelength limit, and no modes propagate with a finite phase speed in the long wavelength limit. We also construct the ratio (P_1/P_2) of the periods of the fundamental mode and its first harmonic, which is expected to prove to be a useful tool in the field of coronal seismology (Andries et al. 2005; McEwan et al. 2006). The ratio P_1/P_2 shows a similar behaviour in this model to previous findings, taking a value of 2 in the long wavelength limit and falling monotonically to 1 in the short wavelength limit.

The second density profile we examined provides an exponentially stratified environment, resulting in a dense footpoint region compared with the apex. The level of stratification is governed by a parameter α ; we choose $\alpha = 2.3$, which provides a difference in density between apex and footpoint by a factor of 100 (which is illustrative of the difference between typical coronal and photospheric regions). The equilibrium is symmetric about the summit of the arcade. We took advantage of symmetry and considered modes that are even or odd disturbances about the apex. We derived dispersion relations for even and odd modes. These take a transcendental form as a result of the introduction of structuring. The stratification has been chosen in such a way that it effectively adds density to the arcade compared with the uniform case, and hence a reduction in oscillatory frequency is noted. Although the dispersion relations for odd and even modes are transcendental, approximate solutions have been derived. Also in the short wavelength limit we can derive an approximate solution which is identical for both even and odd modes. This points to the fact that the frequencies of consecutive even and odd modes converge for growing kL . This approximation in the short wavelength limit also points to the floor value of $c/v_{A0} \rightarrow \exp(-\alpha)$, rather than $c/v_{A0} \rightarrow 1$ which is a case in the homogeneous arcade. The modification in the oscillatory frequencies of the fundamental even and odd modes results in a change in the behaviour of P_1/P_2 , which is now seen to fall below 2 in the long wavelength limit but is still monotonic decreasing towards unity in the short wavelength limit. The eigenfunctions are also modified by the density structuring, developing oscillations in the region of the footpoints and even the fundamental mode may have more than one extrema in some cases.

It has been observed that the change from photospheric to coronal conditions occurs very rapidly over the height of the chromosphere. The previous density profile did not account for this rapid change as it displayed a much more gradual variation. To improve upon this, we introduced a piecewise continuous density profile with uniform corona and exponentially stratified chromospheric region. As in the previous case the stratification has added to the overall density of the arcade compared with a uniform arcade (it they are matched at the apex), which results in a reduction in frequency compared with the uniform case. Again we derived transcendental dispersion relations for even and odd modes separately, but it is found that the phase speeds of consecutive even and odd modes rapidly converge on crossing the $c/v_{A0} = 1$ threshold. As the nature of the solution in the coronal region changes from trigonometric to hyperbolic on crossing $c/v_{A0} = 1$,

mode interaction is necessary, which is apparent in the presence of avoided crossings. It has already been mentioned that the dispersion curves cross the $c/v_{A0} = 1$, line so the floor value has been modified when compared with the homogeneous case; it may be argued that the floor value now lies in the range $[\exp(-\alpha(W/L - 1)), 1]$.

The influence of this density stratification on the ratio P_1/P_2 is found to be the same as in the previous case, with a shift below 2 in the long wavelength limit; but it retains the monotonic decay towards 1 in the short wavelength limit. For this density profile, which resulted in mode interactions between the fundamental and first even modes, P_1 and P_3 , we find the curve P_1/P_3 is not monotonic, having local minima, which corresponds to the avoided crossings between these modes. This is interesting to note as in a situation where even and odd modes are not decoupled (for example, when the equilibrium is non-symmetric), as they are in this case, this behaviour may also become apparent in P_1/P_2 . The modes are seen to display a large number of interactions as the coronal depth varies. These interactions result in the extrema of the eigenfunctions being exchanged between the coronal and chromospheric regions.

Therefore it is clear that the influence of stratification upon this simple model of a coronal arcade results in several interesting modifications to the behaviour, both for the frequencies and eigenfunctions of the resultant modes. Changes to the frequency should be noted in the area of coronal seismology as they are important for such quantities as P_1/P_2 .

In Chapter 5 we returned to the study of an isolated magnetic flux tube, as in Chapter 3, and again we considered the effect of longitudinal structuring. However, in Chapter 5 we examined the effect of the three density profiles used in Chapter 4. The homogeneous case is the same as that examined in Chapter 2, if line-tying is introduced, and provides us with a basic case to refer back to. The first of the stratified density profiles is purely exponential, so shows a gradual change from coronal to photospheric levels. Initially, only internal stratification was introduced and resulted in significant modifications to oscillatory frequency, when compared with a uniform loop which matches the stratified loop at the apex. We also compare the stratified loop with a uniform loop containing equal mass; in this case, a much improved agreement between the oscillatory frequency is noted. Also for higher levels of stratification, mode interactions are observed; interestingly, these appear to correspond to the actual crossings of modes of the uniform loop which have different longitudinal wavenumbers. As the level of stratification increases the loop becomes denser in comparison to its surroundings and becomes a more efficient waveguide. This is illustrated by the fact that if $\rho_i(L)/\rho_i(0) = 200$, the loop supports the fundamental kink mode and also the first three kink harmonics as trapped modes in the thin tube limit. Interestingly, the fast sausage mode is never supported as a trapped mode in the thin tube limit.

Next we considered a uniform loop embedded in a stratified environment. It is found that environmental stratification results in small modifications to the oscillatory frequency compared with

a uniform loop matching the stratified loop at the apex. As found in Chapter 3, the environmental stratification is important in determining the cutoff frequency: the addition of density to the environment reduces the cutoff frequency, which results in an enhancement in leakage. Again a more accurate match between the stratified and uniform environments is obtained if the integrated densities are matched rather than matching the profiles at the apex. As in Chapter 3, increasing the level of stratification about a uniform loop results in a reduction in cutoff frequency to the point where the loop no longer supports trapped modes. Even the fundamental kink mode can be found to be leaky in the thin tube limit, for certain levels of stratification.

The final case considered with this density profile was to combine both internal and external stratification; we also assumed the photospheric surface is uniform. It is found that in this case the approximation of using a uniform loop which matches the stratified case at the apex is very poor due to the modifications in both frequencies and cutoff frequency. However, a more effective method of approximating the stratified case by a uniform case is to match the integrated densities in each of the appropriate regions. In the case where environmental stratification was considered alone, it was found that for certain levels of stratification the fundamental kink mode no longer propagated as a trapped mode in the thin tube limit. However, when stratification of the loop is also taken into account this result was lost and the fundamental kink mode was found to propagate as a trapped mode in the thin tube limit.

The final density profile considered was chosen to more accurately represent the rapid transition between the corona and the photosphere. The profile has a uniform coronal region lying above a rapidly changing chromospheric layer. In this more realistic case the difference in integrated density between the stratified and uniform cases which are matched at the apex is small when compared with the previous case. Although this profile produces similar behaviours to the previous case there are less strong effects. As a result, the approximation obtained using a uniform loop which matches the stratified one at the apex produces excellent agreement. Also it is found that the oscillatory frequency is insensitive to the chromospheric depth in the realistic range. These results demonstrate the robust nature of the Edwin and Roberts (1983) model and gives confidence to the results of coronal seismology based on this model. Nonetheless, if observational data of sufficient accuracy were to become available, it should prove possible to probe stratification effects through the use of more complex models such as that investigated here.

6.1 Future work

6.1.1 Longitudinal flows

Observations show that many coronal loops support field aligned flows. The model considered in Chapter 2 has been extended to include a field aligned flow (Terra-Homem et al., 2003). This flow results in a doppler shift and results in a distinction between modes propagating with the flow and modes propagating against the flow. It would be of interest to extend the coronal loop models considered in Chapters 2 and 5, incorporating a field aligned flow. Due to the structuring along the loop it would be important to enforce a uniform mass flux in order to preserve the structural features of the equilibrium; this would lead to the flow being dependent on the coordinate along the magnetic field. If such a model is to be developed, care would be required in deriving the boundary conditions equivalent to the ones used for a static equilibrium (see (1.44) and (1.45) in chapter 1) as the inclusion of a field aligned flow would alter these conditions, requiring the continuity of the loop displacement rather than velocity.

If such a model was developed it would not only be applicable to coronal loops but, with slight modification to the structure of the equilibrium, it may also be applied to a prominence fibril where flows have also been observed.

6.1.2 Azimuthal symmetry

In this thesis the only loop models are those which are cylindrically symmetric but this need not be the case. There are two aspects to this symmetry the first being a loop of non-circular cross-section; for example, an elliptical cross-section has been considered in Ruderman (2003). However the second aspect, which is to include a density profile with azimuthal dependence, breaks this symmetry and has not yet been tackled. This would be an interesting problem to take on as there would no longer be the distinction between sausage, kink and fluting modes, the resulting oscillations being a superposition of all three types of mode. The idea of a purely sausage, kink or fluting mode seems unlikely in reality even if a mode of oscillation may be predominately of one of the three classes of modes. This model would take a step towards addressing this idea.

6.1.3 Radial profiles

Throughout this thesis boundary of the loop has been taken as a sharp boundary but in reality the boundary would be replaced by a smooth transition from the loop into the environment. As a first step towards modelling a loop of continuous radial profile a slab structure may be considered, where the fast and Alfvén modes remain decoupled in the $\beta = 0$ limit and an analytical solution

is available for certain density profiles (Nakariakov and Roberts, 1995). The density profile may have to be assumed to be of separable form $\rho(r, z) = \rho_r(r)\rho_z(z)$. However, a smoothly varying radial profile in a cylindrical geometry would result in coupling between the fast and Alfvén modes. This coupling occurs at resonant points where the fast mode drives an Alfvén mode, resulting in the damping of the fast mode. The extra complication of mode coupling may mean no analytical solution can be found and a numerical approach would be required.

We have touched on three aspects of the coronal loop model that needs addressing and are reasonably straightforward to tackle. However, there are many more aspects to be explored but it is not easy to see how to proceed analytically. For example, loop curvature could well be an important factor and first steps in understanding the effect of curved structures on oscillatory modes have been taken in analytical models of a 2D nature (e.g. Díaz and Roberts, 2006) but to incorporate curvature in a 3D cylindrical loop requires the use of toroidal coordinates. In this geometry even an appropriate equilibrium is not straightforward (Van Doorselaere et al., 2004) and these complications are reflected in the subsequent wave analysis and their results.

Appendix A

Derivation of equation (3.30)

In this Appendix a derivation of equation (3.30) is given. This equation is a result of the application of boundary conditions (3.7) at the interfaces $z = \pm W$. These boundary conditions imply that the total pressure perturbation must be continuous across this boundary, leading to the requirement that $h_n^e(z)$ be continuous across this boundary. Also, the perturbed magnetic field must be continuous and, as a result of the ideal induction equation (1.19), viz.

$$\frac{\partial \mathbf{B}_1}{\partial t} = \nabla \times (\mathbf{v}_1 \times \mathbf{B}_0), \quad (\text{A.1})$$

the z derivative of the velocity field must be continuous across this boundary. This tells us that $\frac{dh_n^e}{dz}$ is also continuous across this boundary.

The general solution to equation (3.11) for an even disturbance about the apex ($z = 0$) is

$$h_n^e(z) = \begin{cases} A_1 \sin(M_n^{che}(z + L)), & -L < z < -W, \\ A_2 \cos(M_n^e z), & -W < z < W, \\ A_3 \sin(M_n^{che}(L - z)), & W < z < L, \end{cases} \quad (\text{A.2})$$

and its first derivative is

$$\frac{dh_n^e}{dz} = \begin{cases} A_1 M_n^{che} \cos(M_n^{che}(z + L)), & -L < z < -W, \\ -A_2 M_n^e \sin(M_n^e z), & -W < z < W, \\ A_3 M_n^{che} \cos(M_n^{che}(L - z)), & W < z < L. \end{cases} \quad (\text{A.3})$$

Imposing the continuity of (A.2) and (A.3) (taking advantage of the symmetry at the loop apex $z = 0$), we obtain

$$A_2 \cos[M_n^e W] = -A_3 \sin[M_n^{che}(L - W)] \quad (\text{A.4})$$

and

$$-A_2 M_n^e \sin[M_n^e W] = -A_3 M_n^{che} \cos[M_n^{che}(L - W)]. \quad (\text{A.5})$$

These expressions provide a linear homogeneous system for A_2 and A_3 , which has a non-trivial solution if its determinant vanishes. This gives

$$M_n^{che} \cos[M_n^e W] \cos[M_n^{che}(L - W)] - M_n^e \sin[M_n^e W] \sin[M_n^{che}(L - W)] = 0. \quad (\text{A.6})$$

Equation (A.6) is equivalent to equation (3.30), viz.

$$M_n^{che} \cot [M_n^{che}(L - W)] = M_n^e \tan [M_n^e W]. \quad (\text{A.7})$$

In the above derivation it has been assumed the M_n^e and M_n^{che} are real. However, if this is not the case then similar expressions can be derived in terms of hyperbolic functions either by writing the solution to equation (3.11) in terms of such functions or by using the relations

$$\sin(ix) = -i \sinh(x) \quad \text{and} \quad \cos(ix) = \cosh(x). \quad (\text{A.8})$$

Equation (3.31) for the odd modes is derived by a similar method, as are equations (3.34) and (3.35).

Appendix B

Expansions for the solutions of equations (4.28) and (4.29)

The expansions for the $(s + 1)^{th}$ zero, z_{s+1} , of

$$J_\nu(z)Y_\nu(\lambda z) - J_\nu(\lambda z)Y_\nu(z) \quad (\text{B.1})$$

given by

$$z_{s+1} = \beta + \frac{p}{\beta} + \frac{q - p^2}{\beta^3} + \frac{r - 4pq + 2p^3}{\beta^5} + \dots \quad (\text{B.2})$$

where coefficients β , p , q and r are defined by

$$\beta = \frac{(s+1)\pi}{\lambda-1}, \quad p = \frac{\mu-1}{8\lambda}, \quad \mu = 4\nu^2 \quad (\text{B.3})$$

$$q = \frac{(\mu-1)(\mu-25)(\lambda^3-1)}{6(4\lambda)^3(\lambda-1)}, \quad r = \frac{(\mu-1)(\mu^2-114\mu+1073)(\lambda^5-1)}{5(4\lambda)^5(\lambda-1)}. \quad (\text{B.4})$$

Choosing

$$\nu = \frac{kL}{\alpha}, \quad \lambda = \exp(\alpha), \quad \text{and} \quad z = \frac{ckL}{v_{A0}\alpha} \quad (\text{B.5})$$

expression (B.1) is of the same form as dispersion relation (4.28). We then obtain the expansion:

$$\frac{c}{v_{A0}} = \frac{\alpha(s+1)\pi}{kL(\exp(\alpha)-1)} \left[1 + \frac{(4k^2L^2 - \alpha^2)(\exp(\alpha)-1)^2}{8\alpha^2 \exp(\alpha)(s+1)^2\pi^2} + \dots \right] \quad (\text{B.6})$$

for the s^{th} harmonic (with $s = 0$ corresponding to the fundamental mode).

For the even modes we can make use of the same expansion (B.2) which provides an expansion for a large zero of (not necessarily the $(s + 1)^{th}$ zero) of

$$J'_\nu(z)Y_\nu(\lambda z) - J_\nu(\lambda z)Y'_\nu(z). \quad (B.7)$$

Note for this case the coefficients β , p , q and r are defined by

$$\beta = \frac{(s - \frac{1}{2})\pi}{\lambda - 1}, \quad p = \frac{(\mu + 3)\lambda - (\mu - 1)}{8\lambda(\lambda - 1)}, \quad \mu = 4\nu^2, \quad (B.8)$$

$$q = \frac{(\mu^2 + 46\mu - 63)\lambda^3 - (\mu - 1)(\mu - 25)}{6(4\lambda)^3(\lambda - 1)}, \quad (B.9)$$

$$r = \frac{(\mu^3 + 185\mu^2 - 2053\mu + 1899)\lambda^5 - (\mu - 1)(\mu^2 - 114\mu + 1073)}{5(4\lambda)^5(\lambda - 1)}. \quad (B.10)$$

Again, choosing

$$\nu = \frac{kL}{\alpha}, \quad \lambda = \exp(\alpha), \text{ and } z = \frac{ckL}{v_{A0}\alpha}, \quad (B.11)$$

we find expression (B.7) is of the same form as dispersion relation (4.29). Hence we obtain the expansion for the phase speed

$$\frac{c}{v_{A0}} = \frac{\alpha(s - \frac{1}{2})\pi}{kL(\exp(\alpha) - 1)} \left[1 + \frac{[k^2L^2(4\exp(\alpha) - 1) + \alpha^2(\exp(\alpha) + \alpha^2)](\exp(\alpha) - 1)}{8\alpha^2 \exp(\alpha)(s - \frac{1}{2})^2\pi^2} + \dots \right], \quad (B.12)$$

with $s = 0, 1, 2, \dots$. It should be noted that this is not necessarily for the $(s + 1)^{th}$ even harmonic since expansion (B.2) is for a large zero of (B.7).

Appendix C

The arcade dispersion relation

In the investigation of dispersion relation (4.28) for the odd modes of a coronal arcade it is interesting to examine the behaviour for large values of kL . This requires the use of expansions of Bessel functions $J_\nu(\lambda\nu)$ and $Y_\nu(\lambda\nu)$ as $\nu \rightarrow \infty$. It is important to note whether $\lambda > 1$ or $0 < \lambda < 1$ as the expansions for these two cases are different. From the argument in Chapter 4 based on the fact that the solution of equation (4.21) must have a region inside $[0, L]$ where its solution is oscillatory in nature which implies some where in this region

$$\frac{c^2 \exp(2\alpha z/L)}{v_{A0}^2} - 1 > 0, \quad (\text{C.1})$$

so if there is a solution then this condition must be satisfied at $z = L$. Therefore

$$\frac{c^2 \exp(2\alpha)}{v_{A0}^2} - 1 > 0 \quad (\text{C.2})$$

and so

$$\frac{c \exp(\alpha)}{v_{A0}} > 1. \quad (\text{C.3})$$

Therefore the expansions

$$J_{\frac{kL}{\alpha}} \left(\frac{c \exp(\alpha)}{v_{A0}} \frac{kL}{\alpha} \right) \sim \sqrt{\frac{2}{\pi \frac{kL}{\alpha} \sqrt{\frac{c^2 \exp(2\alpha)}{v_{A0}^2} - 1}}} \cos \left(\frac{kL}{\alpha} \sqrt{\frac{c^2 \exp(2\alpha)}{v_{A0}^2} - 1} - \frac{kL}{\alpha} \sec^{-1} \left(\frac{c \exp(\alpha)}{v_{A0}} \right) - \frac{1}{4} \pi \right) \quad (\text{C.4})$$

and

$$Y_{\frac{kL}{\alpha}} \left(\frac{c \exp(\alpha) kL}{v_{A0} \alpha} \right) \sim \sqrt{\frac{2}{\pi \frac{kL}{\alpha} \sqrt{\frac{c^2 \exp(2\alpha)}{v_{A0}^2} - 1}}} \sin \left(\frac{kL}{\alpha} \sqrt{\frac{c^2 \exp(2\alpha)}{v_{A0}^2} - 1} - \frac{kL}{\alpha} \sec^{-1} \left(\frac{c \exp(\alpha)}{v_{A0}} \right) - \frac{1}{4} \pi \right) \quad (C.5)$$

are employed. We have seen from the solution of the full dispersion relation that $c/v_{A0} < 1$ as $kL \rightarrow \infty$ and so we also use the expansions:

$$J_{\frac{kL}{\alpha}} \left(\frac{c kL}{v_{A0} \alpha} \right) \sim \frac{\exp \frac{kL}{\alpha} \left(\sqrt{1 - \frac{c^2}{v_{A0}^2}} - \operatorname{sech}^{-1} \left(\frac{c}{v_{A0}} \right) \right)}{\sqrt{2\pi \frac{kL}{\alpha} \sqrt{1 - \frac{c^2}{v_{A0}^2}}}} \quad (C.6)$$

and

$$Y_{\frac{kL}{\alpha}} \left(\frac{c kL}{v_{A0} \alpha} \right) \sim - \frac{\exp -\frac{kL}{\alpha} \left(\sqrt{1 - \frac{c^2}{v_{A0}^2}} - \operatorname{sech}^{-1} \left(\frac{c}{v_{A0}} \right) \right)}{\sqrt{\frac{1}{2} \pi \frac{kL}{\alpha} \sqrt{1 - \frac{c^2}{v_{A0}^2}}}}. \quad (C.7)$$

Now substituting expansions (C.4), (C.5), (C.6) and (C.7) in dispersion relation (4.28), we obtain the expression for the dispersion relation for large kL :

$$\begin{aligned} & - \sqrt{\frac{2}{\pi \frac{kL}{\alpha} \sqrt{\frac{c^2 \exp(2\alpha)}{v_{A0}^2} - 1}}} \cos \left(\frac{kL}{\alpha} \sqrt{\frac{c^2 \exp(2\alpha)}{v_{A0}^2} - 1} - \frac{kL}{\alpha} \sec^{-1} \left(\frac{c \exp(\alpha)}{v_{A0}} \right) - \frac{1}{4} \pi \right) \\ & \quad - \frac{\exp -\frac{kL}{\alpha} \left(\sqrt{1 - \frac{c^2}{v_{A0}^2}} - \operatorname{sech}^{-1} \left(\frac{c}{v_{A0}} \right) \right)}{\sqrt{\frac{1}{2} \pi \frac{kL}{\alpha} \sqrt{1 - \frac{c^2}{v_{A0}^2}}}} \\ & - \sqrt{\frac{2}{\pi \frac{kL}{\alpha} \sqrt{\frac{c^2 \exp(2\alpha)}{v_{A0}^2} - 1}}} \sin \left(\frac{kL}{\alpha} \sqrt{\frac{c^2 \exp(2\alpha)}{v_{A0}^2} - 1} - \frac{kL}{\alpha} \sec^{-1} \left(\frac{c \exp(\alpha)}{v_{A0}} \right) - \frac{1}{4} \pi \right) \\ & \quad + \frac{\exp \frac{kL}{\alpha} \left(\sqrt{1 - \frac{c^2}{v_{A0}^2}} - \operatorname{sech}^{-1} \left(\frac{c}{v_{A0}} \right) \right)}{\sqrt{2\pi \frac{kL}{\alpha} \sqrt{1 - \frac{c^2}{v_{A0}^2}}}} = 0. \end{aligned} \quad (C.8)$$

Since

$$\sqrt{1 - \frac{c^2}{v_{A0}^2}} - \operatorname{sech}^{-1} \left(\frac{c}{v_{A0}} \right) \leq 0 \quad (C.9)$$

the second term in equation (C.8) goes to zero. Hence equation (C.8) is satisfied when

$$\cos \left(\frac{kL}{\alpha} \sqrt{\frac{c^2 \exp(2\alpha)}{v_{A0}^2} - 1} - \frac{kL}{\alpha} \sec^{-1} \left(\frac{c \exp(\alpha)}{v_{A0}} \right) - \frac{1}{4} \pi \right) = 0. \quad (\text{C.10})$$

This is equivalent to

$$\frac{kL}{\alpha} \left(\sqrt{\frac{c^2 \exp(2\alpha)}{v_{A0}^2} - 1} - \sec^{-1} \left(\frac{c \exp(\alpha)}{v_{A0}} \right) \right) = \frac{(4n - 1)\pi}{4}. \quad (\text{C.11})$$

As the right handside of equation (C.11) is finite and $kL \rightarrow \infty$ then the term in parenthesis must tend to zero, which occurs as $\frac{c \exp(\alpha)}{v_{A0}} \rightarrow 1$. Hence, Taylor expanding the term in parenthesis about $\frac{c \exp(\alpha)}{v_{A0}} = 1$, we find

$$\frac{kL}{\alpha} \left(\frac{2\sqrt{2}}{3} \left(\frac{c \exp(\alpha)}{v_{A0}} - 1 \right)^{\frac{3}{2}} \right) = \frac{(4n - 1)\pi}{4}. \quad (\text{C.12})$$

Thus,

$$\frac{c}{v_{A0}} = \exp(-\alpha) \left(\frac{3(4n - 1)\pi}{8\sqrt{2}} \frac{\alpha}{kL} \right)^{\frac{2}{3}} + \exp(-\alpha), \quad (\text{C.13})$$

or in terms of frequency

$$\frac{\omega L}{v_{A0}} = \exp(-\alpha) \left(\frac{3(4n - 1)\pi}{8\sqrt{2}} \alpha (kL)^{\frac{1}{2}} \right)^{\frac{2}{3}} + \exp(-\alpha) kL. \quad (\text{C.14})$$

A similar approach is can be used to derive an identical expression for the asymptotic behaviour of the even modes described in dispersion relation (4.29).

Appendix D

Derivation of solution (4.24)

To obtain solutions to equation (4.21) we start with the equation (Watson, 1952, p. 98)

$$\frac{d^2 y}{dz^2} + \left[\frac{1}{2} \frac{\psi'''(z)}{\psi'(z)} - \frac{3}{4} \left\{ \frac{\psi''(z)}{\psi'(z)} \right\}^2 + \left\{ \psi^2(z) - \nu^2 + \frac{1}{4} \right\} \left\{ \frac{\psi'(z)}{\psi(z)} \right\}^2 \right] y = 0 \quad (\text{D.1})$$

which has solution

$$y = \sqrt{\frac{\psi(z)}{\psi'(z)}} \xi_\nu(\psi(z)) \quad (\text{D.2})$$

where ξ is a Bessel function. Letting $\psi(z) = \alpha \exp(z)$, equation (D.1) reduces to

$$\frac{d^2 y}{dz^2} + [\alpha^2 \exp(2z) - \nu^2] y = 0 \quad (\text{D.3})$$

and it follows from equation (D.2) this has solution

$$y = \xi_\nu(\alpha \exp(x)). \quad (\text{D.4})$$

Now making the change of variable $z = \beta x$, equation (D.3) becomes

$$\frac{d^2 y}{dx^2} + [\alpha^2 \beta^2 \exp(2\beta x) - \nu^2 \beta^2] y = 0. \quad (\text{D.5})$$

Letting $\gamma = \alpha\beta$ and $\eta = \nu\beta$ equation (D.5) becomes

$$\frac{d^2 y}{dx^2} + [\gamma^2 \exp(2\beta x) - \eta^2] y = 0, \quad (\text{D.6})$$

which is of the same form as (4.21) which we wish to solve. Equation (D.6) has solution

$$y = \xi_{\frac{\nu}{\beta}} \left(\frac{\gamma}{\beta} \exp(\beta x) \right). \quad (\text{D.7})$$

Thus, written in the conventional Bessel function form:

$$y = AJ_{\frac{\nu}{\beta}} \left(\frac{\gamma}{\beta} \exp(\beta x) \right) + BY_{\frac{\nu}{\beta}} \left(\frac{\gamma}{\beta} \exp(\beta x) \right). \quad (\text{D.8})$$

This solution can also be obtained by using the change of variables $z = \frac{\gamma}{\beta} \exp(\beta x)$ in equation (D.6), leading to a Bessel equation of the form

$$\frac{d^2 y}{dz^2} + \frac{1}{z} \frac{dy}{dz} + \left(1 - \frac{\nu^2}{\beta^2 z^2} \right) y = 0, \quad (\text{D.9})$$

which has solutions (assuming $\frac{\nu^2}{\beta^2} > 0$)

$$y(z) = AJ_{\frac{\nu}{\beta}}(z) + BY_{\frac{\nu}{\beta}}(z). \quad (\text{D.10})$$

Returning to the original variables,

$$y(z) = AJ_{\frac{\nu}{\beta}} \left(\frac{\gamma}{\beta} \exp(\beta x) \right) + BY_{\frac{\nu}{\beta}} \left(\frac{\gamma}{\beta} \exp(\beta x) \right). \quad (\text{D.11})$$

Appendix E

Derivation of dispersion relation (4.44)

We now derive dispersion relation (4.44) for the odd modes of a longitudinally structured coronal arcade described in Chapter 4. This structuring is in the form of a non-uniform Alfvén profile $v_A(z)$, which has been chosen to reflect rapid change in density between the corona and photosphere over the relatively small chromospheric region:

$$v_A(z) = \begin{cases} v_{A0} \exp(\alpha(z + W)/L), & -L < z < -W \\ v_{A0}, & -W < z < W \\ v_{A0} \exp(-\alpha(z - W)/L), & W < z < L. \end{cases} \quad (\text{E.1})$$

The speed $v_A(z)$ is symmetric about $z = 0$ and therefore we may separate our consideration of even and odd modes. Also, as a result of this symmetry, we need only consider the region $z \geq 0$. Equation (4.7). viz.

$$\frac{d^2 h}{dz^2} + \left(\frac{\omega^2}{v_A^2(z)} - k^2 \right) h = 0, \quad (\text{E.2})$$

takes the form

$$\frac{d^2 h}{dz^2} + \left(\frac{\omega^2}{v_{A0}^2} \exp(2\alpha(z - W)/L) - k^2 \right) h = 0 \quad (\text{E.3})$$

in the chromospheric region $W < z < L$, with solution

$$h(z) = AJ_{\frac{kL}{\alpha}} \left(\frac{\omega L}{\alpha v_{A0}} \exp(\alpha(z - W)/L) \right) + BY_{\frac{kL}{\alpha}} \left(\frac{\omega L}{\alpha v_{A0}} \exp(\alpha(z - W)/L) \right). \quad (\text{E.4})$$

This has derivative

$$\frac{dh}{dz} = \frac{\omega \exp(\alpha(z-W)/L)}{v_{A0}} \left[AJ'_{\frac{kL}{\alpha}} \left(\frac{\omega L}{\alpha v_{A0}} \exp(\alpha(z-W)/L) \right) + \right. \\ \left. BY'_{\frac{kL}{\alpha}} \left(\frac{\omega L}{\alpha v_{A0}} \exp(\alpha(z-W)/L) \right) \right]. \quad (\text{E.5})$$

In the homogeneous coronal region, $-W < z < W$, equation (E.2) take the form

$$\frac{d^2 h}{dz^2} + M_0^2 h = 0, \quad (\text{E.6})$$

where M_0 is defined by

$$M_0^2 = \frac{\omega^2}{v_{A0}^2} - k^2. \quad (\text{E.7})$$

Equation (E.6) has solution

$$h(z) = C \sin(M_0 z), \quad M_0^2 \geq 0, \quad (\text{E.8})$$

assuming $M_0^2 > 0$ and we have also enforced the condition $h(z = 0) = 0$ in order to obtain the solution corresponding an odd disturbance about $z = 0$.

To obtain the dispersion relation we seek we must apply an appropriate set of boundary conditions at the interface $z = W$:

$$[\mathbf{v}_1] = [\mathbf{B}_1] = [P_T] = 0, \quad (\text{E.9})$$

as discussed in Chapter 1. To satisfy boundary conditions (E.9) it is required that $h(z)$ and its derivative $\frac{dh}{dz}$ be continuous across the interface $z = W$. This leads to the conditions

$$AJ_{\frac{kL}{\alpha}} \left(\frac{\omega L}{\alpha v_{A0}} \right) + BY_{\frac{kL}{\alpha}} \left(\frac{\omega L}{\alpha v_{A0}} \right) - C \sin(M_0 W) = 0 \quad (\text{E.10})$$

for the continuity of $h(z)$ at $z = W$, and

$$\frac{\omega}{v_{A0}} \left[AJ'_{\frac{kL}{\alpha}} \left(\frac{\omega L}{\alpha v_{A0}} \right) + BY'_{\frac{kL}{\alpha}} \left(\frac{\omega L}{\alpha v_{A0}} \right) \right] - CM_0 \cos M_0 W = 0. \quad (\text{E.11})$$

Also the line-tying condition $h(z = L) = 0$ must be enforced, providing the condition

$$AJ_{\frac{kL}{\alpha}} \left(\frac{\omega L}{\alpha v_{A0}} \exp(\alpha(L-W)/L) \right) + BY_{\frac{kL}{\alpha}} \left(\frac{\omega L}{\alpha v_{A0}} \exp(\alpha(L-W)/L) \right) = 0. \quad (\text{E.12})$$

Setting the determinant of this system of linear equations (E.10), (E.11) and (E.12) to zero gives

the dispersion relation we desire:

$$\frac{c}{v_{A0}} \tan \left(kW \sqrt{\frac{c^2}{v_{A0}^2} - 1} \right) = \frac{W \sqrt{\frac{c^2}{v_{A0}^2} - 1} \left(J_{\frac{kL}{\alpha}} \left(\frac{ckL}{\alpha v_{A0}} \exp(\alpha(L-W)/L) \right) Y_{\frac{kL}{\alpha}} \left(\frac{ckL}{\alpha v_{A0}} \right) - Y_{\frac{kL}{\alpha}} \left(\frac{ckL}{\alpha v_{A0}} \exp(\alpha(L-W)/L) \right) J_{\frac{kL}{\alpha}} \left(\frac{ckL}{\alpha v_{A0}} \right) \right)}{\left(J_{\frac{kL}{\alpha}} \left(\frac{ckL}{\alpha v_{A0}} \exp(\alpha(L-W)/L) \right) Y'_{\frac{kL}{\alpha}} \left(\frac{ckL}{\alpha v_{A0}} \right) - Y'_{\frac{kL}{\alpha}} \left(\frac{ckL}{\alpha v_{A0}} \exp(\alpha(L-W)/L) \right) J'_{\frac{kL}{\alpha}} \left(\frac{ckL}{\alpha v_{A0}} \right) \right)} \quad (\text{E.13})$$

Here we have written the result in terms of the phase speed $c = \frac{\omega}{k}$. Throughout this derivation it has been assumed that $M_0^2 = k^2 \left(\frac{c^2}{v_{A0}^2} - 1 \right) > 0$. Equivalent dispersion relations can be obtained, for $M_0^2 < 0$, in terms of hyperbolic functions. Also a similar approach can be taken to find the dispersion relation for the even modes.

Bibliography

- Alfvén, H. (1942). Existence of electromagnetic-hydrodynamic waves. *Nature*, 150:405.
- Abramowitz, M. and Stegun, I. A. (1964). *Handbook of Mathematical Functions*. National Bureau of Standards.
- Alfvén, H. (1943). On the Effect of a Vertical Magnetic Field in a Conducting Atmosphere. *Arkiv for Astronomi*, 29A:1–6.
- Andries, J., Goossens, M., Hollweg, J. V., Arregui, I., and Van Doorselaere, T. (2005). Coronal loop oscillations. Calculation of resonantly damped MHD quasi-mode kink oscillations of longitudinally stratified loops. *A & A*, 430:1109–1118.
- Arfken, G. B. (1985). *Mathematical Methods for Physicists*. Academic Press (3rd ed.).
- Aschwanden, M. J. (2003). Review of Coronal Oscillations – An Observer’s View. In *Turbulence, Waves and Instabilities in the Solar Plasma*, pages 215–237.
- Aschwanden, M. J. (2004). *Physics of the Solar Corona - An Introduction*. Praxis Publishing Ltd, Chichester, UK.
- Aschwanden, M. J., De Pontieu, B., Schrijver, C. J., and Title, A. M. (2002). Transverse Oscillations in Coronal Loops Observed with TRACE - II. Measurements of Geometric and Physical Parameters. *Sol. Phys.*, 206:99–132.
- Aschwanden, M. J., Fletcher, L., Schrijver, C. J., and Alexander, D. (1999). Coronal Loop Oscillations Observed with the Transition Region and Coronal Explorer. *ApJ.*, 520:880–894.
- Bennett, K., Roberts, B., and Narain, U. (1999). Waves in Twisted Magnetic Flux Tubes. *Sol. Phys.*, 185:41–59.
- Berghmans, D. and Clette, F. (1999). Active region EUV transient brightenings - First Results by EIT of SOHO JOP80. *Sol. Phys.*, 186:207–229.
- Brady, C. S. and Arber, T. D. (2005). Damping of vertical coronal loop kink oscillations through wave tunneling. *A & A*, 438:733–740.
- Cowling, T. G. (1976). *Magnetohydrodynamics*. Monographs on Astronomical Subjects, Bristol: Adam Hilger, 1976.
- De Moortel, I. (2006). Propagating mhd waves in coronal loops. In *Phil. Trans. of The Royal Society*, volume 364, pages 461 – 472.
- De Moortel, I., Hood, A. W., and Arber, T. D. (2000a). Phase mixing of Alfvén waves in a

- stratified and radially diverging, open atmosphere. *A & A*, 354:334–348.
- De Moortel, I., Hood, A. W., and Arber, T. D. (2000b). Phase Mixing of Alfvén Waves in an Open and Stratified Atmosphere. In *AIP Conf. Proc. 537: Waves in Dusty, Solar, and Space Plasmas*, page 224.
- De Moortel, I., Hood, A. W., and Ireland, J. (2002a). Coronal seismology through wavelet analysis. *A & A*, 381:311–323.
- De Moortel, I., Hood, A. W., Ireland, J., and Walsh, R. W. (2002b). Longitudinal intensity oscillations in coronal loops observed with TRACE - II. Discussion of Measured Parameters. *Sol. Phys.*, 209:89–108.
- De Moortel, I., Ireland, J., Hood, A. W., and Walsh, R. W. (2002c). The detection of 3 & 5 min period oscillations in coronal loops. *A & A*, 387:L13–L16.
- De Moortel, I., Ireland, J., and Walsh, R. W. (2000c). Observation of oscillations in coronal loops. *A & A*, 355:L23–L26.
- De Moortel, I., Ireland, J., Walsh, R. W., and Hood, A. W. (2002d). Longitudinal intensity oscillations in coronal loops observed with TRACE - I. Overview of Measured Parameters. *Sol. Phys.*, 209:61–88.
- Díaz, A. J. (2004). *Fast Magnetohydrodynamic Waves in Line-tied Solar Coronal Flux Tubes*. PhD thesis, Departament de Física, Universitat de les Illes Balears.
- Díaz, A. J., Oliver, R., and Ballester, J. L. (2002). Fast Magnetohydrodynamic Oscillations in Cylindrical Prominence Fibrils. *ApJ.*, 580:550–565.
- Díaz, A. J., Oliver, R., Ballester, J. L., and Roberts, B. (2004). Fast MHD oscillations in line-tied homogeneous coronal loops. *A & A*, 424:1055–1064.
- Díaz, A. J., Oliver, R., Erdélyi, R., and Ballester, J. L. (2001). Fast MHD oscillations in prominence fine structures. *A & A*, 379:1083–1097.
- Díaz, A. J. and Roberts, B. (2006). Slow magnetohydrodynamic oscillations in a stratified line-tied coronal loop. *A & A*. in press.
- Díaz, A. J., Zaqarashvili, T., and Roberts, B. (2006). Fast magnetohydrodynamic oscillations in a force-free line-tied coronal arcade. *A & A*. in press.
- Edwin, P. M. and Roberts, B. (1982). Wave propagation in a magnetically structured atmosphere. III - The slab in a magnetic environment. *Sol. Phys.*, 76:239–259.
- Edwin, P. M. and Roberts, B. (1983). Wave propagation in a magnetic cylinder. *Sol. Phys.*, 88:179–191.
- Gallagher, P. T., Keenan, F. P., Phillips, K. J. H. and Read, P. D., Rudawy, P., and Rempel, B. R. (1997). *The sun in eclipse*. Springer.
- Goedbloed, J. P. (1983). Lecture Notes on Ideal Magnetohydrodynamics. In *Rijnhuizen Report*, pages 76–83.
- Goedbloed, J. P. and Hagebeuk, H. J. L. (1972). *Phys. Fluids*, 15:1090.
- Golub, L. and Pasachoff, J. M. (1997). *The Solar Corona*. The Solar Corona, by Leon Golub and Jay M. Pasachoff, pp. 388. ISBN 0521480825. Cambridge, UK: Cambridge University Press,

- September 1997.
- Goossens, M., Andries, J., and Arregui, I. (2006). Damping of mhd waves by resonant absorption in the solar atmosphere. In *Phil. Trans. of The Royal Society*, volume 364, page 433.
- Goossens, M., Andries, J., and Aschwanden, M. J. (2002). Coronal loop oscillations. An interpretation in terms of resonant absorption of quasi-mode kink oscillations. *A & A*, 394:L39–L42.
- Hain, K. and Lüst, R. (1958). *Z. Naturforsch*, 13a:936.
- Handy, B. N., Acton, L. W., Kankelborg, C. C., Wolfson, C. J., Akin, D. J., Bruner, M. E., Carvalho, R., Catura, R. C., Chevalier, R., Duncan, D. W., Edwards, C. G., Feinstein, C. N., Freeland, S. L., Friedlaender, F. M., Hoffmann, C. H., Hurlburt, N. E., Jurcevich, B. K., Katz, N. L., Kelly, G. A., Lemen, J. R., Levay, M., Lindgren, R. W., Mathur, D. P., Meyer, S. B., Morrison, S. J., Morrison, M. D., Nightingale, R. W., Pope, T. P., Rehse, R. A., Schrijver, C. J., Shine, R. A., Shing, L., Strong, K. T., Tarbell, T. D., Title, A. M., Torgerson, D. D., Golub, L., Bookbinder, J. A., Caldwell, D., Cheimets, P. N., Davis, W. N., Deluca, E. E., McMullen, R. A., Warren, H. P., Amato, D., Fisher, R., Maldonado, H., and Parkinson, C. (1999). The transition region and coronal explorer. *Sol. Phys.*, 187:229–260.
- Heyvaerts, J. and Priest, E. R. (1976). Thermal evolution of current sheets and flash phase of solar flares. *Sol. Phys.*, 47:223–231.
- Heyvaerts, J. and Priest, E. R. (1983). Coronal heating by phase-mixed shear Alfvén waves. *A & A*, 117:220–234.
- Hood, A. W. (1986). Photospheric line-tying conditions for the MHD stability of coronal magnetic fields. *Sol. Phys.*, 105:307–312.
- Ionson, J. A. (1978). Resonant absorption of Alfvénic surface waves and the heating of solar coronal loops. *ApJ*, 226:650–673.
- James, L. (2003). Coronal loop oscillations. Master's thesis, School of Mathematics, St Andrews University.
- Katsiyannis, A. C., Williams, D. R., McAteer, R. T. J., Gallagher, P. T., Keenan, F. P., and Murtagh, F. (2003). Eclipse observations of high-frequency oscillations in active region coronal loops. *A & A*, 406:709–714.
- Kliem, B., Dammasch, I. E., Curdt, W., and Wilhelm, K. (2002). Correlated Dynamics of Hot and Cool Plasmas in the Main Phase of a Solar Flare. *ApJ*, 568:L61–L65.
- Kosovichev, A. G. (2003). What helioseismology teaches us about the Sun. In *ESA SP-535: Solar Variability as an Input to the Earth's Environment*, pages 795–806.
- Kreyszig, E. (1993). *Advanced Engineering Mathematics*. New York ; Chichester : Wiley, (7th ed.).
- Lang, K. R. (2001). *The Cambridge Encyclopedia of the Sun*. Cambridge University Press.
- Lighthill, J. (1978). *Waves in Fluids*. Cambridge, Cambridge University Press, 1978. 516 p.
- McEwan, M., Donnelly, G. R., Díaz, A. J., and Roberts, B. (2006) Stratification effects in coronal loops. in prep.
- McEwan, M. P. and de Moortel, I. (2006). Longitudinal intensity oscillations observed with

- TRACE: evidence of fine-scale structure. *A & A*, 448:763–770.
- Mendoza-Briceño, C. A., Erdélyi, R., and Sigalotti, L. D. G. (2004). The Effects of Stratification on Oscillating Coronal Loops. *ApJ*, 605:493–502.
- Nakariakov, V. M., Melnikov, V. F., and Reznikova, V. E. (2003). Global sausage modes of coronal loops. *A & A*, 412:L7–L10.
- Nakariakov, V. M., Melnikov, V. F., and Reznikova, V. E. (2005). Global Sausage Magnetoacoustic Modes of Coronal Loops. In *IAU Symposium*, volume 223, pages 653–654.
- Nakariakov, V. M. and Ofman, L. (2001). Determination of the coronal magnetic field by coronal loop oscillations. *A & A*, 372:L53–L56.
- Nakariakov, V. M., Ofman, L., Deluca, E. E., Roberts, B., and Davila, J. M. (1999). TRACE observation of damped coronal loop oscillations: Implications for coronal heating. *Science*, 285:862–864.
- Nakariakov, V. M. and Roberts, B. (1995a). Magnetosonic Waves in Structured Atmospheres with Steady Flows, I. *Sol. Phys.*, 159:213–228.
- Nakariakov, V. M. and Roberts, B. (1995b). On Fast Magnetosonic Coronal Pulsations. *Sol. Phys.*, 159:399–402.
- Nakariakov, V. M. and Verwichte, E. (2005). Coronal Waves and Oscillations. *Living Reviews in Solar Physics*, 2:3.
- Nakariakov, V. M., Verwichte, E., Berghmans, D., and Robbrecht, E. (2000). Slow magnetoacoustic waves in coronal loops. *A & A*, 362:1151–1157.
- Narain, U. and Ulmschneider, P. (1990). Chromospheric and coronal heating mechanisms. *Space Science Reviews*, 54:377–445.
- Ofman, L., Davila, J. M., and Steinolfson, R. S. (1994a). Coronal Heating by the Resonant Absorption of Alfvén Waves. In Rusin, V., Heinzel, P., and Vial, J.-C., editors, *IAU Colloq. 144: Solar Coronal Structures*, page 473.
- Ofman, L., Davila, J. M., and Steinolfson, R. S. (1994b). Coronal heating by the resonant absorption of Alfvén waves: The effect of viscous stress tensor. *ApJ*, 421:360–371.
- Ofman, L., Romoli, M., Poletto, G., Noci, G., and Kohl, J. L. (1997). Ultraviolet Coronagraph Spectrometer Observations of Density Fluctuations in the Solar Wind. *ApJ*, 491:L111–L114.
- Ofman, L. and Wang, T. (2002). Hot Coronal Loop Oscillations Observed by SUMER: Slow Magnetosonic Wave Damping by Thermal Conduction. *ApJ*, 580:L85–L88.
- Ossendrijver, M. (2003). The solar dynamo. *A & A review*, 11:287–367.
- Parker, E. N. (1987). Why do stars emit X rays? *Physics Today*, 40:36–42.
- Phillips, K. J. H. (1992). *Guide to the Sun*. Guide to the Sun, ISBN 052139483X, Cambridge University Press, 1992.
- Phillips, K. J. H., Read, P. D., Gallagher, P. T., Keenan, F. P., Rudawy, P., Rimpolt, B., Berlicki, A., Buczyłko, A., Diego, F., Barnsley, R., Smartt, R. N., Pasachoff, J. M., and Babcock, B. A. (2000). SECIS: The Solar Eclipse Coronal Eclipse Imaging System. *Sol. Phys.*, 193:259–271.
- Priest, E. and Forbes, T. (2000). *Magnetic Reconnection*. Cambridge UP, Cambridge.

- Priest, E. R. (1982). *Solar Magnetohydrodynamics*. D. Reidel Publishing Company.
- Priest, E. R., Foley, C. R., Heyvaerts, J., Arber, T. D., Mackay, D., Culhane, J. L., and Acton, L. W. (2000). A Method to Determine the Heating Mechanisms of the Solar Corona. *ApJ*, 539:1002–1022.
- Reeves, K. K., Shoer, J., Deluca, E. E., Winebarger, A. R., Ofman, L., and Davila, J. M. (2001). New Observations of Oscillating Coronal Loops. *AGU Fall Meeting Abstracts*, page A704.
- Robbrecht, E., Verwichte, E., Berghmans, D., Hochedez, J. F., and Poedts, S. (2000). Slow Magnetoacoustic Waves in Coronal Loops: EIT vs TRACE. In *AIP Conf. Proc. 537: Waves in Dusty, Solar, and Space Plasmas*, page 271.
- Robbrecht, E., Verwichte, E., Berghmans, D., Hochedez, J. F., Poedts, S., and Nakariakov, V. M. (2001). Slow magnetoacoustic waves in coronal loops: EIT and TRACE. *A & A*, 370:591–601.
- Roberts, B. (1981). Wave propagation in a magnetically structured atmosphere. I - Surface waves at a magnetic interface. *Sol. Phys.*, 69:27–38.
- Roberts, B. (1985). Magneto hydrodynamic Waves. In Priest, E. R., editor, *Solar System Magnetic Fields*, pages 37–79. D. Reidel.
- Roberts, B. (1986). Guided MHD waves as a coronal diagnostic tool. In *Coronal and Prominence Plasmas*, pages 325–327.
- Roberts, B. (1991). Magneto hydrodynamic Waves in the Sun. In Priest, E. R. and Hood, A. W., editors, *Advances in Solar System Magnetohydrodynamics*, pages 105–136. Cambridge University Press.
- Roberts, B. (2004). MHD Waves in the Solar Atmosphere. In *ESA SP-547: SOHO 13 Waves, Oscillations and Small-Scale Transients Events in the Solar Atmosphere: Joint View from SOHO and TRACE*, pages 1–14.
- Roberts, B. (2006). Slow mhd waves. In *Phil. Trans. of The Royal Society*, volume 364, page 447.
- Roberts, B., Edwin, P. M., and Benz, A. O. (1984). On coronal oscillations. *ApJ*, 279:857–865.
- Roberts, B. and Webb, A. R. (1978). Vertical motions in an intense magnetic flux tube. *Sol. Phys.*, 56:5–35.
- Ruderman, M. S. (2003). The resonant damping of oscillations of coronal loops with elliptic cross-sections. *A & A*, 409:287–297.
- Ruderman, M. S. and Roberts, B. (2002). The Damping of Coronal Loop Oscillations. *ApJ*, 577:475–486.
- Sakai, J. I., Kawata, T., Yoshida, K., Furusawa, K., and Cramer, N. F. (2000). Simulation of a Collision between Shock Waves and a Magnetic Flux Tube: Excitation of Surface Alfvén Waves and Body Alfvén Waves. *ApJ*, 537:1063–1072.
- Schrijver, C. J., Aschwanden, M. J., and Title, A. M. (2002). Transverse oscillations in coronal loops observed with TRACE - I. An Overview of Events, Movies, and a Discussion of Common Properties and Required Conditions. *Sol. Phys.*, 206:69–98.
- Schrijver, C. J. and Brown, D. S. (2000). Oscillations in the Magnetic Field of the Solar Corona in Response to Flares near the Photosphere. *ApJ*, 537:L69–L72.

- Schultz, A. B., Fraquelli, D., Calzetti, D., Arribas, S., Bergeron, L., Bker, T., Dickinson, M., Holfeltz, S., Monroe, B., Noll, K., and Sosey, M. (2000). NICMOS Coronagraphy. *Bulletin of the American Astronomical Society*, 32:1419.
- Solov'ev, A. A., Mikhalyaev, B. B., and Kiritchek, E. A. (2002). *Plasma Physics Reports*, 28:699.
- Somasundaram, K., Venkatraman, S., and Sengottuvel, M. P. (1999). Hydromagnetic surface waves along compressible cylindrical flux tubes with steady flows. *Plasma Physics and Controlled Fusion*, 41:1421–1428.
- Spiegel, E. A. and Weiss, N. O. (1980). Magnetic activity and variations in solar luminosity. *Nature*, 287:616.
- Spruit, H. C. (1982). Propagation speeds and acoustic damping of waves in magnetic flux tubes. *Sol. Phys.*, 75:3–17.
- Steinolfson, R. S. and Davila, J. M. (1993). Coronal heating by the resonant absorption of Alfvén waves - Importance of the global mode and scaling laws. *ApJ.*, 415:354–363.
- Terra-Homem, M., Erdélyi, R., and Ballai, I. (2003). Linear and non-linear MHD wave propagation in steady-state magnetic cylinders. *Sol. Phys.*, 217:199–223.
- Van Doorselaere, T., Debosscher, A., Andries, J., and Poedts, S. (2004). The effect of curvature on quasi-modes in coronal loops. *A & A*, 424:1065–1074.
- Verwichte, E., Foullon, C., and Nakariakov, V. M. (2006). Fast magnetoacoustic waves in curved coronal loops. I. Trapped and leaky modes. *A & A*, 446:1139–1149.
- Verwichte, E., Nakariakov, V. M., and Cooper, F. C. (2005). Transverse Waves in a Post-Flare Supra Arcade. In *ESA SP-600: The Dynamic Sun: Challenges for Theory and Observations*.
- Verwichte, E., Nakariakov, V. M., Ofman, L., and Deluca, E. E. (2004). Transverse Oscillations in a Coronal Loop Arcade. In *ESA SP-575: SOHO 15 Coronal Heating*, page 460.
- Wang, T., Solanki, S. K., Curdt, W., Innes, D. E., and Dammasch, I. E. (2002a). Doppler Shift Oscillations of Hot Solar Coronal Plasma Seen by SUMER: A Signature of Loop Oscillations? *ApJ*, 574:L101–L104.
- Wang, T. J. (2004). Coronal loop oscillations: Overview of recent results in observations. In *ESA SP-547: SOHO 13 Waves, Oscillations and Small-Scale Transients Events in the Solar Atmosphere: Joint View from SOHO and TRACE*, pages 417–426.
- Wang, T. J., Solanki, S. K., Curdt, W., Innes, D. E., and Dammasch, I. E. (2002b). Hot loop oscillations seen by SUMER: examples and statistics. In *ESA SP-505: SOLMAG 2002. Proceedings of the Magnetic Coupling of the Solar Atmosphere Euroconference*, pages 199–202.
- Wang, T. J., Solanki, S. K., Innes, D. E., and Curdt, W. (2002c). Initial features of an X-class flare observed with SUMER and TRACE. In *ESA SP-505: SOLMAG 2002. Proceedings of the Magnetic Coupling of the Solar Atmosphere Euroconference*, pages 607–610.
- Wang, T. J., Solanki, S. K., Innes, D. E., Curdt, W., and Marsch, E. (2003). Slow-mode standing waves observed by SUMER in hot coronal loops. *A & A*, 402:L17–L20.
- Watson, G. N. (1952). *Theory of Bessel Functions*. Cambridge University Press (2nd ed.).
- Wilhelm, K., Curdt, W., Marsch, E., Schuhle, U., Lemaire, P., Gabriel, A., Vial, J.-C., Grewing,

- M., Huber, M. C. E., Jordan, S. D., Poland, A. I., Thomas, R. J., Kuhne, M., Timothy, J. G., Hassler, D. M., and Siegmund, O. H. W. (1995). SUMER - Solar Ultraviolet Measurements of Emitted Radiation. *Sol. Phys.*, 162:189–231.
- Williams, D. R., Mathioudakis, M., Gallagher, P. T., Phillips, K. J. H., McAteer, R. T. J., Keenan, F. P., Rudawy, P., and Katsiyannis, A. C. (2002). An observational study of a magneto-acoustic wave in the solar corona. *Monthly Notices Roy. Astron. Soc.*, 336:747–752.
- Williams, D. R., Phillips, K. J. H., Rudawy, P., Mathioudakis, M., Gallagher, P. T., O’Shea, E., Keenan, F. P., Read, P., and Rompolt, B. (2001). High-frequency oscillations in a solar active region coronal loop. *Monthly Notices Roy. Astron. Soc.*, 326:428–436.
- Wilson, P. R. (1980). The general dispersion relation for the vibration modes of magnetic flux tubes. *A & A*, 87:121–125.
- Zaitsev, V. V. and Stepanov, A. V. (1975). On the origin of pulsations of type IV solar radio emission. Plasma cylinder oscillations (I). *Issled. Geomagn. Aeron. Fiz. Solntsa*, 37:3–10.
- Zhugzhda, Y. D. (2004). Slow nonlinear waves in magnetic flux tubes. *Physics of Plasmas*, 11:2256.